2014-11-01

Preparation of Active, Stable Supported Iron Catalysts and Deactivation by Carbon of Cobalt Catalysts for Fischer-Tropsch Synthesis

Kamyar Keyvanloo
Brigham Young University - Provo

BYU ScholarsArchive Citation

Keyvanloo, Kamyar, "Preparation of Active, Stable Supported Iron Catalysts and Deactivation by Carbon of Cobalt Catalysts for Fischer-Tropsch Synthesis" (2014). *All Theses and Dissertations*. 5705.
https://scholarsarchive.byu.edu/etd/5705

Preparation of Active, Stable Supported Iron Catalysts and Deactivation by Carbon of Cobalt Catalysts for Fischer-Tropsch Synthesis

Kamyar Keyvanloo

A dissertation/thesis submitted to the faculty of
Brigham Young University
in partial fulfillment of the requirements for the degree of

Doctor of Philosophy

William C. Hecker, Chair
Calvin H. Bartholomew
Morris D. Argyle
John D. Hedengren
W. Vincent Wilding

Department of Chemical Engineering

Brigham Young University

November 2014

ABSTRACT

Preparation of Active, Stable Supported Iron Catalysts and Deactivation by Carbon of Cobalt Catalysts for Fischer-Tropsch Synthesis

Kamyar Keyvanloo
Department of Chemical Engineering, BYU
Doctor of Philosophy

The first half of this dissertation reports the development of supported Fe FT catalysts including the effects of various, carefully chosen preparation methods on the performance of alumina-supported iron/copper/potassium ($FeCuK/Al_2O_3$); it was determined that non-aqueous slurry impregnation and co-impregnation yielded catalysts with activities as high as any reported in the literature. Furthermore, the effects of support properties including pore size, hydroxyl group concentration, and support stabilizer were investigated for $FeCuK/Al_2O_3$ catalysts containing 20 or 40% Fe. For the first time, we report the performance of a *supported* Fe FT catalyst that is not only more active and stable than any *supported* Fe catalyst previously reported, but also has activity equivalent to that of the most active, *unsupported* catalysts. More importantly, the catalyst is extremely stable as evidenced by the fact that after 700 h on stream, its activity and productivity are still increasing. These catalyst properties result from the use of a novel γ-alumina support material doped with silica and pretreated at 1100°C. This unique support has a high pore volume, large pore diameter, and unusually high thermal stability. The ability to pretreat this support at 1100°C enables preparation of a material having a low number of acid sites and weak metal oxide-support interactions, all desirable properties for an FT catalyst.

The second half of this dissertation investigates the effects of operating conditions including the partial pressures of CO and H_2 and temperature on the deactivation by carbon of 25 wt% Co/ 0.25 wt% Pt/Al_2O_3 catalyst. It also reports the kinetics of the main FT reaction on this catalyst. As temperature increases, the H_2 and CO orders for the main reaction (in the absence of deactivation) become more positive and more negative, respectively. A new mechanism was proposed to account for the inhibition effect of CO at high reaction temperatures, which includes H-assisted dissociation of CO to C* and OH*. Further, twelve samples of the $CoPt/Al_2O_3$ catalyst were tested over a period of 800 hours and $X_{CO} < 24\%$, each at a different set of CO and H_2 partial pressures and temperature (220-250°C). At reaction temperature of 230°C, increasing P_{CO} or P_{H2} increases the deactivation rate; possibly due to formation of polymeric carbons. The H_2 and CO partial pressure orders for the deactivation rate at 230°C were found to be 1.12 and 1.43, respectively using a generalized-power-law-expression (GPLE) with limiting activity of 0.7 and 1st order deactivation. For a H_2/CO of 2 ($P_{H2} = 10$ bar and $P_{CO} = 5$ bar) the deactivation rate increases as process temperature increases from 220 to 250°C with an activation energy of 81 kJ/mol. However, at higher CO partial pressure ($P_{CO} = 10$ bar) the deactivation rate for the Co catalyst of this study *decreases* with increasing temperature; this can possibly be attributed to the formation of more active cobalt sites at higher temperatures due to surface reconstruction.

Keywords: Fischer-Tropsch, supported iron, silica-stabilized alumina, cobalt catalyst, deactivation by carbon, kinetics

ACKNOWLEDGEMENTS

I would like to express my highest appreciation to my advisor, Dr. William Hecker for his mentoring and guidance through research while giving me freedom to try new things and responsibilities to become an independent researcher. I have enjoyed your encouragement, friendship, and support—particularly the moments when we discovered new things and approaches to solve scientific issues.

A very special thanks to Dr. Calvin Bartholomew who spent many hours teaching me how to be a better scientist and writer. I have enjoyed every moment of our meetings in which you patiently taught me the fundamentals of catalysis, especially catalyst preparation and deactivation. Your guidance and support played a crucial role in my success.

I wish to acknowledge my committee, especially Dr. Morris Argyle and Dr. John Hedengren, for their support and assistance. Also I would like to thank Dr. Brian Woodfield and his group, especially Maryam Khosravi and Baiyu Huang, from the BYU Chemistry and Biochemistry Department for their contribution; in fact, their unique silica-stabilized alumina support was a key factor in our iron catalyst developments. My special thanks to Dr. Gary Jacobs from the Center for Applied Energy Research at the University of Kentucky, for H_2-TPD and XANES/EXAFS work which was a vital part of our Co deactivation work. Thanks to Dr. J.W. (Hans) Niemantsverdriet and Remco Lancee from Eindhoven University of Technology for XPS results.

This work could have never been possible without the consistent help of the students of the BYU Catalysis Laboratory. Many thanks to Grant Harper, Brad Chandler, Luke Harrison, Jonathon Horton, Dane Bennion, Phillip Childs, Michael Albretsen, Logan Clark, Hector Perez, Trent Okeson, Steven Lanham, McCallin Fisher, Jacob Knudson, and others who spent many days and nights operating the test reactor, preparing and characterizing catalysts, and performing modeling work. A special thanks to Trent Okeson for designing and building the unique wax-extraction system to make characterization of spent catalysts possible.

Finally, I would like to thank my family for their countless love and support—my mother, father, and two brothers (Kaveh and Pooria) who have had the most encouragement, patience, love, and confidence in me. They have inspired me to continue to strive to be the best. Thank you for always being there for me.

TABLES OF CONTENT

LIST OF TABLES

LIST OF FIGURES

Chapter 1 Introduction

This chapter provides background information on Fischer-Tropsch Synthesis (FTS), compares unsupported and supported iron catalyst with brief information on iron catalyst preparation, and discusses cobalt deactivation pathways including poisoning, sintering, oxidation, cobalt aluminate formation, carbon deposition, bulk cobalt carbide, and surface reconstruction.

1.1 Fischer-Tropsch Synthesis

Increasing global concerns regarding dwindling petroleum reserves, the environmental impacts of oil production and transportation, and politically unstable sources of petroleum are driving for the development of alternatives to conventional petroleum resources to supply liquid fuels. Fischer-Tropsch Synthesis (FTS), the production of liquid hydrocarbons from synthesis gas (CO and H_2) is an economically and environmentally-sound method to produce fuels and chemicals from natural gas, coal, and biomass. Processes which convert natural gas, coal, and biomass to liquid fuels are referred to as gas-to-liquids (GTL), coal-to-liquids (CTL), and biomass-to-liquids (BTL). FTS is a key step in GTL processes that are being developed and commercialized to convert remotely located or flared natural gas to sulfur-free diesel fuel.

Because of the renewed interest in the FT process, many companies have invested heavily into developing FTS technology; these include BP, ExxonMobil, Shell, Statoil, Syntroleum, and ConocoPhilips [1]. Sasol with total production beyond 200,000 bbl/day and Shell with a total production of 155,000 bbl/d of liquid fuels are the largest producers of diesel and aviation fuels and chemicals via FTS. The main factors that have contributed to this increasing interest in FT process are:

(1) Increasing prices of crude oil during the past decade to as high as \$150/bbl ,which in the past 3-4 years stabilized around \$100/bbl. A recent study by de Smit and Weckhuysen [2] showed a tripled output of peer reviewed FTS research papers since 1995 as the oil price increased significantly. This revived activity has been very probably stimulated by the increase in crude oil price, although it is also inspired by limitation in oil resources.

(2) Rapid economic and population growth and increasing demand for liquid fuels in large, developing countries (e.g. China and India) has intensified and will continue to greatly intensified the problem. While the United States is the largest petroleum consumer with 18.5 million barrels per day in 2013, demand is increasing in large countries, e.g., China with a consumption of 10.3 million barrels per day. CTL process can be used in China and India as they have large amounts of coal reserves. Interestingly, Sasol has announced it will build CTL plants in the near future in both China and India [3].

(3) Improved environmental awareness and legislative constraints on CO_2 and sulfur emissions have made FTS technology even more attractive. Impacts of oil drilling, oil spills, and flaring of co-produced natural gas are serious environmental concerns surrounding oil production. Furthermore, synthesis fuels are much cleaner than those produced from crude oil. For example, diesel fuel produced from CTL has a sulfur content of less than 0.1 ppm and aromatic content of less than 1%.

Commercial FT plants currently operating or announced are represented in Table 1.1. Two companies, Sasol and Shell, have proven GTL technologies which have been demonstrated in commercial scale GTL plants. PetroSA has completed a semi-commercial demonstration of FT technology at PetroSA's Mosselbay GTL plant. Shell is currently producing 15,000 bbl/d of diesel fuel from natural gas in Bintulu, Malaysia and 140,000 bbl/day of diesel in their Qatar Pearl plant, which owns 15% of the world's gas reserves [4]. Sasol's recently-built Oryx-GTL in Ras Laffan, Qatar jointly owned by Sasol and Qatar Petroleum has a nominal capacity of 34,000 bbl/day. Chevron in a joint venture with the Nigerian National Petroleum Corporation is commissioning a 34,000 bbl/d GTL plant in Nigeria with a cobalt based FT catalyst, which uses Sasol technology. The Escarvaros GTL plant has the same technology and capacity of Oryx-GTL plant in Qatar and is expected to start up by mid 2014. Two commercial FT plants operated by Sasol and PetroSA, use iron catalyst to convert natural gas to liquid. In both cases, unsupported iron catalyst is being used. Sasol is using slurry and fluidized-bed CTL technologies for their iron-based GTL plants in Sasolburg and Secunda to produce mainly chemicals.

Table 1.1. Current commercial GTL/FT plants [4, 5].

Company	Location	Catalyst type	Plant capacity, bbl/day	Start-up date
Sasol	Sasolburg, South Africa	Precipitated iron	5,000	1993
Shell	Bintulu, Malaysia	Co/SiO_2 Co/TiO_2	14,500	1992
PetroSA	Mosselbay, South Africa	Fused iron	22,000	1993
Sasol-QP (Oryx-GTL)	Ras Laffan, Qatar	Co/Al_2O_3	34,000	2007
Shell-QP (Pearl)	Ras Laffan, Qatar	Co/TiO_2	140,000	2011
Chevron-Sasol	Escarvaros, Nigeria	Co/Al_2O_3	34,000	Mid 2014

1.2 FTS catalysts

Group 8 transition metals are known to catalyze the FT reaction. However, only Ni, Co, Fe, and Ru have sufficient CO hydrogenation activity for commercial application. Nickel mainly produces methane at FT reaction temperatures. It also forms nickel carbonyl which facilitates sintering via atomic migration [6]. Ruthenium is the most active FTS catalyst; however, it is prohibitively expensive and relatively scarce for use in industrial scales. As a result, iron and cobalt catalysts are the best two options for commercial FT plants.

The choice of FT catalyst depends on the product distribution desired and the process that is being used. The three key parameters of a catalyst are catalytic activity, selectivity, and longevity. Iron generally produces more olefins and oxygenates than cobalt. The active phase in cobalt FT catalysts is the metallic state while for iron catalysts the active sites are probably iron carbides [7-9].

The principal stoichiometric reactions in FTS include:

$$CO + 3H_2 \rightarrow CH_4 + H_2O \qquad \text{-247 kJ/mol} \tag{1.1}$$

$$CO + 2H_2 \rightarrow -CH_2 + H_2O \qquad \text{-165 kJ/mol} \tag{1.2}$$

$$CO + H_2O \rightarrow H_2 + CO_2 \qquad \text{-42 kJ/mol} \tag{1.3}$$

Oxygen produced from CO dissociation can generally be removed in two ways: (1) oxygen removal as water which occurs with a selectivity of about 99% for cobalt catalysts, and (2) oxygen removal as CO_2 which occurs with a selectivity of 30-50% for iron catalysts because of their high water-gas-shift (WGS; reaction 1.3) activity. Given their low WGS activity and high selectivities for liquid and waxy hydrocarbons, Co catalysts are highly preferred for GTL.

On the other hand, since iron catalysts can produce H_2 via the WGS at a selectivity of 30-50%, they are better suited for CTL and BTL which produce syngas of lower H_2/CO ratios.

1.2.1 Iron catalysts: supported vs. unsupported

Typical commercial iron FT catalysts consist of unsupported iron promoted with copper, potassium, and texturized with silicon oxide. Potassium and copper promoters have found wide use in the preparation of commercial iron FT catalyst. Potassium is a chemical promoter which increases the extent of CO dissociation on Fe, surface coverage of C relative to H, and decreases methane selectivity [10]. Copper serves as a reduction promoter, i.e., it helps the Fe reduce at lower temperatures, dissociates H_2 which spills over to Fe oxide, and thereby improves reducibility of iron. When both Cu and K are present, the reduction and carbiding processes are faster [10] resulting in a higher population of carbide nucleation sites than with only one promoter present [11]. An oxide of silicon or aluminum is typically added to the catalyst at relatively low concentrations (5-20%) as a textural promoter, i.e., providing higher surface area and thermal stability to the catalyst. If an oxide of high thermal stability such as Al_2O_3, SiO_2, or TiO_2 is used as the majority compound (> 50 wt%) for supporting Fe, the resulting catalyst is called a supported Fe catalyst.

Several publications from Bukur et al. [7, 8, 12, 13] describe development of active, selective and stable precipitated iron catalysts (unsupported) including one containing $3Cu/4K/16SiO_2$ per 100 parts Fe with a reaction rate or activity in the form of a weight-time yield of 450 mmol $(CO+H_2)/g_{Fe}/h/MPa$ at 260 °C and 2.2 MPa. This activity is among the highest reported for iron catalysts. Unfortunately, despite favorable high activity and selectivity properties, these unsupported iron catalysts are generally weak mechanically which can lead to high rates of attrition during their use in slurry bubble column reactors (SBCRs). Catalyst attrition causes formation of 1-10 micron diameter particles that are very difficult to separate from product wax in SBCRs. The use of binder materials in the catalyst can decrease the attrition problems somewhat, but may also decrease catalyst activity. Nevertheless, commercial entities have developed attrition-resistant, unsupported Fe FT SBCR catalysts for 5 m SBCRs through the generous use of binders [14-16]; however, these catalysts still suffer attrition due to the higher gas velocities in 10 m SBCRs. Moreover, if sufficient binder is incorporated, the composition of the "unsupported catalyst" approaches that of a supported catalyst of high metal loading.

Thus, in principle an alumina-supported iron catalyst is likely to be stronger and more attrition resistant than an unsupported Fe catalyst incorporating binders [17]. Unfortunately, in practice previous attempts to develop supported iron FT catalysts have met with limited success as most of these catalysts were found to have low activity and high methane selectivity [9, 17, 18]. For example, Bukur et al. [12, 18] reported an Fe catalyst supported on SiO_2 to be nearly three times less active than their most active unsupported catalyst (100 vs. 269 mmol($CO+H_2$)/g_{cat}/-MPa/h) while their alumina-supported catalyst was even less active (~60 mmol($CO+H_2$)/g_{cat}/-MPa/h). The Davis group [17, 19] found a similar result, i.e., their most active alumina-supported Fe catalyst was still 5-fold less productive than unsupported iron (0.09 vs. 0.45 g_{HC}/g_{cat}/h) and had high methane selectivity. The poor performance of these catalysts can be attributed to less than ideal preparation methods and support materials favoring strong Fe oxide-support interactions and attendant low reducibility to active Fe carbides, decoration of the active carbide phase by support moieties [18, 20], or some combination of the above.

In this dissertation we report, for the first time, the successful preparation of a very active and stable supported Fe LTFT catalyst, i.e. an Fe/Cu/K catalyst on a silica-doped γ-alumina (AlSi) support material of high thermal stability but having weak interactions with Fe oxide. Key factors leading to the excellent performance of this catalyst were (1) the use of non-aqueous, wet impregnation in a rotary evaporator for catalyst preparation, (2) utilization of a new silica-stabilized alumina (AlSi) support with very high pore volume and large pores, (3) high temperature pre-treatment of the AlSi support to give a minimal concentration of surface OH groups which are known to interact strongly with Fe precursors during impregnation to form Fe oxide, and (4) stabilization of Fe phases against sintering due to the presence of silica on the support surface. We also prepared an Fe/Cu/K catalyst on three conventional γ-alumina supports and an unsupported FeCuKSi for comparison.

1.2.2 Cobalt catalysts: Deactivation modes

Cobalt catalysts are currently the leading candidates for industrial applications of FTS, especially GTL. The state-of-the-art cobalt FT catalyst consists of four components with the following formulation:

(1) Cobalt metal as an active phase (typically 15-30 wt%)

(2) A noble metal promoter (Pt, Ru, Re, Pd) (typically 0.05-1.0 wt%)

(3) A high surface area oxidic support (Al_2O_3, SiO_2, TiO_2)

(4) A support structural promoter (Zr, Ba, La, Si)

Cobalt catalysts are usually dispersed on an oxide support to maximize efficiency and stability. Iglesia et al. [21, 22] found a linear correlation between FTS reaction rates and metal dispersion at larger cobalt crystallites (d >10 nm), suggesting consistent with Johnson et al. [23], that specific activity or turnover frequency (TOF) is constant in well-reduced catalysts containing moderately-large Co crystallites. Fischer et al. [24] found the turnover frequency (TOF) to increase with crystallite diameter up to 12 nm. Den Breenjen [25] found the TOF to increase up to an average Co crystallite diameter of 6 nm, above which it was found to be constant.

Small cobalt crystallites when supported on oxide supports such as silica, alumina, and titania are more difficult to reduce due to strong interaction of metal oxide with the support. Thus, they are often promoted with noble metals, most especially Pt, Re, Ru, or Pd, to improve the reduction behavior of cobalt oxide crystallites. Typically, metal loadings of Pt and Ru are0.05-0.1 wt% due to their high costs; moreover, higher loadings of Pt and Pd produce excessive light gas selectivity; Re and Pd may be used in concentrations up to 1 wt%. Moreover, it has been shown that Pt and Ru noble metals inhibit polymeric carbon formation by gasifying carbon atoms or carbon oligomers or by increasing the barriers for C-C coupling [26].

In addition to important factors such as activity, selectivity, and mechanical strength, the improved stability or longevity of cobalt FT catalysts is crucial to make their use economically viable. After 80 years of research on FTS, the fundamentals of the process including deactivation pathways remain subjects of debate. Understanding catalyst deactivation pathways is essential for improving catalyst stability and effective regeneration procedures. A typical deactivation profile for Co FT catalysts under industrially relevant conditions is shown in Figure 1.1 [27]. The activity loss consists of two stages; the first initial deactivation regime can last a few days to weeks and the second stage is the long-term deactivation regime.

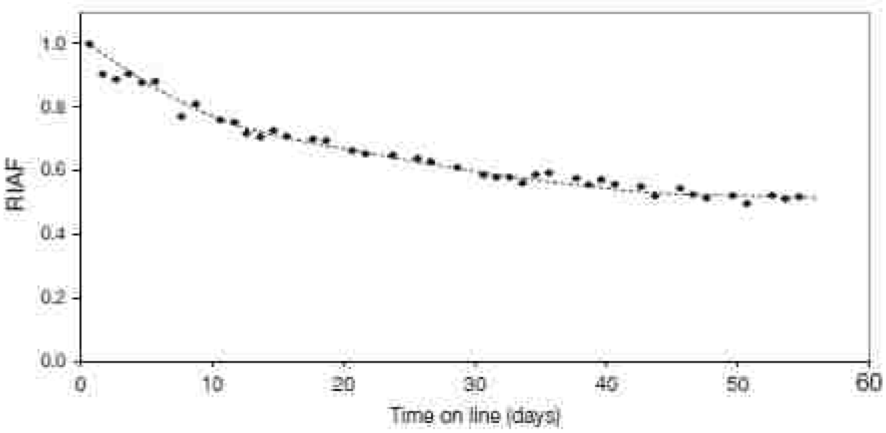

Figure 1.1. Typical normalized activity vs. time for $CoPt/Al_2O_3$ under realistic FT conditions (230 °C, 20 bar, inlet feed of 50-60 vol.% H_2 and 30-40 vol.% CO) [27].

As is apparent, the slope of activity (RIAF) is changing with time suggesting multiple deactivation mechanisms. The proposed mechanisms of Co FT catalyst deactivation include (1) poisoning, (2) sintering, (3) oxidation, (4) cobalt aluminate formation, (5) carbon deposition, (6) bulk cobalt carbide formation, and (7) Co surface reconstruction. These deactivation phenomena are discussed briefly below.

1.2.2.1 Poisoning

Poisoning is strong chemisorption of species on catalytic sites, thereby blocking the sites for reaction. Syngas produced from biomass or coal usually contains a large amount of sulfur and/or nitrogen compounds. Sulfur is a known poison for metals since it adsorbs rapidly and irreversibly. It can physically block three- or four-fold adsorption/reaction sites [28]. Because of the strong chemical bond it electronically modifies the adjacent cobalt sites. Co and Fe suffer 3-4 orders of magnitude activity loss above 15-30 ppb of H_2S [29]; hence sulfur compounds in the feed must be reduced to less than 50 ppb. Nitrogen compounds such as NH_3 and HCN are also poisons for FT catalysts. Their effect is less severe than sulfur compounds and their poisoning is somewhat reversible in pure H_2 or syngas; however, reducing their level to 50 ppb is recommended. Sulfur and nitrogen compounds can be removed by ZnO and acidic adsorbent guard beds, respectively.

1.2.2.2 Sintering

Sintering is agglomeration of metal crystallites which causes loss of catalytic surface area. It is a thermodynamically driven process, whereby smaller, more unstable crystallites grow to form larger counterparts with lower surface energy. Temperature is the most important variable in sintering. Mobility of surface metal atoms is significant above the Tamman temperature, one- fourth of the bulk melting point. The Tamman temperature for cobalt is 253°C, not far from low temperature FT conditions [30]. Considering that FTS is highly exothermic reaction and hot spots may arise during the reaction, the potential for sintering is therefore relatively high. There is a good agreement in the literature on the importance of sintering as one of the main deactivation mechanisms during FTS on Co. High temperature and water accelerate the process. Recently, a water-assisted sintering was proposed by Sadeqzadeh et al. [31, 32]. They postulate that water can partially oxidize surface cobalt metal to form CoO which has a higher surface diffusivity and hence higher probability of colliding and agglomerating with another CoO.

Sintering is a crystallite size dependent process. Smaller crystallites grow during the reaction to form larger counterparts. Sasol reported a 30% drop in activity by sintering of cobalt crystallites [33]. The starting cobalt crystal diameter was 9 nm and it leveled off at about 14 nm after 15 days of commercially-relevant FT operation.

1.2.2.3 Oxidation

There is still debate whether oxidation occurs during commercial FTS. The debate arises from the fact that water, the most abundant byproduct of Co FTS, is an oxidizing agent and may cause surface oxidation of cobalt crystallites. Oxidation is likely to be more important at high CO conversions where the partial pressure of water is high. However, the recent publications provide evidence that Co oxidation does not occur at realistic reaction conditions [27, 30, 34, 35]. Thermodynamic calculations have shown that cobalt crystallites larger than 4.4 nm in diameter cannot oxidize in common FT conditions ($P_{H2O}/P_{H2} < 1.5$, corresponding to 75% CO conversion). That suggests the bulk oxidation of metallic cobalt is not feasible under realistic FTS conditions using a typical FT catalyst. Saib et al. [34] removed wax-coated cobalt FT catalyst samples, having an initial average crystallite diameter of about 6 nm, at various time intervals during reaction in a slurry bubble column reactor, for characterization of the oxidation states of Co by X-ray absorption near edge spectroscopy (XANES). The catalysts were protected in wax from oxidation during the characterization. They found that the cobalt crystallite diameters of above 6 nm are stable to oxidation during realistic FT conditions and that a gradual increase of cobalt metal crystallite size was observed with time. Thus, based on recent publications, oxidation of cobalt crystallites with diameters above 4 nm does not occur under realistic FT reaction conditions.

1.2.2.4 Cobalt aluminate formation

There is also debate on the contribution of cobalt alumina formation as a deactivation mechanism during FT reaction. Deactivation by cobalt aluminate is often described as the formation of irreducible species at the expense of active metallic cobalt. CoO is apparently needed as an intermediate for the formation of cobalt aluminate [5]. This aluminate formation is kinetically hindered at FTS temperatures. However, water which is the main byproduct of FTS can increase the rate of CoO formation for small crystallites ($d_c < 4$ nm) and consequently effect cobalt aluminate formation [36].

Although other researchers reported significant deactivation by formation of cobalt aluminate [37, 38], recent work of Niemantsverdriet's group showed the effect to be very small [35, 39]. Their XANES results on wax-coated spent catalysts demonstrated that cobalt oxide is undergoing more reduction during the reaction and less than 2-3 wt% cobalt aluminate is produced at the expense of residual CoO present in the catalyst following the reduction. This observation led them to conclude that cobalt aluminate formation does not significantly contribute to deactivation during realistic FT conditions.

1.2.2.5 Carbon deposition

CO dissociation is one of the key elementary steps in FTS. The carbon (C or CH_x) formed in this reaction can be converted to FT products via hydrogenation or to stable surface carbon species over time which adversely affect activity through site poisoning or blockage. Although long chain hydrocarbons are the desired products in FTS, those of very high molecular weight can accumulate on the surface blocking sites and/or block small mesopores retarding the rate of diffusion of the reactants from catalyst particles. Carbon in the form of oligomers or graphitic layers may (1) strongly chemisorb on Co crystallites or physically adsorb in multilayers, in either case blocking available active sites for reaction and (2) partially or completely plug mesopores limiting accessible to reactants or removal of products. Deactivation by carbon is typically long-term and accounts for the latter stage of activity loss shown in Figure 2.1.

Different forms of carbon with different surface reactivity can build up on the surface during FT reaction. Table 1.2 summarizes various carbon species on cobalt FT catalysts. Atomic carbon or surface carbides are isolated carbon atoms with carbon-metal bonds resulting from CO dissociation. Bulk carbide refers to Co_xC structure formed by diffusion of carbon into the bulk metal. Surface carbide can be a precursor to these bulk species or to the formation of oligomers. CH_x species are active precursors for formation by FTS of longer chain hydrocarbon products; however, these precursors may also form strongly adsorbed high-molecular weight dehydrogenated hydrocarbons known as coke. It has been proposed that the carbon is mostly present as CH_x during FT reaction which is a hydrogen-enriched environment [40], while others proposed carbon atoms as most abundant surface species during the FT reaction [30, 41, 42].

Polymeric carbon refers to oligomers of carbon species that are connected with covalent bond. It may also refer to carbon chains that contain hydrogen. Polymeric carbon is a less reactive carbon than atomic carbon and can form from polymerization of CH_x species. It may also include aromatic rings with alkyl chains of different length such as graphene or polynulear aromatics [43].

Graphene, the most stable form of carbon, is a single layer of carbon atoms packed into a benzene rings structure [5]. It is also considered as a precursor to graphite. The graphene species has strong C-C bonds and weaker C-metal bonds.

Table 1.2. Different carbon species on cobalt FT catalysts with their corresponding hydrogenation temperatures and conditions under which they were identified.

	Reaction conditions					
Carbon species	Catalyst	Temp, °C	H_2/CO	Pressure, bar	$T_{hyd}{}^a$, °C	Ref.
CH_x	Co (0001)	220	1	1	<100	[44, 45]
Atomic carbon	Co/Al_2O_3	250	CO only	1	180-200	[46]
Bulk carbide	$Na\text{-}Co/Al_2O_3$	240	2	50	<250	[47]
Hydrocarbons	Co/Al_2O_3	220-230	1-3	20	250-330	[48, 49]
Polymeric C	Co/Al_2O_3	220-230	1-3	24	400-500	[48-50]
Graphene	Co/SiO_2	200	2	1	>620	[51]
	Co/Al_2O_3	350	CO only	1	520-550	[48, 49]

[a] T_{hyd} = Temperature of hydrogenation

These different types of carbon have different reactivities with hydrogen. Therefore, the most useful characterization technique successfully employed to distinguish and quantify different surface carbons and/or hydrocarbons is temperature-programmed hydrogenation (TPH) of deactivated catalysts at elevated temperatures while monitoring methane evolution in a mass spectrometer. Using TPH of wax-extracted cobalt FT catalysts removed from their slurry bubble column reactor, Moodley et al. [48] found that polymeric carbon builds up with time on the catalyst surface, causing the long-term deactivation. Since the focus of the second part of this thesis is on deactivation of cobalt FT catalysts by carbon, more specific studies and pertinent data will be provided later in the corresponding chapters.

1.2.2.6 Bulk cobalt carbide

Since the active phase in cobalt FTS is cobalt metal, formation of cobalt carbide causes activity loss. The activation energy for diffusion of carbon into cobalt (145 kJ/mol) is much higher than iron (44-69 kJ/mol) suggesting that reduced Co catalysts are less likely to form cobalt carbide.

Industrial experience by Syntroleum [52] and Sasol [4] on Co/Al_2O_3 showed formation of bulk cobalt carbide during an upset condition in the presence of pure CO over a short time period (2-8 h). Catalyst performance was severely lowered as evident by a 50% drop in CO conversion and a doubling of the methane selectivity. These experiments show that Co carbide is likely to form when a Co catalyst is exposed accidentally, to a high concentration of CO with little H_2 present; moreover, if bulk cobalt carbide forms, it is stable in a syngas environment.

Other researchers showed formation of cobalt carbide during FTS. Jacobs et al. [53] found formation of Co_2C on Co/Al_2O_3 used in a CSTR (18 bar, 220°C, and $H_2/CO = 2$) with synchrotron XRD. This is in agreement with the work of Tavasoli et al. [54] who also detected Co_2C peaks in XRD spectra on $Ru/Co/Al_2O_3$ catalysts tested at 220°C, 20 bar, and $H_2/CO = 2$ for over 40 days. Ducreux et al. [55] also observed the formation of Co_2C on Co/Al_2O_3 and $Ru/Co/TiO_2$ catalysts by in situ XRD and related to the deactivation at 230°C, 3 bar and $H_2/CO = 9$.

On the other hand, XRD and XANES characterizations of spent cobalt catalysts run for several months in a slurry bubble column reactor did not show any cobalt carbide formation [48]. Cobalt carbide was also not found on Co/Al_2O_3 in a CO rich environment ($H_2/CO = 1$) at 220 °C and 20 bar after 260 h time on stream in a CSTR [49].

Accordingly, there is not much consensus from the previous literature whether cobalt carbide forms during realistic FTS conditions. Bulk carbide is considered a metastable species, especially in the presence of H_2 [30] and is rarely observed with ex situ techniques [56].

1.2.2.7 Surface reconstruction

Surface reconstruction a process which results in substantive changes in surface structure due to adsorption or reaction; the process may involve either an increase or decrease in surface roughness and/or -surface energy, with the attendant formation of more or less stable surfaces which can contribute to either higher or lower activity. The detection of these phenomena may not be done by ex situ techniques and requires sophisticated instrumentation such as in situ STM or EXAFS coupled with theoretical computations.

Bezemer et al. [57] reported surface reconstruction of cobalt supported on carbon nanofibers with crystallite diameters ranging over 2.6-27 nm. Performing EXAFS on spent catalysts revealed a decrease in the first shell Co-Co coordination number after exposure to synthesis gas, indicating a reconstruction of the cobalt surface during FTS to one of lower surface energy. Only this deactivation mechanism was detected, i.e., no sintering, oxidation or carbon deposition was observed. Density functional theory (DFT) calculations were also conducted on (111) and (100) fcc-cobalt surfaces with following adsorbates: B, N, O, CO, CH_2, CH, and C[58]. Only carbon was predicted to induce reconstruction. These calculations predict that a coverage of 50% carbon on fcc-Co (111) surface will reconstruct the surface to fcc-Co(100) followed by a clock type reconstruction. The adsorption energy of carbon was predicted to be stabilized by 15 kJ/mol compared to unreconstructed surface, thus predicting formation of stable carbon species which could cause deactivation.

Conversely, it was also reported that reconstruction can result in the formation of the active sites for FTS. Wilson and de Groot [59] reported restructuring of a model flat Co (0001) surface to triangular cobalt islands under CO hydrogenation conditions (250°C, 4 bar, H_2/CO = 2). It has also been proposed that additional B5 sites, considered to be active sites for CO dissociation, are produced during reconstruction [60]. Thus, reconstruction during FTS can be accompanied by a change in surface density resulting in the creation of step sites and additional B5 sites.

1.3 Objectives and overview of dissertation

An original objective of the current work was to investigate the effects of process conditions on the deactivation by carbon of a supported Fe FT catalyst. To do so, we studied the preparation of active, stable supported iron catalysts, which, in fact, led to the development of the most active, stable supported Fe catalyst to date; indeed it was found that for Fe/AlSi catalyst activity increases over 700 h of time on stream. By the time the supported Fe catalyst had been developed, an increasing, widespread, global interest in deactivation of cobalt catalysts used in GTL was highly evident; moreover, our group was in a strong position to contribute substantially. Thus, with the enthusiastic concurrence of my advisors, I switched my study to conduct a more focused, comprehensive investigation of deactivation on carbon of a representative cobalt FT catalyst. This then became my second principal objective along with development of the supported Fe catalyst. The same concepts learned in preparing the supported Fe catalyst were exercised in the preparation of the cobalt catalyst, and in fact, the same silica-doped alumina support, that was the key factor in developing the supported Fe catalyst, was used for Co.

Given that background, the remainder of the dissertation (7 chapters altogether) consists of a chapter addressing experimental methods, two chapters addressing development of results for the supported Fe catalysts, two chapters summarizing results for Co deactivation, and a final chapter with future work recommendations. A preview of Chapters 2-7 follows:

Chapter 2 describes the apparatus and experimental procedures used in the catalyst preparation and characterization of iron and cobalt catalysts.

Chapter 3 focuses on the optimization of catalyst preparation variables for supported iron FT catalysts, which includes catalyst characterizations, activity, selectivity, and stability results.

Chapter 4 discusses the effect of support properties and SiO_2 stabilizer on the activity and stability of supported iron FT catalysts. It also reports on the successful preparation of the most active supported Fe FT catalyst to date and a catalyst that is very stable with <u>no deactivation</u> during 700 h time on stream.

Chapter 5 focuses on the effect of partial pressures of CO and H_2 and temperature on the deactivation by carbon deposition for the cobalt FT catalyst by different characterization techniques on the freshly reduced and wax-extracted spent catalysts.

Chapter 6 reports results of the comprehensive study of the kinetics of both the main reaction and deactivation reaction for the cobalt FT catalyst and describes the development of a macrokinetic model based on a proposed mechanism for main reaction and general power-law expressions (GPLE's) for deactivation.

Chapter 7 identifies possible future works.

Chapter 2 Experimental Techniques

This chapter describes the preparation procedures for the catalyst used in this study, catalyst characterization techniques, a wax-extraction technique used to remove the wax from spent cobalt catalysts, and activity, selectivity, and stability measurements performed using a Fixed-bed reactor. Table 2.1 summarizes preparation methods and compositions of the catalysts prepared in this study, which includes ten supported Fe catalyst, one unsupported Fe, and one supported Co catalyst.

Table 2.1. Overview of all the catalysts prepared in this study.

Catalyst	Solvent	Deposition method	Support type	Metal, wt%	Promoter loading	Timing of impregnation
FeCuKSi[1]	--	SDP[2]	--	75 Fe	4K/5Cu/16Si/100Fe	--
K1 – 20Fe/AlG	NA[3]	SI[4]	AlG[5]	20 Fe	4K/7.5Cu/100Fe	Sequential
K2 – 40Fe/AlG	NA	SI	AlG	40 Fe	4K/7.5Cu/100Fe	Sequential
K3	A[6]	IWI[7]	AlG	20 Fe	4K/7.5Cu/100Fe	Sequential
K4	A	IWI	AlG	20 Fe	8K/7.5Cu/100Fe	Sequential
K5	A	IWI	AlG	20 Fe	4K/7.5Cu/100Fe	co-impregnation[8]
K6	A	IWI	AlG	20 Fe	4K/7.5Cu/100Fe	Sequential
20Fe/AlA	NA	SI	AlA[9]	20 Fe	4K/7.5Cu/100Fe	Sequential
20Fe/AlC	NA	SI	AlC[10]	20 Fe	4K/7.5Cu/100Fe	Sequential
20Fe/AlSi	NA	SI	AlSi[11]	20 Fe	4K/7.5Cu/100Fe	Sequential
40Fe/AlSi	NA	SI	AlSi	40 Fe	4K/7.5Cu/100Fe	Sequential
CoPt/Al_2O_3	NA	SI	AlSi	25 Co	0.25 wt% Pt	co-impregnation

[1] Unsupported Fe catalyst
[2] Solvent-deficient precipitation
[3] NA = Non-aqueous
[4] SI = Slurry impregnation
[5] St. Gobein alumina
[6] A = Aqueous
[7] IWI = Incipient wetness impregnation
[8] Fe, Cu and K are added at the same time in each impregnation step
[9] Alfa-aesar
[10] Alumina provided by Cosmas Inc.
[11] Silica-doped alumina provided by Cosmas Inc.

2.1 Catalyst preparation

2.1.1 Support

2.1.1.1 Alumina support stabilization with La

γ-Al_2O_3 supports (Alfa Aesar and St. Gobein aluminas) were stabilized with La to improve the thermal stability. The alumina support was first dried in air at 100°C for 2 h and calcined to 400°C for 2 h. A chelating agent of Ethylenediaminetetraacetic acid (EDTA, Mallinckrodt Chemicals, 99.4%) and the La precursor of lanthanum nitrate ($La(NO_3)_3.6H_2O$, Fisher Scientific, > 98% pure) were dissolved and poured onto buffer-submerged alumina and stirred in a rotary evaporator for 4 h. The buffer was acetic acid/acetate and produced a constant pH of 5. The solution then was poured off and the impregnated alumina was washed and stirred in rotary evaporator with HPLC grade water for 1 h. This washing was repeated twice and then the support was dried under vacuum at 55 °C overnight. Next, the La_2O_3-Al_2O_3 was bulk calcined in air using three temperature ramping steps: (1) ambient temperature to 100°C at 0.5 °C /min, soaked for 1 hour, (2) 100 to 120°C at 1 °C/min, soaked for 16 hours, and (3) ramped to 700°C at 1 °C/min for 8 h.

2.1.1.2 Silica-doped alumina support (AlSi)

A silica-doped alumina support (AlSi) was prepared using a "one-pot" solvent-deficient method starting with aluminum isopropoxide (AIP, $C_9H_{21}O_3Al$, granular, 98+%) and tetraethyl orthosilicate (TEOS, $SiC_8H_{20}O_4$, liquid, 99.9%), both purchased from Alfa-Aeser. Specifically, water was added to AIP in a 5:1 molar ratio and mixed briefly. TEOS was then added with a small amount of additional water (1:2 molar ratio) in a quantity sufficient to give 5 wt% silica in the final support material. The resulting mixture was then stirred for 30 minutes in a Bosch mixer, followed by thermal treatment at 700°C in air for 2 h to form gamma alumina after heating at ~2.5 °C/min. The product was then cooled to room temperature after which it was heated to 1100°C over 5 h and held at 1100°C for 2 h [61-63].

2.1.2 Iron catalysts

2.1.2.1 Unsupported iron catalyst

Solvent deficient precipitation (SDP) produces metal oxide nanomaterials [61, 64] which can be used as supports, oxide catalysts, or catalyst precursors. An unsupported Fe catalyst was prepared by SDP to compare to the supported Fe catalyst made in this study. A dry mixture of iron nitrate ($Fe(NO_3)_3.9H_2O$, Sigma Aldrich, 98%), copper nitrate ($Cu(NO_3)_2.2.5H_2O$, Sigma Aldrich, 98%), potassium bicarbonate ($KHCO_3$, Sigma Aldrich, 100 wt% dry basis), and silica was added to ammonium bicarbonate ($(NH_4)HCO_3$, Merk) in a solvent deficient environment and mixed for half an hour. After precipitation, the resulting material (without washing) was dried at 120°C overnight and calcined at 300°C for 16 h. The resulting oxide precursors are denoted throughout as FeCuKSi.

2.1.2.2 Supported iron catalysts

As different techniques were used to optimize the preparation of supported Fe catalysts, the details of those preparations will be discussed fully in Chapters 3 and 4.

2.1.3 Cobalt catalyst

One Co/AlSi catalyst was prepared and used for all the deactivation tests of this study. The 5% silica contained in AlSi improves its thermal stability, and allowed the support to be calcined at 1100°C to remove most of the acidic sites. After this step the Co/AlSi catalyst was then prepared by co-impregnation of the support with a non-aqueous solution (50% iso-propanol and 50% acetone; both from Fisher Scientific, 99.8%) containing desired amounts of cobalt nitrate ($Cu(NO_3)_2.6H_2O$, Sigma Aldrich, 98%) in three steps. In the first two steps 10 wt% Co was dissolved in a volume of solution corresponding to 2.5 times above incipient wetness and was then placed in a rotary evaporator and mixed for 12 h to give an uniform Co deposition. The catalyst was then dried slowly in vacuum at 50°C for 12 h followed by 80°C in air overnight. After drying, the samples were calcined at 250°C for 16 h in air. For the third step (last step), an amount of tetraammineplatnium(II) nitrate ($Pt(NH_3)_4(NO_3)_2$, Sigma Aldrich, 99.995%) calculated to give 0.25 wt% Pt in the final catalyst was dissolved in HPLC water and mixed with sufficient cobalt nitrate non-aqueous solution to add 5 wt% Co to the final catalyst in a rotary evaporator for 12 h mixing, followed by additional drying and calcination steps. Nominal composition (on a relative mass basis) of synthesized catalyst was $25Co/0.25Pt/74.75Al_2O_3$.

2.1.4 Bulk calcination, reduction, and passivation

Temperature programmed oxidation (TPO) and temperature-programmed reduction (TPR) measurements of representative samples of each catalyst of this study were carried out in a thermo-gravimetric analyzer (TGA) to determine the temperature program for the calcination and reduction, respectively, of each catalyst.

2.1.4.1 Supported and unsupported iron catalysts

Precursors for all the iron catalysts above were bulk calcined (5–10 g material) at 300°C in flowing air at a GHSV of > 2000 for about 20 h. Temperature was ramped from ambient to 140-160°C at 0.5 °C/min, soaked for 2 hour, then ramped to 210°C at 0.5 °C/min, soaked for 2 hours, and finally ramped to 300°C at 0.5 °C/min for the final soak at 300°C for 10 h.

Calcined iron catalysts were reduced at 280-320°C in 10% H_2/He followed by 100% H_2 at a GHSV of > 2000. Temperature was ramped from ambient temperature to 120°C at 0.5 °C/min, soaked for 1 hour, then ramped to 190-210°C at 0.5 °C/min, soaked for 2 hours, and finally ramped to 280-320°C at 0.5 °C/min for 10 h in 10% H_2. Following the 10 hour soak, the composition was switched to 100% H_2 for an additional 6 hour soak at 300°C. The catalyst was then cooled in He to less than 30°C. The reduced catalyst was carefully passivated by first exposing it to flowing air in helium (< 1% air) followed by gradually increasing the concentration of air so that the wall of the metal reactor tube in contact with the bed had less than 3°C temperature increase.

2.1.4.2 Cobalt catalyst

Approximately 80 g of cobalt catalyst was bulk calcined at 250°C in flowing air at a GHSV of > 2000. Temperature was ramped from ambient temperature to 100°C at 0.5 °C /min, soaked for 2 hour, then ramped to 130°C at 0.5 °C/min, soaked for 2 hours, and finally ramped to 250°C at 0.5 °C/min for 6 h.

The catalyst was further reduced in hydrogen at 450 °C with a GHSV of > 2000 for 64 hours. It was intentionally reduced at high temperature for a longer time than normal to re-sinter cobalt crystallites and start with larger cobalt crystallites to prevent deactivation by sintering during the FT reaction. Temperature was ramped from ambient temperature to 135 °C at 1 °C/min, soaked for 2 hour, then ramped to 230°C at 0.5 °C/min, soaked for 2 hours, and finally ramped to 450°C at 0.5 °C/min for 16 h in 10% H_2. Following the 16 hour soak, the composition was switched to 100% H_2 for an additional 32 hour soak at 450°C. Then the catalyst was passivated as previously described in section 2.1.6.1.

2.1.5 Activation procedure

All catalysts tested in the FB system were activated in syngas (CO and H_2) following *in situ* reduction in H_2.

2.1.5.1 Supported iron catalysts

First, calcined catalysts were reduced in situ at 280-320°C in 10% H_2/He for 10 h followed by 100% H_2 for 6 h. After reduction, the furnace temperature was reduced to 180°C in H_2 and reactants were introduced at a composition of 30% H_2/30% CO/4% Ar/36% He). The system was then pressurized to 20 atm and the furnace temperature was increased gradually to ~ 260°C according to the temperature schedule shown in Table 2.2 to get to a catalyst bed temperature of 280°C. During the temperature increase for the activation step, the flow rates were adjusted to get 50-60% CO conversion at the final temperature. Conversion and temperature during activation was intentionally higher to speed up the time required to carbide the catalyst, fill the pores with wax, and achieve steady state activity. Activation was considered complete only after the ratio of standard deviation to GC peak area was less than 0.02 for effluent values of H_2, CO, and Ar. This usually took 12-24 h. After the activation, the temperature was reduced to the desired temperature and the flow rates were also adjusted to get CO conversion of less than 25% to gather kinetic data.

Table 2.2. Furnace temperature schedule for catalyst activation of supported iron catalysts.

Temperature, °C	Ramp, °C /min	Hold, h
180-205	1	1
215	0.2	2
225	0.2	2
235	0.2	4
245	0.2	4
260	0.2	12

2.1.5.2 Cobalt catalyst

Passivated catalysts were first re-reduced in situ at 450°C in 100% H_2 for 13 h. After reduction, the furnace temperature was decreased to 150°C in H_2 and the reactants were introduced at a composition of 50% H_2/25% CO/3% Ar/22% He). The system was then pressurized to 20 atm. The furnace temperature was then increased to 190°C at 0.5 °C/min, soaked for 4 h, then ramped to 200°C with the same ramp rate for a 14 h soak. Then the temperature was increased to the desired deactivation temperature at 0.5 °C/min with soaking for 4-6 h for each 5 °C. Different holding times were used to have the total time of 24 h to get to the desired furnace temperature. During the temperature increase for the activation step, the flow rates were adjusted to get about 50-60% CO conversion at the final temperature. A rigorous activation procedure was used to ensure a gradual filling of the pores and to prevent runaway problems. After getting to steady-state the activation was considered complete. After the activation, the desired partial pressures were adjusted. The flow rates were also adjusted to give a CO conversion of less than 25%. Low conversions were used not only to give differential kinetics but also to favor carbon deposition and lower partial pressures of water.

2.2 Catalyst characterization

2.2.1 Nitrogen adsorption/desorption

Surface area (SA), pore volume (V_{pore}), and pore size distribution (PSD) were calculated by nitrogen adsorption/desorption isotherms measured using a Micromeritics TriStar 3000 instrument. The samples (0.1-0.3 g) were degassed 120°C for 12 h before measurement. Passivated spent cobalt catalysts were degassed at 30°C in He to prevent further oxidation. The average pore diameter and pore size distribution (PSD) of each of the four alumina support materials were calculated from BET data using a new slab pore model and method proposed by Huang et al. [65] and modified to fit a log-normal PSD [66].

2.2.2 X-ray diffraction

To estimate crystallite diameters, X-ray diffraction patterns were collected for all the catalysts using a PANalytical X'Pert Pro diffractometer with a Cu source and a Ge monochromator tuned to the Cu-Kα1 wavelength (λ = 1.54 A°). Samples (reduced and passivated) were scanned from 10 to 90° using a step size of 0.016° and a step time of 350 s. Diffraction patterns were compared to standard patterns in the database. The average crystallite thicknesses were calculated from the Scherrer equation using the Fe_3O_4, Fe, and Fe_5C_2 peaks located at 2θ= 37.3°, 44.9°, and 43.1°, respectively and for cobalt metal at 2θ= 44.5°. Reduced and wax-extracted spent cobalt catalyst samples were carefully passivated by first exposing each to flowing air in helium (< 1% air) at room temperature followed by gradually increasing concentrations of air in helium while monitoring the temperature of the catalyst bed.

2.2.3 Thermo-gravimetric analysis (TGA) experiments

TPO, TPR, oxygen titration, CO chemisorption, and hydroxyl group measurement were performed on 10–40 mg samples of various catalysts in a Mettler Toledo TGA/DSC 1 equipped with an automated GC 200 gas controller. The flow rates of H_2, CO/Ar (~11.8% Ar), and air were set by valved rotameters, but a GC 200 controller and the TGA software (both from Mettler Toledo) were used to switch the gases automatically during all experiments, and thus run multiple experiments without the necessity of human hands. All the gases were purchased from Airgas at a 99.95% purity.

2.2.3.1 Temperature-programmed oxidation (TPO)

TPO experiments were used to determine appropriate temperature ramps and soaks for controlling byproduct decomposition at low rates. The rate of mass loss was monitored during a constant temperature ramp of 3 °C/min from ambient temperature to 700°C in 100 mL/min of 70–80% air/He.

2.2.3.2 Temperature-programmed reduction (TPR)

TPR experiments were performed to determine catalyst reduction protocols. 10-20 mg of calcined samples were exposed to a reducing gas mixture of 10% H_2/He (H_2-TPR) or 10% syngas (H_2:CO = 1) in He (syngas-TPR), while the temperature was increased at 3 °C/min from ambient (~25°C) to 700°C. In order to deconvolute the weight loss due to release of strongly absorbed water, another set of TGA experiments were performed on the calcined catalysts using the same temperature profile with time, but under pure He flow. The weight loss due to water desorption was subtracted from the total weight loss of the corresponding TPR.

2.2.3.3 *Oxygen titration*

Oxygen titration experiments were performed in the TGA to determine the extent of reduction (EOR) to Fe or Co metal following reduction. The calcined catalyst samples (10-20 mg) were reduced in situ under flowing hydrogen for 16 h at the appropriate reduction temperature. They were then flushed in flowing He at 10°C below the reduction temperature and during subsequent heating to 400°C. 10% O_2 was introduced through the catalyst bed at 400 °C and the amount of oxygen consumed by the sample was found by the increased weight. The extent of reduction to Fe metal (or Co) was calculated assuming that iron in metallic state or in FeO state was oxidized to Fe_2O_3 (and Co or CoO to Co_3O_4). Full oxidation of Cu to CuO was also assumed for iron catalysts and Pt to PtO for Co catalyst.

Equations 2.1 and 2.2 were used in the calculation of dispersion and average Co crystallite diameter, respectively as follows.

$$\%D = \frac{1.18X}{EOR \times W} \tag{2.1}$$

$$d = \frac{94}{\%D} \tag{2.2}$$

where H_2-uptake is denoted as X, catalyst weight as W, dispersion as D, and cobalt crystallite diameter as d.

2.2.3.4 *CO-Uptake*

Gravimetric carbon monoxide adsorption was used as a relative measurement of CO chemisorption site density. Iron or cobalt catalysts were reduced in the TGA in 10% H_2/He at the appropriate reduction temperature and then cooled to room temperature for iron catalysts and to

100°C for the cobalt catalyst, where the CO chemisorption uptakes were measured in 10% CO/He.

CO uptakes for iron catalysts were also measured under reaction conditions as the active phase for iron catalysts is iron carbide. Catalysts were *in-situ* reduced in the TGA in 10% H_2/He at 280°C and cooled to 180°C. Flow was then switched to synthesis gas (H_2/CO/He: 0.05/0.05/0.9 mol) and the sample was heated to 280°C at 1 °C/min and held for 10 h. Following these steps, the samples were cooled to room temperature, and CO chemisorption uptakes were measured in 10% CO/He.

2.2.3.5 Hydroxyl group content measurement

Thermogravimetric analysis (TGA) was performed for alumina samples to determine hydroxyl group content. Pre-calcined alumina samples (St. Gobein (AlG), Alpha-Aesar (AlA), Cosmas alumina (AlC) at 700°C and silica-doped alumina (AlSi) at 1100°C) were heated at a rate of 5 °C/min from room temperature to 1100°C in a He flow of 80 ml/min and held for 2 h. The weight loss between 130 and 1100°C was used to determine the hydroxyl group content.

2.2.4 Temperature-programmed (TP) experiments with mass spectroscopy

Temperature-programmed experiments such as temperature-programmed desorption (TPD) and temperature-programmed hydrogenation (TPH) were performed on a computer-automated fixed-bed reactor system shown schematically in Figure 2.1. All gases were purified before flowing to the reactor system to remove low level impurities such as iron carbonyls, hydrogen sulfide, oxygen, water, etc. A description of the purification system is found in Critchfield's Thesis [67].

A quartz reactor with an internal diameter of 5 mm was used for atmospheric pressure experiments. The middle of the tube was bulb-shaped to minimize pressure drop and temperature gradients through the catalyst bed. The powdered catalyst was supported on a glass frit with porosity of 15-40 μm. For high-pressure experiments, ¼ inch stainless steel tube with a ring slightly smaller than the inner diameter of the tube to support a stainless steel mesh, quartz wool, and catalyst was used. Gas flow to the reactor was controlled by a set of mass flow controllers (Brooks 5890E). The mass flow controllers were interfaced with the computer via National Instruments FieldPoint analog input and output modules (-10 to +10 V) while interfacing of the thermocouple (used to measure reactor temperature) with the computer was accomplished with a thermocouple FieldPoint module. Reactor bed temperature was measured by thermocouples in contact with the bed. After leaving the reactor, the exit gas and liquid effluent passed through a hot trap (90-110°C) and a cold trap (0°C) to collect heavy hydrocarbon and liquid products formed in the high pressure FT reaction. A three-way valve was used after the reactor to send the effluent to the traps or directly to the mass spectrometer bypassing the traps). The latter was used for the cases when there was no liquid or wax production, such as atmospheric FT reaction. Gases leaving the cold traps flowed through spring-loaded back pressure regulators (Swagelok Co., KBP1J0G4A5A20000, typically set to 300 psig) to control the reactor pressure.

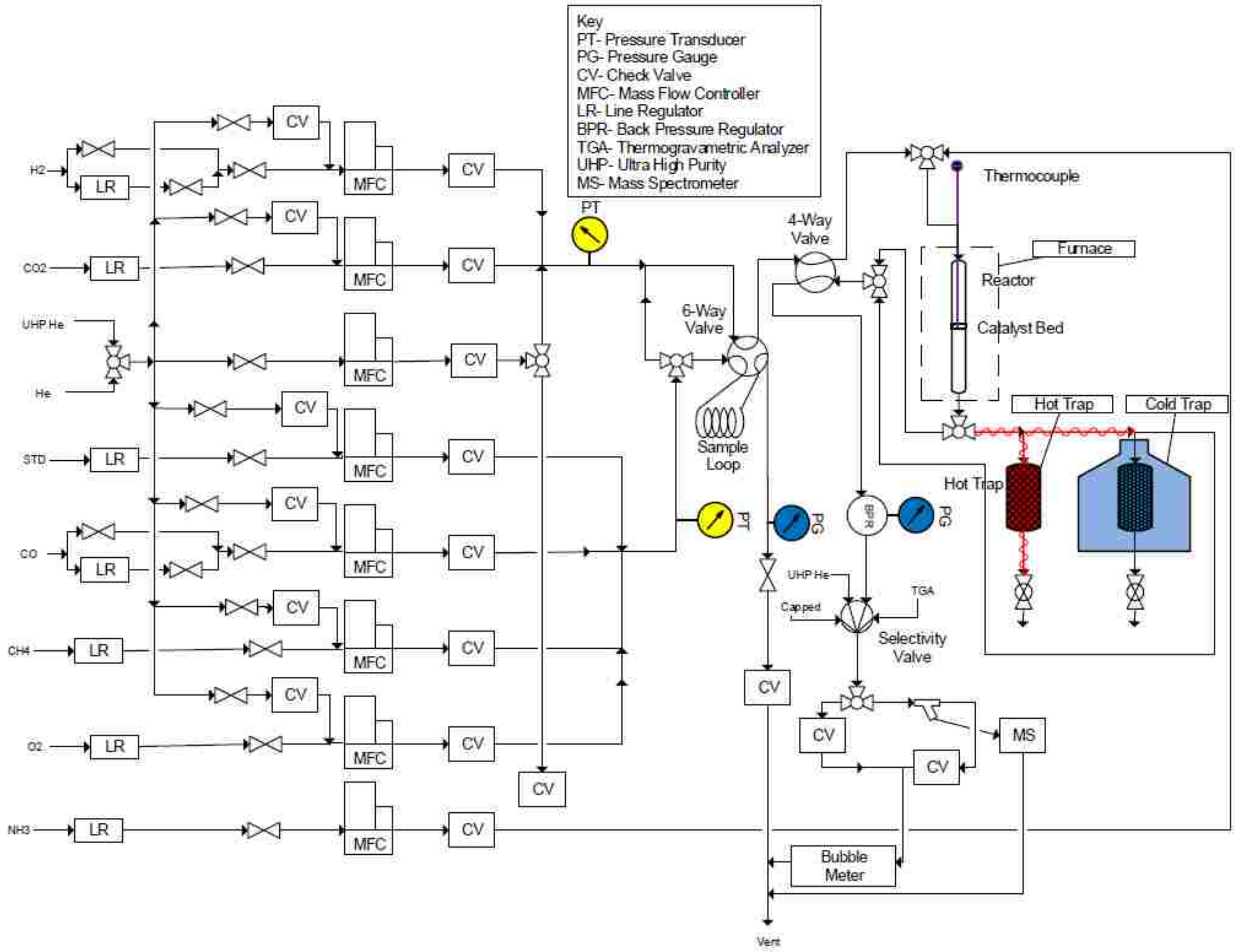

Figure 2.1. Schematic of fixed-bed reactor system for temperature-programmed experiments monitored with mass spectrometer.

Concentrations of gaseous species exiting the reactor were monitored online with a Balzers QuadstarTM Prisma 421 V. 3.0 mass spectrometer. The mass spectrometer system was equipped with two vacuum stages. The first vacuum stage was maintained at about 5 mTorr (with no sample feed) using a mechanical pump. The second vacuum stage was maintained at about 1×10^{-6} Torr with a combination of roughing and turbo pumps. The mass spectrometer was calibrated for CH_4, CO, and CO_2 with individual calibration gas mixtures. For CO-TPD (desorption in He), the mass spectrometer was calibrated with about 1% CO or CO_2 in He and for TPH (desorption in H_2) the calibration gas was about 1% or 10% CH_4 in H_2 for atmospheric FTS reaction and high pressure reaction, respectively.

2.2.4.1 Temperature-programmed desorption of CO (CO-TPD)

About 150 mg of calcined cobalt catalyst was loaded into the reactor. The sample was reduced in situ by flowing 25 ml/min H_2 and 25 ml/min He at 450°C for 6 h. Following reduction, the sample was cooled to 430°C and purged with He for about 1 h. After purging, the sample was cooled to adsorption temperature. The gas switched to 10% CO in He (total flow of 30 ml/min) at 25, 50, 100, and 150°C for 1 h and purged again in He to ambient temperature. Then, CO was desorbed in 10 ml/min He at a heating rate of 20 °C/min. CO (m/z of 28), CO_2 (m/z of 44 and 28) was monitored and recorded during desorption. The observed signals were subsequently converted to concentrations and mole fractions of CO and CO_2 with the corresponding calibration.

Also CO-TPD experiments were done for supported iron catalysts (Chapter 3) with the same procedure described for cobalt except 0.35 g of catalyst was reduced in situ with flowing 50 vol% H_2/He at 280°C, then purged in He at 260°C. The CO adsorption temperature was 150°C.

2.2.4.2 Temperature-programmed desorption of NH_3 (NH_3 -TPD)

Ammonia-TPD experiments were performed on silica-doped alumina support to determine total acid sites. A sample of 100 mg was degassed in-situ at 550°C for 1 h under helium flow of 30 sccm. The sample was cooled to adsorption temperature of 100°C. After 1 h of NH_3 adsorption, it was switched to He to remove any physisorbed ammonia. The sample was then heated in 10 sccm He flow with a ramp rate of 5 °C/min to 500°C. The effluent gas concentrations were determined using a Pfeiffer Vacuum ThermoStar mass spectrometer and were quantified to give number of acid sites.

2.2.4.3 Temperature-programmed hydrogenation (TPH)

TPH experiments were performed to identify different carbon species on the cobalt catalyst. About 25 mg of wax-extracted spent cobalt catalyst was loaded into the TP reactor. Following adsorption of carbon containing species onto the catalysts at given partial pressures and temperature, the catalyst was hydrogenated in 100% H_2 (10 ml/min) while ramping from room temperature to 900°C at 5 °C/min. CH_4 with m/z of 15 and 16 (instead of just 16 to avoid interference from ionized oxygen from water vapor) was monitored with mass spectrometry. Formation of heavier hydrocarbons, m/z of 25 and 43 were also measured.

2.2.5 Nuclear magnetic resonance (NMR)

NMR spectra were obtained on a Bruker Avance I 400 (9.6 T) NMR instrument using a 7 mm (^{29}Si) or a 4 mm (^{27}Al) broadband MAS Probe. All spectra were obtained at room temperature, and a spinning speed of 12.5 kHz for ^{27}Al and 4 kHz for 29Si. The 1D ^{29}Si MAS NMR spectra were obtained using a single pulse Block decay using a 240 s recycle delay, while the ^{1}H-^{29}Si CPMAS spectra was obtained using a 5 ms contact time. The ^{27}Al MAS spectra were obtained using a single pulse Bloch decay. The ^{27}Al chemical shift was referenced to 1M $Al(H_2O)_{6+}$ in water $\delta = 0.0$ ppm, and the ^{29}Si referenced to Q8M8 $\delta = +12.6$ ppm with respect to TMS ($\delta = 0$ ppm). Spectral simulations were performed using DMFIT [68]. NMR experiments were done at Sandia National Laboratories in Albuquerque.

2.2.6 X-ray photoelectron spectroscopy (XPS)

The XPS measurements for cobalt catalysts were carried out on a Kratos AXIS Ultra, equipped with a monochromatic Al Kα X-ray source and a delay-line detector (DLD). The powder samples were dispersed on conducting carbon-tape in the glovebox and the samples were transferred in an inert environment to the measurement chamber. Spectra were obtained using the aluminium anode (Al Kα = 1486.6 eV) operating at 150 W. For the survey scans, a constant pass energy of 160 eV was used and for the region scans, the constant pass energy was 40 eV. Quantification and fitting of the obtained spectra was done use the CasaXPS software and all binding energies were references to the binding energy of the Al 2p peak for the alumina support at 74.4 eV. These experiments were carried out at Eindhoven University of Technology in Niemantsverdriet's group.

2.2.7 XANES/EXAFS

The electronic structure and local atomic structure of calcined, reduced, and spent cobalt catalysts were investigated by XAS near the Co K-edge in transmission mode at the Soft X-ray Microcharacterization Beamline (SXRMB) at the Canadian Light Source, Inc. The spectra (in energy space) were background subtracted and normalized with a Victoreen function and further normalized using a two-polynomial method with degree 1 for the pre-edge and post-edge regions. Changes in the oxidation state of cobalt was analyzed by comparing the XANES region of the spectra using the WinXAS [69] software. EXAFS spectra were also treated using the WinXAS software. After background removal and normalization (previously described), the spectra were converted to k-space and background subtracted in k-space using a cubic spline fit. The data for the calcined catalyst, freshly reduced catalyst, and cobalt metal foil were first analyzed qualitatively over a wider k-range of 2.5 – 10 $Å^{-1}$. However, it was of primary importance to compare the used FTS catalyst to the freshly reduced one. In that case, the used catalyst spectra were of lower quality. To improve the signal to noise ratio, 4 scans were averaged together. The data were smoothed (Fourier smoothing level of 8) and the useful k-range was shorter (3.5 – 9 $Å^{-1}$). For the purpose of comparison, the calcined catalyst, freshly reduced catalyst, and cobalt foil were subjected to the same procedures over the shortened k-range.

Co K-edge experimental data ($k^2 \cdot \chi(k)$) over the shortened k-range were fitted with theoretically generated spectra derived from structural models, assuming the presence of Co metal. With the use of the ATOMS software [70], structural information for FCC Co was transformed into spatial coordinates, which were then employed by the FEFF software [71] to calculate the scattering paths. The scattering paths were thus used as inputs for the FEFFIT software [72] to generate theoretical $\chi(k)$, which were compared to their experimental counterparts. Because of the shortened k-range, it was not possible to obtain a physically meaningful fitting of the data with a complex model consisting of both Co-Co coordination from Co metal and Co-O from CoO. Thus, to deemphasize the contribution from CoO and emphasize the contribution from Co-Co in the metal, a k-weighting of 2 was employed. Structural fitting parameters used in the model included: a global lattice expansion coefficients, a global Δe_0, a global Debye-Waller factor, and local coordination numbers, N_i. The range for the fitting was 1.5 – 2.9 Å. These experiments were carried out at Canadian Light Source Inc. by Dr. Gary Jacobs from University of Kentucky Center for Applied Energy Research (CAER).

2.3 Activity, selectivity, and stability measurements

2.3.1 Fixed-bed reactor description

The catalyst activity, selectivity, and stability as a function of temperature, P_{H2}, P_{CO}, and time were measured under differential conditions (low conversion) in a fixed-bed reactor system containing two reactor beds in parallel. A flow diagram of the reactor system is shown in Figure 2.2. He, CO/Ar (containing 12% Ar which was included as a tracer), and H_2 were purified by flowing through absorbents described by Critchfield [67] to remove low level impurities such as iron carbonyls, hydrogen sulfide, oxygen, water, etc. Each reactor inlet flow system uses three mass flow controllers (Brooks 5850E) for the reactants (He, CO, and H_2) and one mass flow controller (Brooks 5850E) to control the total feed gas composition. The feed gas to each reactor is split two ways with one part going to a bypass line controlled by a dome-loaded back pressure regulator (Grove Valve and Regulator Co. S-91XW typically set to 340 psig) and one line with mass flow controller that fed the corresponding downflow reactor. After leaving the reactor, the exit gas and liquid effluent passed through a hot trap (90-110°C) and a cold trap (0°C) to collect heavy hydrocarbons and liquid products. Gases leaving the cold traps flow through spring-loaded back pressure regulators (one for each reactor, GO Regulator Co., BP8L-1D11IU118, typically set to 300 psig) to control the reactor pressure. The effluent gaseous product is analyzed using an HP5890 gas chromatograph equipped with a thermal conductivity detector (TCD) and 60/80 carboxene-1000 column. Both reactors are encased in the same three zone tube furnace. Furnace temperatures are controlled by three Omega controllers. Reactor bed temperatures are measured by thermocouples in contact with the catalyst beds.

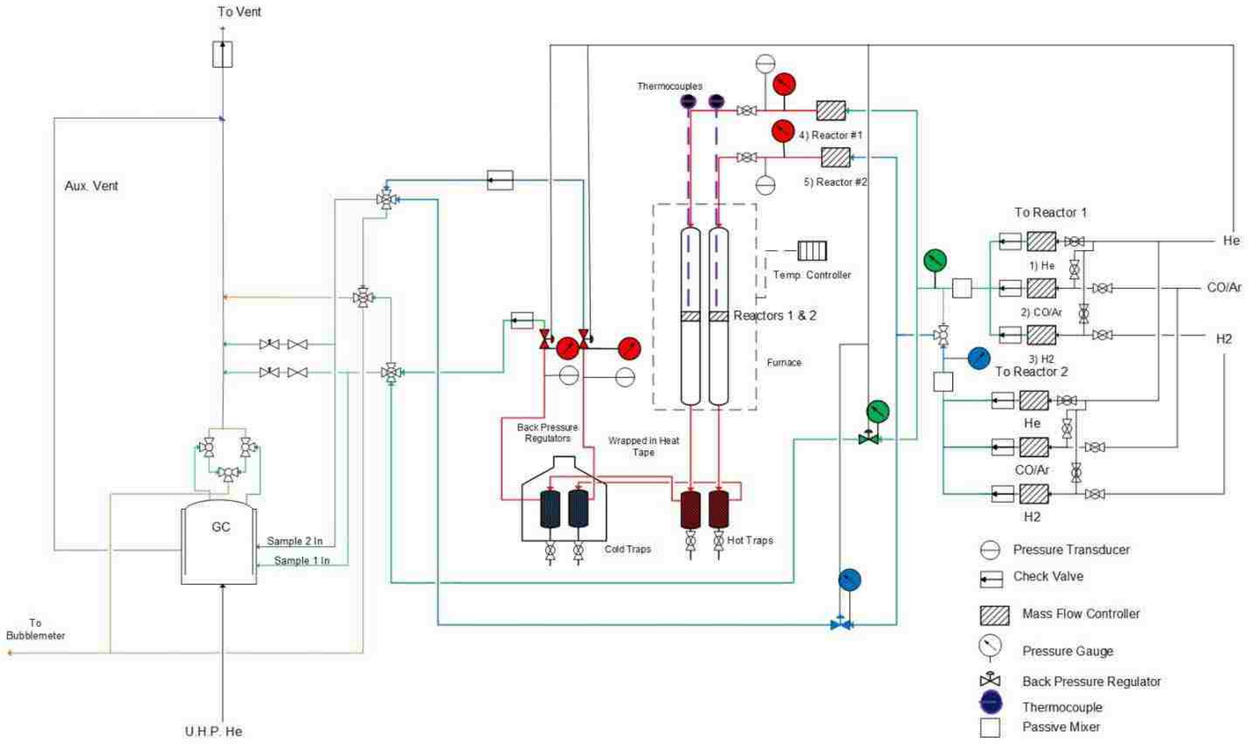

Figure 2.2. Process flow diagram of dual channel fixed bed reactor system.

2.3.2 Catalyst loading

The reactor tubes were fitted with a ring slightly smaller than their inner diameter to hold a metal mesh support. Two stainless steel screens, coarse (100 mesh) and fine (400 mesh) were placed on top of the ring to provide support for the catalyst bed. Enough quartz wool was placed over the mesh to prevent catalyst loss. Each sample was diluted with quartz sand or silicon carbide at a ratio of 10 to 1 (diluent/catalyst) to improve isothermality in the catalytic zone. Quartz wool was also placed on top of the catalyst bed. After reaction spent cobalt catalyst samples were retained to study the effect of different operating conditions on the deactivation behavior and mechanism of Co catalyst.

2.3.3 Wax extraction of spent cobalt catalysts

During the low temperature FTS process with a cobalt catalyst, molten product hydrocarbon wax acts as the liquid phase in the reactor. After the FTS reaction the furnace temperature was cooled to room temperature which allowed this protective wax layer to congeal. This wax layer can interfere with several characterization measurements; therefore, an extraction procedure was developed to remove it. This approach is a modified version of Soxhlet extraction allowed the wax extraction in an inert environment, vacuum drying, and passivating the catalyst for further ex situ characterizations in the same set up. The procedures used for wax extraction ensured that an argon or vacuum atmosphere protected the air sensitive catalyst at all times.

The Soxhlet extraction set-up consisted of 3 sections: a 300 ml Schlenk flask, a ‘filter’ unit with an internal glass frit (porosity = 15 μm) and 30 ml volume and a water-cooled condenser. A check valve was used on top of the condenser to eliminate the diffusion of air from the condenser to the system. The schematic of this system is shown in Figure 2.3. The entire system was evacuated and flushed with helium repeatedly.

Tetrahydrofuran (THF, $CH_2(CH_2)_2CH_2O$, Mallinckrodt Chemicals, stabilized THF) was used as a solvent to extract the wax. During the extraction process the solvent was heated by an oil bath and boiling THF vapour and 10 ml/min He were allowed to pass through the frit which holds the wax protected cobalt catalyst. The vapor condensed and formed a liquid layer on top of the frit (surrounding the catalyst sample). Helium was used to ensure an oxygen-free system. After the glassware was ¾ full of THF, the THF was removed from oil bath and allowed to cool. Cooling allowed the THF to fall through the glass frit, leaving the wax-free catalyst behind. The glassware containing the catalyst was closed while the THF was removed and replaced with fresh THF. A vacuum was then pulled on the system to remove the air introduced to the flask containing THF before opening the valve of glassware containing the catalyst. This procedure was done 8-12 times before drying the catalyst in vacuum overnight. These 8-12 cycles were needed to make sure the catalyst particles were sufficiently wax-free. After drying, the catalyst was passivated in air and helium starting with 1% O_2 and slowly increasing the oxygen content for 24 h, preparing the catalyst for ex situ measurements. The advantage of this method compared to traditional Soxhlet extraction is that clean THF is continuously recycled to the sample and also the wax-extraction, drying, and passivation can be carried out in the same container without the need of transferal in a glove-box.

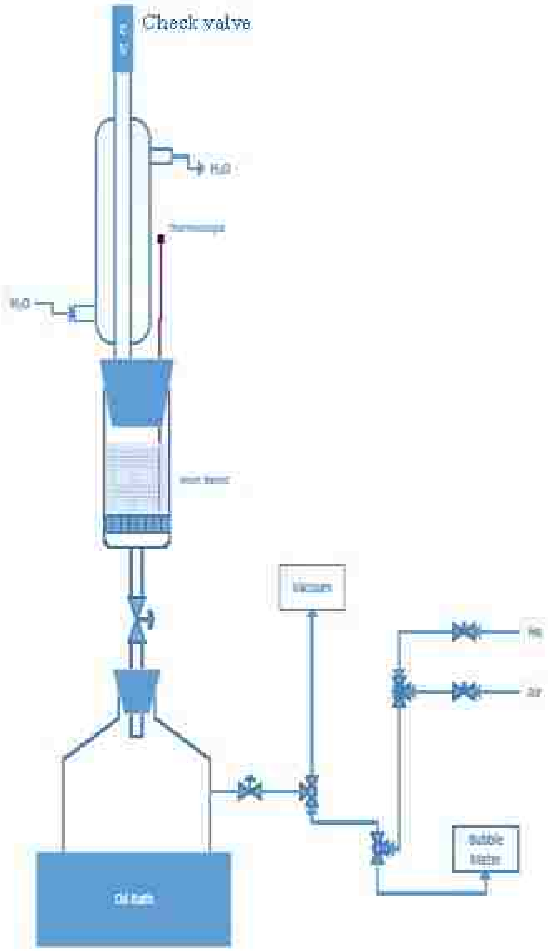

Figure 2.3. Process flow diagram of wax extraction system using modified Soxhlet extraction.

2.3.3.1 *Extent of wax extraction*

Samples of freshly reduced catalyst were tested and compared before and after intentional exposure to wax and wax extraction to establish a reference against the other FB wax-extracted spent catalysts (e.g. amount of wax, TPH peaks for wax) and to understand the extent of wax-extraction. To prepare the "waxed" catalyst, 0.2 g freshly reduced catalyst was added to 0.2 g melted FTS wax over a hot plate, mixed, and then wax-extracted. To determine the effect of wax extraction, H_2-TPR was performed on the freshly reduced catalyst before and after waxing and wax-extraction, comparing the weight loss (Figure 2.4). As shown in Table 2.2 wax extraction removed 91.3% of the wax. Furthermore, freshly reduced wax-extracted sample was evaluated by BET, XPS, CO-uptake, and EOR and compared with freshly reduced catalyst without wax. It was found that wax-extraction does not change the properties of the catalyst as will be discussed fully in Chapter 5.

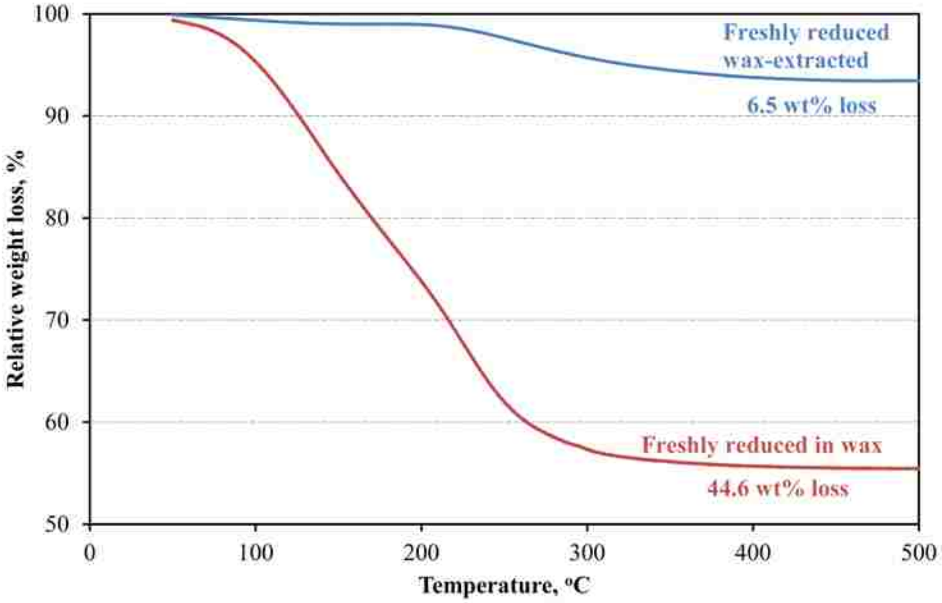

Figure 2.4. H_2-TPR weight loss of a freshly reduced waxed catalyst before and after wax-extraction

Table 2.3. Relative masses of catalyst and wax after H_2-TPR for waxed and wax-extracted catalysts.

ID	Mass of catalyst	Mass of wax	Wax/Catalyst
Extracted	93.5	6.5	0.07
Waxed	55.4	44.6	0.805

2.3.4 Rate and Selectivity Calculations

Gas compositions were found from GC chromatograms from which values for the rate of reaction and selectivity were calculated according to the following relationships.

Equation 2.2 is the reactor performance equation assuming differential reactor conditions. This assumption was checked for CO conversion of 72% and it was found that the error for CO rate constant is 0.6% (Appendix B).

$$\frac{W}{F_{CO}^{0}} = \frac{X_{CO}}{-r_{CO}} \tag{2.2}$$

where W is the weight of catalyst, F_{CO}^{0} is the inlet CO molar flow rate, X_{CO} is the CO conversion, and $-r_{CO}$ is the rate of CO consumption. Calculation of rate depends only on the determination of CO conversion as W and F_{CO}^{0} are known or measured directly.

Ar was premixed with CO as an internal inert tracer to allow an exact measurement of CO conversion (X_{CO}) by using GC peak area (PA) and GC molar response factors (RF) as follows:

$$\frac{\mathrm{n}}{\mathrm{n}^{0}} = \frac{y_{Ar}^{0}}{y_{Ar}} \tag{2.3}$$

$$X_{CO} = 1 - \frac{n_{CO}}{n_{CO}^{0}} = 1 - \frac{y_{CO} \times n}{y_{CO}^{0} \times n^{0}} = 1 - \frac{y_{CO} \times n^{0} \times \frac{y_{Ar}^{0}}{y_{Ar}}}{y_{CO}^{0} \times n^{0}} = 1 - \frac{y_{CO}/y_{Ar}}{y_{CO}^{0}/y_{Ar}^{0}}$$

$$= 1 - \frac{\mathrm{P_{ACO}} \times \mathrm{RF_{CO}} / \mathrm{PA_{Ar}} \times \mathrm{RF_{Ar}}}{\mathrm{PA_{CO}^{0}} \times \mathrm{RF_{CO}} / \mathrm{PA_{Ar}^{0}} \times \mathrm{RF_{Ar}}} = 1 - \frac{\mathrm{PA_{CO}}/\mathrm{PA_{Ar}}}{\mathrm{PA_{CO}^{0}}/\mathrm{PA_{Ar}^{0}}} \tag{2.4}$$

where n_{CO} is outlet molar flowrate of CO and n_{CO}^{0} is inlet molar flowrate of CO. Since the inlet and outlet flowrates of Ar are equal ($n_{Ar} = n_{Ar}^{0}$; $y_{Ar} = y_{Ar}^{0}$), the calculation of CO conversion is independent of GC calibration due to the use of the inert tracer.

In contrast, calculation of selectivity (S) is dependent on the response factors of each species since they appear in Equation 2.5.

$$S_{A} = \frac{n_{A}}{n_{CO}^{0} - n_{CO}} = \frac{y_{A} \times n}{n_{CO}^{0} \times X_{CO}} = \frac{y_{A} \times n^{0} \times \frac{y_{Ar}^{0}}{y_{Ar}}}{X_{CO} \times y_{CO}^{0} \times n^{0}} = \frac{PA_{A} \times RF_{A} / P_{Ar}}{\left(PA_{CO}^{0} \times RF_{CO} / P_{Ar}^{0} \right) \times X_{CO}} \tag{2.5}$$

Chapter 3 Supported Iron: Effect of Preparation Variables

This chapter focuses on the optimization of catalyst preparation variables for supported iron FT catalysts, which includes catalyst characterizations, activity, selectivity, and stability results.

3.1 Introduction

Cobalt (Co) catalysts have been the subject of far more Fischer-Tropsch Synthesis (FTS) research than iron (Fe) catalysts due to their longevity and favorable reaction rates. However, commercial Fe has advantages over Co including lower cost, lower methane selectivity, and high water-gas shift activity. Commercial Fe catalysts produced for FTS are unsupported. Therefore, very little work on supported Fe catalysts is reported in the literature [9, 17, 18].

Since the 1950's, the South African company Sasol has been one of the few in industry to prefer Fe catalysts [73]. Sasol has worked mostly with $Fe/Cu/K/SiO_2$ as an unsupported Fe catalyst. Bukur et al. [12] reported a weight-time yield of 450 mmol $(CO+H_2)/g_{Fe}/h/MPa$ and a C_{2+} hydrocarbon productivity of 0.86 $g_{HC}/g_{Fe}/h$ for $100Fe/3Cu/4K/16SiO_2$ at 260°C and 2.2 MPa. Despite their high activity and favorable selectivity, unsupported Fe catalysts are generally too weak mechanically to be used in slurry bubble column reactors (SBCR's), which are the most thermally efficient and economical reactors [9]. Unfortunately, the severe conditions inside SBCR's grind weaker catalysts into fine powders, resulting in excessive catalyst loss and plugging in the catalyst recovery system. These fine powders also render catalyst separation from the product nearly impossible. The US Department of Energy (DOE) performed a demonstration with a precipitated catalyst in a SBCR and found that attrition of the catalyst quickly plugged the filtering system, which required the reactor to be shut down within 24 h of startup [9]. O'Brien et al. [17] also concluded that supported Fe catalysts are far more attrition resistant than unsupported catalysts. They reported that unsupported precipitated catalysts, even with spray drying prior to calcination, were abraded from an initial particle size distribution of 30–50 μm down to 1–3 μm in just 24 h.

Among supported FT catalysts, the prevalent reasons for preferring Co catalysts over Fe are the inferior rates and selectivities of supported Fe catalysts [74]. Strong metal-support interaction is thought to cause lower activity by reducing the extent of reduction and carburization of the iron [15, 75]. Studies led by Sasol have shown supported Fe catalysts have poor reaction rates and selectivities, compared to unsupported Fe catalysts, due to promoters forming chemical bonds with the support [76]. Therefore, success of supported Fe catalysts may depend on discovery of a preparation technique that weakens these chemical bonds. Since supported iron catalysts have not been extensively studied, the possibility exists that additional research could allow preparation of supported catalysts with improved activity and selectivity properties in addition to good attrition resistance.

A few published studies on supported Fe are available. They have concluded that aqueous impregnation yields strong interactions between iron and potassium oxides and the support, leading to low reducibility of iron or poor iron-promoter contact [18, 20]. Xu and Bartholomew [9] attributed low reducibility of supported catalysts to ineffective preparation methods. In their study, they prepared a silica-supported catalyst (10%Fe/1%Pt/0.2%K/SiO_2) using a non-aqueous evaporative impregnation method. They even removed the water molecules of hydration by bubbling He through the nitrate salt at 80°C. The group also prepared a catalyst without K and another without K or Pt. The three resulting catalysts had high extent of reduction (60–80%) at 300 °C in H_2, moderately high dispersion (5–16%), and moderate FTS activity, although the methane selectivity was still high (6–10%).

Although both aqueous and non-aqueous supported Fe catalysts have been prepared, no studies were identified that directly compared aqueous and non-aqueous preparation methods.

Other researchers have explored promotion of supported Fe catalysts. The two promoters which have been used in preparation of commercial unsupported Fe FT catalyst are potassium (K) and copper (Cu). Because CO and H_2 can both be reducing agents, redox properties of the catalyst during FTS are crucial. The addition of K on Fe-based catalysts affects the catalytic activity for both Fischer-Tropsch Synthesis and the concurrent water-gas shift reaction [77, 78]. The K also affects methane, olefin, and higher hydrocarbon selectivity [78]. Davis [77] investigated the effect of K at different conversions. They found that at low conversions, the lowest potassium loading exhibited the highest activity and at high conversions the activity was slightly enhanced by K addition in the range of K loading in their study (K loading: 0.36-2.2 atomic%). Much higher CO conversions were obtained on 0.02 K/Fe atomic ratio catalysts than K-free catalysts [10]. A K content of 0.04 K/Fe atomic ratio did not exhibit an increase in FTS activity. Thus, the level of promoter loading appears to make a critical difference.

Success of a preparation method also depends on the timing and relative order in which these promoters are impregnated onto the support. Bukur et al. [18] studied supported Fe catalysts on alumina (Al_2O_3) and silica (SiO_2) which were prepared by co-impregnation of ferric nitrate, copper nitrate, and potassium bicarbonate in successive steps to desired levels. They compared the performance of these two catalysts to the performance of two unsupported, precipitated catalysts prepared similarly. Bukur et al. estimated the extent of reduction from Fe_2O_3 to metallic Fe as 19–26% at 400°C for both their alumina-supported and silica-supported Fe/Cu/K catalysts. Their silica-supported catalyst, however, was only one third as active as their most active precipitated Fe/Cu/K/SiO_2 catalyst when compared per gram catalyst (100 vs. 269 mmol(CO+H_2)/g_{cat}/MPa/h at 260°C) and their alumina-supported catalyst was only one fifth as active (i.e., about half as active as the silica-supported catalyst). The methane selectivity of the alumina-supported catalyst was comparable to the unsupported catalysts (3–4 mol%, carbon atom basis), while the methane selectivity of the silica-supported catalyst was higher (6–7 mol%, carbon atom basis).

O'Brien et al. [17] used a different impregnation method for preparing supported Fe catalysts. Ferric nitrate, copper nitrate, and potassium nitrate were melted at 70°C and slowly added to silica, alumina, magnesium silicate, or magnesium aluminate supports. The performance of these supported catalysts was compared with an Fe/Cu/K/SiO_2 precipitated catalyst. The best supported catalyst produced in the study was only one-fifth as productive (on a per gram catalyst basis) as the unsupported catalyst and again displayed higher selectivity to methane. O'Brien et al. did not report extent of reduction and dispersion for their catalysts.

Supported catalysts are one of the viable catalysts for use in SBCR's. Although many preparation techniques have been used, the reported data lack enough consistency to isolate the effect of specific preparation variables. Determining a single preparation method's influence on the properties of a catalyst requires greater consistency. This study has examined four important variables in the preparation of supported Fe catalysts and held all other variables constant to systematically investigate each variable's effect. The goal was to gain deeper insights into these preparation methods as a step toward designing a preparation method capable of producing catalysts with both attrition resistance adequate for use in SBCR's and high activity characteristic of precipitated catalysts. A series of K-promoted Fe catalysts supported on alumina (Al_2O_3) were prepared to examine the effect of the following *variables*: (1) impregnation method (aqueous incipient wetness or non-aqueous slurry), (2) Fe loading level, (3) K loading level, and (4) timing of impregnation (sequential impregnation or co-impregnation of K and Fe, and with or without direct K promotion of the support).

3.2 Experimental

3.2.1 Catalyst preparation

3.2.1.1 General preparation description

The six catalysts examined in this paper (all $Fe/Cu/K/Al_2O_3$) are identified as K1–K6. The timing and specific procedure for loading these metals was distinct for each of these six catalysts. These six combinations of procedures were carefully chosen to yield the most information and data about the effects of each preparation variable. Table 3.1 catalogs the values of each of the 4 preparation variables for the six catalysts.

Table 3.1. Preparation variable values for each of the six studied catalysts.

	Variable 1		Variable 2	Variable 3	Variable 4
Catalyst	**Solvent**	**Deposition Method**	**Fe Loading (wt%)**	**K Loading**	**Timing of Impregnation**
K1	NA[1]	SI[3]	20	4K/100Fe	Sequential impregnation
K2	NA	SI	**40**	4K/100Fe	Sequential impregnation
K3	A[2]	IWI[4]	20	4K/100Fe	Sequential impregnation
K4	A	IWI	20	**8K/100Fe**	Sequential impregnation
K5	A	IWI	20	4K/100Fe	**Co-impregnation**
K6	A	IWI	20	4K/100Fe[5]	**K directly on support plus sequential impregnation**

[1] NA = Non-aqueous
[2] A = Aqueous
[3] SI = Slurry Impregnation (50 vol% acetone, 50 vol% isopropanol)
[4] IWI = Incipient Wetness Impregnation (aqueous)
[5] Plus 0.2 wt% K (per mass of support) added directly onto the support

The full preparation method of each catalyst is only different from the preparation of one other catalyst by a single method. All catalysts were supported on a commercial St. Gobein alumina that was sieved to 30–60 mesh (250-595 μm). Prior to any metal loading, this blank support was calcined in dry air at 700°C for 4 h to remove hydroxyl groups. The metal precursors were iron (III) nitrate nonahydrate (Sigma Aldrich, reagent grade, 98 wt%), copper (II) nitrate hydrate (Sigma Aldrich, reagent grade, 98 wt%), and potassium bicarbonate (Sigma Aldrich, reagent grade, 100 wt% dry basis). The six catalysts were impregnated with Fe, Cu, and K metals in several steps as described below. All of the supported catalysts were also calcined in dry air after each metal impregnation step for 16 h at 300°C.

3.2.1.2 Aqueous incipient wetness or non-aqueous slurry impregnation

The catalysts were impregnated by one of two methods: aqueous (A) incipient wetness impregnation (IWI) or non-aqueous (NA) slurry impregnation (SI). For the aqueous method, the support was impregnated with enough aqueous solution containing the desired amount of iron nitrate and copper nitrate to just fill the pores (10 wt% Fe per loading step). The water was then slowly evaporated over 12 h at 80 °C to leave only the precursors and the support.

For the non-aqueous impregnation method, an equivolume mixture of acetone and isopropanol was chosen as the solvent. Once the appropriate amount of precursor was added, the solution was mixed for 12 h at atmospheric pressure in a Yamato RE800 rotary evaporator turning at 30 rpm. Next, the solvent was evaporated over 12 h at a pressure of 70 mm Hg absolute, while still rotating at 30 rpm.

3.2.1.3 Iron loading level

Most preparation methods included 20 wt% Fe, but one catalyst (K2) was loaded to 40 wt% Fe. Fe and Cu salts were always added simultaneously in 10 wt% Fe steps at the same relative Cu atomic ratio (7.5 Cu/100 Fe). Therefore, Fe and Cu were loaded onto K2 in four separate steps, while all other catalysts had two Fe and Cu loading steps. Each loading step was always followed by calcination.

3.2.1.4 Potassium loading level

Except for catalyst K5, K was added in steps separate from the Fe and Cu addition. For most of the catalysts, K was added in the atomic proportion of 4 K/100 Fe. For K4, the potassium loading was doubled to 8 K/100 Fe. K6 also included additional K promoter loaded directly on the alumina support, which will be described in detail in section 2.1.5.

3.2.1.5 Timing of impregnation

All catalysts, except K5, were prepared by first loading all Fe and Cu together, 10 wt% Fe at a time, and then loading all K in a separate last step. Loading K in a separate step this way is called "sequential impregnation." For K5, all of the salts, including K, were added simultaneously in each step, which is called "co-impregnation." Co-impregnation was only examined for aqueous incipient wetness impregnation because the potassium bicarbonate is not soluble in the non-aqueous solvent.

For the final catalyst, K6, 0.2 wt% potassium (per g support) was added directly onto the support by aqueous incipient wetness impregnation prior to any impregnation of Cu or Fe.

3.2.2 Catalyst characterization

Several characterization techniques were used in this study including: BET, XRD, H_2-TPR, syngas-TPR, EOR, CO-TPD. These techniques were fully explained in Chapter 2 and our published paper [79].

3.2.3 Activity and selectivity measurements

The details of activity and selectivity measurements were described in Chapter 2 and are summarized here.

Fischer-Tropsch synthesis (FTS) was conducted in a fixed-bed reactor (stainless steel, 3/8 inch OD) described previously [80]. Each sample (0.25 g, 250–590 μm) was diluted with 1 g quartz sand or silicon carbide to approach isothermal conditions in the catalytic zone.

Before FTS, the samples were reduced in situ at 280–320°C in 10 mol% H_2 in He for 10 h, followed by pure H_2 for 6 h. After cooling to 180°C, the system was then pressurized to 2.1

MPa in a syngas of 63 mol% H_2 plus CO in He with H_2:CO = 1. Three calibrated Brooks (model number 5850) mass flow controllers were used to produce the reactant mixture from three feed gas cylinders (Airgas, 99.95 mol% H_2; Airgas, 88.2 mol% CO with 11.8 mol% Ar as an internal standard; and Airgas, 99.995 mol% He). The catalysts were activated at 280 °C for 48-90 h with a target CO conversion level of ~50% during this carburization period. Activity and stability data were then obtained over the next 300–400 h as reaction temperatures were varied from 220°C to 260°C.

After leaving the reactor, the exit gas and liquid effluent passed through a hot trap (90°C) and a cold trap (0°C) to respectively collect heavy hydrocarbon waxes and liquid products. The effluent gaseous product was analyzed using an HP5890 gas chromatograph equipped with a thermal conductivity detector and 60/80 carboxen-1000 column to analyze the carbon containing reactants and products up to C_2. CO conversion and selectivities were determined from the calibrated GC analysis, with aid of the Ar internal standard (premixed with the CO reactant).

3.3 Results

3.3.1 Physical properties

3.3.1.1 Nitrogen adsorption/desorption

Results from the nitrogen physisorption analysis, including specific surface area (SA), pore volume (V_{pore}), and average pore diameter (d_{pore}) for the calcined samples, are summarized in Table 3.2. The surface areas of the calcined catalysts were 152–169 m^2/g. Pore volumes were 0.45–0.54 cm^3/g, and average pore diameters were 15.9–17.4 nm. Compared to the fresh St.

Gobein alumina support, these values represent a decrease after impregnation and calcination on average of 24%, 23%, and 9% for SA, V_{pore}, and d_{pore}, respectively.

Table 3.2. Surface area, pore volume, and average pore diameter of St. Gobein support and six catalysts of this study.

Catalyst	BET surface area, m^2/g	Pore volume, cm^3/g	Average pore diameter, nm
St Gobein	216	0.65	18.1
K1	167	0.54	17.4
K2	152	0.45	16.4
K3	167	0.51	15.9
K4	162	0.49	15.9
K5	164	0.52	15.9
K6	169	0.51	16.9

At equivalent Fe loadings, the non-aqueous catalyst has a slightly larger pore volume than the aqueous catalyst (0.54 cm^3/g for K1 and 0.51 cm^3/g for K3). Doubling the Fe loading decreases the pore volume by 17% (0.45 cm^3/g for K2).

Figure 3.1 shows the pore size distributions for all six catalysts. All of the aqueous catalysts (K3 to K6) exhibit broad bimodal distributions, with a large initial peak at about 7 nm and a second peak at about 15 nm. This first peak is especially large for K4 and K6 (the two more potassium-rich catalysts). The two non-aqueous catalysts (K1 and K2) appear to have simple, Gaussian-like, unimodal distributions about a peak at 15 nm. However, closer examination of K1 shows that a smaller peak appears at about 7 nm, precisely the same pore size as the first peak in the aqueous catalysts. This first peak disappears for the higher Fe loading (K2).

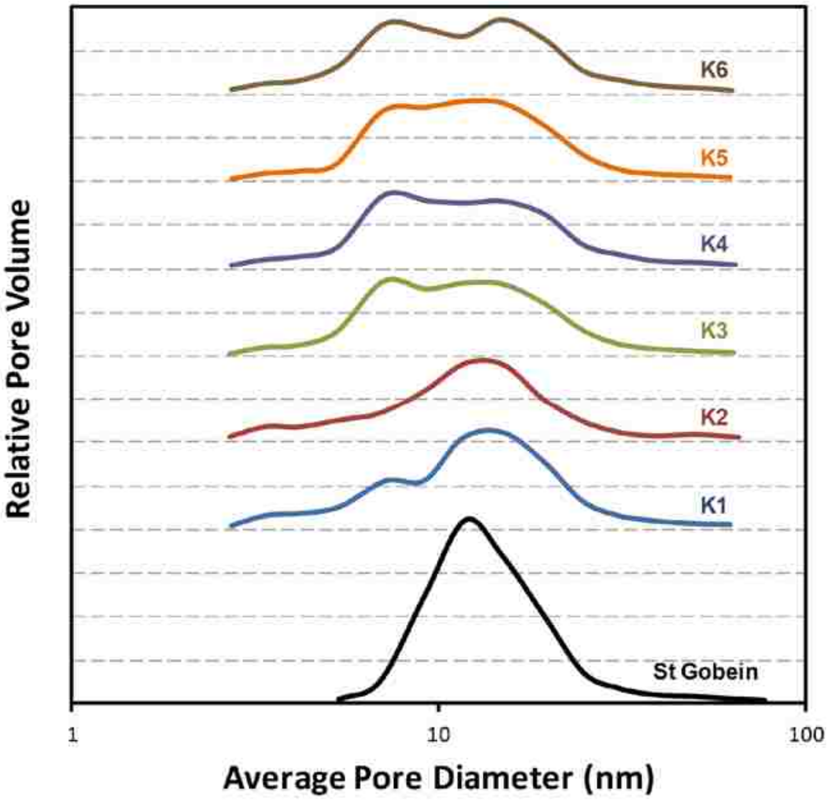

Figure 3.1. Pore size distributions

3.3.1.2 X-ray diffraction

X-ray diffraction patterns of all six catalysts after reduction at 280 °C and passivation confirm the presence of γ-Al_2O_3 with α-Fe^0 and/or Fe_3O_4, except in the case of K6. The crystallite sizes for Fe_3O_4 and Fe^0 are given in Table 3.3. The Fe peaks for K6 were undetectable due possibly to crystallite sizes below the detection limit (~3 nm) or due to overlap with alumina.

Table 3.3. Fe^0 and Fe_3O_4 particle sizes estimated from XRD.

Catalyst	XRD	
	Fe_3O_4 particle size, nm	Fe^0 particle size, nm
K1		5.6
K2	6.4	11.6
K3	6.4	4.9
K4		8.6
K5	7.3	
K6	No Fe detected	

Figure 3.2 shows the XRD patterns for all six catalysts. Overlapping alumina peaks dwarf the Fe^0 peak for all catalysts with 20 wt% Fe (K1 and K3 through K5). In contrast, the 40 wt% Fe catalyst, K2, has a large Fe^0 peak beside an alumina peak, which is visible as a shoulder to the right.

As shown in Figure 3.2, the first five prepared catalysts displayed Fe^0 peaks. Table 3.3 shows that doubling the Fe loading doubles the Fe^0 crystallite size (11.6 nm for K2 compared to 5.6 nm for K1). At equivalent Fe and K loading, the aqueous catalyst (K3) has a slightly smaller Fe^0 crystallite size than the non-aqueous catalyst (K1) (4.9 vs. 5.6 nm respectively). All else being equal, doubling K loading increases the Fe^0 size by 75% (K4 vs. K3). Dry et al. [81] similarly found that K promotion increases the crystallite size of Fe metal. However, when additional potassium is impregnated directly onto the support as in K6, the opposite effect is observed. The increased basicity of the support likely provides a more favorable surface interaction, which leads to higher dispersion and apparently, to crystallite sizes below the XRD detection limit.

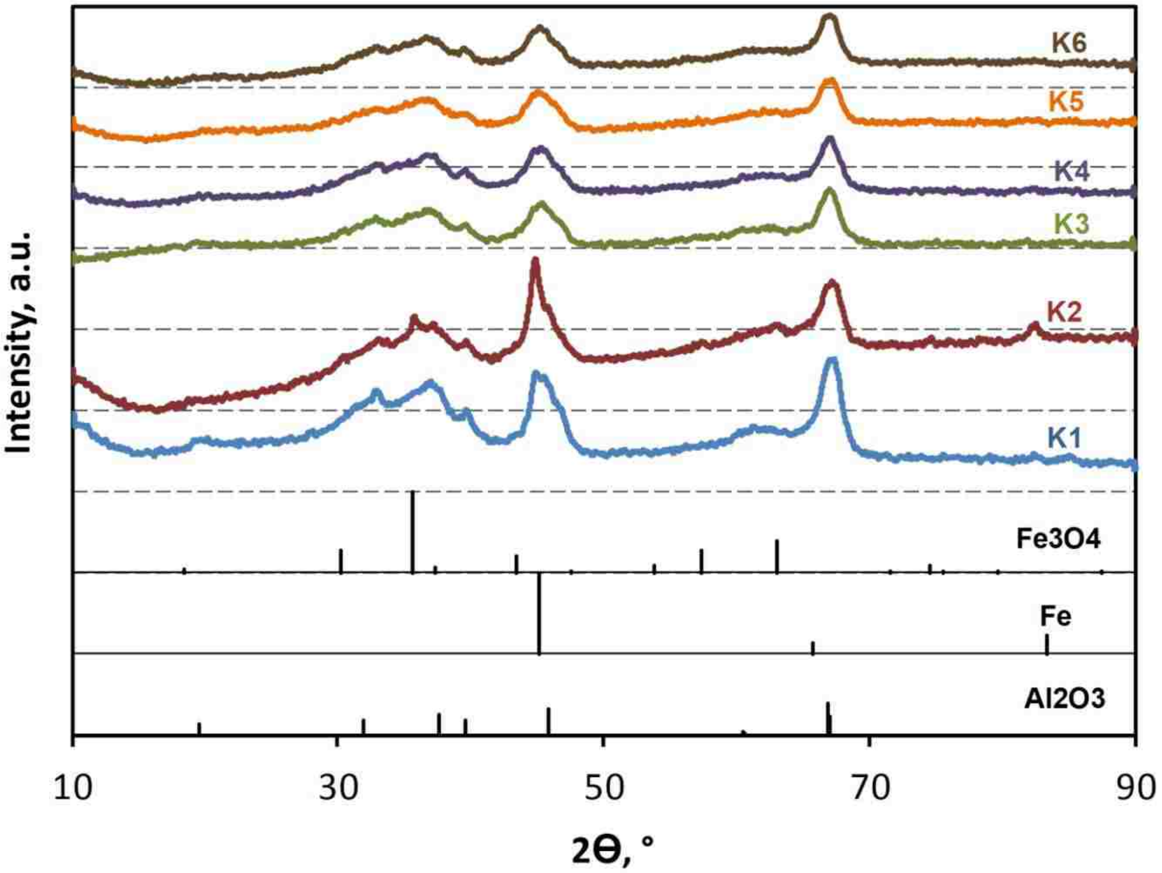

Figure 3.2. X-ray diffraction patterns of passivated reduced catalysts with standards for γ-Al_2O_3, α-Fe, and Fe_3O_4.

3.3.2 Catalyst reducibility

3.3.2.1 H_2-TPR

H_2-TPR was used to investigate the effect of preparation variables on the reduction behavior of the catalysts. As shown in Figure 3.3, the reduction of all six catalysts occurred in three stages with temperature ranges of 205-240°C, 310-390°C, and 470-630°C, respectively for the first, second, and third stage. The first stage is reduction from Fe_2O_3 to intermediate Fe_3O_4 and/or FeO and appears to contain two peaks, with the less intense peak generally appearing as a low temperature shoulder in Figure 3.3. Catalysts K2 and K5 have two distinct peaks in this first stage, but the rest of the catalysts have shoulders centered at a temperature of ~205°C. This shoulder may be assigned to the reduction of CuO to Cu and/or Fe_2O_3 to Fe_3O_4.The second stage is an intermediate peak associated with further reduction to Fe metal. The third stage, which occurs at high temperatures, could be due to reduction of an iron-support compound, such as iron aluminate, that is too amorphous to be detected by XRD.

The highest peak on all catalysts occurs during the first stage of reduction and is relatively sharp. In contrast, the second stage, with its associated peak, is much broader, indicating that the second stage is slower.

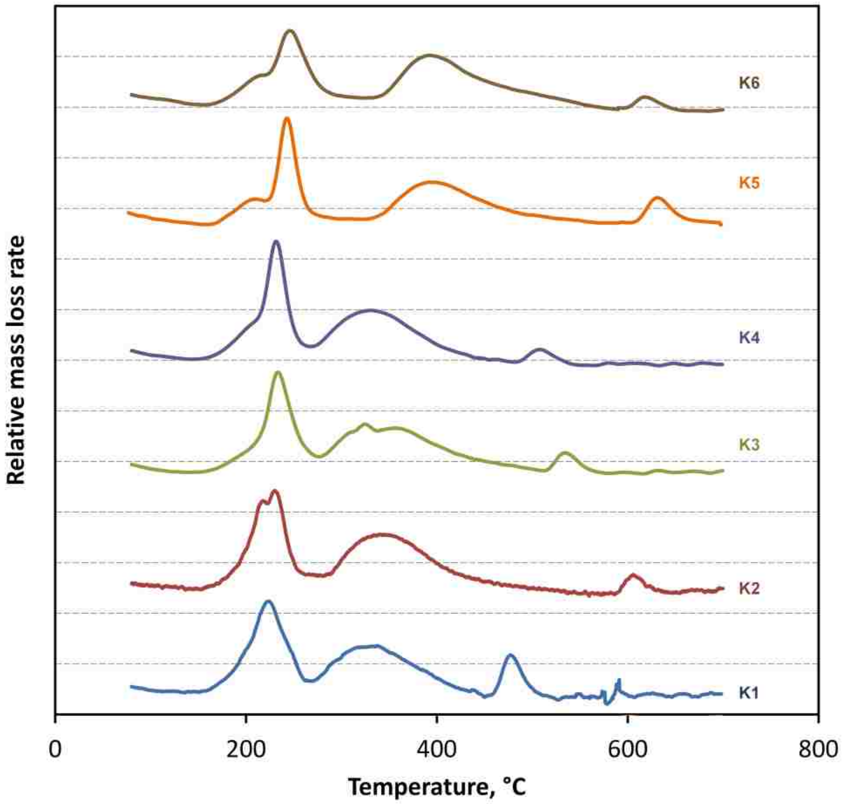

Figure 3.3. H_2-temperature programmed reduction profiles of supported iron catalysts.

The extent of reduction for each TPR peak, reported in Table 3.4, was calculated by dividing the measured weight loss by the theoretical weight loss corresponding to each transition from Fe_2O_3 to Fe, including the complete reduction of CuO to Cu. The extents of reduction for the first stage (from ~205°C to 240°C) range from 20.9 to 41.0%. These values are considerably higher than the theoretical value shown in Table 3.5 for reduction of Fe_2O_3 to Fe_3O_4 including CuO to Cu (14.8% extent of reduction), but closer to the theoretical value for the reduction of Fe_2O_3 to FeO (36.1% extent of reduction). This suggests that the intermediate phase in the reduction of Fe_2O_3 to Fe is likely FeO, rather than Fe_3O_4. This observation is consistent with Zhang et al. [82] who reported that FeO, not Fe_3O_4, is the intermediate for supported Fe catalysts. As reported in Table 3.4, the extents of reduction for the second stage (33.5–48.8%), which is FeO to Fe metal, are less than the theoretical value (63.9%), indicating that some FeO remains in each of the six catalysts.

Table 3.4. Actual extent of reduction after TPR.

Catalyst	Extent of reduction, %	
	First stage	Second stage
K1	31.4	39.6
K2	20.9	34.1
K3	38.0	42.6
K4	40.7	33.5
K5	37.8	48.8
K6	41.0	47.8

Table 3.5. Theoretical extent of reduction.

	Theoretical Extent of Reduction, %
$Fe_2O_3 \rightarrow Fe_3O_4$	14.8
$Fe_2O_3 \rightarrow FeO$	36.1
$FeO \rightarrow Fe$	63.9

The highest peak for the non-aqueous catalysts (K1 and K2) occurs at lower temperatures than the four aqueous catalysts (~220°C vs 230–245°C). However, as mentioned previously, a low temperature shoulder or peak occurs around 205°C for all of the catalysts. K1 and K2 also have the smallest extents of reduction for both the first and second stages. K2 has an even smaller extent of reduction than K1, indicating that the additional 20 wt% Fe relative to K1 is only partially reducible. For K3 and K4, the temperatures where the highest peaks occur in the first two reduction stages are very comparable (~230°C and 330°C, respectively). However, both of these peaks for K5 and K6 have shifted to much higher temperatures, to ~245°C for the first stage and to ~400°C (70°C higher) for the second. This shift to higher temperatures indicates that K5 and K6 are more difficult to reduce than the other four catalysts.

3.3.2.2 Oxygen titration

The extent of reduction for the six catalysts calculated after oxygen titration at 400°C (preceded by hydrogen reduction at 280°C) ranged from 25–44%, as shown in Table 3.6. The non-aqueous catalysts (K1 and K2) again have lower EOR than the aqueous catalysts (K3–K6): 25–30% vs. 38–44%. The catalyst with 40 wt% Fe loading (K2) has a lower EOR (and is more oxidized) than 20 wt% Fe (K1), despite having larger metallic Fe crystallites (shown in Table 3.3). Co-impregnation (K5) results in the lowest EOR among the aqueous catalysts.

The catalysts with higher K loadings, whether added during the last stage of catalyst preparation (K4) or added to the support (K6), retain the highest extent of reduction (42–44%) following oxygen titration.

Table 3.6. Extent of reduction following oxygen titration at 400°C.

Catalyst	EOR, %
K1	30.0
K2	25.0
K3	40.5
K4	44.3
K5	38.4
K6	42.4

3.3.3 Catalyst carbiding

3.3.3.1 Syngas-TPR

To evaluate the reduction/carburization behavior of the catalysts, syngas-TPR's were performed on the calcined catalysts. Figure 3.4 shows the results of these syngas-TPR profiles for the six catalysts up to 350°C, the range over which the reduction/carburization of the catalysts are performed. The observed weight losses under a H_2/CO atmosphere are a combination of several competing reactions including: (1) reduction of Fe_2O_3 to lower iron oxides or iron metal (the first two peaks, 150-200°C) and (2) carbiding of the iron oxides or iron metal to iron carbides (the last peak, 280-310°C). The two step reduction of Fe_2O_3 to lower iron oxides or iron metal and its carbide occur at lower temperatures for the non-aqueous catalysts, K1 and K2. K2, with 40 wt% Fe, reduces at lower temperatures compared to K1 with 20 wt% Fe, but the reduction peak area for K2 is nearly the same as K1, which indicates a lower extent of reduction, as previously observed during the H_2-TPR. Interestingly, increasing the potassium loading in the case of K4 compared with K3 appears to facilitate easier reduction and carbiding. Co-impregnation of iron and potassium in catalyst K5, intended to produce better contact between them, results in lower reduction temperatures for the first two peaks; however, the carburization temperature does not change significantly and remains ~305°C.

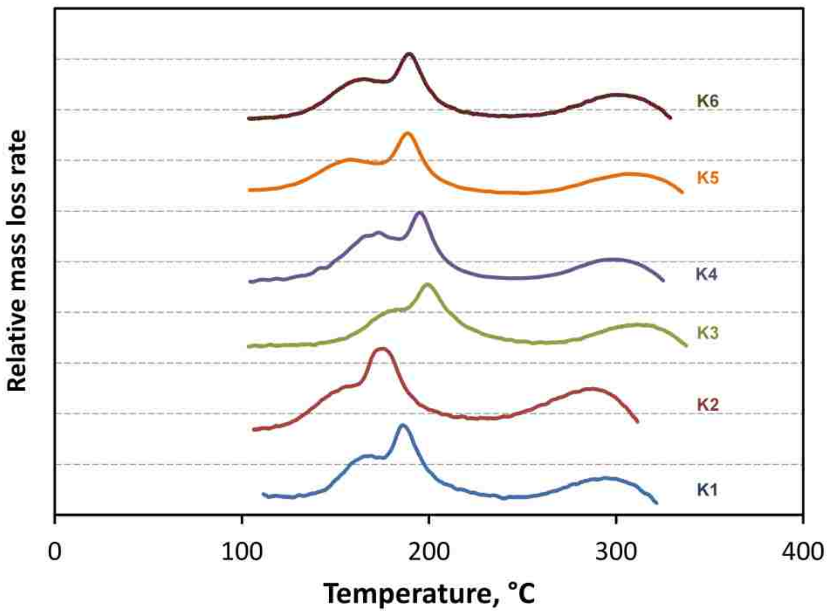

Figure 3.4. Syngas-TPR profile of the alumina supported iron catalysts up to 350°C.

3.3.3.2 CO-TPD

CO adsorption and dissociation on the iron surface are key elementary steps in FTS [28]. To study the effects of the various preparation variables on CO adsorption, desorption, and dissociation, the amount of CO and CO_2 evolved during CO-TPD were measured after pre-adsorption of CO, as shown in Figure 3.5a and 3.5b respectively. Mass spectroscopy measurements indicate two peaks: the first peak (~220°C) is attributed to desorption of molecular CO (see Equation 3.1), while the second broad peak at higher temperatures (between ~450 and 650°C) is attributed to desorption of CO after recombination of dissociated carbon and oxygen on the surface (see Equation 3.2).

$$CO + * \leftrightarrow CO^* \qquad (3.1)$$

$$CO^* + * \leftrightarrow C^* + O^* \qquad (3.2)$$

In Figure 3.5a, the first peak is much smaller than the second peak, which shows that CO dissociates readily on the surface at an adsorption temperature of 150°C. For the aqueous catalysts (K3–K6), the second peak (recombination peak) is a wide or bimodal peak, beginning at significantly lower temperatures (428–455°C) compared to the same peak for the non-aqueous catalysts (~530°C). On the non-aqueous catalysts, in contrast, recombined CO elutes in a single peak at ~600°C. This second peak ends at ~650°C for all six catalysts.

Comparing Figure 3.5b with Figure 3.5a, the CO_2 desorption patterns are qualitatively quite different, where the CO_2 desorbs at up to three different temperatures, indicating up to three different sites at which CO_2 is formed. The three peaks include a relatively large one at low temperatures (230–255°C) and progressively smaller peaks at higher temperatures (390–415°C and 605–650°C).

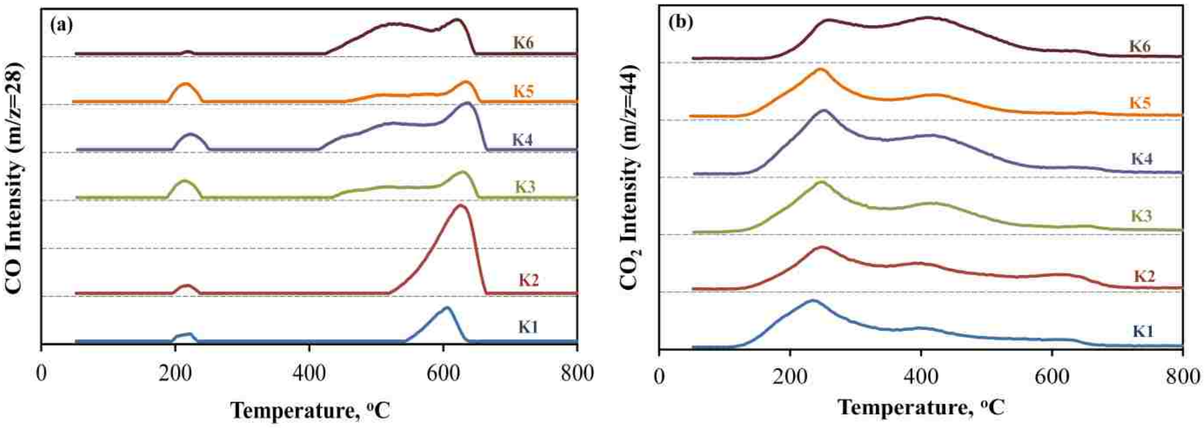

Figure 3.5. (a) CO spectra and (b) CO_2 spectra of CO-TPD after CO adsorption at 150°C.

Table 3.7 shows the amount of CO and CO_2 evolution and the total ($CO+CO_2$) uptake on each catalyst. As expected, the Fe loading had a large positive effect on the total ($CO+CO_2$) uptake, since additional Fe creates more adsorption sites (61.6 µmol/g_{cat} for K1 vs 104.1

μmol/g_{cat} for K2). However, on a per gram Fe basis, the 40 wt% Fe catalyst absorbs less CO than the 20 wt% Fe catalyst (260 μmol/g_{Fe} for K2 vs 308 μmol/g_{Fe} for K1), indicating that not all of the additional Fe in K2 is available on the surface. Among the 20 wt% Fe catalysts, the two catalysts with additional potassium (K4 and K6) had the highest total ($CO+CO_2$) uptake. For K4, with twice as much potassium as K3, molecular CO desorption did not change (see the 1st peak of Figure 3.5), but dissociated CO that recombined and desorbed (the 2nd peak of Figure 3.5) increased from 19.5 to 47.3 μmol/g_{cat}. The additional potassium on the support of K6 decreased desorption of molecular CO to a mere 0.2 μmol/g_{cat}, but increased the total ($CO+CO_2$) uptake to 99.0 μmol/g_{cat} compared to 80.3 μmol/g_{cat} for K3. Co-impregnation (K5) slightly lowered ($CO+CO_2$) uptake (compared to K3). K1 and K5 have very comparable CO and CO_2 desorption behavior.

Table 3.7. CO uptakes on different catalysts measured by CO-TPD.

		CO signal, μmol/g_{cat}		CO_2 signal, μmol/g_{cat}	Total CO + CO_2 uptake, μmol/g_{cat}
	CO: Low temp peak	CO: High temp peaks	Total CO Peaks		
K1	1.4	12.4	13.8	47.8	61.6
K2	1.5	49.2	50.7	53.4	104.1
K3	4.4	19.5	23.9	56.5	80.3
K4	4.2	47.3	51.5	72.2	123.8
K5	4.7	12.4	17.1	43.4	60.6
K6	0.2	39.2	39.4	59.5	99.0

3.3.4 FTS performance

3.3.4.1 Catalyst activity and selectivity

Activity/selectivity data were obtained at similar conversion levels of 19–28%, temperatures of 220–260°C, a total pressure of 2.2 MPa, and a constant H_2:CO feed ratio of 1.0 for the common particle size of 250 to 590 µm (30-60 mesh); therefore, measured values of activity and selectivity for the six catalysts are directly comparable. The activity for another sample of K5 with a smaller particle size of 125-177 µm (80-120 mesh) was also reported. At the operating conditions reported in Table 3.8, the catalysts have a range of reaction rates from 95 to 160 mmol $(CO+H_2)/g_{cat}/h$. Apart from the preparation variables selected and discussed in this paper, these catalysts were prepared identically. Therefore, the preparation variables examined in this paper have the largest effects on the differences in performance of the catalysts.

K5 and K6 were the most active catalysts, while K2 and K4 were the least active. Interestingly, K2 and K4 had the largest Fe loading and the largest K loading respectively. K1 and K5 had slightly better selectivity, as measured by methane production, than the other four catalysts (16–16.4% vs. 17.2–18%). Comparison of activity data from K1 (non-aqueous) with activity data from K3 (aqueous) shows that the non-aqueous slurry impregnation yields catalysts with 14% higher reaction rates (130 vs. 114 mmol $(CO+H_2)/g_{cat}/h$) and slightly lower methane selectivities (16.0% vs. 17.9% methane). Surprisingly, doubling the Fe loading level from 20 wt% (K1) to 40 wt% (K2) decreased the reaction rate by 17%. Similarly, doubling K promotion from 4K/100Fe (K3) to 8K/100Fe (K4) lowered the reaction rate by 17%, while methane selectivity did not improve. On the other hand, direct K promotion of the support in addition to 4K/100Fe (K6) led to a significantly improved observed reaction rate (as compared with K3).

However, as will be shown, direct K promotion sacrifices catalyst stability. Co-impregnation yielded a catalyst (K5) with a rate 40% higher than one prepared by sequential impregnation (K3). Co-impregnation also led to lower methane selectivity compared to sequential impregnation (16.4% compared to 17.9%).

The most active catalyst, K5, was also tested with an average particle diameter of ~150 μm (80-120 mesh). The rate increased about 31% and methane and CO_2 selectivities decreased from 16.4 to 13.2% and 41 to 33%, respectively as average catalyst particle size decreased by a factor of 3 from 420 to 150 μm. A rate increase of only 31% with a decrease in particle diameter of almost a factor of 3 indicates a minimal and decreasing pore diffusion effect. The productivity of K5 also increased about 34% to 0.75 $g_{HC}/g_{cat}/h$. The next most active supported iron catalyst (K1) was also tested at the smaller particle sizes, but no significant changes in rate or selectivity were observed, further indicating the negligible pore diffusion effect for the catalysts at the conditions of this study.

3.3.4.2 Catalyst stability

The reaction rate was periodically measured at 250°C over time to directly compare the stability of the catalysts. Figure 3.6 shows the results of these measurements as a function of time on stream. (Data prior to ~60 h on stream during the induction period of catalyst carburization are not shown because the temperature and flow conditions were optimized for catalyst activation.) The non-aqueous catalysts, K1 and K2, are the most stable. Although K5 and K6 were initially the most active catalysts, this stability analysis conducted at 250°C reveals that neither is very stable. K6, in particular, deactivates to nearly half its initial rate in only 175 h on stream. Extrapolating this steep rate of deactivation beyond the measured 235 h on stream, K6 would have the lowest activity of the six after 300 h or less.

Table 3.8. Performance of six catalysts of this study in fixed-bed reactor tests. T = 260°C, $H_2/CO = 1$, $P_{H2}^0 = 0.66$ MPa, $P_{CO}^0 = 0.66$ MPa, $P_{tot} = 2.2$ MPa.

Catalyst ID	**K1**	**K2**	**K3**	**K4**	**K5**		**K6**
Catalyst particle size	30-60[b]	30-60	30-60	30-60	30-60	80-120[b]	30-60
Time on stream, h	95	126	119	119	118	60	120
Space velocity, Nl/g_{cat}/h	23	23	21	19	21	22	23
CO conversion, %	21	19	19	20	28	19	24
Rate[c]	130	108	114	95	160	210	149
Hydrocarbon Selectivity[d], mol%							
CH_4	16.0	17.2	17.9	18.0	16.4	13.2	17.5
C_{3+}	76	75	73.6	73.1	74.5	81.5	73.1
CO_2 selectivity, %	39.5	42.7	40.2	43.9	40.9	33.3	42.4
Catalyst productivity[e]	0.47	0.39	0.39	0.33	0.56	0.75	0.49

[a] 30-60 mesh size is equivalent to 250-595 μm.
[b] 80-120 mesh size is equivalent to 125-177 μm.
[c] mmol ($CO+H_2$)/g_{cat} /h
[b] CO_2-free basis
[c] g_{HC} /g_{cat}/h

Initially, K5 likewise has a favorable reaction rate, but quickly deactivates. It is unclear whether the reaction rate is stabilizing for K5 after 300 h on stream. If so, K5 could possess the best combination of activity and stability of any catalyst in this study. This lab plans to conduct an additional stability study with K5 in the future, but the data available at this time are insufficient to distinguish the performance of either K1 or K5 as preferable over the other. For a comprehensive view of the quality of these six catalysts, the activity and selectivity characteristics of the catalysts shown in Table 3.8 should be considered in light of this stability analysis.

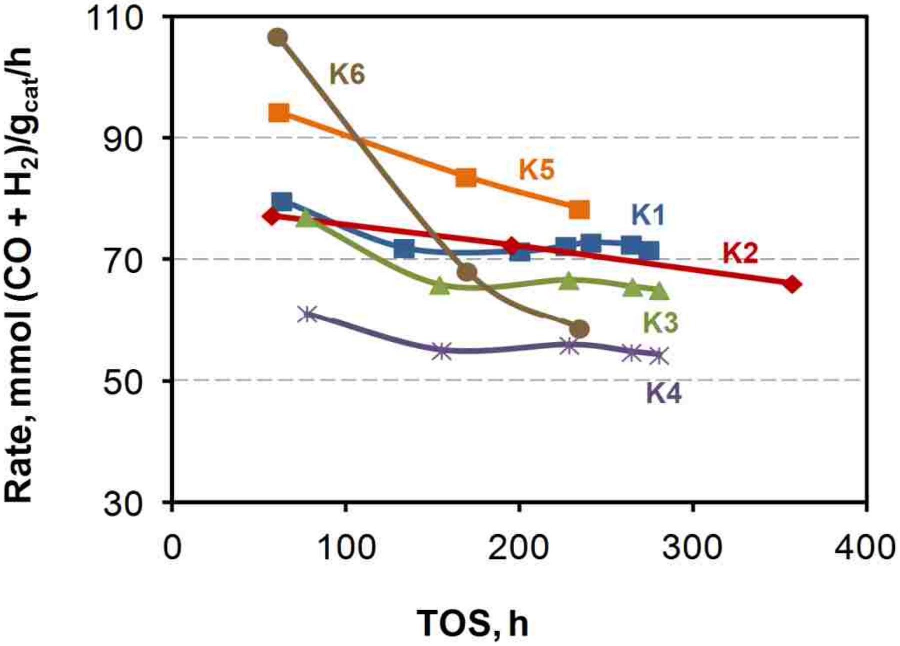

Figure 3.6. Catalyst activity at 250°C ($PH_2^0 = 0.66$ MPa, $P_{CO}^0 = 0.66$ MPa, $P_{tot} = 2.2$ MPa) vs. time on stream.

3.3.4.3 Activity comparison to literature

The FTS performance of the two best catalysts in this study (K1 and K5) was compared with some of the best Fe catalysts reported in the literature, including both supported and unsupported Fe catalysts. The reported data were collected at a variety of reactant concentrations and temperatures. Therefore, to make the comparison, a simple model was used to estimate an apparent reaction rate constant, which accounts for differences in partial pressures. A first-order reaction with respect to hydrogen and zero order in CO was assumed to calculate the apparent reaction rate constant.

A brief summary of the experimental conditions in this study follows to facilitate comparison with the literature results. The temperature and total pressure of K1 and K5 were held constant at 260°C and 2.2 MPa. These supported catalysts were sieved to a particle size of 80-120 mesh (average particle diameters of 150 μm). For this comparison study, the reaction was performed at relatively high conversions (up to 70%) to directly compare the reaction rates and productivities with the literature reports at similar conversion levels, and the ratio of H_2/CO in the feed was about 0.67. Other catalysts reported in literature and shown in Table 3.9 were tested at nearly the same conditions. This comparison to the literature data is limited by these inconsistencies in operating conditions. As is well-reported in literature [83], higher conversion and lower H_2/CO result in slightly lower activity and lower methane selectivity. In addition, the catalysts in this paper were tested in a fixed bed reactor, while most other reported FTS rates were measured in slurry reactors. The values shown in Table 3.9 can be used to further understand the effects of the techniques used to prepare K1 and K5.

The catalysts reported in Table 3.9 are among the most competitive reported in the literature to date. Using rate per MPa for comparison removes much of the bias of differing conversions and H_2/CO ratios. Although K5 (supported iron) has a lower rate than the most reactive unsupported catalyst in Table 3.9, TAMU1 (154 vs 269 mmol $(CO+H_2)/g_{cat}/MPa/h$), K5 produced virtually the same rate as a commercial unsupported catalyst, from Ruhrchemie, as reported by Bukur's group [84] (154 vs. 155 mmol $(CO+H_2)/g_{cat}/h$, respectively).

The activities of K1 and K5 are superior to any supported catalysts reported in the literature prior to publication of our recent work on Fe supported on silica doped alumina (described in Chapter 4) [85]. Both K1 and K5 have 17-40% higher reaction rates than the next most reactive supported catalyst (TAMU2, 40Fe/SiO_2). Per gram Fe, the extremely high reaction rates of K1 and K5 demonstrate how effective the Fe is utilized in each catalyst (570 mmol $(CO+H_2)/g_{Fe}/MPa/h$ for K1 and 770 mmol $(CO+H_2)/g_{Fe}/MPa/h$ for K5).

Hydrocarbon selectivities (based on methane production) for K1 and K5 are less favorable than those prepared by Bukur et al. (see Table 3.9). The C1 selectivity of K5 on a CO_2-free basis is higher (11.4 vs. 7%) than that of Bukur's supported catalyst (TAMU2). This lab recently reported successful preparation of a supported Fe catalyst using a thermally stable silica-doped alumina support (AlSi) [85]. This catalyst yielded a methane selectivity of 9.6% at similar operating conditions (reaction T = 260°C, $H_2/CO = 0.66$, and $X_{CO} = 72\%$) to TAMU2. In addition, this AlSi-supported Fe catalyst is more active than all the catalysts in Table 3.9 [85]. More significantly for this similar AlSi-supported Fe catalyst, increasing the conversion from 23 to 72% resulted in only moderately lower activity, with the 1st order rate constant decreasing from 396 to 325 mmol $(CO+H_2)/g_{cat}/MPa/h$), and productivity decreasing from 0.72 to 0.50 $g_{HC}/g_{Fe}/h$. The activities of the catalysts in the present study are 1.5-3 times higher than the other supported iron catalysts reported in Table 3.9.

3.4 Discussion

By carefully pairing and comparing catalysts with only one dissimilar preparation variable, the direct effects of each specific preparation method on catalyst activity, selectivity and stability can be discerned. The differences in each pair of catalysts are analyzed below and labeled by their associated preparation variable.

Table 3.9. Comparison of K1 and K5 performance with catalysts reported in the literature.

	Catalyst							
	BYU[a]		**TAMU1**[b]	**Ruhrchemie**[c]	**TAMU2**[d]	**TAMU3**[e]	**U. Kentucky**[f]	**BYU-Xu**[g]
Run ID	K1	K5	Unsupp.	Unsupp.	SiO_2/supp	Al_2O_3/supp	Al_2O_3/supp	SiO_2/supp
Literature ref.	This study		[12]	[84]	[18]	[18]	[17]	[9]
Reactor	Fixed bed		slurry	slurry	slurry	slurry	slurry	Fixed bed
Temp., °C	260	260	260	260	260	260	250	265
Pressure, MPa	2.2[h]	2.2[h]	2.2	1.5	1.5	1.5	1.3	1
Inlet H_2/CO	0.67	0.68	0.68	0.67	0.67	0.67	0.7	1
Space velocity[i]	5.0	3.7	3.5	2.2	1.4	1.3	0.68	1.9
TOS, h	183	183	86		100	100	300	150
X_{CO}, %	39	70	84	66			60	77
Rate ($-r_{CO}$)[j]	38[k]	52[k]	76	38			18	14
Rate constant[l]	114[m]	154[m]	269	155	101	50.7		62.1
Rate constant[n]	570[m]	770[m]	450	290	300	150		621
H.C. selectivities, wt% [o]								
CH_4	10	11.4	3	5.3	7	3.5	5.8	6.8
C_{3+}	85.8	83.6	90.1					
C_1+C_2	14.2	16.4	6.3					
Cat. prod.[p]	0.26	0.29	0.51	0.27			0.076	0.3
Cat. prod.[q]	1.3	1.45	0.86	0.51			0.35	3

[a] 100Fe/7.5Cu/4K/400Al_2O_3. [b] 100Fe/3Cu/4K/16SiO_2. [c] 100Fe/5Cu/4.2K/25SiO_2. [d] 100Fe/5Cu/6K/139SiO_2.
[e] 100Fe/5Cu/9K/139Al_2O_3. [f] 100Fe/6Cu/8.1K/250Al_2O_3. [g] 10Fe/1Pt/0.2K/88.8SiO_2.
[h] $P_{H2}{}^0$ = 0.66 MPa, $P_{CO}{}^0$ = 0.66 MPa, P_{tot} = 2.2 MPa
[i] Nl/g_{cat}/h. [j] mmol (CO)/g_{cat}/h
[k] average rate from inlet to the outlet of reactor
[l] mmol ($CO+H_2$)/g_{cat}/MPa/h
[m] an isothermal integral reactor model was used to calculate the rate constants with a rate expression of the form kP_{H2}; volume change factors of -0.44 and -0.425 were assumed for K1 and K5, respectively.
[n] mmol ($CO+H_2$)/g_{Fe}/MPa/h [o] CO_2 free basis.
[p] g_{HC}/g_{cat}/h, where HC are defined for BYU catalysts as C_{3+}
[q] $C_3{}^+$ productivity: g_{HC}/g_{Fe}/h, where HC are defined for BYU catalysts as C_{3+}

3.4.1 Choice of solvent: aqueous vs non-aqueous (K1 vs. K3)

Control of distribution of active precursors is dependent upon the impregnation method and drying step. A uniform distribution in incipient wetness impregnation is usually difficult to obtain. However, wet impregnation in a rotary evaporator greatly facilitates uniform filling of the pores with the precursor solution. Recently, Sasol showed that slurry impregnation, as in the case of the non-aqueous preparation method, leads to better dispersion compared to an incipient wetness preparation method [86, 87]. Also, several papers from de Jong's group showed that improved dispersion in turn improves stability; higher dispersion introduces physical voids between active sites, thus reducing sintering [75, 88, 89].

Tymowski et al. [90] conducted a set of transmission electron microscopy (TEM) tomography experiments that show water does not wet pores smaller than 50 nm, while non-aqueous solvents wet pores as small as 4 nm. This difference allows non-aqueous impregnation to disperse the active phase throughout a wider range of pore sizes, leading to improved dispersion and activity. In addition, the metal deposited in this smaller range of pores (4 nm to 50 nm) with non-aqueous solvents may strengthen the pores against collapse. This may explain why K1 has slightly larger pore volume than K3 (0.54 vs. 0.51 cm^3/g). As observed in the BET results section, K1 exhibits a muted first peak at 7 nm that corresponds to peaks in the aqueous catalysts. The non-aqueous catalyst's first peak disappearing may be due to smaller pores (5–7 nm in diameter) being filled with Fe during impregnation. This argument also explains why this first pore size distribution peak on K2 (40 wt % Fe) has disappeared altogether.

During drying of each sample after impregnation, especially the ones using an aqueous solution, capillary transport may cause the active precursor to accumulate at pore entrances, ultimately leading to a shell-type distribution of metals. Tymowski et al. [90] also hypothesized that metals could be drawn out of pores in the drying step of preparation, leading to pore plugging. Iglesia's group [10] proposed that sintering can occur via pore mouth pinching in the last stages of evaporation of the solvent during preparation. They stated that this sintering is particularly severe for solvents with high surface tensions. Therefore, the lower surface tension of the non-aqueous solvent (50 vol% acetone, 50 vol% isopropanol) may lead to better dispersion for K1 and K2 by way of less disruptive drying. (The surface tensions of acetone, isopropanol, and water at 20°C are 23.4, 23.0, and 72.8 mN/m, respectively.)

As stated in the preparation section, K1 and K2 were prepared in a rotary evaporator with non-aqueous slurry solution, while the aqueous catalysts were prepared by incipient wetness impregnation. Both the slurry impregnation and the non-aqueous solution likely contributed to improve the uniform distribution of the active precursors, consequently resulting in higher activity (130 vs. 114 mmol $(CO+H_2)/g_{cat}/h$) and better stability for K1.

3.4.2 Fe loading level: 20 wt% vs 40 wt% (K1 vs K2)

Bukur et al. [18] stated that high metal loading for supported Fe catalysts is essential to achieve high reactor productivity. However, pore plugging can be exacerbated by higher metal loadings. In this study, as previously mentioned, doubling the Fe loading actually decreased the reaction rate per g of catalyst by 17%. The additional Fe in K2 (20 wt% more than K1) appears to block the pores from reactants, as evidenced by a 17% lower pore volume of K2 than K1. In addition, H_2-TPR results show that the additional Fe in K2 is harder to reduce than K1. For each support, an optimal Fe loading exists that fills the pore volume without blocking reactants from accessing the pores. This optimal loading level likely depends on the pore volume of the support used. In another paper produced by our group (see Chapter 4) [83], catalysts on another support (with double the pore volume of St. Gobein alumina) exhibited improved activity with 40 wt% Fe compared to 20 wt% Fe. For the procedure used to prepare K1 and K2, a critical threshold exists somewhere below 40 wt% Fe for maximum surface area per gram Fe. Therefore, the optimal Fe loading for catalysts on the St. Gobein support must be a loading less than 40 wt%.

3.4.3 Potassium loading level: 4K/100Fe vs 8K/100Fe (K3 vs K4)

Generally, K promotion of FT catalysts is thought to increase activity of both FTS and the water-gas shift reaction. Davis [77] studied trends for potassium-promoted FTS at various conversion levels. He found additional K actually decreases FTS activity at low CO conversions, where K seems to act as a poison. As conversion increases, hydrogen becomes a limiting reagent and FTS begins to depend on hydrogen formed by the water-gas shift reaction. At high conversion, K slightly enhances the FTS activity. Therefore, at intermediate conversions, a K loading exists that produces a catalyst with maximum FTS activity. Specifically, Li et al. [10] observed that K addition above the amount required to create surface density of 2 atom/nm^2 does not increase reaction rate.

For this particular set of catalysts, the additional K applied to K4 appears to have surpassed the loading for maximum rate (for operation at low conversions, <28%). This explains why K4 has a lower reaction rate than K3. Alternatively, Torres Galvis et al. [88] showed that lowering the Fe carbide particle size on carbon nanofibers increased the catalytic activity. In the case of K4, doubling the K loading increased the crystallite sizes of Fe metal (8.6 vs. 4.9 nm), which may also contribute to the lower activity observed of K4 compared to K3. Surprisingly, the methane selectivity of K4 was virtually unaffected by the additional K at this level of CO conversion (20%).

3.4.4 Impregnation timing: sequential impregnation vs co-impregnation; direct surface promotion of the support (K3, K5, K6)

Catalyst preparation by co-impregnation (K5) produces a rate 40% larger than sequential impregnation (K3). H_2-TPR results (Figure 3.3) for K5 reveal the reason for this significant difference: the profile for K5 exhibits shifts to higher temperatures for the first and second peak, by 15°C and 70°C, respectively, compared to the profile for K3. The addition of K and Fe simultaneously seems to have placed the two metals in close contact, making K5 less reducible [77]. This close contact is likely also the cause of the improved reaction rate and methane selectivity for co-impregnation (K5). This TPR peak shift is coupled with a lower EOR than the other aqueous catalysts, likely again due to intimate contact of Fe and K.

Dry and Oosthuizen [81] reported that K^+ ions are an effective promoter because they increase surface basicity. Surface basicity improves dissociation of CO and leads to production of longer hydrocarbons. CO-TPD results demonstrate higher ($CO+CO_2$) uptake on K6 than K3 (99 vs. 80.3 $\mu mol/g_{cat}$) as surface basicity increased by loading of K on the support. Therefore, adding K on the support increased the rate by 31% (relative to K3). Unfortunately, the data presented in Figure 3.4 clearly demonstrate that K6 is not a stable catalyst. During the first 200 h of testing, K6 deactivated dramatically due probably to carbon deposition on the surface of the catalyst, or possibly redistribution of the potassium.

CO-TPD showed that K4 and K6 both have significant dissociation of CO on the surface. Recently, Ribeiro et al., [91] using in-situ TPR-extended X-ray absorption fine structure/X-ray absorption near edge spectroscopy (EXAFS/XANES), found that the rate of carburization correlates with the basicity of the alkali oxide, which is consistent with higher CO dissociation on both K4 and K6 that have higher potassium loading. Furthermore, they reported that the Hägg carbide is the most abundant iron carbide, which is consistent with our observations for K1, with the XRD reported in Chapter 4; Figure 4.4b. Both of these potassium-rich catalysts probably deactivate due to carbon deposition brought on by basic catalyst surfaces. Addition of K on the surface of the alumina clearly exacerbated the deactivation of K6 compared to not adding it (K3).

H_2-TPR results show a shift to higher reduction temperatures for K6 compared to K3. This effect is not simply caused by additional potassium, because K4 exhibited no such change. Possibly, the peaks for K6 have shifted due to Fe or FeO interacting with the potassium-modified surface of the alumina.

3.5 Conclusion

The effects of the four catalyst preparation variables studied by comparing the catalyst performance of pairs of catalysts with only a single preparation variable differing between them were significant. The resulting observations are summarized below:

1. **Aqueous incipient wetness vs. non-aqueous slurry:** K1 (non-aqueous slurry) has 14% higher activity and improved stability compared to K3 (aqueous incipient wetness). Non-aqueous solvents allow for a more gentle drying process that apparently does not disturb the impregnated Fe within the pore.
2. **Fe loading level:** K1 (20 wt% Fe) has a 17% higher reaction rate than K2 (40 wt% Fe) per gram of catalyst. In this case, lower Fe loading may avoid blocking the pores on St. Gobein alumina and so yields greater rates compared to the higher Fe loading.
3. **K loading level:** K3 (4 K/100 Fe) has a 20% higher reaction rate than K4 (8 K/100 Fe). Additional K beyond 4 K/100 Fe acts as a poison at the low conversions used in this study (<28%).
4. **Timing of impregnation:** K5 (co-impregnation) has a 40% higher rate than K3 (sequential impregnation) at 260°C. Co-impregnation of Fe and K yields a catalyst with intimate contact between Fe and K inside the catalyst pores. K6 (direct K promotion of the support) deactivates sharply in the first 200 h on stream, while K3 (no K promotion of

the support) is far more stable. Direct K-promotion of the support increases the FTS reaction rate, but also appears to increase the rate of carbon deposition.

Based on these results, we predict that the optimal sequence of preparation methods (for this St. Gobein alumina support) combines non-aqueous slurry impregnation with co-impregnation of Fe and K metals, with 20 wt% Fe and 4 K/100 Fe. The optimal preparation method also does not directly promote the support with K. The optimal Fe loading could be less than or greater than 20 wt%, but an Fe loading as high as 40 wt% blocks the pores limiting reactant access to active sites. Likewise, the optimal K loading could be less than or greater than 4 K/100 Fe, but must be less than 8 K/100 Fe for low CO conversions. Since K1 and K5 had the best activity, stability, and selectivity performance of the six catalysts, perhaps a catalyst prepared by both non-aqueous slurry impregnation (K1) and co-impregnation (K5) would perform better than K1 and K5. Unfortunately, a catalyst could not be prepared with this combination of preparation variables because the potassium precursor (potassium bicarbonate) is not soluble in the non-aqueous solvent. Another potassium precursor that would allow successful combination of these two preparation methods may yield superior catalysts. Measured performance of K1 and K5 demonstrates that supported Fe catalysts can have high reaction rates and high productivity, even more promising than all of the supported iron catalysts from the literature compared in this paper.

Chapter 4 Supported Iron: Effects of Support Material and SiO_2 Stabilizer

This chapter discusses the effect of support properties and SiO_2 stabilizer on the activity and stability of supported iron FT catalysts. It also reports on the successful preparation of the most active supported Fe FT catalyst to date and a catalyst that is very stable with no deactivation for 700 h time on stream.

4.1 Introduction

The Fischer-Tropsch (FT) Synthesis (FTS) is a commercially proven, economically viable, and environmentally sound process for the production of hydrocarbon fuels from natural gas, coal, and biomass. Nevertheless, improvements in catalyst technology are desirable to improve the efficiency and economy of this process. Iron catalysts are considered to be more favorable than cobalt catalysts for the production of long-chain hydrocarbons from coal or biomass because of their low cost, low methane selectivity, and high water-gas shift (WGS) activity; WGS activity is needed for internal production of H_2 during FTS because of the inherently low H_2/CO ratios in syngas from coal or biomass.

Typical commercial iron FT catalysts consist of unsupported iron promoted with copper, potassium, and silicon dioxide. Precipitated FeCuK catalysts have been used successfully at Sasol for more than 50 years to produce long-chain hydrocarbons from coal synthesis gas in their low-temperature Arge tubular fixed-bed reactors [76]. Several publications from Bukur et al. [7, 8, 13] describe development of active, selective and stable precipitated iron catalysts. Upon optimization of catalyst composition and pretreatment conditions, a weight-time yield of 450 mmol $(CO+H_2)/g_{Fe}/h/MPa$ and a C_{2+} hydrocarbon productivity of 0.86 $g_{HC}/g_{Fe}/h$ for $100Fe/3Cu/4K/16SiO_2$ at 260°C and 2.2 MPa were reported [12]. This activity is among the highest reported for iron catalysts. Unfortunately, despite favorable high activity and selectivity properties, precipitated iron catalysts are generally mechanically too weak for use in slurry bubble column reactors (SBCRs) due to high rates of attrition of fine particles leading to difficulty in solid/wax separation. For example, extensive catalyst attrition was observed in an SBCR reactor operated by DOE at LaPorte, Texas requiring shutdown after only one day of operation [92]. Spray drying the catalyst with silica binders followed by calcination has been used by Sasol and Synfuels China to alleviate this problem [14] but the attrition resistance of unsupported Fe catalyst may not be adequate for the long-term, given higher rates of attrition observed during high velocity operation in large diameter SBCRs [93].

It is well known that supported metal catalysts have high attrition resistance due to the inherently high mechanical strength of the support [17]. Supports also generally (1) facilitate preparation of catalysts with much higher dispersion of the active phase or phases and (2) stabilize the active phase(s) against sintering [76].

Previous attempts to develop supported iron catalysts have largely met with limited success, i.e. most of these catalysts were found to have low activity and high methane selectivity [9, 17, 18]. Interestingly, the poor catalyst performance can be correlated in most cases with preparation methods which led to strong Fe oxide-support interactions and low reducibility or in the case of Fe/carbon catalysts contamination or decoration of the active phase by the support [9, 18, 20]. For example, Cagnoli et al. [94] studied the influence of Al_2O_3 and SiO_2 supports on the activity and selectivity of iron catalysts of very high dispersion and small crystallite size (average diameters of 1.2 and 1.4 nm for Al_2O_3 and SiO_2 respectively). The activity of the alumina supported catalyst was one order of magnitude lower than the silica supported. Since the crystallite diameter in both catalysts was the same, this difference in activity was attributed to higher metal-support interaction of the iron with alumina. This assumption was also verified by the formation of two compounds; namely, $FeAlO_3$ and $FeAl_2O_4$. The alumina supported catalyst also showed higher methane selectivity and lower olefin selectivity. Bukur et al. [13] found that the FTS activity was decreased by the addition of silica or alumina to precipitated Fe (basis of 100 parts of Fe) as follows: unpromoted unsupported > 8 Al_2O_3 ~ 8 SiO_2 > 24 Al_2O_3 > 24 SiO_2 >100 SiO_2. The order can be explained by a lower extent of reduction of Fe and lower effectiveness of potassium due to its interaction with the alumina or silica. In another study of supported Fe Bukur et al. [18] found the silica-supported catalyst was nearly three-fold less active than their group's most active precipitated (unsupported) iron catalyst on a per gram catalyst basis (100 vs. 269 $mmol(CO+H_2)/g_{cat}/MPa/h$) while the alumina-supported catalyst was 5 fold less active.

In contrast to other studies [18, 81, 94], O'Brien et al. [17] found Fe/Al_2O_3 to be twice as active as Fe/silica but still 5-fold less productive than unsupported iron (0.09 vs. 0.45 $g_{HC}/g_{cat}/h$). Methane selectivity was also higher on silica-supported catalysts, which is opposite from the results observed in Cagnoli's study [94].

Barrault et al. [95] found that the activity of iron dispersed on high surface area alumina was lower and its methane selectivity higher than for iron dispersed on low surface area alumina; activity was highest on an alumina of mid-range surface area (80 m^2/g). These results corroborate the hypothesis that well-dispersed iron generally interacts strongly with the support, leading to low activity and high methane selectivity.

Rameswaren and Bartholomew [20] demonstrated that iron interaction with the support declines with decreasing hydroxyl concentration of the support. Increasing the dehydroxylation temperature enhanced the TOF and decreased methane selectivity. Xu and Bartholomew [9] adapted the same principles in their preparation of 10% Fe/silica and FePt/silica catalysts via nonaqueous evaporative impregnation of a previously dehydroxylated silica support. Nevertheless, their reported activity was still 4-fold lower than Bukur's best unsupported catalyst (62 vs. 269 mmol($CO+H_2$)/g cat/MPa/h) probably due to the low Fe loading.

Weakly interactive α-alumina and carbon nanofiber supports were used by de Jong's group [75] to decrease the interaction between iron and the support for high temperature FT to produce olefins. Iron oxide crystallite size was reported to be 14 ± 5 nm on a 6% Fe/α-Al_2O_3 catalyst. Unfortunately, the low-surface area support limited Fe loading and metal dispersion to less than optimal. In another paper, de Jong et al. [88] showed that activity increases with decreasing iron carbide particle size on an inert support.

In summary the catalytic performance of supported Fe catalysts and particularly the effects of support properties on their activity and stability have not been thoroughly investigated. Previous efforts to develop an active, supported Fe catalyst have been largely unsuccessful, in our opinion, due to strong Fe oxide-support interactions and low reducibility caused by less than optimal choices of preparation method, support material and support pretreatment. Consequently, the purpose of the subject study was to investigate systematically the role of the support variables. To acquire a reliable data set, six different catalysts were prepared on alumina supports using the same preparation method and amount of active components (including 20% Fe) except two catalysts with higher (40%) Fe loading. Selecting four different alumina supports with different physical and chemical properties and two different Fe loadings allowed us to investigate the effects on catalyst activity and stability of:

(1) physical properties of the support, e.g. pore volume and pore diameter.

(2) surface chemistry of the support, i.e. hydroxyl groups which can be controlled by thermal pretreatment of the support.

(3) silica vs. lanthana as a stabilizer.

It will be demonstrated that by carefully tailoring these properties it was possible to develop alumina-supported Fe catalysts having higher activity per gram than previously reported. The use of silica-stabilized alumina, which enables high temperature dehydroxylation while still maintaining high surface area and large pore volume, was a key to producing very active and stable catalysts. This approach may have general application to improvements in catalyst performance resulting from higher dispersion and lower metal oxide-support interactions.

4.2 Experimental

4.2.1 Catalyst preparation

A series of six alumina supported iron catalysts with four different alumina supports (St. Gobein alumina (AlG), Alfa-Aesar alumina (AlA), AlC, and AlSi; the last two made by Cosmas Inc.) were investigated in this study. To increase the thermal stability of the supports, 3 wt% La was added to AlG, AlA, and AlC, while AlSi consisted of alumina doped with 5% SiO_2 as described previously [85]. The supports were first sieved to 30-60 mesh and calcined at 700°C in air for 4 h prior to impregnation, except AlSi, which was calcined at 1100°C. All four catalysts were promoted with Cu and K and prepared by slurry impregnation using a non-aqueous solution (50% iso-propanol and 50% acetone) containing desired amounts of ferric nitrate and copper nitrate in multiple steps. In each step 10 wt% Fe with the desired amount of Cu was dissolved in a volume of solution corresponding to 10% above incipient wetness and then was placed in a rotary evaporator and mixed for 12 h to give uniform Fe and Cu deposition. After each impregnation, the catalysts were dried very slowly in vacuum at 50 °C followed by 80 °C in an oven overnight and calcined at 300 °C for 16 h. Following the final addition step of Fe and Cu, potassium was added by incipient wetness impregnation as potassium bicarbonate. Nominal compositions (on a relative mass basis) of reduced catalysts were $100Fe/7.5Cu/4K/400Al_2O_3$ for a nominal iron loading of 20% and $100Fe/7.5Cu/4K/150Al_2O_3$ for an iron loading of 40%. Preparation of unsupported iron catalyst ($FeCuKSiO_2$) was described previously in Chapter 2 (section 2.1.1).

4.2.2 Catalyst characterization

Several characterization techniques were used in this study including: BET, XRD, hydroxyl group measurement, NH_3-TPD, H_2-TPR, syngas-TPR, EOR, NMR. These techniques were fully described in Chapter 2 and our published paper [83].

4.2.3 Activity and selectivity measurements

Fischer-Tropsch Synthesis (FTS) was conducted in a fixed-bed reactor (stainless steel, 3/8 inch OD) described previously [80]. Each sample (0.25 g, 250-590 μm) was diluted with 1 g quartz sand or silicon carbide to improve isothermality in the catalytic zone.

Before FTS, the samples were reduced in situ and the temperature was ramped to 280-320°C from room temperature in 10% H_2/He for 10 h followed by 100% H_2 for 6 h. After cooling to 180°C, the system was then pressurized to 2.2 MPa in a syngas of 63 mol% H_2 plus CO in He with H_2:CO = 1. The catalysts were activated at 280°C for 48-90 h with a target CO conversion level of ~50% during this carburization period. Activity and stability data were then obtained over the next 200-700 hours as reaction temperatures were varied from 220°C to 260°C.

After leaving the reactor, the exit gas and liquid effluent passed through a hot trap (90°C) and a cold trap (0°C) to collect heavy hydrocarbons and liquid products. The effluent gaseous product was analyzed using an HP5890 gas chromatograph equipped with a thermal conductivity detector and 60/80 carboxene-1000 column. CO conversion and selectivities were determined with aid of an Ar tracer.

4.3 Results

4.3.1 Physical properties

4.3.1.1 Nitrogen adsorption/desorption

The average pore diameter and pore size distribution (PSD) of each of the four alumina support materials were calculated from BET data using a new slab pore model and method proposed by Huang et al. [65] and modified to fit a log-normal PSD [66].

The BET data for calcined catalyst samples and unimpregnated supports are summarized in Table 4.1. The surface areas for the four supports ranged from 216 to 288 m^2/g; the average pore diameters (1st peak) were 9.6-18.1 nm, and pore volumes were 0.60-1.06 cm^3/g. Most of the samples had a narrow Gaussian-like unimodal pore size distribution as shown in Figure 4.1. However, for AlSi a broad bimodal distribution with some macroporosity (dp > 50 nm) was observed; these large pores are expected to better accommodate diffusion of reactants in and products out of the pores than in the other catalysts. The first and second peak for AlSi are centered at 17.3 and 45.2 nm, respectively (a small peak around 8 nm for AlSi is not considered). Figure 4.2 shows the BET surface area, pore volume, and pore diameter of the AlSi as a function of calcination temperature from 700 to 1200°C. At elevated calcination temperatures up to 1200°C, the AlSi support still has very good BET properties with surface area of 110 m^2/g, pore volume of 0.59 cm^3/g, and pore diameter of 29.5 nm at 1200°C. As is apparent, the BET properties for AlSi are much higher than for conventional alumina supports such as St. Gobein at the same calcination temperature of 700°C. For instance, the pore volume of the AlSi is 1.83 cm^3/g (see Figure 4.2); three times higher than that of St. Gobein alumina (0.65 cm^3/g) at 700°C. AlSi has the highest pore diameter and pore volume among all the supports. On the other hand, for AlC a very narrow pore size distribution centered at 9 nm is evident.

Table 4.1. Surface area, pore volumes and pore diameters of calcined catalysts and supports.

Sample	BET surface area, m^2/g	Pore volume, cm^3/g	Average pore diameter, nm	
			1st peak	2nd peak
AlG	216	0.65	18.1	-
20Fe/AlG	204	0.55	17.4	-
40Fe/AlG	152	0.46	16.4	-
AlA	228	0.84	16.0	-
20Fe/AlA	209	0.62	15.0	-
AlC	288	0.60	9.6	-
20Fe/AlC	247	0.45	9.0	-
AlSi	224	1.06	17.3	45.2
20Fe/AlSi	216	0.82	20.7	33.1
40Fe/AlSi	173	0.64	21.8	28.5

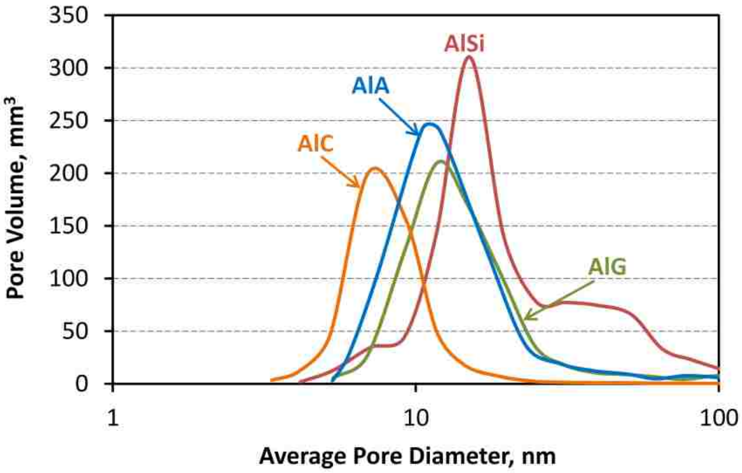

Figure 4.1. Pore size distribution of supports calculated from BET data using a new slab pore model [65]

After impregnation with 20 wt% Fe and calcination, surface area and pore volume (V_{pore}) decreased on average by 10 and 22%, respectively; average decreases in surface area and V_{pore} following addition of 40% Fe were 26 and 34% respectively. Nevertheless, the pore volume of 40Fe/AlSi is comfortably high (0.64 cm^3/g), even with 40% iron loading. Decreases in average pore diameter with increases in Fe loading were generally small (about 10%). However, in the case of 40Fe/AlSi, the diameter of the primary peak increased by 20% and that of the secondary peak decreased by 37%.

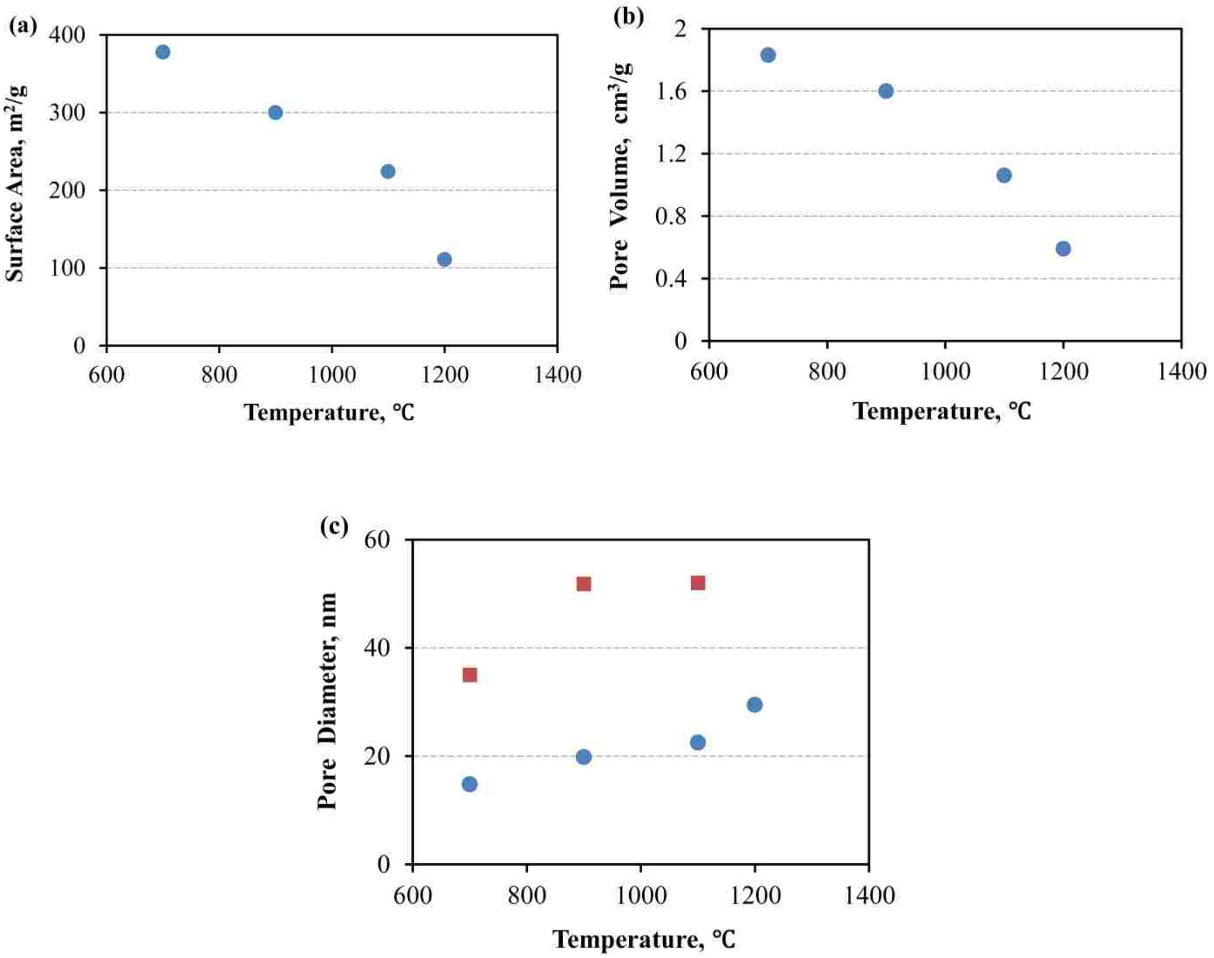

Figure 4.2. (a) BET surface area, (b) pore volume, and (c) average pore diameters of AlSi as a function of calcination temperature. The two sets of data for the pore diameter correspond to the two peaks in the bimodal distribution shown in Figure 4.2 and Table 4.1.

4.3.1.2 X-ray diffraction

Figure 4.3 shows the XRD data for the AlSi at different calcination temperatures. From the XRD data it is observed that the alumina in the AlSi remains γ-alumina up to 1100°C, theta peaks start to appear at 1200°C, and alpha peaks appear at 1300°C. By contrast, Horiuchi et al. [96] observed for their silica-doped alumina the theta phase appeared at 1100°C.

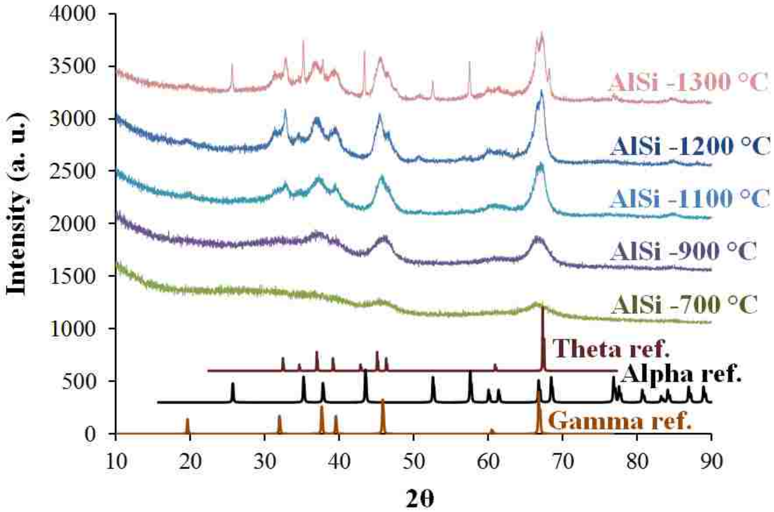

Figure 4.3. X-ray diffraction patterns of AlSi as a function of temperature confirming the AlSi support is essentially γ-alumina at 1100°C.

X-ray diffraction patterns of all catalysts reduced at 280 °C and passivated confirmed the presence of γ-Al_2O_3, Fe^0 and/or Fe_3O_4. As shown by data in Figure 4.4a and Table 4.2, all catalysts contained Fe^0 and/or a significant fraction of Fe_3O_4 as might be expected for such a low reduction temperature. The only difference between X-ray diffraction patterns of reduced samples was the width and intensity of Fe or Fe_3O_4 peaks. No potassium or copper were detected in XRD, probably because of their low concentrations and/or high dispersions. In addition, XRD patterns of the carbided 40Fe/AlG and 40Fe/AlSi (see Figure 4.4b) at 280 °C for 10 h in $H_2/CO=1$ shows Fe_5C_2. The average Fe_3O_4, Fe^0 and Fe_5C_2 diameters as calculated from the peaks located at $2\theta=37.3°$, $2\theta=44.9°$, and $2\theta=43.1°$, respectively, are given in Table 4.2. It was not possible to estimate crystallite diameter (d_{crstlt}) for Fe^0 from XRD for 20Fe/AlSi, since average d_{crstlt} was too small.

Estimated crystallite diameters of Fe^0 ($d_{Fe}{}^0$) or Fe_3O_4 ($d_{Fe3O4}{}^0$) in the case of 20Fe/AlSi are smaller than average pore diameters of the support calculated from nitrogen desorption branches (d_{pore}). An interesting observation is that the d_{Fe^0} for the catalysts (20Fe/AlC and 20Fe/AlA) in which Fe interacted most strongly with the support (i.e. extent of reduction was lowest)) were roughly 50-70% of their corresponding support pore diameters, while the catalysts with higher extent of reduction (20Fe/AlG and 20Fe/AlSi) had crystallite diameters in the same range of only 23-29% of their corresponding support pore diameter, which may indicate relatively little agglomeration of primary iron particles to larger particles, even though d_{pore} of 20Fe/AlSi is 25% larger than that of 20Fe/AlG. By increasing iron loading to 40% from 20%, the estimated particle size (d_{Fe^0}) for Fe/AlG was nearly doubled. In both carbided samples (40Fe/AlG and 40Fe/AlSi), the d_{crstlt} for Fe_5C_2 was around 8 nm.

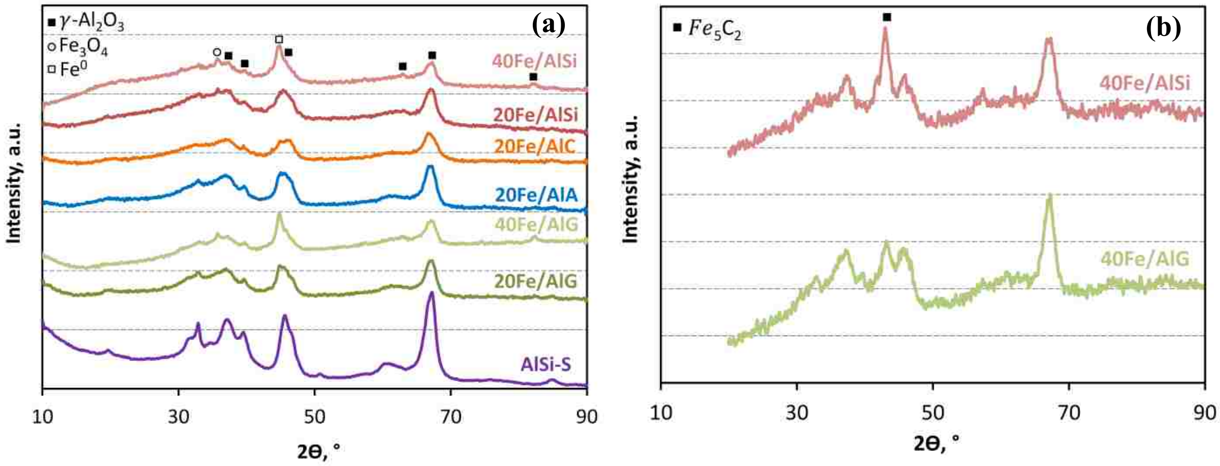

Figure 4.4. X-ray diffraction patterns of (a) reduced and (b) carbided catalysts.

That the average crystallite sizes calculated from XRD are lower than the average pore diameters of their corresponding supports suggests that most of the crystallites are located inside the pores.

Table 4.2. Fe^0, Fe_3O_4, Fe_5C_2 crystallite sizes estimated from XRD. Catalysts were reduced at 280°C in 10% H_2/He for 10 h followed by 100% H_2 for 6 h. 40Fe/AlG and 40Fe/AlSi were carbided at 280°C for 10 h in H_2/CO=1. Reduced and carbided samples were carefully passivated in 1% O_2/He.

Catalyst	XRD, nm			
	Reduced catalysts		Carbided catalysts	$d_{Fe}{}^0/d_{pore}$
	Fe_3O_4	Fe^0	Fe_5C_2	
20Fe/AlG		5.6		0.31
40Fe/AlG	6.4	11.6	8.1	0.64
20Fe/AlA		8.0		0.50
20Fe/AlC		6.6		0.69
20Fe/AlSi	5.2			
40Fe/AlSi	4.4	9.4	7.9	0.42

4.3.2 Catalyst reducibility

4.3.2.1 H_2-Temperature programmed reduction (H_2-TPR)

H_2-TPR was used to investigate the effect of the different alumina materials and metal loading on the reduction behavior of catalysts. As shown in Figure 4.5, the reduction process on supported catalysts occurred in three stages. The first two peaks (below about 400°C) likely indicate a two-step reduction of Fe_2O_3 to iron metal with intermediate iron oxides (Fe_3O_4, FeO). The third stage which occurs at high temperatures is probably due to the presence of a surface Fe aluminate.

Maximum reduction rate for the first reduction peak are centered between 217 and 250°C. The second stage of reduction is much slower on all six catalysts as indicated by lower peak intensities. Extent of reduction (EOR) was determined by dividing the actual weight loss by the theoretical weight loss corresponding to conversion of Fe_2O_3 to Fe and of CuO to Cu. Values for EOR are reported in Table 4.3 for stage 1, stage 2, and overall reduction. For the low temperature range (stage 1) they vary between 20.9 and 31.4% which is higher than the theoretical value for reduction of Fe_2O_3 to Fe_3O_4 and CuO to Cu (14.8%) and lower than the theoretical value for the reduction of metal oxides to FeO and Cu (36.1%). This suggests that after stage 1 reduction (up to 280°C) the iron, on average, is reduced further than to Fe_3O_4, but well short of being Fe metal (100%), and may well be a mixture of FeO and Fe_3O_4. The most reduced of the six catalysts are 20Fe/AlG and 40Fe/AlSi.

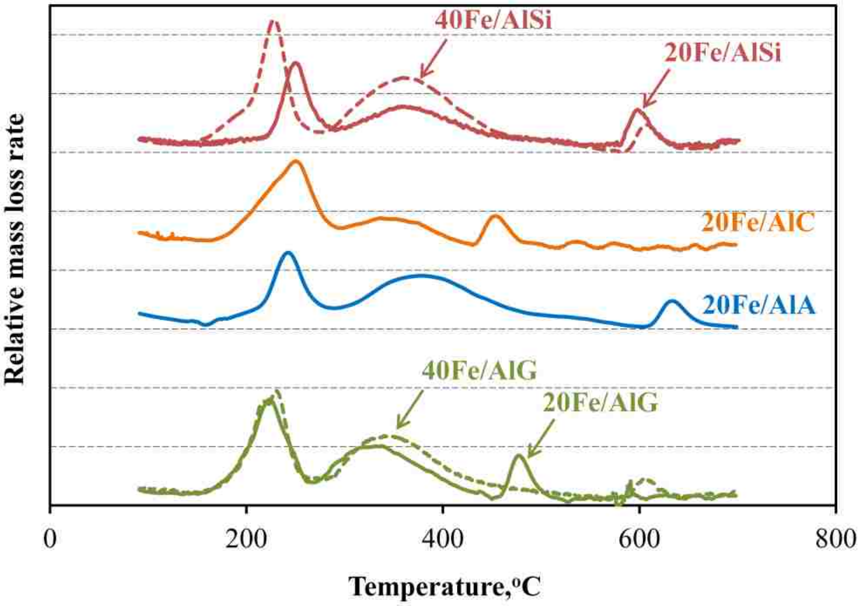

Figure 4.5. TPR profiles of the supported iron catalysts.

The reduction process for the second stage is less than the theoretical value for FeO → Fe (63.9%) and the overall (combined) reduction is significantly less than 100% for all catalysts indicating none are close to being all Fe metal. Four of the catalysts have overall EOR's in the 70-74% range. These values would be consistent with 40% FeO and 60% Fe metal. Among the catalysts, 40Fe/AlSi has a sharp narrow peak for the first stage compared to broader peaks for the other catalysts and its low-temperature reduction area shifted to 20°C lower and ends sooner with increased Fe loading (from 20 to 40%). This shift was not seen for the AlG support. Lower reduction temperatures imply easier reduction and weaker metal-support interactions. These TPR results were consistent with the XRD results as indicated by the fact that the weight losses for the first peak up to 280°C were between the amount required to go to Fe_3O_4 and FeO.

Table 4.3. Extents of Reduction determined from H_2-TPR data.

Catalyst	Extent of iron reduction[1], %		
	First stage	Second stage	Combined
20Fe/AlG	31.4	39.6	71.0
40Fe/AlG	20.9	34.1	55.0
20Fe/AlA	21.9	49.5	71.4
20Fe/AlC	28.4	23.3	51.7
20Fe/AlSi	24.9	49.5	74.4
40Fe/AlSi	30.4	39.8	70.2

[a] determined by dividing the actual weight loss by the theoretical weight loss corresponding to conversion of Fe_2O_3 to Fe and of CuO to Cu

Note : theoretical reduction from Fe_2O_3 to Fe_3O_4 and CuO to Cu is 14.8%
theoretical reduction from Fe_2O_3 to FeO (and CuO to Cu) is 36%

4.3.2.2 Hydroxyl group measurement

The hydroxyl group contents of calcined alumina samples were determined using TGA. Generally, during temperature-programmed heating of a high surface area oxide (e.g. alumina or silica) in inert gas or vacuum, two mass loss events are observed: (1) removal of physisorbed water at low temperatures and (2) removal of hydroxyl groups as water at high temperatures [97]. As shown in Figure 4.6, the first step (removal of physisorbed water) is abrupt in the range of 25-130°C. The second step, due to slow dehydration of alumina hydroxide, is observed by a weight loss in the range of 130-1100 °C which occurs by the following reaction:

$$2Al(OH)_3 \rightarrow Al_2O_3 + 3H_2O \tag{4.1}$$

In this study, pre-calcined alumina samples (AlG, AlA, AlC at 700 °C and AlSi at 1100 °C) were heated from room temperature to 1100 °C in He flow and held for 2 h (Figure 4.6). As observed in Figure 4.6, the weight loss curves for AlG and AlA follow similar trends, while that for AlSi shows a mass loss up to 600 °C and becomes unchanged after 600 up to 1100 °C. Among the samples, AlC had the highest rate of dehydration and dehydroxylation. After reaching 1100 °C, there can be seen a constant decrease in mass for all the samples, although it has a slower rate for AlC and AlSi. This constant rate loss might be attributed to the dehydroxylation of final OH groups as the porous structure starts to collapse from the γ-alumina phase to α-alumina.

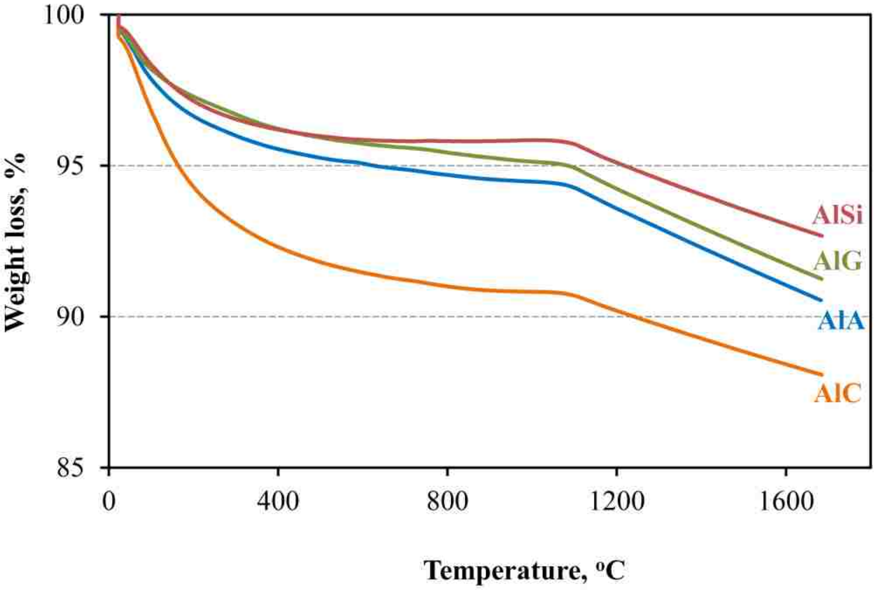

Figure 4.6. Thermo gravimetric curves for dehydration and dehydroxylation of alumina samples. The samples were heated from room temperature to 1100°C in He flow and held for 2 h.

To deconvolute the peaks and distinguish between dehydration and dehydroxylation, we ran another TGA experiment in which the temperature was held at 130°C for 2 h to desorb physisorbed water from the alumina surface. The selection of 130°C for dehydration is in agreement with the literature [97] where the desorption of water is claimed to be complete between 100 – 130°C. The mass of the sample of this point after dehydration is designated as W_{130}.

The hydroxyl group content of the given support was then determined as moles of hydroxyl removed per gram of alumina, as follows:

$$n_{OH} = \frac{2(W_{130} - W_{1100})}{M_{H2O} \times 100} \tag{4.2}$$

where $(W_{130} - W_{1100})$ is the mass loss (wt%) occurring between 130°C and 1100°C. These weight losses were used to determine moles of hydroxyls left per gram of alumina at some given temperature above 130°C.

The physisorbed water content determined for W_{130} values and the total hydroxyl group content of aluminas at 1100°C are presented in Table 4.4. The AlSi had the lowest OH group content and that for AlC was the highest among the alumina samples. The greater the OH group content, the higher amount of physisorbed water was found on the samples. This result is consistent with the fact that alumina is hydrophilic in nature because of the presence of hydroxyl groups on the surface [98].

Table 4.4. Concentrations of physisorbed water and OH groups for alumina samples.

	AlG	AlA	AlC	AlSi
First[a] mass loss, %	2.7	3.4	5.5	2.6
Second[b] mass loss, %	3.6	3.9	5.1	2.4
Physisorbed water, mmol/g_{Al2O3}	1.5	1.9	3.1	1.4
OH group content, mmol/g_{Al2O3}	4.0	4.4	5.6	2.7

[a] weight loss up to 130°C

[b] weight loss between 130 and 1100°C

4.3.2.3 Acidity measurements

The total acidity of the AlSi support at different calcination temperatures were determined using NH_3-TPD measurements. As shown in Figure 4.7, a dehydroxylation temperature of 1100°C is very effective in removing most of the acidic sites on AlSi, i.e., the acid site concentration is only 48 μmol/g_{cat} compared to 162 and 236 μmol/g_{cat} on AlSi calcined at 900 and 700°C, respectively. Decreasing OH group content and acidic sites by calcining the support material at high temperatures makes the surface of the alumina more hydrophobic, which decreases the likelihood of further hydroxylation during catalyst preparation and FT reaction in which water is formed [9, 99]. Another advantage of removing hydroxyl groups and acidic sites by calcining at high temperatures is to reduce cracking to light hydrocarbons and formation of methane via a formate species [100].

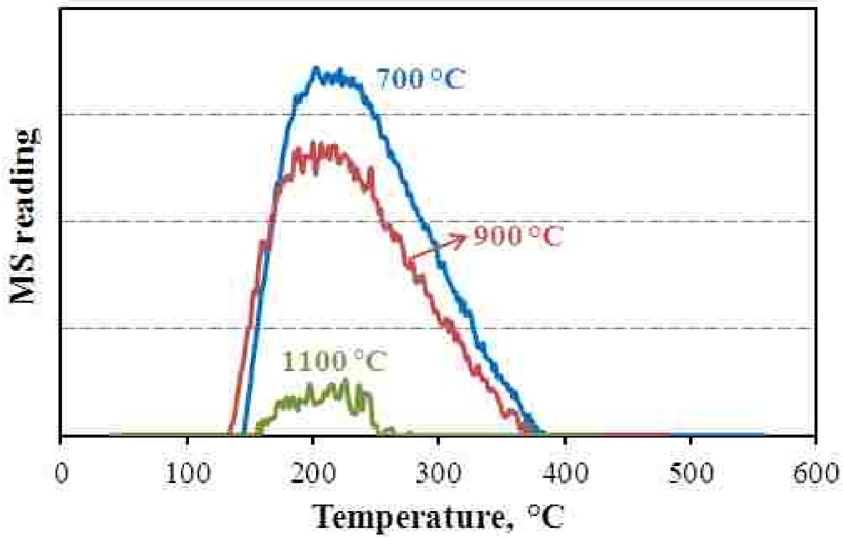

Figure 4.7. Ammonia-TPD measurements on AlSi calcined at 700, 900, and 1100°C demonstrating the reduction in acid sites as calcination temperature is increased.

4.3.2.4 Oxygen titration

The extent of reduction to iron metal (EOR) after hydrogen reduction at 280°C was measured using oxygen titration, and the results are shown in Table 4.5. They range from 15 to 31% with the two AlSi supported catalysts showing two of the highest values. High EOR of Fe/AlSi might be explained by the fact that the AlSi was calcined at higher temperature than the other supports (1100°C vs. 700°C), which leads to lower hydroxyl groups on the alumina surface. Surprisingly, 20Fe/AlG had the highest extent of reduction among supported catalysts with 20% iron loading, although the support was calcined at 700°C. The EOR results are consistent with the TPR, which showed lower reduction temperature for 20Fe/AlG and 40Fe/AlSi.

The EOR values measured in this study for the AlSi and AlG catalysts were higher than those reported by Bukur and Sivaraj [18] on alumina- and silica-supported FeCuK catalysts after reduction in H_2 at about 400°C (19-26%), while they are lower than those for silica-supported FePtK (EOR: 70% after reduction in H_2 at 300°C) reported by Xu and Bartholomew [9]. However, the extent of reductions found by different techniques should be compared with care. Borg et al. [101] reported significantly higher values for extent of reduction calculated from H_2-TPR than those from oxygen titration data on cobalt supported catalysts. They suggest that oxidation of reduced catalysts with oxygen at 400°C is not complete. Therefore, for our supported Fe catalysts, our oxygen titration measurements may be giving low values of EOR due to oxidation of iron metal to Fe_3O_4, FeO or Fe_2O_3 or to a mixture of these, instead of all Fe_2O_3 as is assumed in the calculation. Nevertheless, the results should be meaningful on a relative basis.

Table 4.5. Extent of reduction (EOR) to Fe metal determined from oxygen titration after reduction of each sample at 280°C with 10% H_2/He in TGA.

Catalyst	EOR[a], %
20Fe/AlG	30
40Fe/AlG	25
20Fe/AlA	16.3
20Fe/AlC	15
20Fe/AlSi	27
40Fe/AlSi	31

[a] 95% confidence interval was determined to be ± 2.3% of each EOR value

4.3.3 Catalyst carbiding

4.3.3.1 Syngas-TPR

Although H_2-TPR provides useful information on the relative reducibility of the calcined form of the different catalysts, it does not provide information on the reduction/carburization process under actual pretreatment and FT conditions. In the latter case, the catalyst is exposed to syngas to form iron carbides which are apparently the active phase in FT [7-9]. To estimate the reduction/carburization behavior of our catalysts, we performed syngas-TPR on the calcined catalysts. Figure 4.8 focuses in on the syngas-TPR profiles of the six supported iron catalysts of this study; part (a) shows the profiles up to 350°C and inverts the spectra so that weight loss is shown as positive peaks and part (b) shows the entire profiles up to 700°C, including large weight gain between 350-700 °C. The observed weight changes under a H_2/CO atmosphere are a combination of several competing reactions including: (1) reduction of Fe_2O_3 to lower iron oxides or iron metal; (2) carbiding of the iron oxides or iron metal to iron carbides (e.g. Fe_5C_2); and (3) carbon deposition (carburization) by Boudouard reaction ($2CO \rightarrow C + CO_2$). Stage (1) is weight losing and stage (2) can be weight losing or weight gaining depending on whether the iron carbide is formed from Fe oxide or Fe metal; here the net change is weight losing for stage 2. Stage 3 is weight gaining due to carbon deposition. In Figure 4.8a, for most of the catalysts, there are two peaks observed at low temperatures (150-220°C), attributed to reduction of Fe_2O_3 to lower iron oxides and a third peak (290-320°C) representing the carbiding step. The weight losses per iron atom are shown in Table 4.6 for the reduction stage (first two peaks) and the carbiding stage (third peak). For reference, 30% would signify complete reduction of Fe_2O_3 to Fe^0. The reduction peaks for 20Fe/AlG are narrower compared with broader peaks for 20Fe/AlSi and 20Fe/AlC, which shows a facile reduction for 20Fe/AlG. The reduction of 20Fe/AlC is more complete but also ends at high temperatures. The reduction on 20Fe/AlA is done sooner at around 223°C, but it has lower weight loss than the other 20% iron catalysts. Both 40Fe/AlSi and 40Fe/AlG have lower reduction temperatures compared to their corresponding 20% Fe catalysts, but the reduction peak area for 40Fe/AlG is nearly the same as 20Fe/AlG, which suggests lower extent of reduction. 40Fe/AlSi has easier reduction/carbiding than 20Fe/AlSi as evidenced by lower reduction/carbiding temperatures and sharper reduction peaks. Theoretical weight losses for reduction of Fe_2O_3 to Fe_3O_4, FeO, Fe and iron carbide (χ-Fe_5C_2) are approximately: 3.3, 10, 30, and 24%, respectively. The experimental weight losses (9-28%) vary greatly but suggest all samples are reduced to at least FeO on average (except 40Fe/AlG).

The data (Table 4.6) indicate that the carbiding of all catalysts was incomplete, since total weight losses (reduction + carbiding) were less than 24%. The reduction starts at lower temperatures in syngas-TPR compared with H_2-TPR (Figure 4.5), which shows CO to be a more effective reducing agent. These results, along with the H_2-TPR results which suggested FeO as an intermediate, are not inconsistent with the reduction/carbiding process under H_2 and CO (1:1) of $Fe_2O_3 \rightarrow FeO \rightarrow$ iron carbide.

Table 4.6. Mass losses of reduction and carbiding stages as shown by syngas-TPR (Figure 4.8a).

Catalyst	Mass loss per iron atom, %		
	Reduction stage (1)	Carbiding stage (2)	Total (1) + (2)
20Fe/AlG	14.5	5.5	20.0
40Fe/AlG	6.2	4.6	10.8
20Fe/AlA	9.2	3.5	12.7
20Fe/AlC	14.3	2.8	17.1
20Fe/AlSi	10.2	4.8	15.0
40Fe/AlSi	7.5	4.4	11.9

Figure 4.8b shows that in the third stage, weight gained by carburization, there are very large peaks around 460-480°C. This sudden increase in weight indicates that carbon deposition is the dominate reaction after 330°C, and shows the carburization extent of these catalysts. 20Fe/AlC had the lowest weight gain, and 20Fe/AlG, 20Fe/AlSi and especially 40Fe/AlSi had the highest gains. Weight gain on 40Fe/AlSi was twice that of all others. Zhang et al. [82] performed CO-TPR on unsupported iron manganese promoted with Cu and K. Their results show that their carburization peaks were only slightly larger than the reduction peaks, but in our case, for our supported iron catalysts, the carburization peaks (stage 3, carbon deposition) were 5-10 times larger than the reduction peaks.

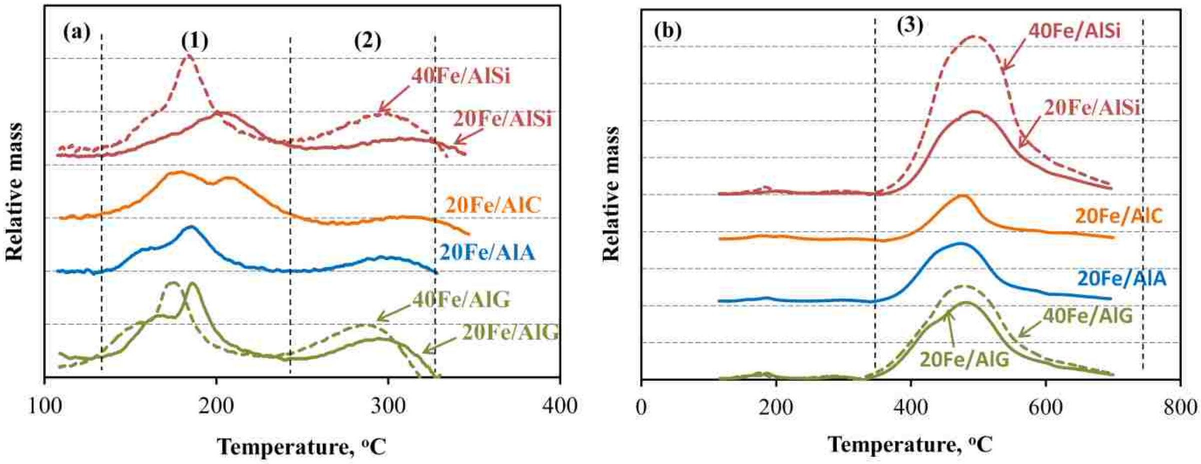

Figure 4.8. Syngas-TPR profile of the alumina supported iron catalysts (a) up to 350 °C and (b) up to 700°C. Profiles were obtained by ramping in 10% syngas/He (H_2/CO=1) at 3 °C/min up to 700°C.

4.3.3.2 CO-chemisorption

CO chemisorption uptake data were obtained for each catalyst as an indication of their active site densities. It is believed that iron carbide is the active site during FTS for iron catalysts [9]; therefore, CO-uptake measurements were carried out on the carbided catalysts, and the results are shown in Table 4.7. These range from 121-280 μmol/g_{cat} for 20% Fe loading and 288-

355 μmol/g_{cat} for 40% Fe loading, and show a trend of increasing uptake with increasing the loading. Higher CO uptake for 20Fe/AlSi among 20% Fe catalysts implies having higher activity as it has more iron carbide sites.

Table 4.7. CO-chemisorption of the carbided catalysts, following 10 h of syngas at 280°C in TGA.

Catalyst	CO uptake, μmol/g[a]
20Fe/AlG	204
40Fe/AlG	262
20Fe/AlA	176
20Fe/AlC	121
20Fe/AlSi	280
40Fe/AlSi	355

[a] per gram calcined catalyst

4.3.4 FTS performance

4.3.4.1 Activity and selectivity

Table 4.8 compares FTS performance including CO conversion, CO+ H_2 conversion, CO+H_2 activity (reaction rate), selectivity, and productivity for the six alumina supported iron catalysts of this study. All data were obtained at approximately the same differential reactor conversion level (18-21%) and at 260 °C; therefore, measured values of activity and selectivity are directly comparable. It is clear for these data that the support material does make a difference, as the activities of the four catalysts at 20% Fe loading vary by over a factor of two (63 – 133 mmol(CO+H_2)/g_{cat}/h). The catalyst supported on AlG (St. Gobein) and AlSi (BYU) aluminas are the most active, whereas those on AlA (alfa-aesar) and AlC (BYU) are the least active. The effect of increasing weight loading from 20 to 40% depends greatly on support: for AlSi the activity on a per mass of catalyst basis increases by 20%, while for AlG the activity decreased by ~ 16%. CO_2 selectivity as an indicator of the extent of the water-gas shift reaction is the highest for the AlG support and lowest for the AlSi support. Increasing iron loading tends to increase the WGS activity, e.g. the CO_2 selectivities are 30.8 and 38.1% for 20Fe/AlSi and 40Fe/AlSi, respectively. Steady-state methane selectivity is 11.2% on 20Fe/AlC compared to 15.5-17.3% on the other supports; however, the activity of 20Fe/AlC is also the lowest. Accordingly, productivity of C_{3+} hydrocarbons is the lowest for 20Fe/AlC. It is the highest for the 20Fe/AlG and the two AlSi, which are very similar (0.45-0.47 $g_{HC}/g_{cat}/h$).

Table 4.8. Performance of six catalysts of this study in fixed-bed reactor. T = 260 °C, $H_2/CO = 1$, $P_{H2}^0 = 0.66$ MPa, $P_{CO}^0 = 0.66$ MPa, $P_{tot} = 2.2$ MPa.[a]

Catalyst ID	20Fe/AlG	40Fe/AlG	20Fe/AlA	20Fe/AlC	20Fe/AlSi	40Fe/AlSi [b]
Space velocity, $Nl/g_{cat}/h$	22.5	22.3	15.0	10.4	22.4	22.0
Time on stream, h	95	126	177	95	149	246
CO conversion, %	20.9	18.7	19.2	21.3	18.6	20.2
(H_2+CO) Conversion, %	20.7	17.3	20.4	22.1	21.7	20.7
Activity, mmol(CO+H_2)/g_{cat}/h	129.6	107.5	84.3	63.2	133.2	153.3
CO_2 selectivity, %	39.5	42.7	38.7	34.7	30.8	38.1
H.C. selectivity[c], %						
CH_4	16.1	17.3	16.3	11.2	15.6	15.5
C_{3+}	76.5	75.1	73.9	83.2	76.7	76.0
Catalyst productivity, $g_{HC}/g_{cat}/h$	0.47	0.39	0.29	0.25	0.47	0.45

[a] All catalyst samples were 30/60 mesh.
[b] This test was conducted at 256 °C, the activity was corrected to 260 °C using E_A = 100 kJ/mol.
[c] CO_2-free basis.

4.3.4.2 Stability

Figure 4.9 shows changes in activity (mmol (CO+H_2)/g_{cat}/h) as a function of time on stream up to between 250 and 700 hours for the six catalysts of this study for the common particle size of 250 to 590 μm (30-60 mesh). It also shows the activity for another sample of 40Fe/AlSi with a smaller particle size of 125-177 μm (80-120 mesh). (Note there are some gaps in the data in Figure 4.9 since the catalysts were being tested at different conditions to obtain other data that are not shown.) Unsupported iron catalyst ($FeCuKSiO_2$) was also prepared and tested in this laboratory to compare with supported catalysts. The initial activities on these catalysts were collected after activation, which took 60-100 hours. Most supported iron catalysts had higher initial activity than $FeCuKSiO_2$ except 20Fe/AlA and 20Fe/AlC. Except for Fe/AlSi, Fe/alumina catalysts deactivated after the activation period. 20Fe/AlA started with higher activity than 20Fe/AlC (62 vs. 40 mmol $(CO+H_2)/g_{cat}/h$), but the activity dropped to nearly the same as 20Fe/AlC after 190 h on stream. Among the catalysts, 20Fe/AlA had the highest deactivation rate after 190 h on stream with a 31% drop in activity followed by 20Fe/AlG with a 9% drop. Both catalysts reached steady-state after 130-190 h on stream. But the activity of 40Fe/AlG continues to decrease linearly at a deactivation rate of 6% even after 350 h on stream. With the exception of Fe/AlSi catalysts, activity loss was least for 20Fe/AlC. On the other hand, activity was observed to increase for both Fe/silica-doped alumina (AlSi) catalysts even after 700 h. Indeed the activity for 40Fe/AlSi (80/120) after 700 h was about 13% higher than its initial activity. In addition, activities for 20Fe/AlSi and 40Fe/AlSi (30/60) followed the same stability trends of increasing activity with time on stream; 20Fe/AlSi increased 12.8% in 700 h and the 40Fe/AlSi increased 7% in 470 h.

4.3.4.3 Catalyst particle size effect

As noted above, all catalysts were initially tested at a 30-60 mesh particle size (250-595 μm, average = 420 μm), but the 40Fe/AlSi was also tested at 80-120 mesh, (average = 150 μm) to investigate the effect of pore diffusion resistance. It was not believed that there would be an effect as the activation energy for the six Fe/alumina catalysts ranged from 110 to 145 kJ/mol, which is larger than the value of 100 kJ/mol reported in previous literature [102]. Surprisingly, activity increased about 30% (see Figure 4.9), and methane selectivity decreased slightly from 15.5 to 14.3% (compare to Table 4.8) as average catalyst particle size decreased by a factor of 3 from 420 to 150 μm. Also, the fact that the rate increase was only 30% with a decrease in particle diameter of almost 3 times indicates a minimal and decreasing pore diffusion effect.

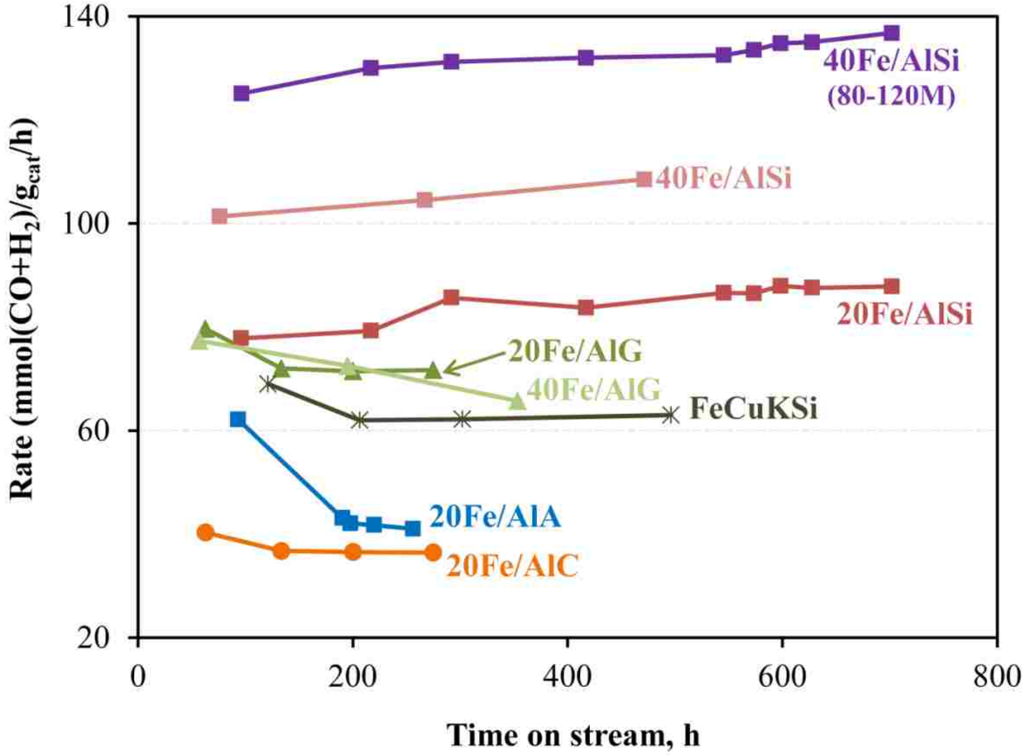

Figure 4.9. Catalyst stability with time on stream at 250°C, H_2/CO:1, total pressure of 2.2 MPa, 30-60 mesh size except for the catalyst of highest rate.

4.3.4.4 Comparison to literature

It is instructive to compare the FTS performance of our best catalyst (40Fe/AlSi) with results reported in the literature for other Fe based catalysts. To do so, a simple kinetic model was used to estimate apparent first order reaction rate constants (1st order in H_2 and zero order in CO), which accounts for relatively moderate differences in total pressure, partial pressures, and reactor type [18]. Figure 4.10 and Tables 4.9 and 4.10 compare the performance of the 40Fe/AlSi (150 μm) catalyst with results reported previously for supported and unsupported Fe catalysts.

Previous to this work, it was generally observed that unsupported Fe catalysts are significantly more active than supported Fe catalysts. The apparent rate constant (per gram of catalyst) for our alumina-supported catalyst (40Fe/AlSi) is 3 times more active than the silica-supported catalyst reported by Bukur et al., and 6-fold more active than their alumina-supported (297 vs 51 mmol $(H_2+CO)/g_{cat}/MPa/h$). Moreover, the rate constant (per gram of catalyst) of our 40Fe/AlSi is nearly 10% higher than that of the most active *unsupported* catalyst of Bukur et al.; i.e. 297 mmol $(H_2+CO)/g_{cat}/MPa/h$ versus 269 mmol $(H_2+CO)/g_{cat}/MPa/h$, and 65% more active on a per g Fe basis, i.e. 743 vs 450 mmol $(H_2+CO)/g_{Fe}/MPa/h$. In addition, the catalyst productivity is the same per gram catalyst and about 40% higher per g of Fe. The C_{3+} selectivity on a CO_2-free basis of the 40Fe/AlSi is slightly lower (86 vs 90%) since $CH_4+C_2H_6$ selectivity is higher (12.4 vs. 6.3%) for 40Fe/AlSi.

A comparison to Xu and Bartholomew [9] shows our CO depletion rates ($-r_{CO}$) are about six times those reported for their $FePtK/SiO_2$, even though 40Fe/AlSi was tested at slightly lower temperatures (260 vs. 265°C). Results from Mobil's unsupported iron catalysts are also regarded as one of the most successful runs in a slurry reactor. For essentially the same process conditions of temperature and H_2/CO, but higher pressure (2.2 vs. 1.5 MPa), our alumina-supported iron catalyst is significantly more active than their unsupported iron catalyst (743 vs. 265 mmol $(CO+H_2)/g_{Fe}/MPa/h$). A recent test by the Davis group on an unsupported iron catalyst shows higher productivity than our 40Fe/AlSi (0.72 vs. 0.50 $g_{HC}/g_{cat}/h$) [78]. Activity and productivity comparisons are also made to other unsupported and supported catalysts in Figure 4.10 and

Tables 4.9 and 4.10 including comparisons to industrial catalyst from Ruhrchemie [84] as well as academic catalysts from UC Berkeley [10] and U. Kentucky [17, 103].

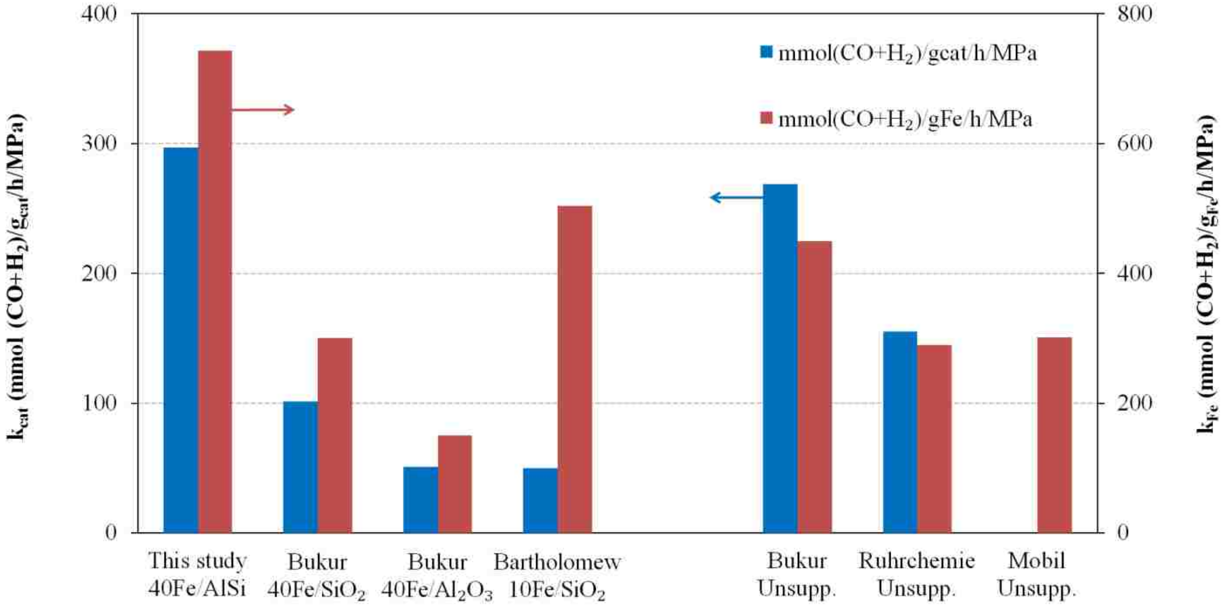

Figure 4.10. Comparison of first order rate constants for various supported and unsupported iron catalysts at 260°C. The left axis in represents the rate constant per gram of catalyst (blue) and right axis is the rate constant per gram of Fe (red).

4.4 Discussion

The results of this work demonstrate for the first time the preparation of a supported Fe catalyst of high activity and stability for Fischer-Tropsch Synthesis. This was made possible through (1) use of a non-aqueous, wet slurry impregnation method which facilitates a uniform spatial distribution of Fe, Cu, and K over the support while minimizing oxidation of the iron precursor (details are reported in [79]); (2) incorporation of a silica-stabilized alumina support (a) of high thermal stability enabling dehydroxylation of the support at a very high temperature (1100 °C) which in turn prevents strong interaction of iron oxide with the oxide support thereby facilitating Fe reduction to the carbide while preventing Fe-support compounds; (b) of large pore volume, and pore diameter which facilitates incorporation of high Fe loadings (e.g. 40 wt.%)

without pore blockage; and (c) containing silicon oxide species coordinated with the alumina surface, forming aluminosilicate groups which anchor and thereby limit migration of active Fe carbide crystallites, facilitating higher dispersion and preventing active phase sintering.

Table 4.9. Comparison of BYU 40Fe/AlSi with other supported Fe catalysts at 260°C.

	BYU-this study		TAMU-Bukur	TAMU-Bukur	U. Kentucky-Davis[2]	BYU-Bartholomew
Catalyst	40Fe/AlSi[a]		Fe/SiO$_2$[b]	Fe/Al$_2$O$_3$[c]	Fe/Al$_2$O$_3$[d]	10Fe/SiO$_2$[e]
Literature reference	This study		[18]	[18]	[17]	[9]
Reactor type	Fixed-bed		Slurry	Slurry	Slurry	Fixed-bed
Pressure, MPa	2.2[f]	2.2[g]	1.5	1.5	1.3	1.0
Inlet molar H$_2$/CO	1.0	0.66	0.67	0.67	0.7	1.0
Space velocity, Nl/g$_{cat}$/h	37.2	5.6	1.35	1.32	0.68	1.92
TOS, h	713	512	100	100	300	150
CO conversion, %	22.6	72	--	--	60	77
%CO converted to CO$_2$	40	46	--	--	--	47
rate, mmol(CO)/g$_{cat}$/h	118	85[h]	--	--	28	12[j]
k$_{cat}$, mmol(CO+H$_2$)/g$_{cat}$/MPa/h	396	297[i]	101	51	--	50[j]
k$_{Fe}$, mmol(CO+H$_2$)/g$_{Fe}$/MPa/h	989	743[i]	300	150	--	504[j]
H.C. selectivities[k], mol%						
CH$_4$	14.3	9.6	7.0	3.5	5.8[l]	6.8[l]
C$_{3+}$	77.7	86.0	--	--	--	--
CH$_4$+C$_2$H$_6$	17.9	12.4	--	--	--	--
Cat. Prod., g$_{HC}$/g$_{cat}$/h [m]	0.72	0.50	--	--	0.12	0.3[n]
Cat. Prod., g$_{HC}$/g$_{Fe}$/h [m]	1.81	1.25	--	--	0.53	3[n]

[a] 80/120 mesh size. 100Fe/7.5Cu/4K/150Al$_2$O$_3$.

[b] 100Fe/5Cu/6K/139SiO$_2$.

[c] 100Fe/5Cu/9K/139Al$_2$O$_3$.

[d] 100Fe/6Cu/8K/250Al$_2$O$_3$.

[e] 100Fe/10Pt/2K/88.8SiO$_2$.

[f] P_{H2}^0 = 0.66 MPa, P_{CO}^0 = 0.66 MPa

[g] P_{H2}^0 = 0.6 MPa, P_{CO}^0 = 0.9 MPa

[h] average rate from inlet to outlet of the reactor

[i] isothermal integral reaction was assumed to find the rates with rate expression of kP_{H2}. Expansion factor of -0.45 was also assumed.

[j] rates are corrected to 260°C using E_A = 100 kJ/mol

[k] CO$_2$-free basis

[l] at 250°C

[m] HC are defined for BYU catalysts as C$_{3+}$

[n] at 265°C

Table 4.10. Comparison of BYU 40Fe/AlSi with unsupported Fe catalysts at 260°C.

	BYU-this study		TAMU-Bukur	Kentucky-Davis	Berkeley-Iglesia	Ruhrchemie	Mobil
Catalyst	40Fe/AlSi[a]		Unsupp.[b]	Unsupp.[c]	Unsupp.[d]	Unsupp.[e]	Unsupp.
Literature reference	This study		[12]	[78]	[10]	[84]	[104]
Reactor type	Fixed-bed		slurry	slurry	FB	slurry	slurry
Run temperature, °C	260	260	260	260	235	260	257
Pressure, MPa	2.2[f]	2.2[g]	2.2	1.30	2.14	1.5	1.5
Inlet molar H_2/CO	1	0.66	0.68	0.67	2.0	0.67	0.73
Space velocity, Nl/g_{cat}/h	37.2	5.6	3.5		11.0	2.2	2.3[h]
TOS, h	713	512	314			86	475
CO conversion, %	22.6	72	84	79	51	66	90
rate, mmol(CO)/g_{cat}/h	118	85[i]	76			38	34[j]
k_{cat}, mmol(CO)/g_{cat}/Mpa/h	194	184[k]	170		185[l]	97	
k_{cat}, mmol(CO+H_2)/g_{cat}/MPa/h	396	297[k]	269			155	
k_{Fe}, mmol(CO+H_2)/g_{Fe}/MPa/h	989	743[k]	450			290	265[j]
H.C. selectivities[m], mol%							
CH_4	14.3	9.6	2.6			5.3	2.3
C_{3+}	77.7	86.0	90.1				92
CH_4+C_2H_6	17.9	12.4	6.3				5
Cat. Prod., g_{HC}/g_{cat}/h [n]	0.72	0.50	0.51	0.74		0.27	
Cat. Prod., g_{HC}/g_{Fe}/h [n]	1.81	1.25	0.86	1.22		0.51	0.44[j]

[a] 80/120 mesh size. 100Fe/7.5Cu/4K/150Al_2O_3.

[b] 100Fe/3Cu/4K/16SiO_2.

[c] 100Fe/5.1Si/2Cu/3.0K.

[d] Fe/Zn/K/Cu.

[e] 100Fe/5Cu/4.2K/25SiO_2.

[f] P_{H2}^0 = 0.66 MPa, P_{CO}^0 = 0.66 MPa

[g] P_{H2}^0 = 0.6 MPa, P_{CO}^0 = 0.9 MPa

[h] Nl/g_{Fe}/h

[i] average rate from inlet to outlet of the reactor

[j] rates are corrected to 260°C using E_A = 100 kJ/mol

[k] isothermal integral reaction was assumed to find the rates with rate expression of kP_{H2}. Expansion factor of -0.45 was also assumed.

[l] rates are corrected to 260°C using E_A = 100 kJ/mol

[m] CO_2-free basis

[n] HC are defined for BYU catalysts as C_{3+}

The results of this study provide new data and activity-structure correlations for six Fe/K/Cu catalysts on four alumina supports, each having unique physical and chemical properties and all of commercial or semi-commercial origin. Following discussion addresses the effects on activity and stability of support properties, including physical properties, hydroxyl group concentration, silica stabilizer, and Fe loading; it also includes an important correlation of steady-state activity with CO adsorption on freshly carbided catalysts.

It should be emphasized that this study did not focus on selectivity or selectivity correlations. The supported catalysts discussed have not yet been optimized for selectivity. The authors acknowledge that the methane selectivity for the supported materials is undesirably high. Thus, the clear need for further separate study to reduce methane selectivity for supported Fe catalysts is recognized.

4.4.1 Effects of support pore size, pore volume, and CO uptake

Catalytic activity tests in this study were designed to measure intrinsic catalytic activity; samples for testing were prepared as coarse powders (average diameter of 450 microns) which according to our calculations and experience have adequately short paths for pore diffusion to minimize pore diffusional resistance under typical reaction conditions for an iron catalyst of typical activity. However, as previously mentioned (see section 3.4.3) the reaction rate of 40Fe/AlSi was sufficiently high that a 30% higher rate was observed on smaller (150 micron) catalyst particles. Effects of pore diffusion on rate are likely to be proportionally smaller for the other catalysts of lower activity. Moreover, a strong correlation of steady-state activity after about 100 h of reaction with CO uptake for freshly carbided catalysts (shown later in the discussion) suggests that initial steady-state rates, including 150 micron catalyst particles for the unusually active 40Fe/AlSi, are close to intrinsic and hence largely free of a pore diffusional disguise.

Our results (Figure 4.11) show intrinsic activity correlates positively with pore diameter; a rough trend of increasing activity with increasing pore volume was also apparent (but is not shown in this paper). Similar results were reported by Saib et al. [105] and Khodakov [106] for cobalt/silica catalysts, i.e. the cobalt-time yield was enhanced by increasing the pore diameter up to 35 nm [106]. Saib et al. [105] showed that extent of reduction of cobalt in Co/silica increases with increasing pore diameter which appeared to translate to higher Co surface area. A similar correlation from this study of Fe catalysts is presented in the following section. However, Xu et al. [9] have shown that intrinsic activity does not correlate with the quantity of bulk carbide in the working Fe catalyst.

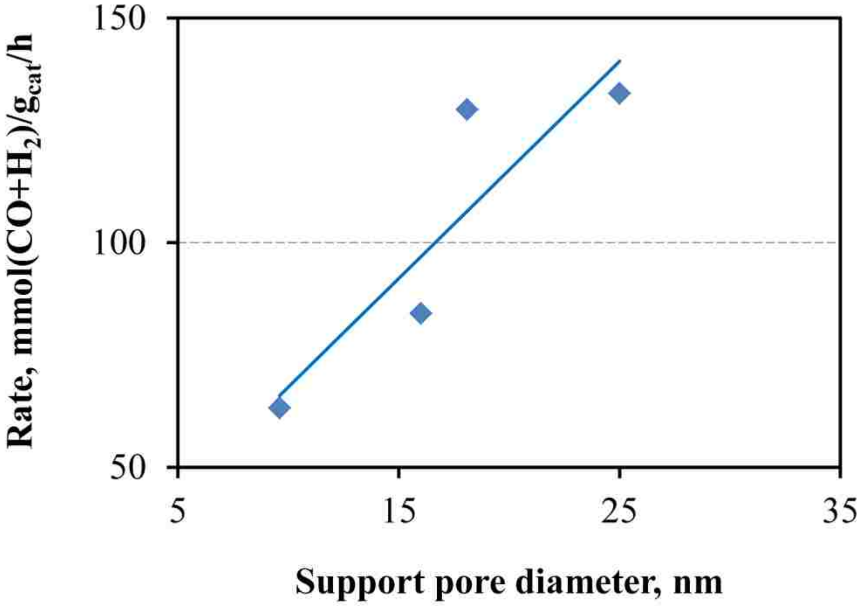

Figure 4.11. Intrinsic activity as a function of average pore size of different aluminas used as catalytic supports. Note that the pore diameter value for AlSi of 25 nm was determined as an integrated average of the 2 major peaks in Figure 4.2.

It is also possible to correlate activity with chemisorbed uptakes of CO or H_2 on the active iron carbide phase. Indeed, a strong correlation of activity with CO uptake on carbided samples is evident in Figure 4.12 for the six catalysts of this study. Our correlation between active site density and FTS activity is consistent with Xu et al. [9], who correlated FTS activity and H_2 uptake on used, carbided samples.

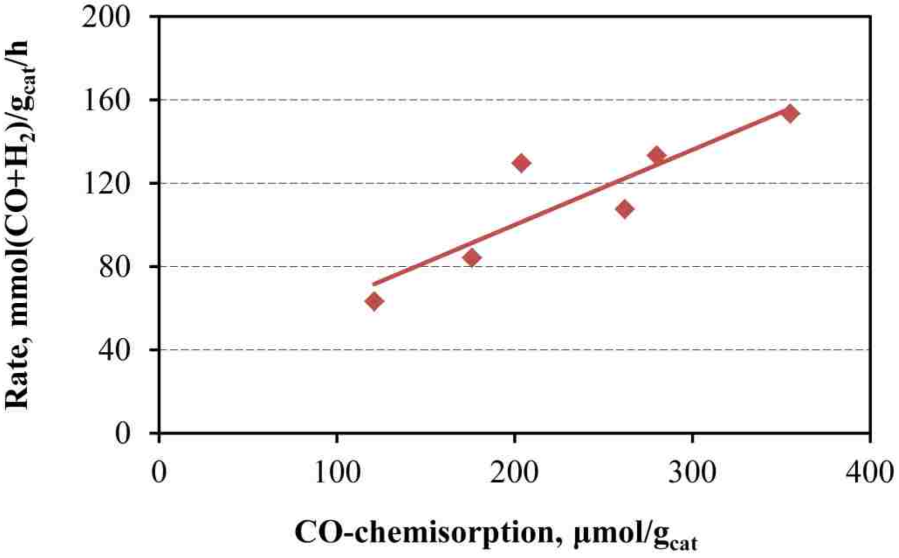

Figure 4.12. FTS rate (rate of ($CO+H_2$) Fe catalysts measured at 260 °C (time on stream ~ 90 h) as a function of CO uptake of freshly carbided catalysts (carbiding for 10 hours at 280 °C).

Thus, trends in initial steady-state intrinsic rates (Figures. 4.11 and 4.12) for our supported Fe catalysts may be largely due to the extent of surface carbides formed during the syngas carbiding processes which is likely to be affected by the extent of Fe oxide reduction in the earlier H_2 reduction step (addressed in the next section) and by support surface area, pore diameter, and pore volume. That fouling and/or partial blockage of pores with inactive carbons contributes to loss of activity of 40Fe/AlG is consistent with the limited capacity of the AlG support due to a low pore volume to accommodate inactive carbons. This conclusion is supported by syngas-TPR data in Figure 4.8b and extent of carburization data (Figure 4.13). For example, Figure 4.13 shows a correlation between the extent of carburization found from the third stage of syngas-TPR (Figure 4.8b) and pore diameter of the support. Large pore sizes characteristic of Fe/AlSi facilitate the long-term accessibility of active sites inside the pores for the reaction; moreover, a large pore volume provides more available space to accommodate carbon depositing during the reaction and limits the possibility of pore blockage. This phenomenon can be exacerbated if the active phase is not evenly distributed throughout the pellet, e.g., is found close to the pore entrance. Thus, in small diameter pores, carbon could be deposited at the pore entrance limiting access of the reactants. That pore blockage and lower dispersion (typically observed at higher metal loadings) may be a problem in the 40Fe/AlG relative to 20Fe/AlG is evident from the low values of CO uptake/%Fe ratios of 6.6 and 10.2 μmol/g-%, respectively. The absence of this problem can be inferred from Figure 4.13 showing twice the extent of carburization for 40Fe/AlSi relative to 20Fe/AlSi, while on the other hand, the inability to accommodate only slightly more carbon is apparent from the extent of carburization for 40Fe/AlG compared with 20Fe/AlG.

4.4.2 Effects of hydroxyl group concentration

The results of this study provide evidence of correlations between hydroxyl group concentration on the alumina surface, extent of reduction in H_2, and activity. Figure 4.14a shows a correlation of decreasing hydroxyl group concentration with increasing extent of reduction, while Figure 4.14b shows a correlation of increasing catalytic activity with increasing extent of reduction. These results imply that (1) a lower OH group content is associated with a higher extent of reduction; i.e. a weaker metal oxide-support interaction, and that (2) a higher extent of reduction is associated with higher catalyst activity. For example, as OH group concentration decreases from 5.6 mmol/g_{Al2O3} for AlC to 2.7 mmol/g_{Al2O3} for 20Fe/AlSi, the extent of reduction increases from 15% to 27% (20% Fe loading), and consequently activity is doubled from 63.2 to 133 mmol(CO+H_2)/g_{cat}/h. Thus, it appears that a higher extent of reduction in H_2 leads to higher surface carbide surface area during carbiding in syngas.

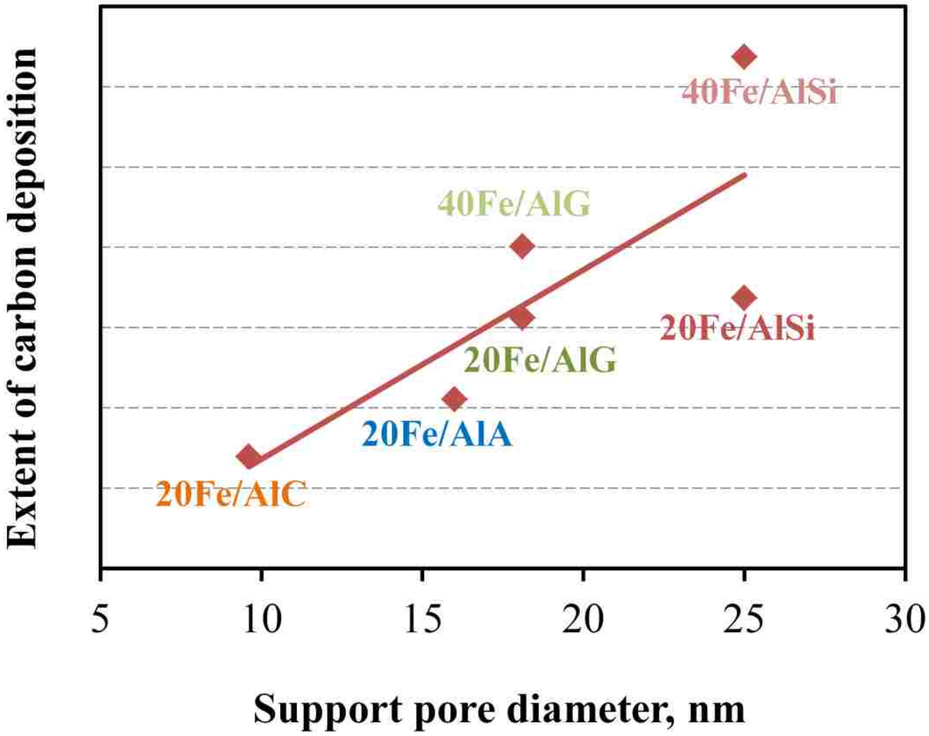

Figure 4.13. Extent of carburization found from the third stage of syngas-TPR (Figure 4.8b) as a function of pore diameter of the support. Note that the pore diameter value for AlSi of 25 nm was determined as an integrated average of the 2 major peaks in Figure 4.2.

This result is consistent with that of Rameswaran and Bartholomew [20], who reported high dispersion of iron particles on dehydroxylated alumina associated with a higher TOF for FTS. A study conducted by Brenner et al. [107] revealed that oxidation to Fe(III) occurs on the OH groups of hydroxylated alumina, and therefore produces a high density of FeO crystallites which are difficult to reduce and carbide. Based on their work and the results presented in this study, it appears that the nucleation of FeO particles is favored on hydroxylated alumina surfaces while highly reducible Fe_2O_3 and Fe_3O_4 clusters are formed in the near absence of surface OH groups. Moreover, because FeO interacts strongly with the alumina supports, reduction in H_2 and or syngas is more difficult. Thus, 20Fe/AlA and 20Fe/AlC with higher concentrations of surface hydroxyls have lower extents of reduction explaining in part their lower initial activities.

A positive correlation between catalyst activity and extent of reduction to Fe metal following reduction in H_2 is evident in Figure 4.14b. However, since the working catalyst in FTS is Fe carbide, a correlation between extent of reduction and extent of carbiding would be more meaningful. Extent of carbiding was calculated by dividing the observed mass loss for the carbiding stage of syngas-TPR (stage 2 in Figure 4.8a and Table 4.6) by the theoretical mass loss of 14% corresponding to the carbiding of FeO to Fe_5C_2. We assumed FeO to be a short-lived intermediate phase for the reduction/carbiding process from Fe_2O_3 to Fe carbide. As shown in Figure 4.14c, the extent of carbiding correlates linearly with extent of reduction. While this may explain further the positive correlation between reaction rate and EOR in H_2 in Figure 4.14b, the most important correlation is activity versus chemisorption sites for the carbided catalyst shown previously in Figure 4.12.

4.4.3 Effects of silica vs. lanthana stabilization of alumina support

Sintering has been reported as one of the deactivation pathways in FTS [88]. It is characterized by the growth of active phase crystallites with an accompanying loss of catalytic surface area. It has been shown in previous work [108] that small carbide crystallites are not stable during FTS, especially at high conversions where water partial pressures are likely to be high enough to oxidize iron carbide crystallites.

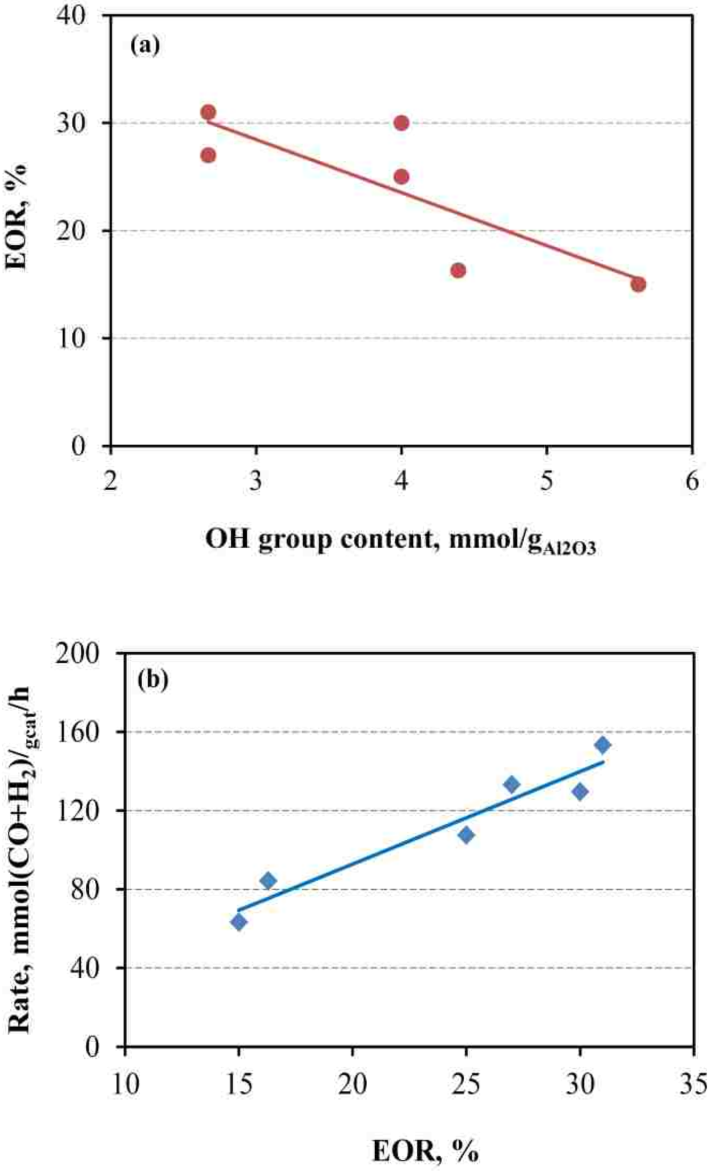
(a)
EOR, %
40
30
20
10
0
2
3
4
5
6
OH group content, mmol/g$_{Al2O3}$
(b)
Rate, mmol(CO+H$_2$)/$_{gcat}$/h
200
160
120
80
40
0
10
15
20
25
30
35
EOR, %

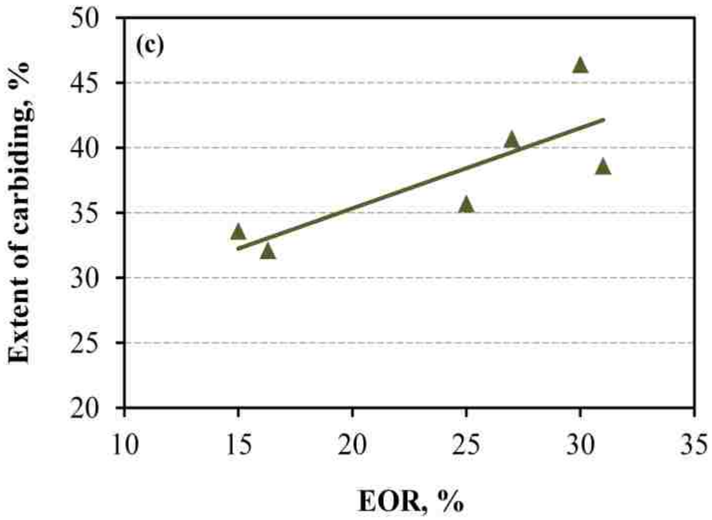

Figure 4.14. (a) EOR to Fe metal as a function of hydroxyl group content, (b) catalyst activity (rate of (CO+H_2) at 260 °C) as a function of EOR, and (c) extent of carbiding found from syngas-TPR as a function of EOR.

The results of this work show that all catalysts supported on La-stabilized alumina undergo significant deactivation (see Figure 4.9). This is more pronounced for 20Fe/AlA and 40Fe/AlG. On the other hand, iron catalysts supported on silica-doped alumina are very stable; indeed, the activity of 40% Fe/AlSi increases up to 700 hours on stream. 20Fe/AlSi and 20Fe/AlG with nearly the same crystallite sizes (~ 5.5 nm) have initially about the same activity, but 20Fe/AlSi is much more stable than 20Fe/AlG during FTS.

Silica-doped alumina, itself, has been shown to be inherently highly thermally and hydrothermally stable. For example, Horiuchi et al. [109] reported that high surface areas and pore volumes of supports containing 2.5-10% silica in alumina prepared by an aerogel method were stable even following heating to 1300 °C in air. Their work also reveals that a monolayer of silica may exist on the surface of alumina doped with 8% silica; however, Si atoms were also detected in the bulk structure by ^{29}Si NMR. This and other previous studies provide evidence that cation vacancies in alumina are occupied by Si atoms, which suppress surface diffusion of Al atoms at elevated temperatures. ^{27}Al MAS NMR spectra of pure alumina and 5% silica doped alumina (AlSi) samples show peaks at $\delta \sim +15$, 40, and 75 ppm (Figure 4.15a). These peaks are assigned to aluminum in octahedral, tetrahedral, and five coordinated environments, respectively [110, 111]. These results show that the percent of tetrahedral Al in alumina with 0% silica and 5% silica is constant (Figure 4.15a). We believe that aluminum in tetrahedral sites is not replaced by silicon as reported by Heemeier et al. [112], but rather Si enters the tetrahedral vacancies in the defect spinel structure of alumina and forms a Si-Al spinel phase of high porosity and structural stability. Alumina with silica wt%< 28 forms a Si-Al spinel structure [113]. ^{29}Si MAS NMR (Figure 4.14b) also shows a peak from -81 to 89 ppm which is attributed to $Si(OAl)_4$ and $Si(OAl)_3OH$. No peak is observed at -110 ppm which is assigned to the separate SiO_4 phase, confirming that silicon ions form a Si-Al spinel phase and retard the alpha to gamma transition. This suggests why AlSi maintains its structure to significantly higher temperatures than conventional γ-aluminas. The inherent structural stability of this Si-doped alumina spinel accounts for the enhanced support porosity and thermal/hydrothermal stability of the γ-Al_2O_3 phase at high temperatures, i.e. up to 1200 °C. The enhanced thermal and hydrothermal stability of this support may explain in part the exceptional stability of Fe/AlSi catalysts.

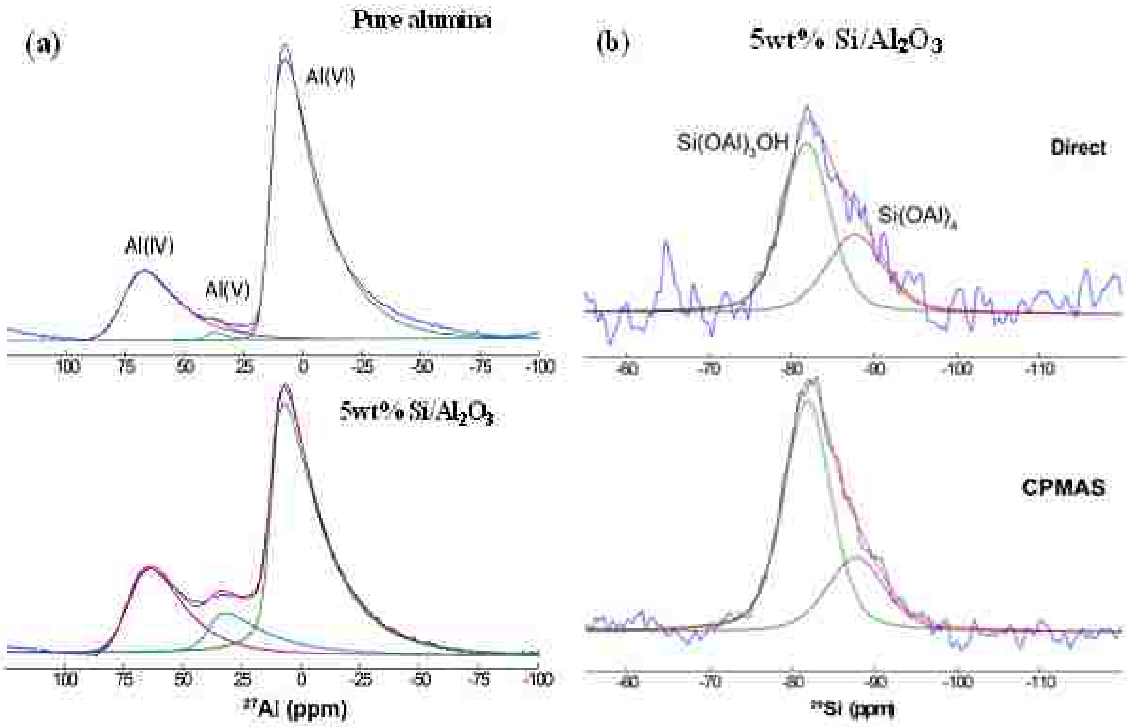

Figure 4.15. (a) ^{27}Al MAS NMR for pure alumina and 5 wt% BYU silica-doped alumina (AlSi) (b) ^{29}Si MAS NMR and ^{29}Si CPMAS for 5 wt% BYU silica-doped alumina (AlSi).

This high thermal stability of silica-doped alumina enables high temperature dehydroxylation of the support, while maintaining the γ-Al_2O_3 structure with high surface area and large pore volume and pore diameters. The other supports which have La_2O_3 as a stabilizer exhibit faster transformation of γ-Al_2O_3 to α-Al_2O_3 as evidenced by faster rate of weight loss in TGA experiments (Figure 4.6). Thus, they could not be dehydroxylated at 1100 °C like AlSi which has silica as a stabilizer.

The stability of Fe/AlSi may also derive from the apparent relatively stronger interaction of Fe carbide crystallites with the silica/alumina surface leading to a high resistance to sintering. The small primary crystallite size of silica-doped alumina, estimated from XRD to be around 5 nm and its high surface area are consistent with a Si-Al spinel structure, a large fraction of which resides on the surface. Since iron interacts relatively strongly with silica surfaces, Si-O or Si-O-Al groups on the surface of said support could anchor iron carbide crystallites to the support surface and prevent their migration and agglomeration associated with sintering [90, 114]. This hypothesis is consistent with the work of van Steen's group [114] who recently found that surface silicate groups play an important role in inhibition of the sintering process. This anchoring is consistent with slightly lower EOR for 20Fe/AlSi than 20Fe/AlG (30 vs. 27%); however, the EOR is still higher than the other supports which had higher hydroxyl group concentration. Thus, a higher dispersion of iron carbide particles on the dehydroxylated support and the associated higher active site density serve to increase catalyst activity while the silica/alumina support prevents sintering by anchoring Fe carbide crystallites to the silica-rich surface.

Furthermore, Mogorsi et al. [114] found that surface silicate groups result in an increase in the hydrogen availability on the surface by reducing the strength of CO adsorption. An increased surface hydrogen will result in an increase in activity. This result is also consistent with what we found for Fe/Si-Al_2O_3, which showed an enhanced activity compared with Fe/La-Al_2O_3 as it has surface silicate groups.

4.5 Conclusions

Preparation and testing of six supported Fe FT catalysts using the same preparation procedure but four different alumina materials and two different Fe weight loadings were carried out to investigate the direct effects of support properties including physical properties, surface chemistry, and use of SiO_2 vs. La_2O_3 as a stabilizer on the performance of the catalysts.

(1) The data from this study demonstrate a strong relationship between the properties of the starting support and the activity and stability of the final catalyst. The activity of four 20% Fe catalysts using different support materials vary by over a factor of two, the most active being ~3 times more active and productive than Bukur's silica supported Fe FT catalyst. The stabilities of these catalysts are also very different. The activity of 20Fe/AlA dropped by 31% after 190 h on stream, while the activity of 20Fe/AlSi increased by 13% after 700 h.

(2) Effects of Fe loading vary greatly depending on support pore sizes and pore volume. The activity of Fe/AlG decreased by 17% when Fe loading was increased from 20 to 40% whereas the activity of Fe/AlSi with larger pore volumes and diameters increased by 15%.

(3) Large pore volume and pore diameters of the support accommodate higher Fe loading without pore blocking. This large pore volume may also help in uniform distribution of the active phase into the pore and greater accessibility of the active phase to the reactants. The correlation of higher carburization at higher loading for Fe/AlSi is consistent with its larger pore volume which accommodates a greater amount of carbon. A positive correlation between intrinsic activity and pore diameter of the support was also found.

(4) Correlations are evident between OH groups removed from the support surface, extent of reduction and activity. Higher calcination temperature of the AlSi support resulted in greater removal of the hydroxyl groups and more effective reduction/carbiding (higher EOR), which consequently lead to higher activity.

(5) Silica as a dopant in alumina improves performance in two ways: (a) it suppresses the phase transformation of γ-Al_2O_3 to α-Al_2O_3 at elevated temperatures and thus it enables effective dehydroxylation of the alumina surface at high temperatures, (b) it anchors the active phase to the alumina surface and prevents active phase crystallites from deactivation by sintering.

Chapter 5 Kinetics of Deactivation of Cobalt FT Catalysts by Carbon: Effects of CO and H_2 Partial Pressures and Temperature

This chapter reports the effect of partial pressures of CO and H_2 and temperature on the deactivation by only carbon deposition in the absence of other forms of deactivation for the cobalt FT catalyst. The freshly reduced and wax-extracted spent catalysts were characterized by BET, XRD, H_2-TPR, XPS, XAENS/EXAFS, TPH, CO-chemisorption, and EOR.

5.1 Introduction

Alumina supported cobalt catalysts are typically preferred for gas-to-liquid (GTL) processes instead of iron catalysts because of their high hydrocarbon synthesis activity, low water-gas shift activity, and high selectivity to linear paraffins [115]. However, over several months (9-12 months) of operation expensive cobalt catalysts deactivate, losing up to 30-50% activity with a similar drop in hydrocarbon productivity. Understanding causes/mechanisms of deactivation is of great importance in maximizing catalyst life and improving FTS economics.

Proposed mechanisms for cobalt catalyst deactivation are (1) poisoning, (2) oxidation, (3) cobalt-support interactions, (4) sintering of cobalt nanoparticles, and (5) carbon and heavy hydrocarbon deposition [5, 35]. The latter two mechanisms have been shown to have the most effect on Co FT catalysts, while the former three can be excluded as deactivation mechanisms for commercial FT conditions [35]. For commercial conditions sintering of cobalt nanoparticles usually occurs within the first 10-15 days on stream, but appears to be negligible after that [33].

By choosing the right experimental procedures, however, sintering of cobalt nanoparticles can be limited to occur the first few hours on stream and then diminish [32, 116-118]. Thus, carbon deposition is the mechanism that causes deactivation over the whole life cycle of Co FT catalysts (9-12 months).

Menon [119] has classified FTS as a carbon insensitive reaction due to the presence of high partial pressures of hydrogen during the FT reaction. However, Moodley et al. [48] have shown that, over long periods of time, carbon deposits on the surface of the catalyst, forming stable oligomeric and polymeric carbon that will not leave the surface of the catalyst at FTS conditions. Carbon may (1) act as a poison by binding irreversibly to the catalyst surface and blocking available active sites for reaction [28, 48, 49], (2) physically plug mesopores and thereby decrease the accessibility of the reactants and products to the gas phase [28], (3) form bulk cobalt carbide which can cause activity loss [120], (4) electronically inhibit the activity by subsurface carbon [121], and (5) reconstruct the surface which may either increase or decrease activity [40, 43, 58]. Bulk cobalt carbides are metastable during FTS and are apparently not observed using XANES on wax protected cobalt catalysts after several months of FT reaction in a slurry bubble column reactor [34]. However, their formation has been reported by other groups using in situ [55] and synchrotron XRD [120]. Surface reconstruction could work as a deactivation mechanism to form less active planar sites and also assist in the formation of the active sites for FTS [35]. Carbon deposition and buildup appears to be one of the main reasons for the deactivation of the catalyst over the full life of the catalyst [58]. While carbon is clearly implicated in surface reconstruction and deactivation by poisoning and pore plugging, heavy hydrocarbons (hard waxes, i.e. 50+ carbon atoms) have also been proposed to clog catalyst pores. Niemela and Krause [122] have observed deactivation of Co/SiO_2 due to the presence of wax in the pores of the catalyst. Pennline and Pollack [123] showed that removing wax, by Soxhlet extraction and hydrogen treatment, from deactivated cobalt catalysts supported on zeolite, renewed the catalyst to be as active as a freshly reduced catalyst. Although regenerating catalysts at low temperatures removes wax from the surface of the catalyst, hydrogen-resistant carbon remains on the surface of the catalyst preventing catalysts from performing at original values of productivity. Moodley et al. [48] carried out temperature-programmed hydrogenation (TPH) of wax-extracted cobalt catalyst samples, removed from a 100 barrel/day slurry bubble column FT reactor after they had been aged over a period of 6 months, to identify the type of carbon species formed as a function of time on stream. They found that the fraction of more reactive atomic carbon and wax diminishes over time, while more stable polymeric carbon species are gradually formed and thought to cause the observed deactivation.

The effects of H_2 and CO partial pressure on the deactivation by carbon of cobalt FT catalysts have been examined in a few studies [31, 49, 124-126]. Moodley [4] used TPH to study a 20 wt% $Co/Pt/Al_2O_3$ catalyst at low pressure FTS conditions (1 bar, 230°C) for only 3 h time on stream (TOS) to determine the effects of different H_2/CO ratios on formation of polymeric carbon. Keeping the CO partial pressure constant, they found that lower H_2/CO ratios produce more stable polymeric carbon species. In view of the low pressure and TOS, these results may have qualitative value but cannot be applied quantitatively to FTS at high pressure and long term reaction.

Peña et al. [49] observed that a lower H_2/CO ratio increases the amount of strongly adsorbed hydrocarbons on a 15 wt% Co/Al_2O_3 in a continuously stirred tank reactor (20 bar, 220°C, $X_{CO,t=0}$ = 30%), thereby blocking catalyst pores and contributing to a faster rate of deactivation. By deconvolution of TPH profiles, they showed that the amount of polymeric carbon did not change noticeably and; therefore, was not causing the deactivation. These previous results agree with conventional wisdom, which holds that lower H_2/CO causes faster deactivation, since higher H_2/CO ratio would more likely result in removing the carbon from the surface by hydrogenation. For example, Dry [121] showed that a lower $P_{H2}/(P_{CO})^2$ ratio increased the rate of carbon deposition for iron catalysts; the same concept could be applied for cobalt catalysts as well. However, other studies have determined the opposite effect of this conventional thought. Peña et al. [125] showed that a higher H_2/CO ratio increased the rate of deactivation on a 15 wt% Co/Al_2O_3 catalyst at high-temperature FTS conditions (230°C, 20 bar, $X_{CO,t=0}$ = 60-70%). Careful inspection of their TPH results showed that higher H_2/CO ratio led to higher amounts of polymeric carbon formation, which can cause the deactivation at a higher H_2/CO ratio. Peña et al. [49] also showed that high conversion (X_{CO} = 70%) nearly doubles carbon deposition (12.5 vs. 5.6 wt%) compared with lower conversion (both at H_2/CO = 1). This is not consistent with conventional wisdom, where higher X_{CO} increases higher partial pressures of H_2O thereby gasifying the carbon and reversing carbon deposition [125].

Sintering, oxidation and formation of cobalt-support compounds are also observed at higher H_2/CO ratios and higher conversions. Bremaud et al. [124] observed a faster rate of deactivation with an increase in H_2/CO ratio, postulating that an increased H_2/CO ratio would form more water and thus lead to deactivation by oxidation. Sadeqzadeh et al. [31] showed as well, using Co/Al_2O_3, that higher H_2/CO ratios at constant gas flow rate increased the rate of deactivation of the catalyst by sintering of cobalt crystallites. Also, Zhou et al. [126] found that higher H_2/CO ratios increase the rate of deactivation on Co/SiO_2; from TPR and XPS data, they postulated greater interaction between the support and the cobalt which forms Co silicate at higher H_2/CO ratios. At high conversion (X_{CO} = 80.1%), Tavasoli et al. [54] observed deactivation by cobalt aluminate formation, confirmed by TPR and XRD. Thus, it appears that sintering or cobalt-support compound formation can seriously complicate studies of deactivation by carbon.

Just as different partial pressures affect deactivation rate, different operating temperatures also affect the deactivation of the catalyst in FTS. Moodley's work [4] on the effect of temperature on cobalt catalysts indicates that increasing temperature increases the rate of deactivation. His work was done using a 20 wt% $Co/Pt/Al_2O_3$ at temperatures of 240, 260, and 270°C at H_2/CO: 1.6 and 20 bar. Sadeqzadeh et al. [127] showed that increasing the temperature from 220°C to 240°C increases the rate of deactivation for 25 wt% $Co/Pt/Al_2O_3$ at H_2/CO: 2, 20 bar, and X_{CO} = 60-70%. In contrast to other studies [4, 127], Ma et al. [128] found that deactivation rate decreases with temperature for 25 wt% $Co/Ru/Al_2O_3$ catalyst at 2.5 MPa, H_2/CO: 2.1, and $X_{CO} \leq 60\%$, possibly due to a more stable catalytic structure at higher temperatures.

To summarize, the previous studies show contradictory effects, e.g. that both higher and lower H_2/CO ratios result in faster deactivation due to the formation of carbon, cobalt-aluminate, and/or sintering. Further, these forms of deactivation were not, in general, studied separately. In addition, these studies varied CO and H_2 partial pressures together rather than separately; therefore, it is not possible to understand the individual effects H_2 and CO partial pressures on Co FT catalyst deactivation. Thus, there are no previous systematic studies of the effects of partial pressures of H_2 and CO on long-term deactivation by carbon deposition for Co FT catalysts in the absence of other forms of deactivation. In addition, there are only a few studies for the effect of temperature on deactivation by carbon [4, 127, 128]; and their conclusions are contradictory concluding that increasing the operating temperature can both decrease and increase deactivation for Co FTS.

Consequently, the purpose of the current study was to investigate, systematically, the effects of H_2 and CO partial pressures and temperature on the deactivation of Co FT catalysts by carbon. Eleven deactivation runs (as well as a repeat run) at 220-250°C and 20 bar were completed in a FB reactor each for 700-900 h time on stream (TOS), changing the partial pressure of H_2, CO or temperature, while keeping the other parameters constant. This study provides, for the first time, new data defining quantitatively the long-term deactivation by carbon for cobalt FT catalysts in the absence of the other deactivation mechanisms. Sintering was eliminated through design of a catalyst with relatively large Co crystallites and a very stable support; plugging of pores by heavy waxy hydrocarbon was avoided by using a large pore support; and both H_2O-assisted sintering and formation of cobalt-support compounds were eliminated by operating at lower conversions (lower partial pressures of H_2O). The data and perspectives gathered from this study should enable operation at substantially lower rates of deactivation and provide the possibility of significantly increasing catalyst life.

5.2 Experimental

5.2.1 Catalyst preparation

The 25 wt% Co/ 0.25 wt% Pt/Al_2O_3 catalyst used for all the deactivation tests for this study was prepared with silica-doped alumina support (calcined at 1100°C prior to impregnation) and reduced in H_2 at 450°C for 72 h as described in Chapter 2. This high reduction temperature was purposefully selected to have large cobalt crystallites and slow down sintering as a deactivation mechanism.

5.2.2 Reference catalysts (Ref. catalysts)

In order to understand the type of carbon species binding to the surface of our catalysts, four reference catalysts were prepared and pretreated in CO at specific conditions which enabled specific carbonaceous species to form on the surface of the catalyst as previously described by Moodley et al. [48].

The unsupported Co and CoPt and supported $CoPt/Al_2O_3$ catalysts were reduced in flowing 50% H_2 (balance He), while ramping at a rate of 1 °C/min from room temperature to 450°C, then holding for 6 h. After reduction, the temperature was lowered to 430°C and the catalyst was purged in He for 90 min. The temperature was then lowered to the desired reaction temperature (250°C for Co, CoPt, $CoPt/Al_2O_3$ and 350°C for $CoPt/Al_2O_3$), where the catalyst was treated in CO for 16 h as summarized in Table 5.1. The temperature was then lowered in He until reaching room temperature, then the catalyst was passivated in 1% O_2 (balance He).

Table 5.1. Reference catalysts and CO exposure temperatures.

Ref.	Catalyst	CO exposure temp, °C
1	$CoPt/Al_2O_3$	250
2	CoPt	250
3	Co	250
4	$CoPt/Al_2O_3$	350

5.2.3 Activity and selectivity measurements

Fischer-Tropsch Synthesis (FTS) was conducted in a fixed-bed reactor (stainless steel, 3/8 inch OD) described previously [80]. Each sample (0.20 g, 63-90 μm) was diluted with 2 g silicon carbide to improve isothermality in the catalytic zone.

Before FTS, the passivated catalysts were re-reduced in situ up to 450°C for 6 h in 100% H_2. After cooling to 150°C, the system was then pressurized to 20 bar in syngas ($H_2/CO = 2$, 10 bar H_2, 5 bar CO, balance He), and the temperature was slowly ramped from 150°C to 220-250°C for 48-72 h to gradually fill up the pores and prevent runaway reaction with a target CO conversion level of ~50% at the final temperature for the run. The partial pressures were then adjusted to the desired partial pressures for the run and the total flowrate was increased to give a CO conversion of less than 25% which was used for all runs to favor carbon deposition and lower partial pressures of water. Activity and stability data were then obtained over the next 700-900 hours as inlet partial pressures and temperature remained constant.

After leaving the reactor, the exit gas and liquid effluent passed through a hot trap (~90°C) and a cold trap (~0°C) to collect heavy hydrocarbons and liquid products. The effluent gaseous product was analyzed using an HP5890 gas chromatograph equipped with a thermal conductivity detector and 60/80 carboxene-1000 column. CO conversion and selectivities were determined with the aid of an Ar tracer. The gas chromatograph was calibrated only for hydrocarbons CH_4 and C_2H_6; therefore, selectivities of C_3^+ rather than C_5^+ were determined in this study.

After the catalytic test, each of the catalysts was covered by wax produced during the fixed bed test and transported to a wax extraction system as described in section 2.3.3.

5.2.4 Catalyst characterization

Several characterization techniques were used in this study including: BET, XRD, H_2-TPR, XANES/EXAFS, XPS, TPH, EOR, and CO-uptake. These techniques were fully explained in Chapter 2. In addition to the calculation of EOR from oxygen titration (see section 2.2.3.3) it was also determined from TPR experiments. Passivated, reduced samples were re-reduced up to 800°C in the TGA, and any weight loss occurred after 450°C, which was the bulk reduction temperature, was used in the calculation to find the weight of unreduced cobalt.

H_2-uptake was measured by TPD for the freshly reduced catalyst and found to be 175 μmol/g and it was carried out at University of Kentucky Center for Applied Energy Research (CAER). H_2-uptake measurement (purging step at room temperature) was done at. CO-uptake for the freshly reduced catalysts was 227 μmol/g giving a surface CO/Co ratio of 0.62, assuming a surface H/Co ratio of one. The H_2-uptake for the freshly reduced catalyst was used in combination with the EOR to calculate Co dispersion, site density, and Co crystallite size. CO-uptakes were measured for spent catalysts and compared with the CO-uptake of the fresh catalyst.

5.3 Results

5.3.1 Reference catalysts (Ref. catalysts)

The three Ref. catalysts described in section 5.2.2 (alumina supported CoPt, unsupported CoPt, and unsupported Co) were reduced in 50% H_2 (balance He) at 450°C for 6 h, and purged at 430°C in He for 90 minutes. The sample temperature was then lowered to 250°C (for samples of all three catalysts) and 350°C for a second sample of $CoPt/Al_2O_3$ catalyst, exposed to flowing

CO for 16 h, cooled to room temperature, and passivated in 1% O_2/He. Several tests (TPH, XRD, XPS, BET) were subsequently conducted on these four reference catalysts (Ref.). The TPH results are displayed in Figure 5.1. TPH profiles of Refs. 1-3 consist mainly of low and medium temperature peaks around 215-280 and 430-490°C, which can be assigned to cobalt carbide and polymeric carbon, respectively (two carbide peaks in the case of Ref. 2). Presence of the carbide was further confirmed by XRD (not shown here) and XPS (Figure 5.2) on Ref. 1-3. The Ref. 4 TPH profile consists of a single high-temperature (HT) peak at 560°C which can be associated with graphitic carbon (very small HT peaks are observed for the Ref. 3).

XPS was used to determine type of carbon on the surface of these Refs. and C 1s XPS signals are shown in Figure 5.2. A very low-intense C 1s peak at 284.5 eV is observed for passivated freshly reduced catalyst which was not covered with wax nor exposed to FTS probably due to carbon contamination inside the XPS chamber or from the supporting conducting carbon tape [49]. The XPS spectrum for the freshly reduced wax-extracted catalyst exhibited a peak at 284.9 eV, which corresponds to $–CH_2\text{-}CH_2–$ molecular fragments [23]. According to literature, the peak at ~284.5 eV for Refs. 1 and 2 (supported and unsupported Pt/Co treated at 250°C) can be attributed to polymeric carbon [40, 49]. The XPS C 1s spectrum of Ref. 4 (supported Pt/Co treated at 350°C) displayed an intense peak at 283.5 eV, which can be assigned to graphitic carbon. Thus, there is a clear distinction from XPS (283.5 vs 284.5 eV) between graphitic carbon formed at 350°C and polymeric carbon formed at 250°C. The higher intensity of the graphitic carbon peak in Ref. 4 compared to the peak for polymeric carbon in Ref. 1 shows much larger quantity (> 20 x) of deposited carbon consistent with the higher intensity of TPH profile for Ref. 4. Although a higher binding energy for graphitic carbon at low coverage is expected, the observed lower binding energy of graphitic carbon compared to polymeric carbon in this study can be explained by differential sample charging due to a higher coverage of carbon overlaying a conducting layer.

Comparison of the TPH profiles for Refs. 1-3 allows us to understand the effects of the alumina support and Pt promoter on the binding strength of carbon to the surface of the catalyst: (1) a lower peak temperature of 428°C for Ref. 2 vs. 490°C for Ref. 1 indicates that polymeric carbon is more resistant to hydrogenation on supported CoPt (Ref. 1) than on unsupported CoPt (Ref. 2) and (2) polymeric carbon is more stable in the absence of Pt as evidenced by the higher peak temperature for Co (Ref. 3) vs. CoPt (Ref. 2); Moreover, reactive atomic carbon (LT peak) is predominant for CoPt (Reference 2) relative to Co (Ref. 3), while on Co (Ref. 3) polymeric carbon dominates the surface.

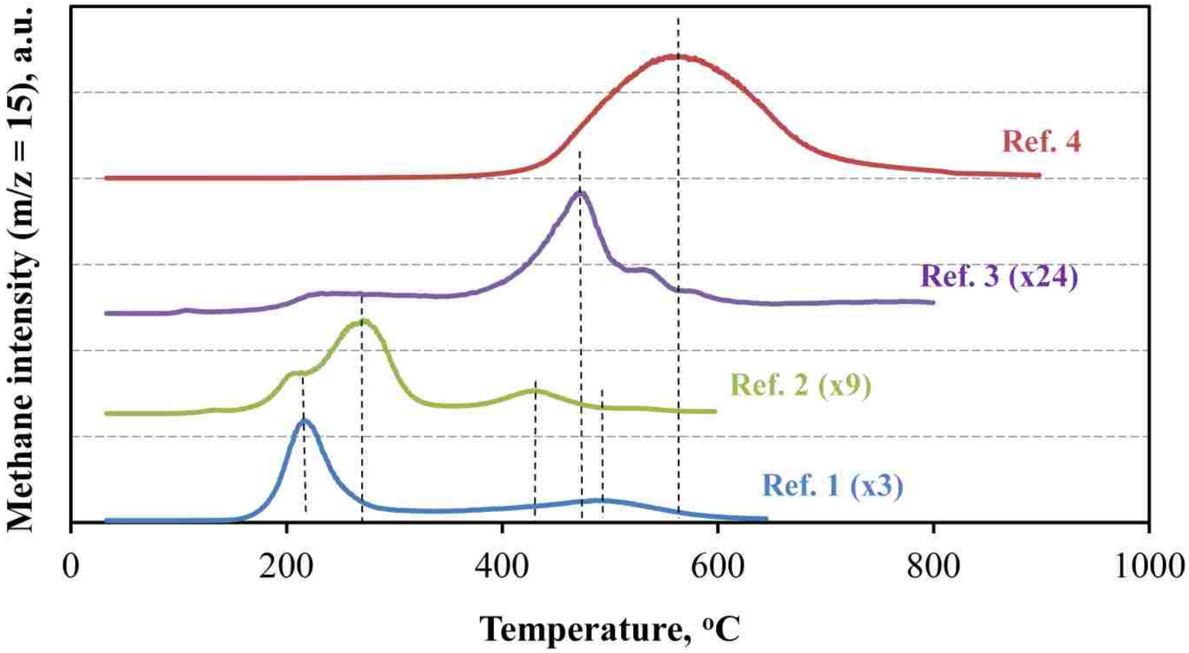

Figure 5.1. TPH profiles of reference catalysts (Refs. 1-4).

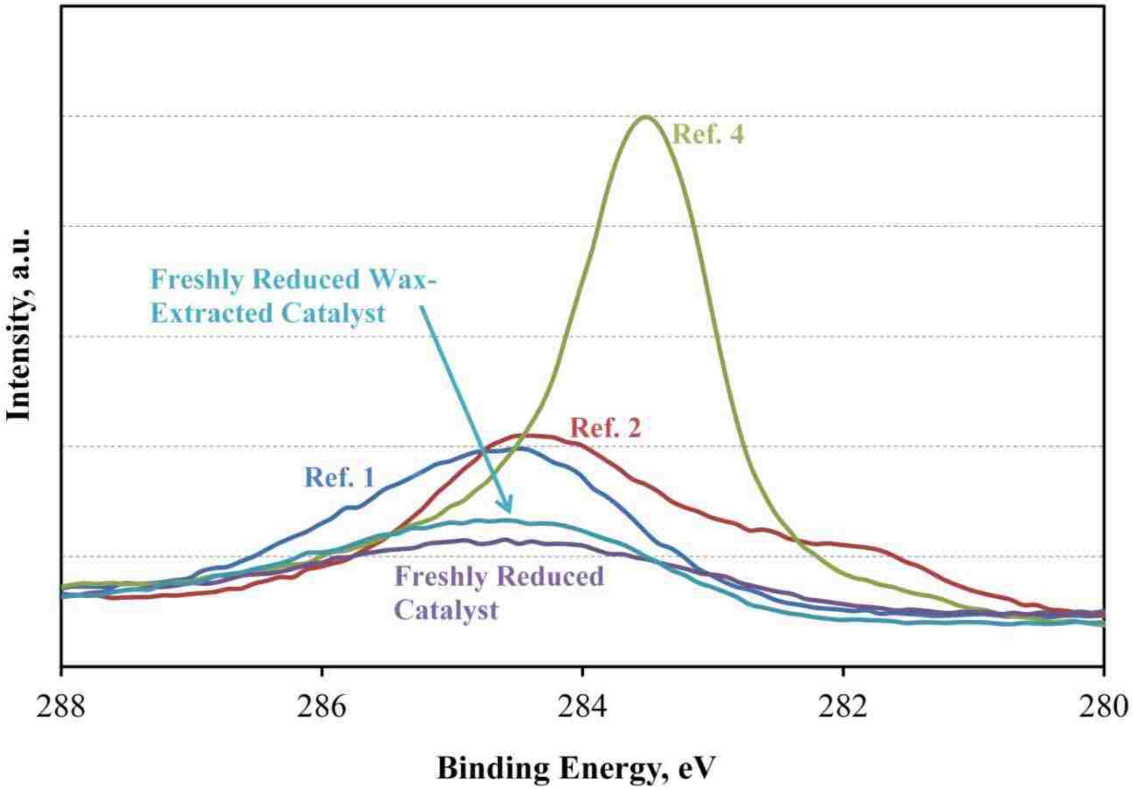

Figure 5.2. XPS spectra of the C 1s region for Ref. catalysts.

5.3.2 FTS performance with time

Eleven samples of a 25 wt% $CoPt/Al_2O_3$ were tested over a period of 800 hours, each at a different set of CO and H_2 partial pressures and temperature (220-250°C) while inlet flowrates were held constant. Each catalyst sample was activated at reaction temperature, 20 bar, $H_2/CO = 2$, and $X_{CO} = 50\%$ for 70 h. At 70 h TOS P_{H2}, P_{CO} and total flowrate were adjusted to the desired partial pressures and ~ 20% CO conversion and the system was allowed to come to steady-state within 100 h TOS. Initial steady-state activity and selectivity data at 100 h are reported in Table 5.2. The catalyst activity shown for Run 3 at standard conditions ($H_2/CO = 2$, 230°C, 20 bar) of 58.4 mmol/g_{cat}/h is 70% higher than a value of 34.8 mmol/g_{cat}/h reported by Pena et al. [125] for a similar Co catalyst at nearly the same process conditions. As seen from the data in Table 5.2

initial activity of our catalyst, increases with increasing partial pressure of hydrogen and decreases with increasing partial pressure of CO. Moreover, at higher H_2/CO ratios higher productivities and higher methane selectivities are observed. For example, the methane selectivity dropped from 14.0 to 4.2% when H_2/CO decreased from 2 to 1 at 220°C. Also, as temperature increases CH_4 selectivity and the rate increase and C_3^+ decreases.

Table 5.2. Catalyst performance at ~100 h TOS for 25 wt% $CoPt/Al_2O_3$ at different partial pressures of H_2 and CO at 230-250 °C and 20 bar.

Run	Temp., °C	P_{H2}, bar	P_{CO}, bar	H_2/CO	Rate, mmol/g_{cat}/h[a]	X_{CO}[a], %	Productivity[b], g_{HC}/g_{cat}/h	H.C. Selectivity[c], %		
								CH_4	C_2	C_3^+
1	230	5	5	1	34.4	16.2	0.42	9.8	1.1	86.5
2	230	15	5	3	81.6	22.9	0.89	20.6	1.9	77.1
3	230	10	5	2	58.4	21.2	0.67	15.4	1.8	81.8
4	230	10	7.3	1.4	44.6	22	0.52	13.1	1.7	83.5
5	230	10	10	1	37.8	20.5	0.47	7.35	1.8	88.6
5-repeat	230	10	10	1	34.9	21.5	0.42	8.9	2.7	85.3
6	240	10	5	2	92.7	24	1.03	18	2.2	78.8
7	250	10	5	2	244	24	2.54	21.2	3.4	73.7
8	240	5	5	1	41.4	20.5	0.48	11.1	2.1	82.7
9	250	10	10	1	78.7	19.2	0.96	9.4	1	86.8
10	220	10	5	2	33.0	22.1	0.33	14.0	1.6	83.6
11	220	10	10	1	22.5	21.4	0.25	4.2	1.0	92.8

[a] CO conversion
[b] Productivity is defined as C_3^+
[c] Hydrocarbon selectivity

Starting at 100 h, rate data and hydrocarbon selectivities were measured over 700 h to determine deactivation rates. Relative or normalized activity (activity of the catalyst at time *t* divided by the activity of the given catalyst) versus time on stream is reported in Figure 5.3. Each test was conducted at about 20% (± 4%) CO conversion and hence a low partial pressure of H_2O, thereby minimizing Co-support spinel formation. Oxidation of small Co crystallites or H_2O-assisted sintering was not observed due to the high reduction temperature and large Co crystallite sizes used. Run 5 ($P_{H2} = P_{CO} = 10$ bar) was repeated to check the reproducibility of the FB deactivation runs as shown in Figure 5.4. After the initial activation period, the CO conversion of both runs followed the same trend of deactivation for 700 h, confirming the reproducibility of our tests. At 230°C, the highest rates of deactivation were observed in Runs 2 and 5, involving the highest and lowest H_2/CO ratios of this study (Run 2: $H_2/CO = 3$; Run 5: $H_2/CO = 1$). The result for Run 2 was unexpected, since we had supposed that deactivation rate would be lower for a higher H_2/CO ratio (this phenomenon will be discussed later). Surprisingly, the lowest rate of deactivation was observed in Run 1, for which the H_2/CO ratio was the same as in Run 5 but partial pressures were lower (i.e., in Run 1, $P_{H2} = P_{CO} = 5$ bar).

Relative activities versus TOS at different temperatures are shown in Figures 5.3b and 5.3c. Figure 5.3b compares the effect of temperature on deactivation rate at H_2/CO of 2. It is clear that deactivation rate increases with temperature at P_{CO} of 5 bar and H_2/CO of 2. When comparing Run 1 and Run 8 ($P_{H2} = 5$ bar; $P_{CO} = 5$ bar) in Figure 5.3c, the deactivation rate, again increases with increasing temperature; however, this is not the case for Runs 5, 9, and 11 ($P_{H2} = P_{CO} = 10$ bar), where deactivation rate decreases with increasing temperature.

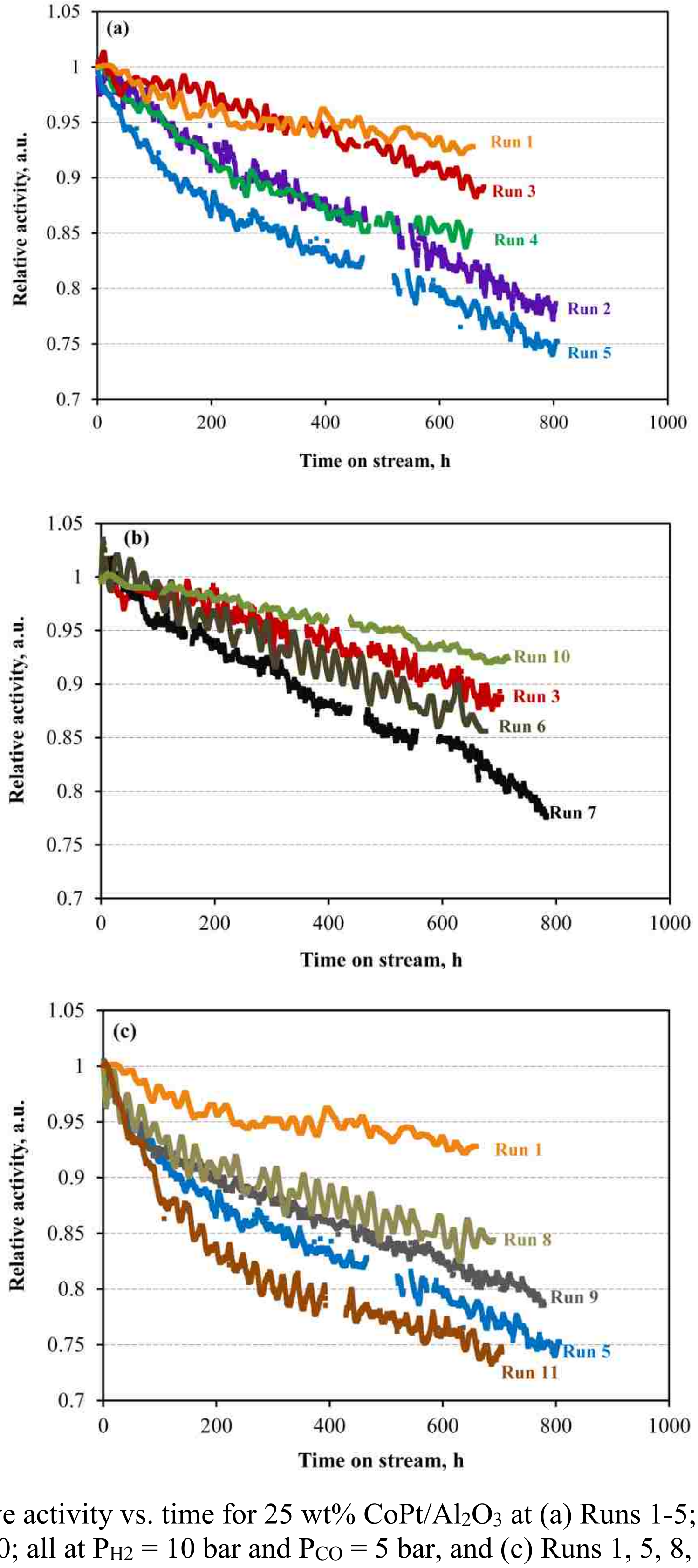

Figure 5.3. Relative activity vs. time for 25 wt% $CoPt/Al_2O_3$ at (a) Runs 1-5; all at 230°C, (b) Runs 3, 6, 7, and 10; all at $P_{H2} = 10$ bar and $P_{CO} = 5$ bar, and (c) Runs 1, 5, 8, 9, 11; all at H_2/CO of 1.

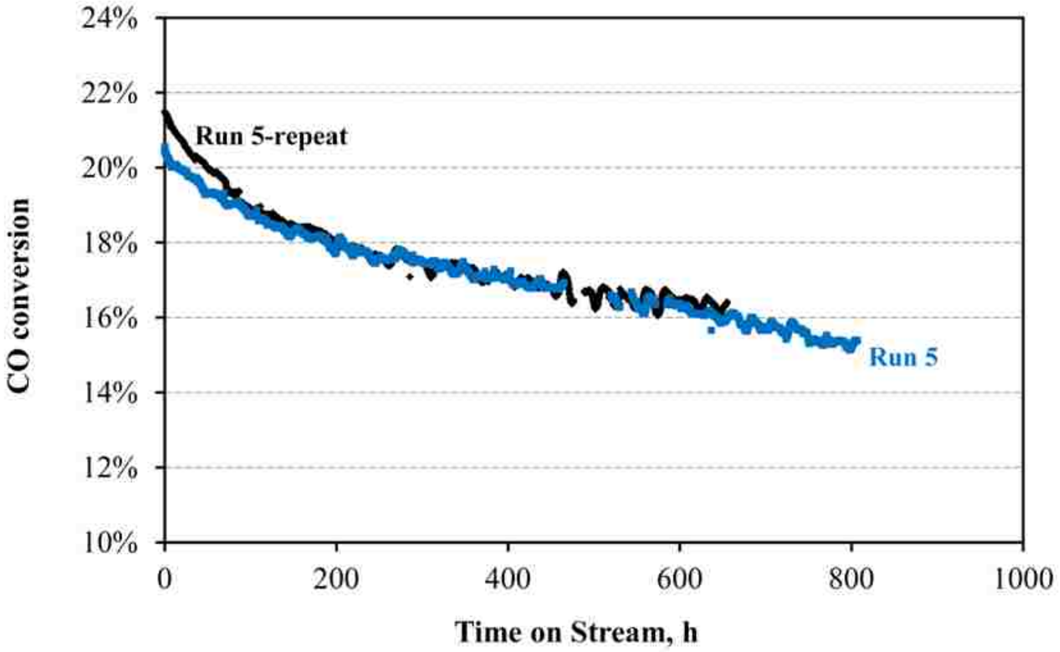

Figure 5.4. CO conversion of FB run (Run 5) and repeated FB run (Run 5-repeat) at 230°C, 20 bar, P_{H2}=10 = P_{CO} = 10 bar.

Methane selectivity remained constant with TOS in Runs 1-3, 6-8, and 10 (Figure 5.5e); however, in Runs 4 (Figure 5.5a), 5 (Figure 5.5b), 9 (Figure 5.5c), and 11 (Figure 5.5d) all at higher partial pressures of CO (Run 4 at P_{CO} = 7.3 bar, other at P_{CO} = 10 bar), a trend of increasing CH_4 selectivity is observed over 600-800 h. This result is consistent with Peña et al. [125], who only observed an increase in CH_4 selectivity at high partial pressures of CO as CO conversion decreased due to deactivation by carbon. Productivities for Runs 1-3, 6-8, and 10 were observed to decrease proportional to the decrease in rate; however, decreases in productivity for Runs 4, 5, 9, 11, as shown in Figure 5.5 due to both deteriorating selectivity and decreasing rate, since both the rate and methane selectivity are changing as the catalyst deactivates.

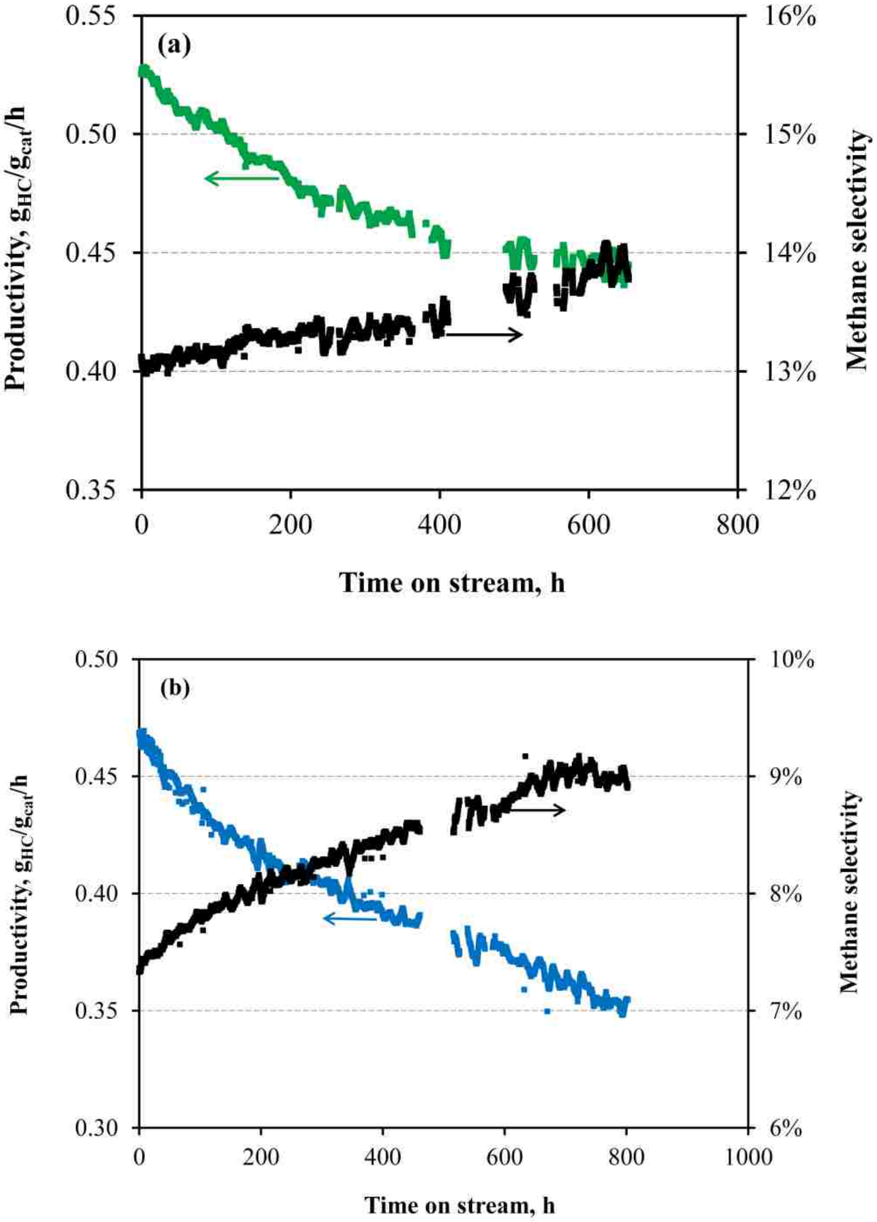
(a)
Productivity, g_HC/g_cat/h
Methane selectivity
0.55
0.50
0.45
0.40
0.35
16%
15%
14%
13%
12%
0
200
400
600
800
Time on stream, h
(b)
Productivity, g_HC/g_cat/h
Methane selectivity
0.50
0.45
0.40
0.35
0.30
10%
9%
8%
7%
6%
0
200
400
600
800
1000
Time on stream, h

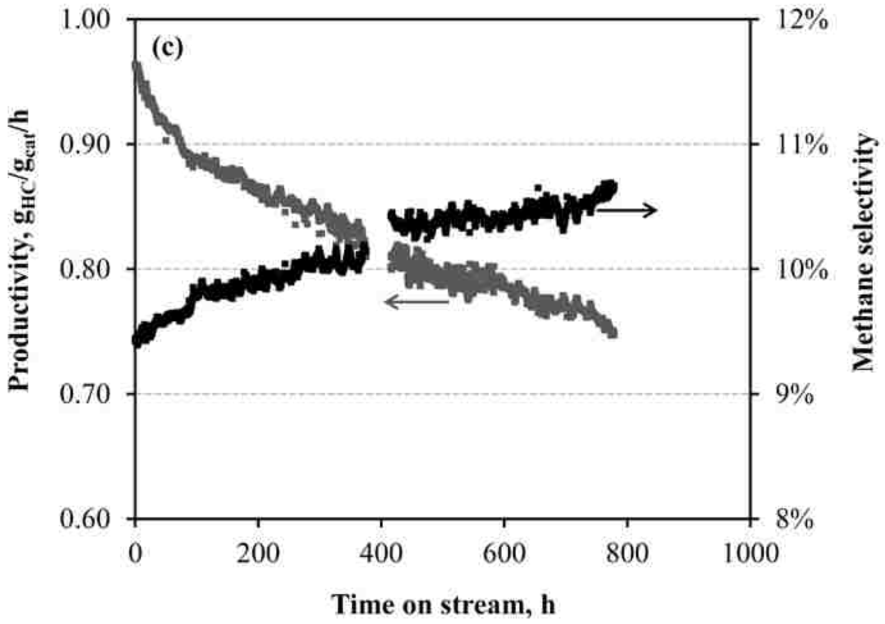
(c)
Productivity, $g_{HC}/g_{cat}/h$
Methane selectivity
Time on stream, h
1.00
0.90
0.80
0.70
0.60
12%
11%
10%
9%
8%
0
200
400
600
800
1000

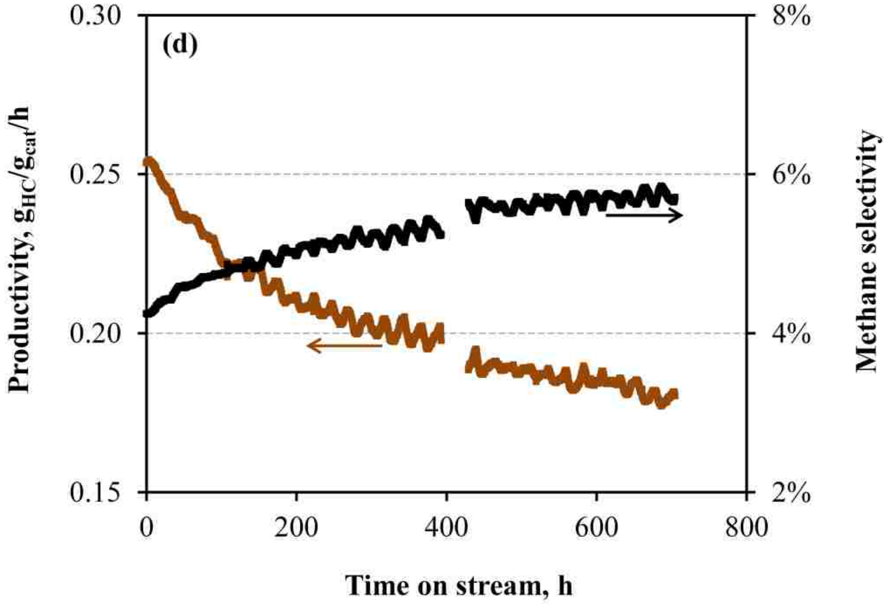
(d)
Productivity, $g_{HC}/g_{cat}/h$
Methane selectivity
Time on stream, h
0.30
0.25
0.20
0.15
8%
6%
4%
2%
0
200
400
600
800

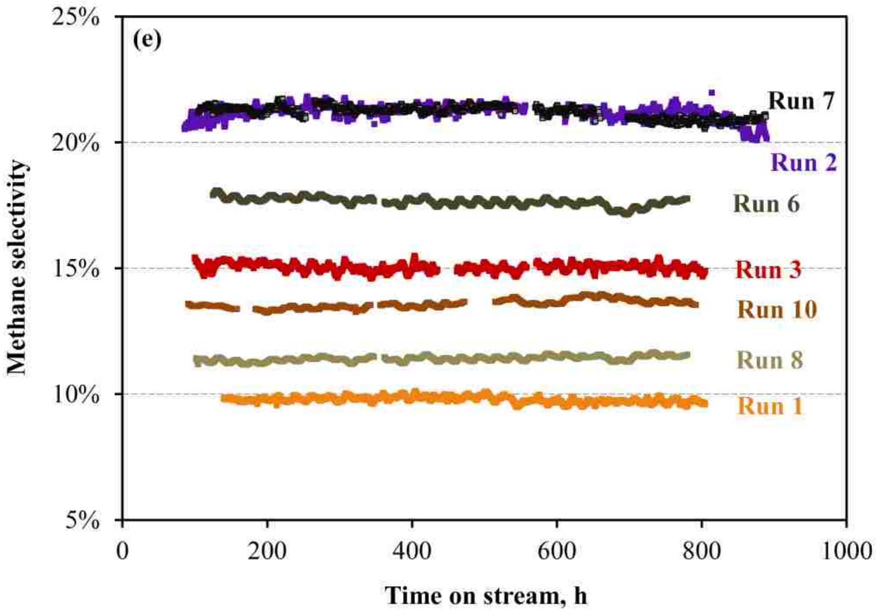

Figure 5.5. Productivity and methane selectivity of (a) Run 4 (P_{H2}=10 bar, P_{CO}=7.3 bar) (b) Run 5 (P_{H2}=10 bar, P_{CO}=10 bar) at 230°C and 20 bar, (c) Run 9 (P_{H2}=10 bar, P_{CO}=10 bar) at 250°C and 20 bar, and (d) Run 11 (P_{H2}=10 bar, P_{CO}=10 bar) at 220°C and 20 bar and (e) methane selectivity of other runs showing relatively constant methane selectivity over 800 – 900 h.

5.3.3 Nitrogen adsorption/desorption

Through the use of nitrogen adsorption/desorption BET surface area, average pore diameters, and pore volume of the reduced catalyst, Refs., and each of the wax-extracted spent catalysts were determined using a new slab pore model and method proposed by Huang et al. [65] and modified to fit a log-normal PSD [66]. These data are summarized in Table 5.3. A broad bimodal pore size distribution was found for the freshly reduced catalyst with the first and second peaks centered at 12.6 and 40.2 nm, respectively. The freshly reduced wax-extracted catalyst was also tested to determine the effect of residual wax on the BET, indicating that (1) the BET surface area was within experimental error of the freshly reduced catalyst and (2) that the total pore volume was only slightly lower (6%) than the freshly reduced catalyst. The BET results of the Refs. indicate that polymeric carbon (Ref. 1) decreases both surface area and total pore volume by 16 and 20%, respectively, while graphitic carbon (Ref. 4) causes a significant increase in surface area (Table 5.3) relative to the reduced catalyst, probably because of the large surface area of graphitic carbon. It appears that graphitic carbon forms in the larger pore diameters of the catalyst since the second pore diameter peak for the reduced catalyst dropped from 40.2 to 16.4 nm. Nevertheless, the catalyst still has a higher pore volume than Ref. 1 (polymeric carbon).

After FT reaction at different process conditions, the surface area and pore volume of the catalyst samples after wax-extraction decreased by 0 - 27% and 15 - 25%, respectively. Among the catalysts at 230°C, the lowest surface area was found for Run 5 which had high partial pressures of H_2 and CO ($P_{CO} = P_{H2} = 10$) but a H_2/CO ratio of 1. In addition at 230°C, the lowest pore volume was for Runs 1 and 5 (H_2/CO = 1); however, the highest pore volume was for Run 2 with higher H_2/CO (H_2/CO = 3). Total pore volume and surface area, on average, are lowest on catalysts tested at 240°C and highest on catalysts tested at 250°C. The differences in terms of pore volume and BET surface seem to be significant because they are outside the confidence intervals as shown with the freshly reduced catalyst.

Table 5.3. Surface area, pore volume, and pore diameter of freshly reduced, Refs., and FB wax-extracted spent catalysts.

Catalyst (T - P_{H2}/P_{CO})	BET Surface Area, m^2/g	Average Pore Diameter, nm		Total Pore Volume, cm^3/g
		Peak 1	Peak 2	
Reduced[a]	111± 5.8[b]	12.6	40.2	0.639 ± .0180[b]
Reduced Wax-Extracted[c]	106	14.3	38.6	0.603
Ref. 1[d]	97	14.4	38.3	0.521
Ref. 4[e]	152	12.1	16.4	0.56
Run1 (230°C - 5/5)	95	13.4	40.2	0.487
Run 2 (230°C - 15/5)	94	14.4	40.2	0.54
Run 3 (230°C - 10/5)	111	14.3	36.3	0.516
Run 4 (230°C - 10/7.3)	93	12.8	38.2	0.522
Run 5 (230°C - 10/10)	81	13.2	36.3	0.499
Run 6 (240°C - 10/5)	101	13.8	34.6	0.503
Run 7 (250°C - 10/5)	103	12.9	44.4	0.511
Run 8 (240°C - 5/5)	85	12.8	32.9	0.478
Run 9 (250°C - 10/10)	92	13.9	36.4	0.501

[a] Freshly reduced sample without wax

[b] 95% Confidence Interval found using Student's t-test with 3 degrees of freedom

[c] Freshly reduced wax-extracted sample

[d] Ref. 1 is $Pt/Co/Al_2O_3$ treated in CO at 250°C

[e] Ref. 4 is $Pt/Co/Al_2O_3$ treated in CO at 350°C

5.3.4 X-ray diffraction (XRD)

XRD measurements were conducted for the catalysts before and after the FT reaction and compared against standards as shown in Figure 5.6. Each scan of the wax extracted catalysts compares very well to the freshly reduced catalyst, showing mainly the presence of cobalt and the alumina support. A small peak for Co_3O_4 at $2\theta = 36.9°$ is present for all samples, including the calcined sample, except for Run 4. Thus, Co_3O_4 is apparently present in the passivated samples (except for Run 4), although other workers have assigned this peak to CoO after passivation [48, 49]. No peaks are apparent where the most intense ($2\theta = 36.5°$) line for bulk CoO is expected, even though 8.8% of the bulk cobalt is estimated to be present as CoO after reduction in hydrogen (see section 5.3.9). By assuming passivation would oxidize the first three monolayers of Co, Co_3O_4 was estimated to be present with 334 μmol Co_3O_4/g_{cat}, while CoO would only be present with 250 μmol CoO/g_{cat}. Unreduced CoO is typically present as a surface $CoAl_2O_4$ spinel (observed by TPR) which is indistinguishable from the Al_2O_3 support [129]. Bulk cobalt carbide (Co_2C) also appears to be absent from the wax-extracted catalysts even under hydrogen poor conditions ($H_2/CO=1$, Runs 1, 5, 8, and 9), which is consistent with Peña et al. [49] and Moodley et al. [48]; however, this does not necessarily indicate that bulk cobalt carbide does not exist on the catalyst because it is rarely seen by *ex situ* characterizations [56]. Using the Scherrer equation, the average cobalt metal crystallite diameter of the freshly reduced catalyst and wax-extracted FB catalysts after 700-800 h TOS was estimated to be about 12 nm indicating that sintering did not occur (determined using $2\theta = 44.3°$). The XRD profiles (not displayed) for the wax-extracted spent FB catalyst samples tested at different temperatures are the same as the samples tested at 230°C meaning no cobalt carbide was found and the estimated cobalt crystallite size was found to be ~12 nm.

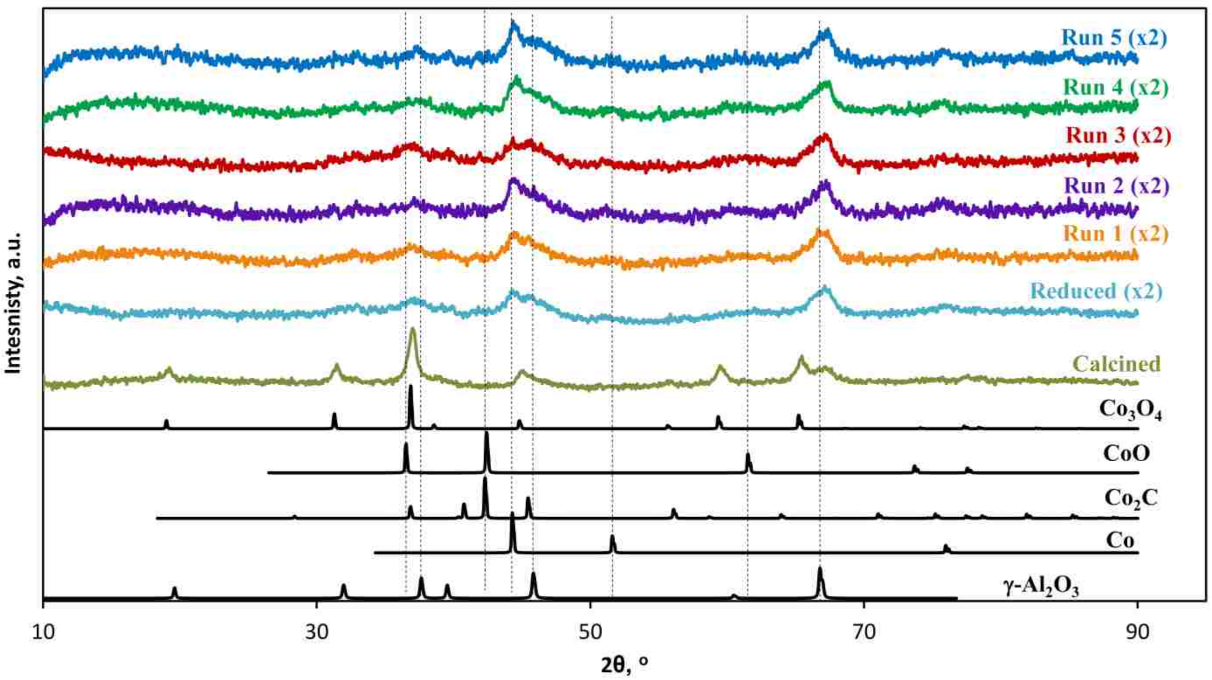

Figure 5.6. X-Ray diffraction of, FB wax-extracted catalysts, calcined catalyst, freshly reduced catalyst, and ICDD standards.

5.3.5 Temperature programmed reduction (TPR)

The nine wax-extracted spent catalysts were tested using H_2-TPR to determine formation of cobalt aluminate and different carbon species on the surface. The calcined catalyst was used as a Ref. to determine the peak position and extent of cobalt aluminate formation. As can be seen in Figure 5.7, there are three significant peaks but four stages of mass loss in the calcined catalyst: (1) transformation of bulk Co_3O_4 to bulk CoO indicated by two peaks below 200 °C (the first of which is probably due to reduction of Co in the near vicinity of Pt), (2) reduction of bulk CoO to Co occurring at 330°C (3) progressive reduction from 400 to about 535°C of strongly bound CoO (to Al_2O_3), and (4) reduction of cobalt aluminate to cobalt metal at 560°C. From the relative peak areas, about 3% of the cobalt in the calcined sample is present as aluminate. This cobalt aluminate peak is also present in the spent catalysts (Runs 1-5) but to a greater extent than in the calcined catalyst. Cobalt aluminate formation is 6 - 7 wt% of the cobalt for Runs 1-5 if the peak areas are compared to that for the calcined catalyst. The other peaks on the wax-extracted spent catalysts cannot be compared to the peaks found on the calcined catalyst, since the peaks on the calcined catalyst show the weight loss of oxygen due to reduction of Co_3O_4 to Co.

There appears to be additional stages of mass loss in each of the wax-extracted spent catalysts besides the cobalt aluminate peak. These stages of mass loss, occurring at temperatures of about 180, 230, and 420, could be assigned to residual wax and/or atomic carbon and/or bulk cobalt carbide, residual wax in narrow pores and/or oligomers, and polymeric carbon, respectively. It should be noted that among the catalysts tested at 230°C Runs 1 and 5 display the greatest formation of wax/hydrocarbons (the first two peaks) on the surface, while Run 2 has the lowest. Interestingly, Runs 1 and 5 had hydrogen poor conditions ($H_2/CO = 1$) and Run 2 had hydrogen rich condition ($H_2/CO = 3$). Since the H_2-TPR weight losses of spent catalysts can be from oxygen loss of the passivation step and/or physisorbed water in addition to carbon hydrogenation, the identification of carbon species is done more accurately with TPH characterization (see section 5.3.7).

For the FB catalysts run at different temperatures, the results are very similar to the FB catalysts run at 230°C. Cobalt aluminate formation with 700-900 h TOS increased, ranging from 5.5 - 7 wt% increase of the cobalt for Runs 6 - 9, with Run 7 (250°C) having the highest cobalt aluminate formation. This amount of cobalt aluminate formation is in the same range as the cobalt aluminate formation of the catalysts run at 230°C, showing that temperature does not have a large effect on cobalt aluminate formation. Also, the most carbon present is on both catalysts run at 250°C (Run 7 and Run 9) regardless of ratio.

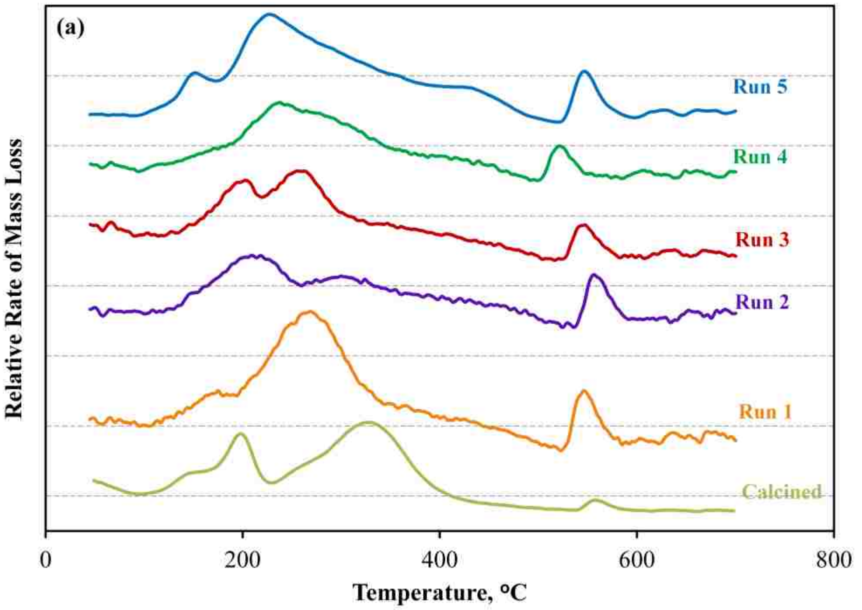

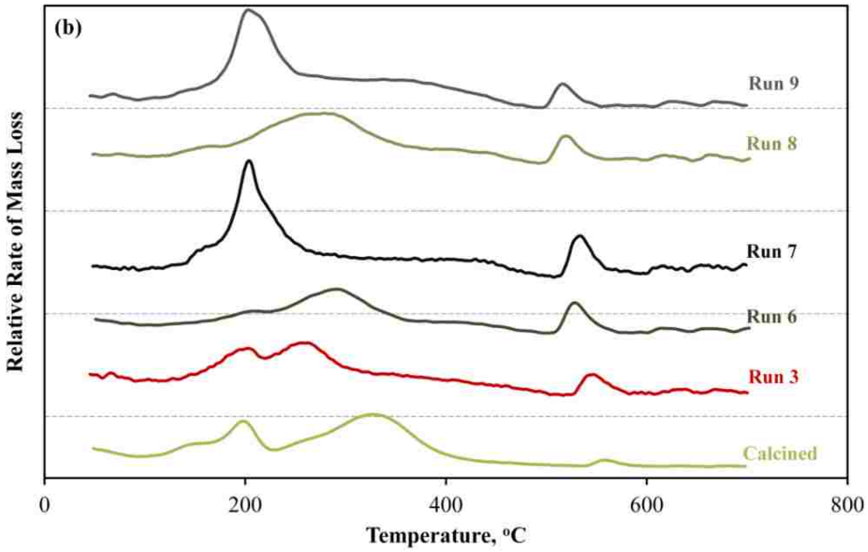

Figure 5.7. TPR profiles of calcined fresh catalyst and wax-extracted spent catalysts for (a) Runs 1-5 and (b) Runs 6-9.

5.3.6 XANES/EXAFS

To determine whether cobalt crystallites oxidize during FTS, wax coated cobalt samples which experienced the most deactivation among the catalysts tested at 230°C (Run 5) were removed from the FTS reactor after 800 h and analyzed with XANES and EXAFS. Figure 5.8

compares the normalized XANES spectra of the calcined, freshly reduced, and wax-coated spent catalyst (Run 5) samples with that of the reference Co metal foil. By comparison with the literature, the line shape of Co in the calcined catalyst resembles Co_3O_4 [130] and the freshly reduced catalyst contains both an oxidized component and cobalt metal. The shift in the energy of the white line to lower energy indicates that the oxide component is no longer Co_3O_4, but rather CoO [130]. In comparing the spectra of the freshly reduced and spent catalyst samples, the decrease in the white line intensity after running FTS indicates that the spent catalyst sample is more reduced than that of the freshly reduced one.

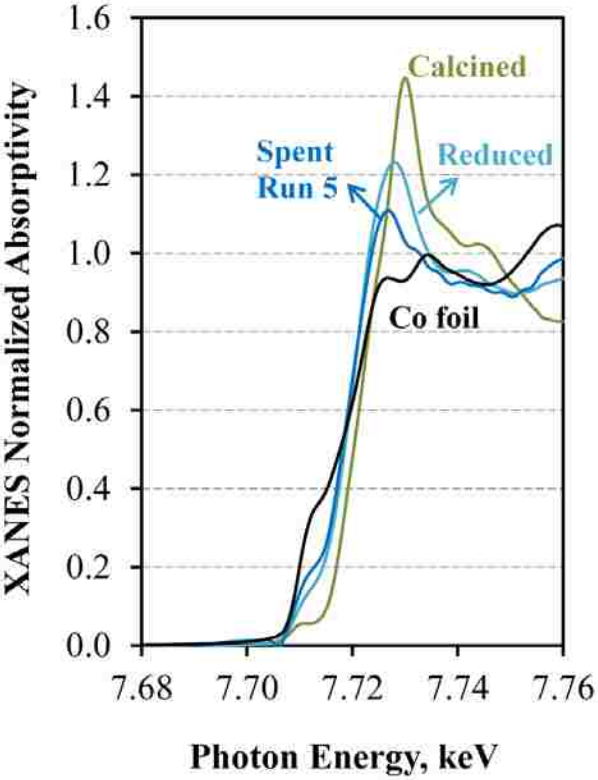

Figure 5.8. Normalized XANES spectra (Co K-edge) for calcined, freshly reduced, and wax-coated spent catalyst (Run 5: $P_{H2} = P_{CO} = 10$ bar and 230°C).

The left-hand side of Figure 5.9 compares the Fourier transform magnitude spectra of the freshly reduced catalyst with that of the Co metal foil and the calcined catalyst. Qualitatively, the freshly reduced catalyst contains two major contributions, Co-Co metal coordination and Co-O coordination from CoO. One cannot rule out a contribution from Co-Co in CoO. The data are consistent with XANES that the freshly reduced catalyst is a mixture of Co metal and CoO.

The right-hand side of Figure 5.9 compares the Fourier transform magnitude spectra of references and catalysts for the shortened k-range, in order to compare with the spent catalyst sample. The spent catalyst sample shows an increase in the peaks for Co-Co metal coordination in both the first and second shells. Increased Co-Co coordination may come from two sources: (1) reduction of CoO and/or (2) sintering processes (e.g., agglomeration of Co metal or Ostwald ripening).

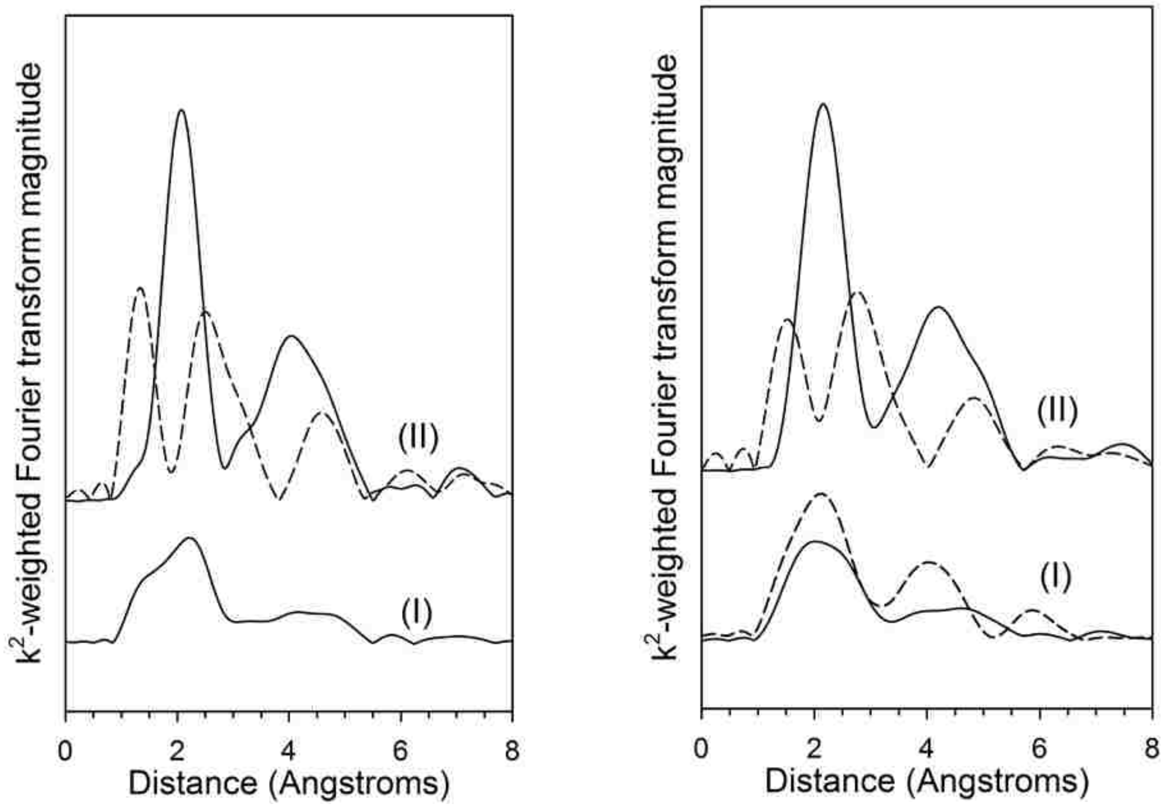

Figure 5.9. Co K-edge EXAFS k^2-weighted Fourier transform magnitude spectra over (left) longer k-range of 2.5 – 10 angstroms^{-1} and (right) shorter k-range of 3.5- 9 angstroms^{-1} for (I) (solid) freshly reduced catalyst and (dashed) spent catalyst (Run 5: $P_{H2} = P_{CO}$ = 10 bar and 230°C) and (II) (solid) Co metal foil and (dashed) calcined catalyst.

An attempt was made to fit the chi data over the shortened k-range in order to fairly compare the freshly reduced and spent catalyst samples. On the left hand side of Figure 5.10, it is obvious that the amplitude is greater for oscillations associated with Co-Co metallic coordination in the spent catalyst sample (i.e., IIIa) relative to the freshly reduced one (IIa), by comparison with the Co metallic foil reference spectrum (Ia). It was not possible to obtain a physically meaningful fitting by including both Co-O from CoO and Co-Co metallic coordination in a complex model. Nevertheless, a reasonable fitting of the data was obtained by de-emphasizing the Co-O contribution and emphasizing the Co-Co metallic contribution by employing a k^2 weighting during fitting. Comparisons of the filtered data (r-range of 1.5 – 2.9 Å) with the theoretical fitting are provided in both k-space (b) and r-space (c). The fitting is good at the high k-range as expected, and poorer in the low k-range. The fitting parameters are listed in Table 5.4. An increase in Co-Co metal coordination number is observed after running FTS in comparison with the freshly reduced catalyst sample. The r-factor was 0.038, which is a reasonable (but not excellent) fitting over such a shortened k-range.

Table 5.4. Results of EXAFS fitting parameters for catalysts and reference compound acquired near the Co K-edge. The fitting ranges were $\Delta k = 3.5 – 9$ $Å^{-1}$ and $\Delta R = 1.5 – 2.9$ Å. $S_0^2 = 0.9$.

Sample Description	N Co-Co in Co^0	R Co-Co in Co^0 (Å)	e_0 (eV)	σ^2 ($Å^2$)	r-factor
Co foil	**12**	2.484 (0.0095)	5.86 (1.57)	0.00705 (0.00048)	0.038
Freshly reduced catalyst	3.9 (0.89)				
Spent catalyst sample	5.0 (0.40)				

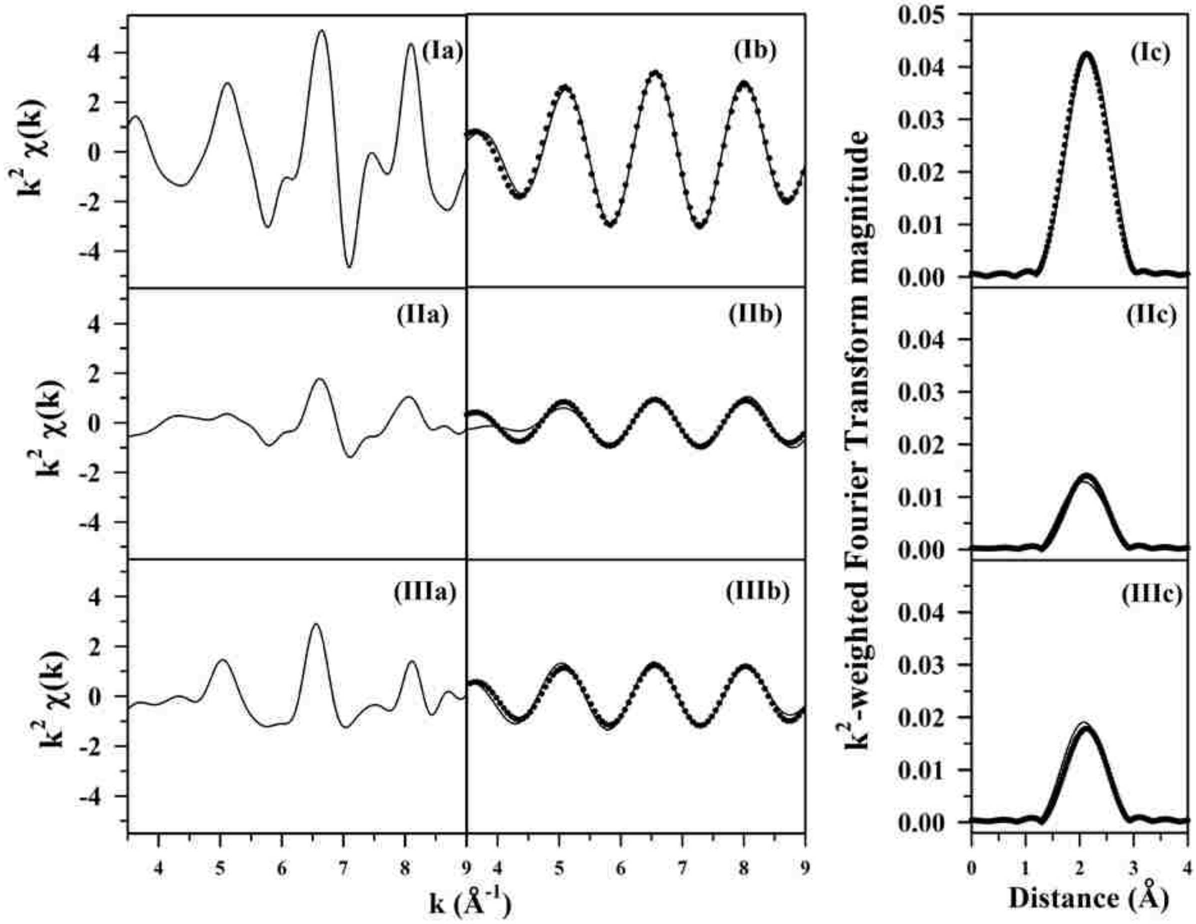

Figure 5.10. EXAFS results at the Co K-edge, including (a) (left) the raw k^2-weighted χ (k) versus k (b) (middle) (solid line) the filtered $k^2 \cdot \chi$ (k) versus k and (filled circles) the result of the fitting; and (c) (right) (solid line) the Fourier transform spectra with (filled circles) the result of the fitting. Model was weighted to k^2 to emphasize Co-Co scattering and only considered Co-Co metal coordination in the fitting. Because of the low quality of the spent catalyst spectra, the fitting range was 3.5 – 9 angstroms^{-1} and the r-range was 1.5 – 2.9 angstroms. (I) Co metal foil; (II) freshly reduced catalyst; (III) spent catalyst (Run 5: $P_{H2} = P_{CO}$ = 10 bar and 230°C).

5.3.7 XPS Results

The FB wax-extracted spent catalyst samples were evaluated by XPS in the Co 2p and the C 1s regions. XPS can provide quantitative chemical information on catalyst surfaces to a depth of 0.3 – 3 nm [28]. The fact that a cobalt signal is visible after wax extraction implies the wax has been removed to submonolayer levels. Since the catalyst was passivated in-situ after wax extraction, some surface cobalt oxide is expected; therefore, the Co 2p spectra (not shown here) do indicate the presence of both metallic cobalt and cobalt oxide. This is consistent with the results of Moodley et al. [48], who also observed metallic cobalt and cobalt oxide on the surface of their wax-extracted catalyst samples after several days on stream.

Figure 5.11 shows the XPS C 1s spectra for freshly reduced (without wax), freshly reduced wax-extracted, and wax-extracted spent catalyst samples. The very low-intensity C 1s peak for the freshly reduced passivated sample can be attributed to carbon contamination in the XPS chamber or from the supporting conducting carbon tape, as mentioned in section 5.3.1. All peaks for wax-extracted spent catalyst samples appear at binding energies of 284.2 to 284.8 eV. From the XPS data for Ref. 1 (Figures 5.2 and 5.11), the C 1s peak at about 284.5 eV can be assigned to amorphous polymeric carbon. Since this peak (284.5 eV) is broad, it may also include a contribution at 284.9 eV due to long chain hydrocarbon products, consistent with a peak observed at the same energy for the freshly-reduced catalyst surface after wax-extraction. The XPS C 1s spectra for wax-extracted catalyst samples of Runs 1, 3 and 5 consist of a broad peak centered at 284.8 eV which may correspond to mixture of polymeric carbon and wax, with wax (284.9 eV) predominating. Peaks at 283.0 eV and 283.5 eV corresponding to the carbon in the form of cobalt carbide and graphitic carbon (Ref. 4; Figure 5.2), respectively were not observed in the C 1s XPS spectra of all five spent wax-extracted catalysts, suggesting the absence of cobalt carbide or graphitic carbon after FT reaction.

5.3.8 Temperature-programmed hydrogenation (TPH) on wax extracted catalysts

TPH was used to identify the types of carbon present on the surface of the wax-extracted spent catalysts. The methane evolution profiles for the series of catalyst samples tested at 230°C and 240-250°C are shown in Figure 5.12a and 5.12c, respectively. A freshly reduced catalyst which was coated in wax, wax-extracted, and then passivated was also characterized using TPH to determine the peak position for wax and extent of wax left on the surface following extraction. It is evident that there are three peaks associated with three different types of carbonaceous species based on their reactivity toward hydrogen around 250, 300, and 360-420°C for FB wax-extracted samples. The freshly reduced wax-extracted sample only consists of the first two peaks and the only source of carbon is the residual hydrocarbons that are still present after Soxhlet wax extraction. Therefore, the first two peaks can be associated at least to some extent to waxy hydrocarbons. The second peak for this sample is broader at around 300°C, which may correspond to the transformation of hydrocarbons during hydrocracking of residual wax [48].

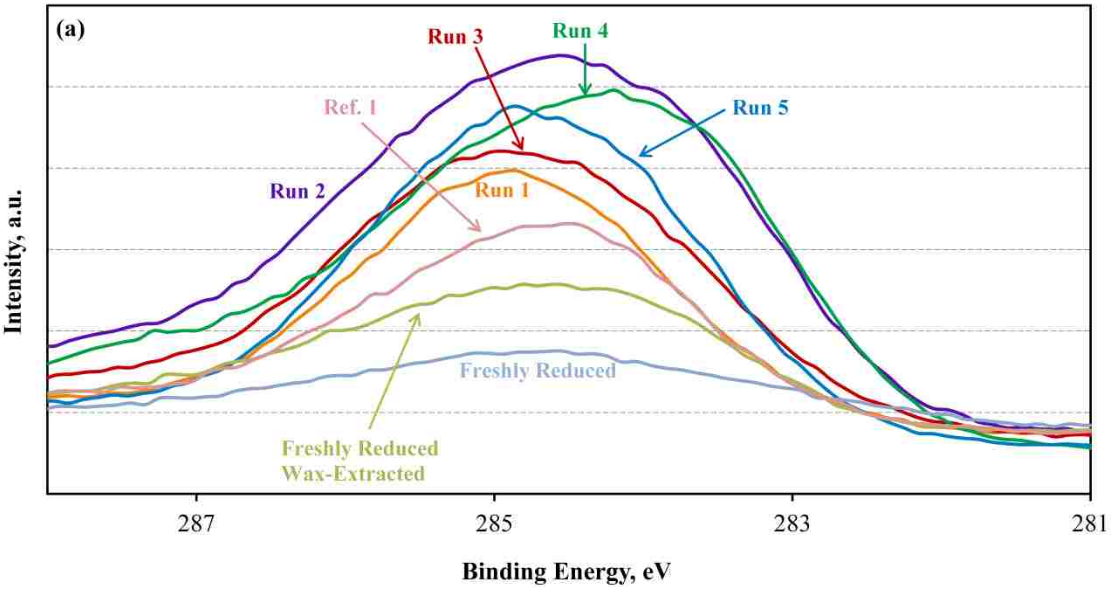

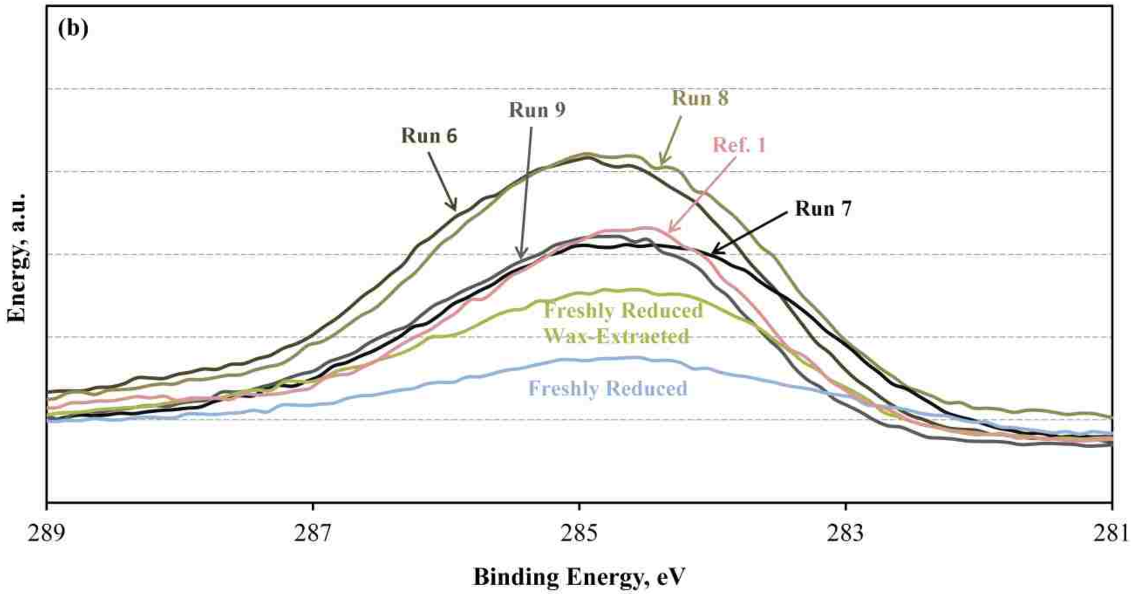

Figure 5.11. X-ray photoelectron spectra of the C 1s region for freshly reduced (without wax), freshly reduced wax-extracted, Ref. 1, and FB wax-extracted catalysts (a) Runs 1-5, (b) Runs 6-9.

It has been reported that atomic or surface carbidic carbon is hydrogenated at around 200°C [50]; therefore a part of the first peak can also be assigned to atomic carbon. Bulk cobalt carbide can also contribute to the TPH profiles, since it is hydrogenated at around 250°C. However, bulk cobalt carbide was not detected by XRD, although this does not rule out the possibility of the carbide, because bulk cobalt carbide is reportedly metastable and may not be detectable with ex situ techniques [56].

To further confirm the presence of wax, higher mass numbers were recorded by mass spectroscopy to determine the presence of ethane due to hydrocracking of wax (Figure 5.12b). The mass spectrum of C_2H_6 consist of two peaks at the same two lowest temperatures as Figure 5.12a but not much of the 3rd peak, indicating that a significant portion of peaks 1 and 2 corresponds to the hydrogenation of waxy hydrocarbons.

The second peak of the TPH profile for the freshly reduced wax-extracted sample is much broader and lower intensity than the first peak, while the second peak of FB wax-extracted samples (except for Runs 2 and 6) is of higher intensity . This indicates that the second peak of the TPH profile for spent catalysts can, in addition, be due to oligomeric carbons, which are intermediate species in the formation of a more stable polymeric carbon.

The third peak (Runs 1-9, Figure 5.12a and 5.12b) can be assigned to hydrogen-resistant polymeric carbon and high molecular weight, condensed hydrocarbons (coke) starting around 360°C and ending about 500°C. It should be noted that peak 3 cannot be observed on the wax extracted, freshly reduced catalyst indicating the absence of these types of carbons/coke in that sample.

Comparing the TPH profiles of spent catalysts and Refs. provides further information on the nature of carbon deposits on $CoPt/Al_2O_3$. The Refs. were prepared by depositing carbon via CO disproportionation at 250 and 350°C to produce a catalyst containing carbon without the presence of wax. Both atomic and polymeric carbons were deposited on alumina supported cobalt and unsupported cobalt catalysts during CO disproportionation at 250°C (Ref. 1 and Ref. 2). Based on the TPH data for the Ref. samples (Section 5.3.1), the less reactive carbon observed at high temperature (> 360°C) for TPH profiles of spent catalysts can clearly be assigned to polymeric carbon associated with the metal. That the higher temperature peak for the TPH profile of Ref. 1 (supported CoPt) is observed at about 60°C higher temperature relative to Ref. 2 (unsupported CoPt) suggests that a portion of the polymeric carbon is also present on the support.

A high temperature peak observed for polymeric carbon at around 470°C for Ref. samples 1-3 (treated with CO at 250°C) is about 90°C higher than the high temperature peak (third peak) of TPH profiles (Figure 5.12a and 5.12c) for spent catalysts (Runs 1-9). The peak at higher temperature for the Ref. samples can be assigned to non-hydrogenated polymeric carbon since they were treated with CO (no H_2). On the other hand, hydrogenated polymeric carbons are likely present on spent catalysts after FT reaction, in both CO and H_2, as evident by lower temperature of hydrogenation, indicating that this hydrogen-containing polymeric carbon is easier to hydrogenate.

From the TPH profile for Ref. 4, the catalyst treated with CO at 350°C, a new very high temperature peak is observed at 560°C which is assigned to non-hydrogen-containing graphitic carbon. Since this peak is not observed on the spent catalysts, the stable carbon on spent catalysts which occurs at around 360°C and ends at about 500°C is likely not non-hydrogen-containing graphitic carbon. These results do not rule out the possibility of graphene being present in the spent catalyst and thus hydrogenated during TPH at 360-500°C. For the Ref. 1 sample (supported Pt/Co) treated in only CO, a peak at 280-300°C was not observed, although it was observed in the spent catalysts at 280-300°C after FTS in CO and H_2. Therefore, peak 2 for the spent catalysts is likely due to waxy hydrocarbons and/or hydrogenated precursors located in the pores of the alumina for the spent catalysts (Figure 5.12a and 5.12c).

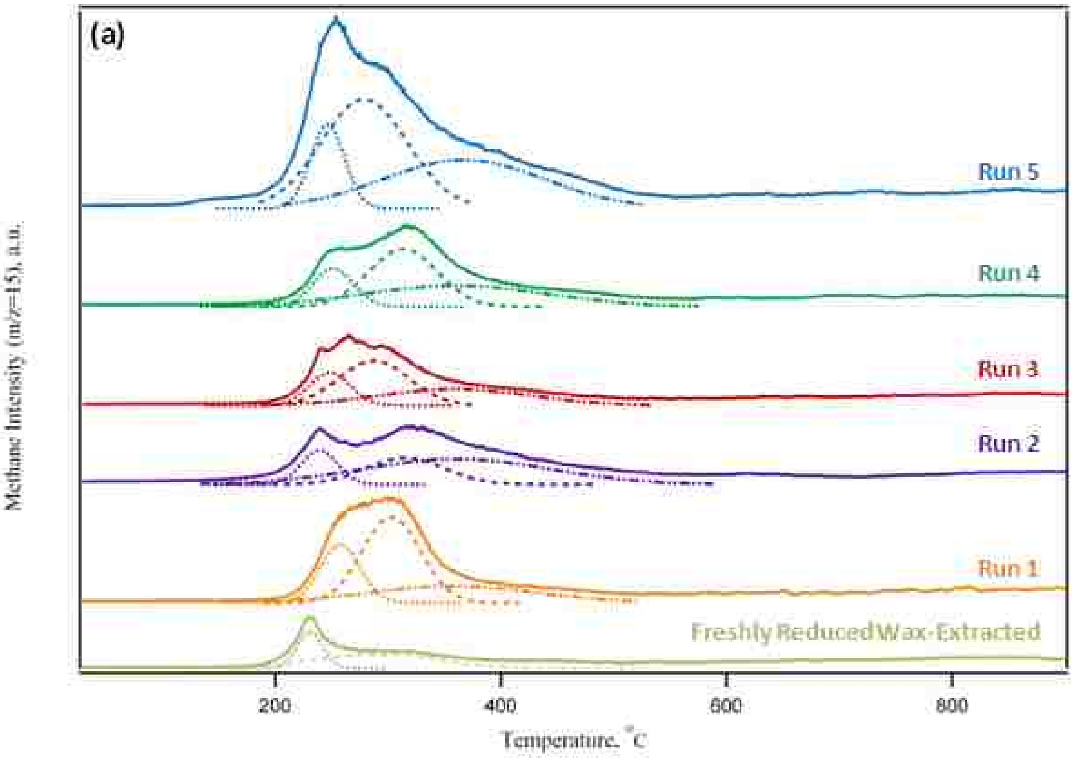
(a)
Methane Intensity (m/z=15), a.u.
Run 5
Run 4
Run 3
Run 2
Run 1
Freshly Reduced Wax-Extracted
200
400
600
800
Temperature, °C

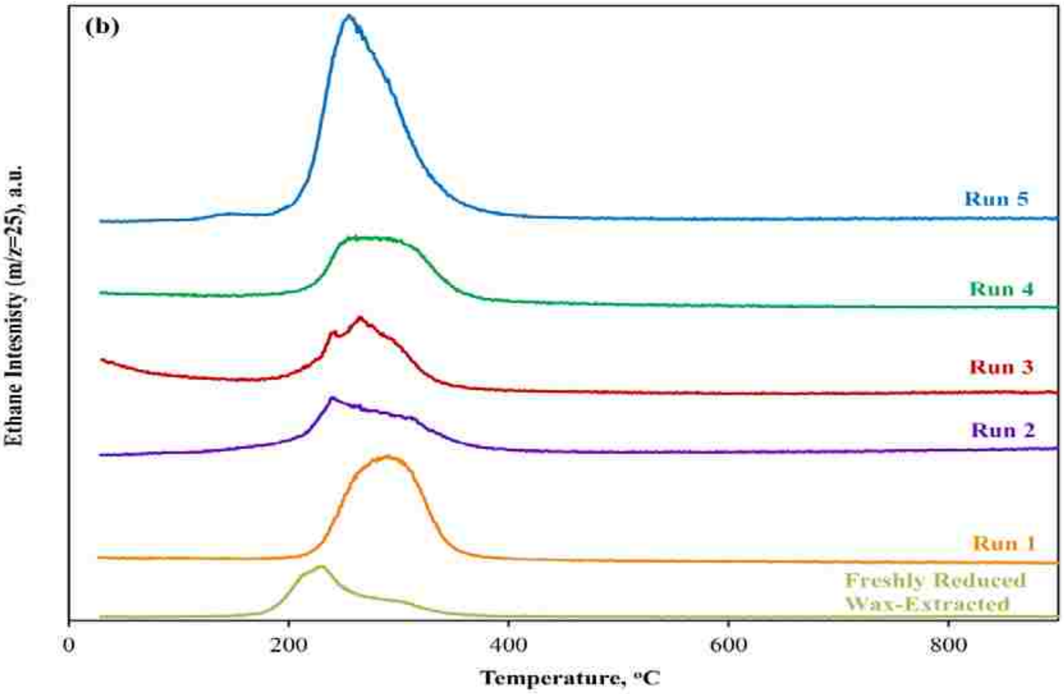
(b)
Ethane Intesnisty (m/z=25), a.u.
Run 5
Run 4
Run 3
Run 2
Run 1
Freshly Reduced
Wax-Extracted
0
200
400
600
800
Temperature, °C

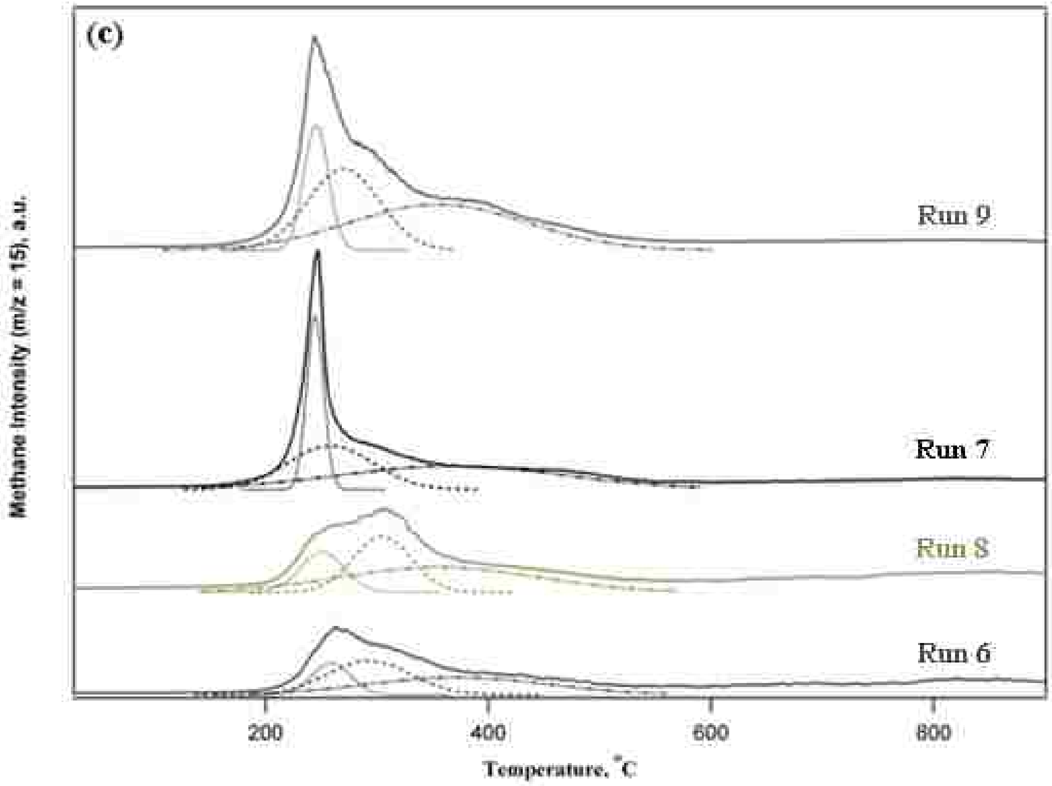

Figure 5.12. TPH of wax-extracted spent catalysts and freshly reduced wax-extracted catalyst for (a) m/z=15 for Runs 1-5, (b) m/z=25 for Runs 1-5, and (c) m/z=15 for Runs 6-9.

The methane evolution of the TPH profiles was deconvoluted with Gaussian peaks using a similar procedure used by Xu and Bartholomew [127] for spent iron catalysts and Moodley et al. [48] for spent Co/Al_2O_3 catalysts. Integration of peak areas for the TPH profiles is reported in Table 5.5. From the peak areas, it is observed that the amount of less reactive species (Peak 3) is increasing as the partial pressure of both CO and H_2 increase (Runs 2 and 5 with 15/5 and 10/10). In addition, the combination of peaks 1 and 2 for runs tested at 230°C (Runs 1-5), which is mostly wax and hydrocarbons, is higher for Runs 1 and 5 ($H_2/CO = 1$) and lowest for Run 2 ($H_2/CO = 3$). This observation is consistent with the fact that lighter hydrocarbons are formed at higher H_2/CO ratios.

The amount of polymeric carbon is increasing as the temperatures increases at $H_2/CO = 2$ (Runs 6, 7, and 3). However, the amount of less reactive carbon decreases with temperature (Runs 3 and 9) at H_2/CO ratio of 1 with $P_{H2} = P_{CO} = 10$.

Table 5.5. Integration of CH_4 peaks for TPH on wax-extracted spent FB catalyst samples.

Catalyst ($T – P_{H2}/P_{CO}$)	Peak 1, $\mu mol/g_{cat}$	Peak 2, $\mu mol/g_{cat}$	Peak 3, $\mu mol/g_{cat}$	Total, $\mu mol/g_{cat}$
Fresh reduced	196	380	0	576
Run1 (230°C - 5/5)	502	1046	536	2084
Run 2 (230°C - 15/5)	262	468	944	1673
Run 3 (230°C - 10/5)	299	697	632	1628
Run 4 (230°C - 10/7.3)	314	812	788	1914
Run 5 (230°C - 10/10)	588	1942	1662	4191
Run 6 (240°C - 10/5)	345	604	702	1651
Run 7 (250°C - 10/5)	627	816	1091	2535
Run 8 (240°C - 5/5)	443	602	1056	2102
Run 9 (250°C - 10/10)	667	1431	1483	3581

5.3.9 CO-chemisorption

CO chemisorption was used to determine Co surface area before and after FT reaction, and thus loss of surface area during reaction. These losses could be due to deposited carbon that blocks active cobalt sites and/or sintering that can also reduce cobalt surface area. To evaluate the effect of sintering and hydrogen resistant carbon (polymeric carbon), CO-uptakes were performed, in which the wax-extracted spent catalysts were re-reduced in H_2 at different temperatures (350°C and 450°C). Re-reducing the wax-extracted spent catalysts at 450°C removes almost all of the deposited carbon, allowing sintering's effect to be determined. CO-uptake values for wax-extracted FB catalysts reduced at 450°C were comparable to the freshly reduced catalyst (not shown here), indicating that no sintering happened during~800 h TOS. It should be noted that the catalysts were already bulk-reduced at 450°C for 72 h and they were re-reduced at the same temperature before CO-uptake measurements; therefore, change of dispersion due to reduction is not expected.

CO-uptake values of wax-extracted spent FB catalysts re-reduced at 350°C are compared to the freshly reduced catalyst in Table 5.6. As seen by the uptake value for the freshly reduced wax-extracted catalyst (212 $\mu mol/g_{cat}$), re-reducing the spent catalysts at 350°C removes most of the wax present on the catalyst, leaving mainly polymeric carbon on the surface of the catalyst. A significant decrease (20-40%) in CO-uptake values was observed for the spent FB catalysts (wax-extracted) indicating the interaction of polymeric carbon species with cobalt. CO uptake decreases and fraction of original Co sites lost increases as the total pressure of H_2 and CO increases (Figure 5.13). The lowest CO-uptake values for catalyst samples tested at 230°C were seen for Runs 2 and 5, the FB runs with the highest total pressure of CO and H_2. Run 1 with the lowest total pressure of CO and H_2 and Run 3 as our standard condition ($H_2/CO=2$) are shown displayed with the highest CO-uptakes after reaction for catalyst samples tested at 230°C. At H_2/CO of 2, CO-uptake decreases as the temperature increases to 250 from 230°C.

Table 5.6. CO-uptake data on freshly reduced catalyst and wax-extracted spent FB catalysts.

Catalyst (T - P_{H2}/P_{CO})	CO-uptake[a], μmol/g_{cat}
Freshly reduced[b]	227
Freshly reduced wax-extracted[c]	212
Run1 (230°C - 5/5)	191
Run 2 (230°C - 15/5)	150
Run 3 (230°C - 10/5)	186
Run 4 (230°C - 10/7.3)	168
Run 5 (230°C - 10/10)	141
Run 6 (240°C - 10/5)	171
Run 7 (250°C - 10/5)	157
Run 8 (240°C - 5/5)	162
Run 9 (250°C - 10/10)	145

[a] All catalysts were re-reduced at 350°C to obtain CO-uptake values.

[b] Freshly reduced catalyst without wax

[c] Freshly reduced catalyst coated in wax and then the wax was extracted as described in section 5.3.2.

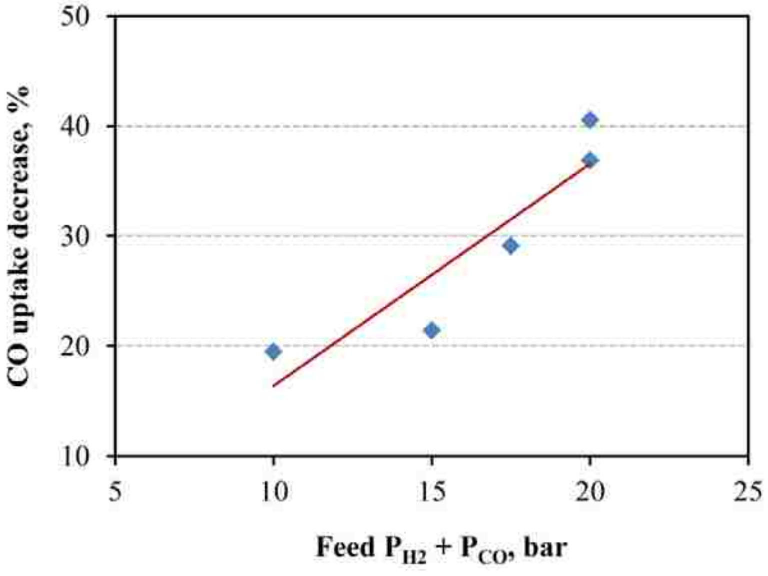

Figure 5.13. CO uptake decrease as a function of inlet partial pressures of H_2 and CO for Runs 1-5; all at 230°C.

5.3.10 Extent of reduction (EOR), dispersion, and crystallite size

The EOR of the freshly reduced catalyst at 450°C was estimated, from the TPR profile (section 5.2.4) to be 91.2%. Assuming the EOR for the Pt promoter to be 100%, the dispersion for freshly reduced catalyst was estimated to be 8.6% from the EOR and measured H_2 uptake (Section 5.2.4). The cobalt crystallite diameter is calculated from the dispersion to be 10.9 nm in good agreement with the measured value from XRD of 12 nm.

The EOR for wax-extracted FB spent catalyst samples was determined using TPR and also oxygen titration by re-reducing the catalysts at 450°C to remove any hydrogen resistant carbon. The EOR of each of the wax-extracted FB spent catalyst samples (Runs 1-9) was nearly the same (91 ± 2%) as for the freshly reduced catalyst.

5.4 Discussion

The results of this study provide (1) new data regarding the effects of partial pressures of CO and H_2, temperature, and polymeric carbon on the rate of deactivation during FTS under commercially representative FT reaction conditions over a period of 800 h and (2) insights into the types and distributions of carbonaceous species deposited under these conditions of synthesis.

5.4.1 Exclusion of deactivation mechanisms other than deposits of carbonaceous or hydrocarbonaceous species

The results of this study show for the first time the impact of carbon deposition by polymeric carbon on the deactivation of FT cobalt catalysts in the absence of other deactivation mechanisms. It is emphasized that our catalyst and experiments were purposely designed to isolate the effects of carbon on deactivation.

(1) Poisoning by sulfur and nitrogen compounds was not an issue because (a) high purity gases were used and the preparation of the catalyst involved materials of high purity and (b) no change in CO-uptake was observed for the Co catalyst regenerated in H_2 at 450°C for 3 h, conditions which would not remove a significant quantity of adsorbed sulfur or completely remove adsorbed nitrogen species.

(2) Oxidation of Co metal to Co oxide was avoided by having a negligible fraction of cobalt particle sizes less than 2 nm [35] (our average crystallite diameter of 12 nm), and by running the FB system at X_{CO} between 16 and 24%, thereby keeping the partial pressure of water low enough to prevent oxidation. XANES results show that the catalyst does not undergo oxidation during these FTS conditions. Instead a gradual reduction over an 800 h period takes place with the spent sample closely resembling the spectrum of a Co foil. This is consistent with the literature for the initial decay period prior to leveling off for both research [131] and commercial [34] Co catalysts.

(3) Our observation of only 3 wt% increase in cobalt aluminate formation for the wax-extracted spent catalyst relative to the calcined catalyst indicates that Co aluminate formation is a relatively minor cause of deactivation. Saib et al. [34] have concluded that aluminate is not formed via oxidation of active cobalt metal; instead, CoO present in the working catalyst is the principal intermediate in the formation of cobalt aluminate. Given our observation that EOR is not changed during 800 h of reaction, i.e. EOR is 91% ± 2% for both freshly reduced and re-reduced (at 450°C) wax-extracted spent catalysts, and net reduction was found from

XANES/EXAFS results after 800 h TOS, we conclude in agreement with Saib et al. and Jacobs et al. [34, 131] that none of the metallic Co in our catalysts forms an aluminate; instead, Co aluminate is formed from the unreduced CoO, i.e. about 3% Co aluminate and 6% CoO are present in the freshly reduced catalyst, while about 6% Co aluminate and less than 3% CoO are present in the re-reduced, wax-extracted spent catalyst.

(4) Data from this study obtained by XRD, CO-chemisorption, and EOR provide clear evidence that sintering of cobalt nanoparticles did not contribute to the deactivation of the catalyst, i.e., the dispersion of the cobalt particles remained the same before and after reaction. The absence of sintering can be attributed to a careful design of the catalyst, using a stable silica-doped alumina support [62, 83, 85] and a high reduction temperature (450°C) to produce large cobalt crystallites [average crystallite diameter (ACD) of 12 nm] stable against sintering. That no sintering was observed in our catalysts having an ACD of 12 nm after 30 day (800 h) runs is consistent with the observations of Overett et al. [33, 35] that following a 100 day test, cobalt ACD increased to 12-14 nm from an initial value of 9 nm; all of the sintering occurred during the first 10 days and was contributed to 30% loss in activity.

EXAFS results show an increase in Co-Co metal coordination for a spent catalyst sample after 800 h TOS, which can be assigned to (1) reduction of CoO and/or (2) sintering. Since no sintering was observed with XRD analysis of the catalyst sample before and after the reaction and is consistent with XANES results, the increase in Co-Co metal coordination can be due to net reduction of CoO.

From the forgoing discussion it is evident that deactivation mechanisms other than those related to deposition of polymeric carbons and hydrocarbons do not contribute significantly to the deactivation of our Co catalysts over a wide range of partial pressures of H_2 and CO and temperatures; therefore, it is concluded that this study is unique and singular for better understanding the impact of carbon only on the deactivation of Co FTS catalysts.

5.4.2 Effects of polymeric carbon on catalyst properties, CO-uptake, and activity

We previously discussed (in the Introduction) how different forms of carbon can cause deactivation in different ways. Our investigation focused on deactivation of Co FT catalysts by wax, atomic carbon, and polymeric carbon (some of which may be condensed hydrocarbons). Bulk cobalt carbide was not observed (by XRD) on our spent catalysts; this observation is consistent with Moodley et al. [48] who reported no cobalt carbide presence even after several months of FT operation with a commercial Co catalyst similar to ours.

Our results show that accumulation of atomic carbon and clogging of catalyst pores by heavy wax left after wax-extraction are not important deactivation pathways. In fact, TPH profiles for Runs 1-5 (Fig. 5.10a) show that the largest amounts of atomic carbon and wax were present in Runs 1 and 5 (as indicated by the areas of Peak 1), yet the deactivation rate of Run 5 is the greatest and Run 1 is the least of all the FB catalyst tests (Figure 5.3). Moreover, following Run 2, the FB test with the second highest deactivation rate (Figure 5.3), the catalyst was found to contain the least amount of atomic carbon and wax (see Peak 1 in Figure 5.12a). BET data for wax-extracted, spent catalyst samples (Table 5.33) are consistent with the Peak 1 areas for TPH in that the lowest pore volumes, i.e., the largest amounts of hard wax, were found in Runs 1 and 5, while the highest pore volume (smallest quantity of hard wax) was found in Run 2. Thus, it is evident that the quantity of residual, hard wax does not correlate with deactivation rate in these runs. In other words, these results indicate that residual hard wax does not lower activity by physically blocking pores at least for our catalysts. This result contradicts those of previous studies [49, 122, 123] where wax was observed to clog catalyst pores. Our observation can be explained by the exceptionally high mesopore volume (1.06 cm^3/g following calcination at 1100°C [85]) of the silica-doped alumina support used for our catalysts thus preventing complete blockage by wax of the large catalyst pores. Indeed, the pore volume of our freshly reduced catalyst is 0.649 cm^3/g, nearly twice the pore volume of the Co/Al_2O_3 catalyst (0.35 cm^3/g) used by Peña et al [49, 125]. Moreover, after 700-900 h TOS, pore volumes of wax-extracted catalyst samples test in Runs 1 and 5 of 0.487 cm^3/g and 0.499 cm^3/g respectively (Table 5.3), are substantial, even though these two catalysts contain the largest quantities of residual, hard wax of the five catalyst samples tested at 230°C (Figure 5.12b). The pore volumes of the wax-extracted catalyst samples (0.48 to 0.52 cm^3/g) are a factor of two larger than those of other studies (0.23-0.31 cm^3/g) [49, 125]. Therefore, the pore volumes of the wax-extracted spent catalyst samples of this study are apparently above the threshold at which wax blocks catalyst pores, and contributes to deactivation.

Recently, it has been proposed that polymeric carbon causes long-term deactivation for cobalt FT catalysts [48, 49]. Our results also show a positive correlation between average deactivation rate ($-\Delta \boldsymbol{a}/\Delta t$) and the quantity of polymeric carbon on the catalyst determined by TPH (Peak 3) after 30 days (800 h) (Figure 5.14a) and between CO uptake decrease and polymeric carbon (Figure 5.14b), in both cases for the same catalyst treated at five different sets of H_2 and CO partial pressures at 230°C and four different sets of temperatures and partial pressures. Based on our experimental results showing a gradual drop in activity with time (Figure 5.3), it appears that polymeric carbon gradually forms during reaction, is stable at FTS conditions, and based on the loss of CO-uptake after 30 days, occupies cobalt metal sites, thereby decreases activity, the extent of which varies with reaction conditions (P_{H2}, P_{CO}, T). Given that (1) CO-uptake measurements were evaluated after regenerating the catalyst at 350°C, which removed atomic carbon, oligomeric carbon, and most of the wax (Peaks 1 and 2) thus leaving only polymeric carbon and (2) the original CO uptake was completely recovered after partially regenerating in H_2 the freshly-reduced, wax-extracted catalyst at 350°C, it follows that the decrease in CO-uptake for spent catalysts was only due to site-poisoning by polymeric carbon. It should be emphasized that catalyst dispersion would not have changed during H_2 regeneration at 350°C, since the catalyst was originally bulk reduced at 450°C.

5.4.3 Effects of P_{H2}, P_{CO} and H_2/CO Ratio on Deactivation

Based on the quantitative measurement of different carbon species on the spent catalysts as a function of H_2 and CO partial pressures, the effective monolayers of atomic, oligomeric, and polymeric carbon (or polymeric hydrocarbons) after 800 h TOS are calculated as shown in Table 5.7. Assuming that the amount of residual wax was similar for all five wax-extracted spent catalyst samples, the amount of wax found from TPH of the freshly reduced wax-extracted catalyst was subtracted from those of the wax-extracted spent catalyst samples to find the amounts of atomic and oligomeric carbons present in Peaks 1 and 2, respectively; these corrected quantities for Peaks 1 and 2 and the quantity of polymeric carbon (Peak 3) were further normalized to the total number of Co sites from H_2 chemisorption. The calculated data indicate that roughly a monolayer of atomic carbon is formed on the Co surface in Runs 1 and 5 involving a H_2/CO ratio of one at 230°C, while only a 0.19 to 0.34 of a monolayer of atomic carbon is formed at higher H_2/CO ratios at 230°C. Moreover, there are trends of decreasing atomic and oligomeric carbons with increasing H_2/CO ratio. Except for Runs 2, 3, 6 and 8, several monolayers of oligomeric carbon form while 1.5-4.7 monolayers of polymeric carbons (or condensed hydrocarbons) form on all nine samples. It should be noted that higher combined partial pressures of H_2 and CO at a total pressure of 20 bar (balance is He) and 230°C favor the formation of polymeric carbon.

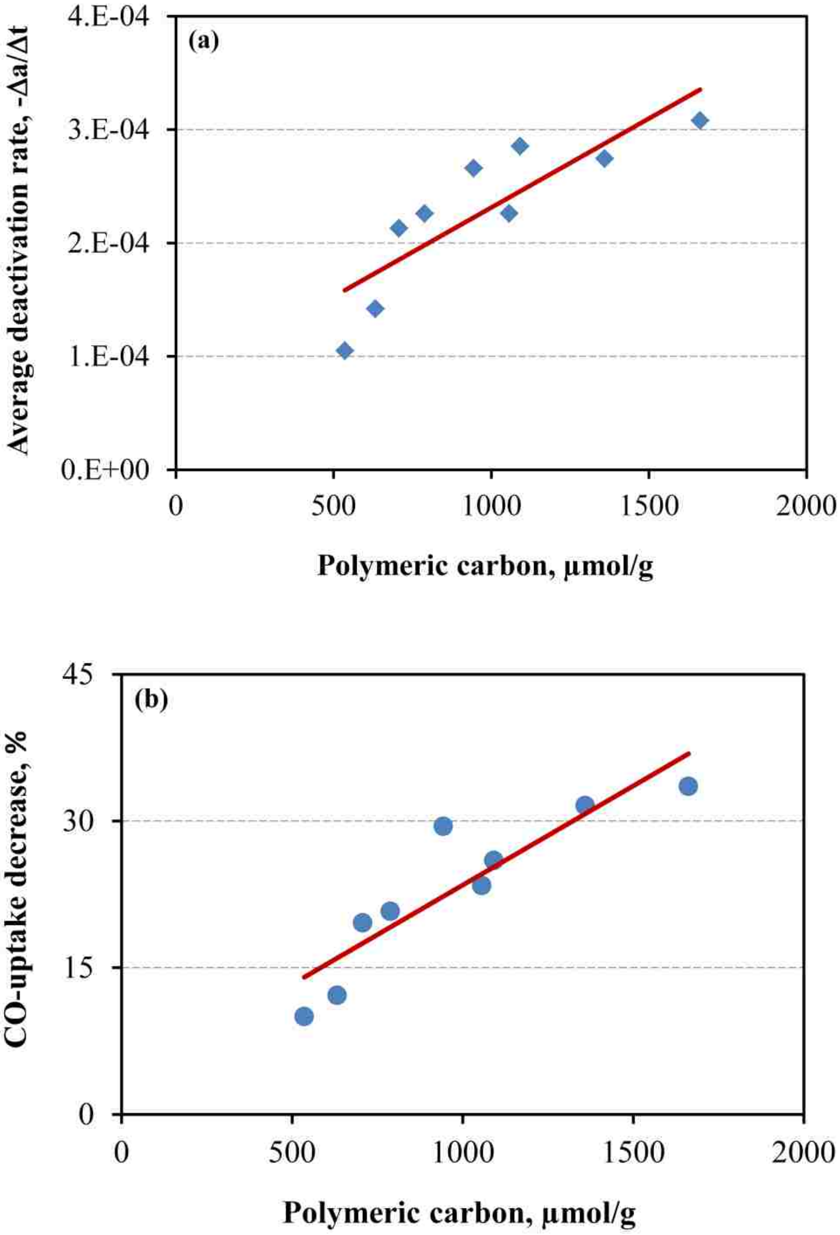

Figure 5.14. (a) Average deactivation rate and (b) CO-uptake decrease from the value of CO-uptake for wax-extracted freshly-reduced sample (Table 5.6) as a function of polymeric carbon on FB wax extracted catalyst samples (Runs 1-9).

Table 5.7. Monolayer carbon equivalents of TPH peak areas following FT synthesis for 800 h at 230-250°C and 20 bar.

Catalyst (T - P_{H2}/P_{CO})	Peak 1[a]	Peak 2[a]	Peak 3[b]
Run1 (230°C - 5/5)	0.87	1.9	1.5
Run 2 (230°C - 15/5)	0.19	0.25	2.7
Run 3 (230°C - 10/5)	0.29	0.90	1.8
Run 4 (230°C - 10/7.3)	0.34	1.2	2.3
Run 5 (230°C - 10/10)	1.1	4.5	4.7
Run 6 (240°C - 10/5)	0.43	0.64	2.0
Run 7 (250°C - 10/5)	1.2	1.2	3.1
Run 8 (240°C - 5/5)	0.71	0.64	3.0
Run 9 (250°C - 10/10)	1.3	3.0	4.2

[a] Peaks 1 and 2 of TPH profiles consist of atomic and oligomeric carbons in addition to wax, respectively.

[a,b] Carbon monolayers were found by subtracting the amount of wax found from TPH profile for freshly-reduced wax-extracted catalyst from those of the spent catalysts divided by total number of cobalt sites found from H_2-uptake. The amount of residual wax was assumed to be the same for all the wax-extracted spent catalyst samples.

While other groups [31, 49, 124-126] studied the effects of H_2/CO ratio at a constant total pressure without diluent, our results show that effects of partial pressures of H_2 and CO must be evaluated separately. Moreover our results show that increasing P_{CO} at constant P_{H2} (decreasing H_2/CO ratio), increases deactivation rate, while increasing P_{H2} at constant P_{CO} (increasing H_2/CO ratio) also increases deactivation rate. It follows logically that increasing total pressure in the absence of a diluent increases deactivation rate via the formation of polymeric carbon species. Our observation is consistent with that of Sadeqzadeh et al. [31] who found that higher total syngas pressure increases the deactivation rate for cobalt FT catalysts, although they did not attribute it to a specific cause.

It is important to address possible reasons for higher rates of polymeric carbon or condensed hydrocarbon formation causing higher rates of deactivation at high partial pressures of hydrogen. We hypothesize that higher partial pressures of CO result in higher carbon coverage which facilitates C-C coupling to form carbon oligomers which further couple to hydrogen-poor polymeric chains, rings, and layers. It is reported that at higher partial pressures of hydrogen carbons deposited on iron catalysts are gasified, thereby reducing the extent of carbon-induced deactivation [132]. Logically, one might suppose that increasing H_2 partial pressure would decrease the extent of deactivation by carbon on Co catalysts. However, we observe that during FTS at 230°C higher rates of polymeric carbon formation occur at <u>higher</u> partial pressures of hydrogen, consequently causing faster deactivation (see Figure 5.3). Our observation is in agreement with Peña et al. [49] who previously reported that at the same flowrate (but different conversions, most notably at higher conversion) formation of polymeric carbon and thus deactivation rate <u>increases</u> with increasing H_2/CO ratio. However, it should be noted that in their study, catalyst deactivation probably occurred by more than one mechanism, especially in experiments at high conversion and thus high P_{H2O}, which, the same group indicated in a separate paper, can facilitate deactivation through “water-assisted sintering” [31]. Recently, Weststrate et al. [40, 43] proposed that polymeric carbon can be formed on cobalt catalysts via cyclo-polymerization reactions with C_2H_x species as intermediates. Thus, higher H_2 partial pressures can possibly increase the probability for the formation of C_2H_x species and consequently aromatic structures and/or hydrogenated polymeric carbons. Aromatic ring formation is expected to be an irreversible process, resulting in carbon build-up under FTS conditions.

5.4.4 Effect of temperature on deactivation

Formation of polymeric carbon was also evaluated at different temperatures using $H_2/CO = 2$ as a baseline condition. As temperature increases from 230 to 250°C, the amount of polymeric carbon or hydrogenated polymeric carbon increases from 1.8 to 3.1 monolayers (Table 5.7); consequently, the rate of deactivation increases. This observation is consistent with Moodley et al. [4] who found that polymeric carbon and deactivation rate increased with temperature (240-270°C) at $H_2/CO = 1.7$ and P = 20 bar. Sadeqzedah et al. [127] also found increasing temperature increases deactivation rate. However, this trend does not exist when comparing Runs 5 and 9, where the deactivation rate at 250°C (Run 9) is less then at 230°C (Run 5). Recent density functional theory calculations on fcc-Co (111) show that a carbon coverage of 50% will reconstruct the surface to fcc-Co(100) followed by a clock type reconstruction [58]. On the other hand, surface reconstruction is a dynamic process which results in simultaneous roughening of the surface to produce active edge and B5 sites with an attendant increase in surface energy, and also formation of less active planar sites, thereby lowering the surface energy [35, 58-60]. As is apparent in Table 5.7, the atomic carbon monolayer is increasing as temperature increases from 230 to 250°C. Therefore, it can be hypothesized that cobalt structure tends to become more stable at higher temperatures and high CO partial pressures, resulting in lower deactivation rate. This observation is consistent with Ma et al. [128], who also found higher deactivation at lower temperatures for 25 wt% $Co/Ru/Al_2O_3$ catalyst at 2.5 MPa, H_2/CO:2.1, and attributed this phenomenon to changes in Co structure.

5.5 Conclusions

Twelve samples of a 25 wt% Co/ 0.25 wt% Pt/Al_2O_3 (Al_2O_3 is doped with 5 mol% SiO_2 as a stabilizer) were tested over a period of 800 hours and $X_{CO} < 24\%$, each at a different sets of CO and H_2 partial pressures and temperature (220-250°C). This study provides, for the first time, new data defining quantitatively the long-term deactivation by carbon deposition for cobalt FT catalysts in the absence of the other deactivation mechanisms. Sintering, oxidation, cobalt-support formation, and physically plugging of pores by heavy waxy hydrocarbons were eliminated through design of a catalyst with relatively large Co crystallites (~12 nm), a very stable and large pore support ($V_p = 1.06$ cm^3/g), and by operating at low conversions ($X_{CO} <$ 24%) and thus low partial pressures of H_2O.

1- Deactivation may be caused by either polymeric carbons or condensed hydrocarbons. Thus, at a reaction temperature of 230°C, deactivation rate increases with (a) increasing P_{CO} at constant P_{H2} (decreasing H_2/CO ratio) due to formation of a hydrogen-poor, polymeric carbons (graphitic-like) or (b) increasing P_{H2} at constant P_{CO} (increasing H_2/CO ratio) due to formation of hydrogen-rich, condensed polymeric hydrocarbons.

2- At low CO partial pressure ($P_{CO} = 5$ bar; $H_2/CO = 2$ and 1), deactivation rate increases with increasing temperature; however, at high partial pressure of CO ($P_{CO} = 10$ bar) and H_2/CO of 1, deactivation rate increases as temperature decreases.

3- There is a positive correlation between average deactivation rate ($-\Delta \boldsymbol{a}/\Delta t$) and the quantity of polymeric carbon deposited on the catalyst after 800 h.

4- There is a correlation between average deactivation rate and the fraction of Co sites lost during 800 h runs.

5- At high partial pressures of CO (> 7.5 bar) regardless of operating temperature, methane selectivity increases as the catalyst deactivates; however, methane selectivity was constant over 800 h at low CO partial pressure (P_{CO} = 5 bar).

Chapter 6 Reaction and Deactivation Kinetics for Cobalt FTS

This chapter reports results of the comprehensive study of the kinetics of both the main reaction and deactivation reaction for the cobalt FT catalyst and describes the development of a macrokinetic model based on a proposed mechanism for main reaction and general power-law expressions (GPLE's) for deactivation.

6.1 Introduction

As discussed fully in Chapter 5, a number of recent papers [49, 124-127] have addressed the effect of H_2/CO ratio and temperature for the deactivation by carbon of cobalt FT catalysts. There is not much agreement regarding effects of H_2/CO on the deactivation of cobalt catalysts. Contrary to conventional wisdom that higher H_2/CO ratio would more likely result in removing the carbon from the surface by hydrogenation [121], other researchers [31, 124-127] reported faster deactivation by sintering, cobalt aluminate formation and also carbon deposition at higher H_2/CO ratios. Part of this discrepancy is due to the fact that there has been no single systematic study to investigate the effect of the partial pressures of H_2 and CO separately, since previous studies have varied the partial pressures together rather than separately.

These same kinds of contradictions have also been observed for effects of temperature on the deactivation of Co by carbon. While increasing temperature has been reported to increase the rate of deactivation [4, 127], Ma et al. [127] have reported a slower deactivation rate at 220°C than 205°C for 25 wt.% Co/Ru/Al_2O_3 catalyst hypothesizing that a more stable catalytic structure was created at higher temperatures.

Among the previous papers addressing the deactivation kinetics for Co FT catalyst [31, 32, 49, 54, 124-127, 133], deactivation rates in several [54, 126, 133] were fit to unrealistic simple power-law expressions (SPLE's), which predict a zero value for activity at long times on stream (TOS), while it has been reported that Co activity typically trends to a limiting value during FTS [116]. Argyle et al. [116] address this issue in their paper. The authors observe that SPLE models' fit deactivation data for sintering and carbon deposition poorly, yielding unrealistic deactivation orders of 4-15, while first or second order general power-law expressions (GPLE's), which include a non-zero value of limiting activity, fit most data very well, consistent with physically meaningful systems. In their study [116] activity-time data from several previous studies involving different deactivation mechanisms were fitted to 1st and 2nd order GPLE expressions. It was found that activity-time data involving simultaneous mechanisms could be modeled; for example, a combination of 1st and 2nd order GPLE models for carbon deposition and sintering, respectively, provides a very precise fit of activity-time data.

Recently, Sadeqzadeh et al. [127] developed a semi-empirical/mechanistic model to represent the activity-time data (deactivation by carbon) at different temperatures and syngas ratios. It was assumed that atomic carbon formed from CO dissociation is the principal cause of deactivation. Their model assumes that the decrease in available active sites for FT reaction with time is a function only of CO partial pressure. The main reaction rate expression was multiplied by available site coverage to incorporate the activity changes with time. However, several limitations of this model are evident: (1) atomic carbon, a precursor to chain growth of hydrocarbons, is a relatively short-lived active center; the presence of which doesn't contribute to deactivation, and (2) activity-time data were collected only up to 100 h TOS, and thus cannot be used predicting long-term deactivation by carbon observed to occur over hundreds of hours.

It is apparent from a careful review of the literature that no previous comprehensive study has been conducted of the quantitative effects of H_2 and CO partial pressures and of temperature on deactivation kinetics by inactive carbons of Co FTS catalysts. One of the principal objectives of this dissertation study was to conduct such an experimental study of these effects coupled with development of model to fit the resulting data. In this chapter activity-time data are reported for a $CoPt/Al_2O_3$ catalyst during reaction and simultaneous carbon deposition as a function of P_{H2}, P_{CO}, and temperature. Eight deactivation runs at FT conditions (220-250°C and 20 bar) for a 25 wt% Co/ 0.25 wt% Pt/Al_2O_3 catalyst were carried out in a FB reactor over 800-900 h at different partial pressures of H_2 and CO and H_2/CO ratio as presented in Chapter 5. It is demonstrated that these seven experimental deactivation data sets can be statistically well fit by first or second order GPLE models. Since the deactivation mechanism and models are coupled with those of the main reaction, a separate kinetic study of the main reaction in the absence of deactivation was also performed at T = 210-240°C, H_2/CO = 1.5-3, and P = 20 bar.

6.2 Methodology

6.2.1 Kinetic and deactivation experimental designs and collection of data

Reaction kinetic experiments were carried out for 25 wt% Co/ 0.25 wt% Pt/Al_2O_3 using a fractional factorial design with four levels of temperature (210, 220, 230, 240°C) and three levels of P_{H2} (6, 8, 12 bar) and P_{CO} (2.7, 4, 6 bar) as shown in Figure 6.1 to study the effect of each factor on response values and provide a sufficiently wide range of experimental data needed for developing a representative rate expression with concentration and temperature dependencies. To minimize catalyst pore resistance, catalyst particles with a diameter of 63-88 µm (170-230 mesh size) were used. The baseline conditions were repeated to assess if catalyst deactivation had occurred during the experimental runs. No deactivation was observed over the 450 h period in which data were taken.

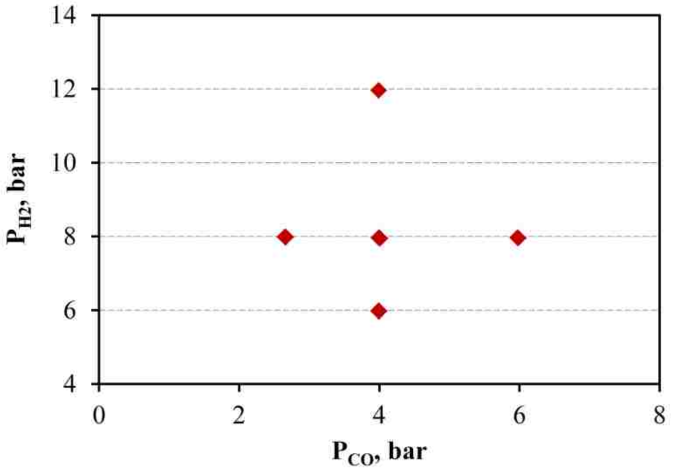

Figure 6.1. Domain of H_2 and CO partial pressures for reaction kinetic experiments in the absence of deactivation.

To determine deactivation rates, eight samples of the cobalt catalyst were tested over a period of 800-900 h, each at a different set of CO and H_2 partial pressures and temperature (in the range of 220-250°C) while flowrate was held constant (see Table 6.1). Each catalyst sample was activated at the desired deactivation temperature (furnace temperature was ramped slowly to get to the deactivation temperature), 20 bar, $H_2/CO = 2$, and X_{CO} of 50% for 70 h. At 70 h TOS P_{H2}, P_{CO} and total flowrate were adjusted to reach desired partial pressures and about 20% conversion reaching steady-state within 100 h. Starting at 100 h, activity-time data were obtained.

Table 6.1. Process conditions (feed H_2 and CO partial pressures and reaction temperature) for seven deactivation experiments at 20 bar.

Run	Temp., °C	P_{H2}, bar	P_{CO}, bar	H_2/CO
1	230	5	5	1
2	230	15	5	3
3	230	10	5	2
4	230	10	7.3	1.4
5	230	10	10	1
6	240	10	5	2
7	250	10	5	2
10	220	10	5	2

6.2.2 Reaction and deactivation kinetics

The FTS reaction and deactivation kinetics can be linked by the activity of the catalyst. Activity (a) is a primary function of time, and a secondary function of temperature and concentrations and is defined as the CO rate normalized by the initial rate.

$$\boldsymbol{a} = \frac{-r_{CO}}{(-r_{CO})_{t=0}} = \frac{-r_m}{(-r_m)_{t=0}} \tag{6.1}$$

The rate of the main reaction (r_m) and deactivation rate (r_d) are defined as follows:

$$-\mathrm{r}_m = k(\mathrm{T})f_1(\mathrm{T,C})\mathbf{a} \tag{6.2}$$

$$\mathrm{r}_d = -\mathrm{d}\mathbf{a} \,/\, \mathrm{dt} = k_d\, f_2(\mathrm{T,C})\, \mathbf{a}^d \tag{6.3}$$

where k(T) is the rate constant, f_1(T, C) and f_2(T, C) are functions of reactant and product concentrations and temperature for the main reaction and deactivation, respectively, subscript ‘d’ stands for deactivation and superscript ‘d’ is the order of deactivation.

A generalized power-law equation (GPLE) was proposed by Fuentes [115] which results in more reasonable reaction orders, e.g. first or second order, compared to simple power law expressions in which the a_∞ term is omitted. This deactivation rate equation is in the form of

$$-\mathrm{d}\mathbf{a} \,/\, \mathrm{dt} \;=\; k_d\, f(\mathrm{C})\, (\boldsymbol{a} - \boldsymbol{a}_\infty)^d \tag{6.4}$$

where a_∞ is the activity at infinite reaction time. Intrinsic kinetics are coupled with the deactivation kinetics; therefore, the catalyst must be studied under conditions of deactivation as well as without deactivation to determine the kinetic parameters in each equation.

Since the CO conversion for reaction kinetics and deactivation kinetic runs was kept at less than 24%, differential conditions could be assumed (as a special case for FTS) and the CSTR performance equation was used to predict the CO rate.

$$\frac{W}{F_{CO}{}^{0}} = \frac{X_{CO}}{-r_m} \tag{6.5}$$

Since the partial pressures of CO and H_2 are changing as the catalyst deactivates, Equations 6.4 and 6.5 should be solved simultaneously.

In reaction rate modeling, estimates of pre-exponential factor (A_0) and the activation energy (E) for a rate constant *k* are known to be highly statistically correlated.

$$k = A_0 \exp\left({}^{-E}\!/_{RT}\right) \tag{6.6}$$

This correlation means that (1) estimate of A_0 can vary over a wide range for a given E (and vice-versa) and (2) such data may not be reliable enough to be used in mechanistic interpretations or reactor design, especially when extrapolation beyond measured temperatures is needed. A reduction in correlation between A_0 and E of Equation 6.6 is proposed by Box [118] which can be achieved by reparameterization as follows:

$$k = k^* \exp\left(\frac{-E}{R}\left(\frac{1}{T} - \frac{1}{T_{ave}}\right)\right) \tag{6.7}$$

where

$$k^* = A_0 \exp\left({}^{-E}/_{RT_{ave}}\right) \tag{6.8}$$

and T_{ave} is a reference temperature, usually the mean temperature. This reparameterization was used for estimating the kinetic parameters of the main reaction.

6.2.3 Statistical analysis

Once the kinetic data in the absence of deactivation were obtained, the nlsLM function in the R package minpack.lm was used to fit the kinetic models to the data [132]. The nlsLM function uses a modified Levenberg-Marquardt fitting algorithm. To check how well each model fit the data, a lack-of-fit (L.o.F) test was performed by comparing the variability between the raw data and the model predictions to the variability in raw data obtained at the same conditions. An insignificant lack-of-fit test indicates that predictions from the model at a certain set of conditions will be as accurate as performing additional experiments at those conditions. Models with lack-of-fit P-values greater than 0.10, are assumed to be significant and cannot be ruled out based on statistics. While macrokinetics and statistics cannot be used to prove that a model represents the only reaction pathway that FTS takes, they can tell us if it is a plausible kinetic pathway.

6.3 Results and discussion

6.3.1 Kinetics of main reaction in the absence of deactivation

Rate data obtained for the CoPt/Al_2O_3 catalyst at 20 bar over a range of temperatures (210-240°C) and H_2/CO ratios (1.3-3) are listed in Table D.1 (Appendix D) and plotted as a function of partial pressures of hydrogen and CO in Figure 6.2. Rate data from reaction at different feed concentrations and temperatures were regressed using the power-law expression in Equation 6.9 to give exponents listed in Table 6.2.

$$r_m = k(P_{H2})^x(P_{CO})^y \tag{6.9}$$

Activity of the catalyst increases with increasing P_{H2} and the H_2 order becomes more positive at higher temperatures (Table 6.2 and Figure 6.2); H_2 order (proportional to the slope of rate vs P_{H2}) ranges from 0.56 to 0.77. At low temperatures (210-220°C) CO consumption rate increases with increasing CO partial pressure (positive CO order), while the rate decreases with increasing P_{CO} (negative CO order) at high temperatures (230-240°C). As shown in Table 6.2, CO order changes from a positive value of 0.31 at 210°C to a negative value of -0.64 at 240°C. CO has a strong inhibition influence over cobalt catalysts to the extent that it has a significantly negative reaction order under commercially relevant reaction conditions [117].

The average H_2 and CO orders of 0.69 and -0.53 and activation energy of 129 kJ/mol were obtained using all the rate data in the temperature range of 210-240°C regressed to the power-law expression of Equation 6.9 and using Equation 6.7 for the temperature dependence and minimizing squared errors.

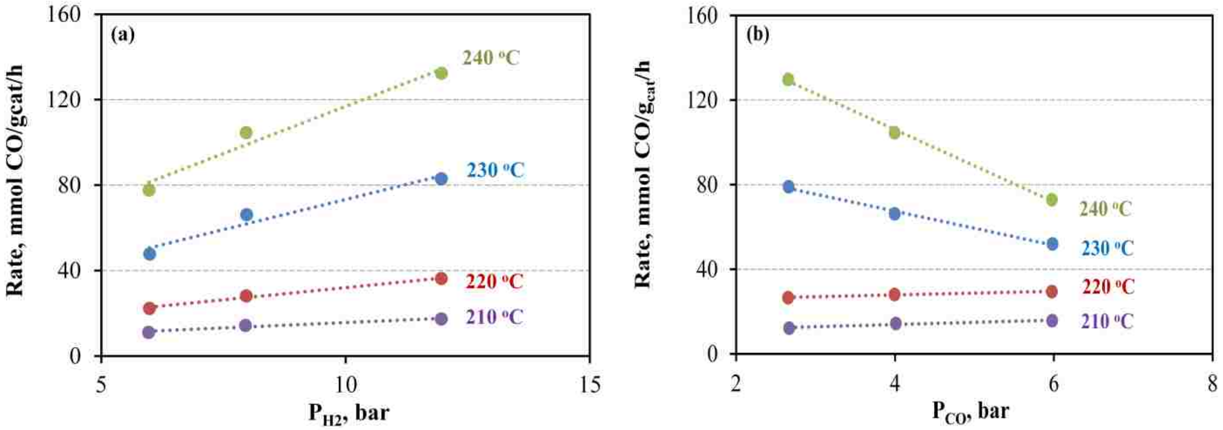

Figure 6.2. Effects of (a) P_{H2} at constant P_{CO} (4 bar) and (b) P_{CO} at constant P_{H2} (8 bar) on rate (mmol (CO)/g_{cat}/h) at different temperatures for 25 wt% CoPt/Al_2O_3 catalyst. The rates are adjusted to the desired temperature with activation energy of 129 kJ/mol found from power-law fit as shown in Table 6.2.

Table 6.2. Rate constants, pre-exponential factor, activation energy and reaction orders of H_2 and CO for CoPt/Al_2O_3 at P_{CO}^0 = 2.7-6 bar, P_{H2}^0 = 6-12 bar and X_{CO} < 24%.

Temp., °C	*k* [a], mmol/g/h/bar$^{(x+y)}$	A[b] mmol/g/h/bar$^{0.16}$	E_{act}, kJ/mol	H_2 order (x)	CO order (y)
210	2.85	--	--	0.56	0.31
220	5.94	--	--	0.66	0.12
230	29.9	--	--	0.70	-0.51
240	48.8	--	--	0.77	-0.64
210-240	--	6E14 ± 1E14	129 ± 6	0.69 ± 0.008	-0.53 ± 0.008

[a] rate constant unit is mmol/g/h/bar^{x+y}, where x and y are the H_2 and CO reaction orders, respectively.[b] pre-exponential factor was estimated for the temperature range of 210-240°C. Rate data were adjusted to the desired temperature with activation energy of 129 kJ/mol found from power-law fit.

Rate data are also plotted in Arrhenius form in Figure 6.3 for different feed gas concentrations and activation energies of 107-169 kJ/mol are predicted. Interestingly, the reaction is more temperature dependent (higher activation energy) as CO partial pressure is decreased (constant P_{H2}) but activation energy does not change as hydrogen partial pressure is decreased (constant P_{CO}).

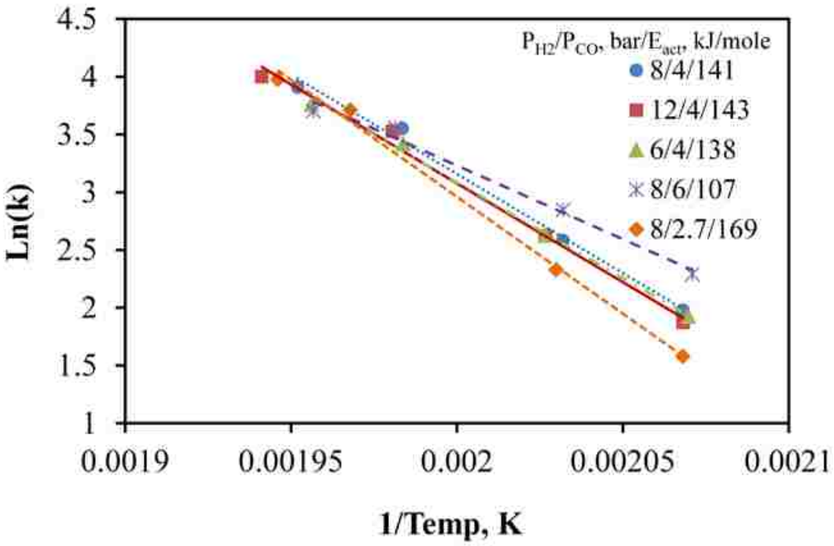

Figure 6.3. Apparent activation energies for CoPt/Al_2O_3 at 20 bar and different feed gas concentrations.

Changes in both H_2 and CO orders with temperature and activation energy with feed concentration argue for use of a shifting-order rate expression such as Langmuir-Hinshelwood (LH) type. The other advantage of LH model is that it can be applied more reliably for extrapolation of rate to different temperatures and feed concentrations.

A sequence of elementary steps for the FT reaction on a cobalt catalyst is proposed in Figure 6.4, in which CO dissociates via parallel H-assisted and unassisted routes (Carbide mechanism). The direct CO dissociation (step 3) forms C* and O* from CO*, while subsequent reactions with H* yield the CH_2* monomers (steps 4, 10). The O* atoms formed in step 3 are removed as H_2O via stepwise reactions with H*.

In the parallel H-assisted CO activation route (step 5, Figure 6.4), CO^* forms formyl intermediates (HCO*) via reactions with H* or atomic carbon and OH* (step 5'). For cobalt catalysts, the activation barrier for H* addition to the C-atom in CO* (to form HCO*) is predicted from the UBI-QEP, a bond order-binding energy model, to be smaller than for unassisted CO* dissociation (101 vs. 153 kJ/mol, respectively) [134]. HCO* can dissociate to CH* and OH* with further reaction with H* or subsequent hydrogenation at the O* atom in HCO* species can also happen to form hydroxymethylene (HCOH*) intermediates with even much lower activation barrier of 51.9 kJ/mol [134]. HCOH* dissociation then leads to CH* species that ultimately form monomers and initiators required for chain growth (step 10). OH* groups formed in step 8 are removed as H_2O.

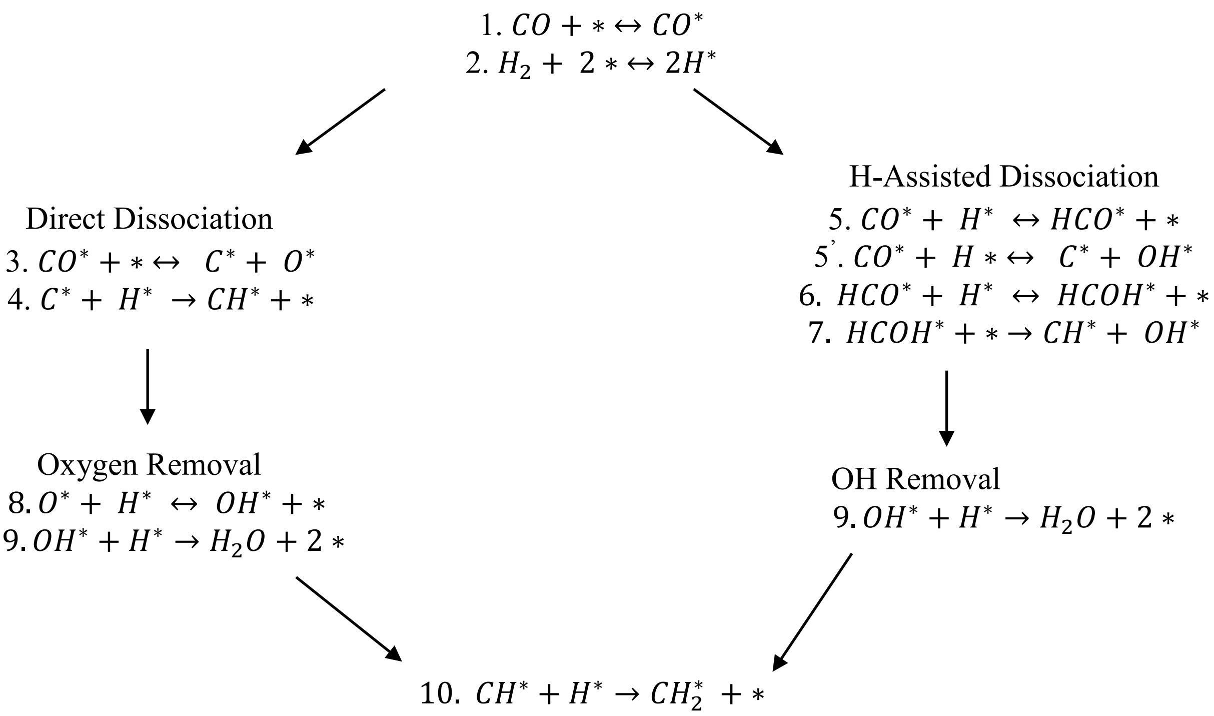

1. $CO + * \leftrightarrow CO^*$
2. $H_2 + 2* \leftrightarrow 2H^*$

Direct Dissociation
3. $CO^* + * \leftrightarrow C^* + O^*$
4. $C^* + H^* \rightarrow CH^* + *$

H-Assisted Dissociation
5. $CO^* + H^* \leftrightarrow HCO^* + *$
5'. $CO^* + H* \leftrightarrow C^* + OH^*$
6. $HCO^* + H^* \leftrightarrow HCOH^* + *$
7. $HCOH^* + * \rightarrow CH^* + OH^*$

Oxygen Removal
8. $O^* + H^* \leftrightarrow OH^* + *$
9. $OH^* + H^* \rightarrow H_2O + 2*$

OH Removal
9. $OH^* + H^* \rightarrow H_2O + 2*$

10. $CH^* + H^* \rightarrow CH_2^* + *$

Figure 6.4. Proposed elementary steps for FTS on Co catalysts.

The LH models considered in this study have been organized into two model classes: (1) direct CO dissociation (Carbide mechanisms) and (2) hydrogen assisted dissociation and are presented in Table 6.3 with their corresponding assumptions made to derive the rate expression.

Reaction 5' was also included in derivation of Model 8 (derivation of Model 8 is shown in Appendix E). Each rate expression was derived with various assumptions for rate-determining step and most abundant surface intermediates (MASI), and these are indicated in Table 6.6.

Kinetic parameters obtained by least square fits of rate data to each model and their corresponding P-values for two-parameter and three-parameter models are reported in Tables 6.4 and 6.5, respectively. Power-law model parameters are also shown in Table 6.5 for comparison. As mentioned in section 6.2.3 the criteria for discriminating between the models is selected to be a P-value of above 0.1. The power-law predicts the data more reliably than LH models 2 and 6 since its P-value of 0.065 is larger than 0.030. Among the two-parameter models, it seems that model 5 with a P-value of 0.34 provides the best fit. However, the estimated heat of CO adsorption (the denominator term, $K'P_{CO}$) was found to be a positive value of 148 kJ/mol instead of a negative value. Therefore, it is not consistent with physical reality, i.e. the proposed mechanism using the CO adsorption elementary step (step 1 in Figure 6.4) to get the $K'P_{CO}$ term. This is also true for models 1 and 3 predicting a positive value for heats of CO adsorption. Therefore, the only two-parameter model for which its predicted kinetic parameters are consistent with theory and has a P-value of above 0.1 is model 4, which will be used to represent the main reaction rate expression for the deactivation study.

Table 6.3. Different rate expressions and their corresponding assumptions.

Model	Rate expression	CO dissociation	RLS[a]	MASI[b]
1	$\frac{kP_{H2}P_{CO}}{(1+K'P_{CO})^2}$	H-assisted	7	CO^*
2	$\frac{kP_{H2}P_{CO}}{\left(1+k'P_{CO}{P_{H2}}^{0.5}\right)^2}$	H-assisted	7	HCO^*
3	$\frac{kP_{H2}{P_{CO}}^{0.5}}{(1+K'P_{CO})^2}$	H-assisted	10	CO^*
4	$\frac{kP_{H2}{P_{CO}}^{0.5}}{\left(1+k'P_{CO}{P_{H2}}^{0.5}\right)^2}$	H-assisted	10	HCO^*
5	$\frac{k{P_{H2}}^{0.75}{P_{CO}}^{0.5}}{(1+K'P_{CO})^2}$	Direct	4 and 9	CO^*
6	$\frac{k{P_{H2}}^{0.75}{P_{CO}}^{0.5}}{\left(1+k'{P_{CO}}^{0.5}{P_{H2}}^{0.25}\right)^2}$	Direct	4 and 9	C^*
7	$k(P_{H2})^x(P_{CO})^y$	Not based on theory		
8[c]	$\frac{kP_{H2}{P_{CO}}^{0.5}}{\left(1+k'P_{CO}+K''{P_{H2}}^{0.5}\right)^2}$	H-assisted[d]	10	CO^*, H^* and C^*
9	$\frac{k{P_{H2}}^{0.75}{P_{CO}}^{0.5}}{\left(1+K'P_{CO}+k'{P_{CO}}^{0.5}{P_{H2}}^{0.25}\right)^2}$	Direct	4 and 9	CO^* and C^*

[a] RLS = Rate Limiting Step
[b] MASI = Most Abundant Surface Intermediate
[c] Details of derivation is shown in Appendix E.
[d] Reaction # 5' is also included in derivation of Model 8.

Models 1, 3, and 5, at high reaction temperature, would predict that $K'P_{CO}$ (equilibrium constant, K' for CO adsorption) decreases to much smaller than 1 and the denominator term can therefore be ignored, yielding an overall CO reaction order of 1 for model 1 and 0.5 for models 3 and 5. However, as was shown by the data (Table 6.2), CO order becomes more negative as the temperature increases; thus, suggesting a rate constant for P_{CO} (rather than heats of adsorption) in the denominator to yield an overall negative CO order at high temperatures. On the other hand, the reaction order for H_2 increases at higher temperatures suggesting a heat of adsorption term for H_2 in the denominator, which can be negligible at higher temperatures and results in more positive overall H_2 order. By considering these effects, the three-parameter model 8 (see Table 6.5) with rate expression involving a P_{CO} term with rate constant and heat of adsorption for P_{H2} resulted in a rate expression with by far the best P-value of 0.48. Adding another term in the denominator of model 5 by assuming two MASIs' as presented in model 9 only slightly increases the P-value to 0.37 from 0.34; however, as mentioned earlier this model is not consistent with theory as it was found a positive value for heat of CO adsorption.

Table 6.4. Estimated kinetic parameters for two-parameter models.

Model	A^a, mmol/g/h/bar^{x+y}	E, kJ/mol	A'^a, mmol/g/h/bar^{x+y}	$E'(\Delta H)$, kJ/mol	P-value
1	8.1E41 ± 2E41	389 ± 40	4.7E18 ± 1E18	181 ± 23	0.076
2	3.7E26 ± 1E26	244 ± 48	1.9E8 ± 6E6	87 ± 39	0.03
3	6.8E30 ± 1E30	286 ± 19	1.9E17 ± 4E16	173 ± 19	0.09
4	7.1E23 ± 1E23	219 ± 19	5E9 ± 1E8	105 ± 25	0.10
5	2.4E28 ± 2E27	260 ± 11	5.4E14 ±1E8	148 ± 12	0.34
6	4.8E37 ± 5.5E37	339 ± 103	1.4E13 ± 9.9E12	124 ± 55	0.03

[a] pre-exponential unit is mmol/g/h/bar^{x+y}, where x and y are the H_2 and CO reaction orders, respectively.

Table 6.5. Estimated kinetic parameters for three-parameter models.

Model	A[a]	E, kJ/mol	A'[a] or x[b],	$E'(\Delta H)$ or y[b] kJ/mol	A''[a]	E'' (ΔH), kJ/mol	P-value
7	6E14 ± 1E14	129 ± 6	0.69 ± 0.008	-0.53 ± 0.008	--	--	0.065
8	1.8E26 ± 1.4E26	234 ± 126	9.2E13 ± 3.8E12	137 ± 67	6.8E-3 ± 3.7E-3	-18.6 ± 14	0.48
9	4.1E26 ± 1.3E26	242 ± 51	2.9E14 ± 5.7E13	146 ± 31	7.4E-3 ± 7.5E-3	-9.3 ± 139	0.37

[a] pre-exponential unit is mmol/g/h/bar^{x+y}, where x and y are the H_2 and CO reaction orders, respectively.
[b] x and y are the H_2 and CO reaction orders, respectively used in Equation 6.9 (power-law model).

The parity plots of the preferred kinetic models with two-parameters (model 4) and three-parameters (model 8) are shown in Figure 6.5. As discussed earlier the three-parameter model with equilibrium constant for hydrogen and rate constant for CO in denominator clearly predicts the data very well with r^2 of 0.994.

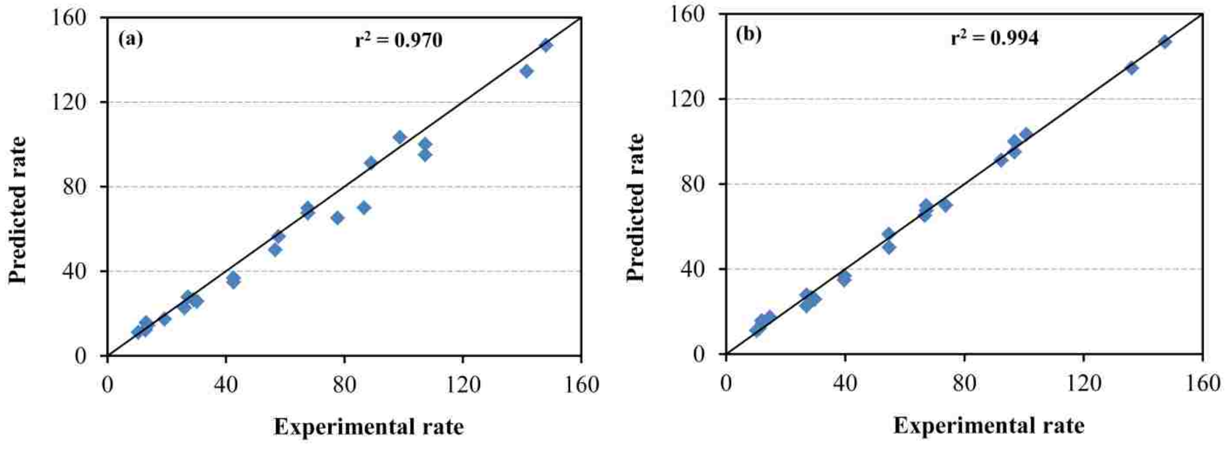

Figure 6.5. Parity plot of best kinetic models for (a) two-parameter model 4 and (b) three-parameter model 8.

6.3.2 Kinetics of deactivation

Eight samples of the cobalt catalyst were tested over a period of 800-900 h, each at a different set of CO and H_2 partial pressures and a range of temperature, higher than for the reaction kinetic studies, while flowrate was held constant (see Table 6.1). Measurement of deactivation rate by carbon in the absence of the other deactivation mechanisms was achieved by: (1) operating at CO conversions less than 24% and lower partial pressures of water, conditions which favor carbon deposition while preventing water-assisted sintering and oxidation; and (2) reducing the Co catalyst at a high temperature (450°C) to ensure that the average crystallite size was sufficiently large to obviate sintering.

6.3.2.1 Effects of H_2 and CO partial pressures

The five sets of activity-time data at 230°C for different partial pressures of H_2 and CO as shown in Table 6.1 were fit to a concentration-dependent GPLE deactivation rate model of the form

$$-\mathrm{d}\mathbf{a} \,/\, \mathrm{dt} \;=\; k_d\, {P_{H2}}^{\alpha}\, {P_{CO}}^{\beta}(\boldsymbol{a} - \boldsymbol{a}_{\infty})^{d} \tag{6.10}$$

Activity at infinite reaction time ($\boldsymbol{a}_{\infty}$) was varied between 0 and 0.7, while deactivation order (d) was held constant at 1; in another set of experiments, while holding $\boldsymbol{a}_{\infty}$ constant at 0.7, *d* was varied in the range of 0 to 2. Values of rate constant (k_d), H_2 and CO orders and r-squared (r^2) are reported in Table 6.6.

It is apparent from data in Table 6.6 that the fit improves at higher values of $\boldsymbol{a}_{\infty}$; moreover, r^2 increases from 0.75 to 0.89 as deactivation order increases from 0 to 1 at a $\boldsymbol{a}_{\infty}$ of 0.7, although, the values of r^2 are the same within experimental error for d = 1 and 2. As *d* increases from 0 to 2, H_2 and CO orders increase from 0.83 and 0.95 to 1.36 and 1.83, respectively. H_2 and CO orders at $\boldsymbol{a}_\infty$ of 0.7 and d of 1 were found to be 1.12 and 1.43, respectively, indicating that the deactivation rate at 230°C increases as either or both partial pressures of H_2 and CO increase, as discussed in Chapter 5. At 230°C and $\boldsymbol{a}_\infty = 0.7$, zero, first and second order deactivation rate constants were found to be 1.66×10^{-4}, 1.66×10^{-4}, and 2.16×10^{-4} day^{-1}, respectively.

Table 6.6. Deactivation rate parameters for $d = 0, 0.5, 1$, and 2 with $\mathbf{a}_\infty$ of 0.3, 0.5, 0.7 obtained from fitting five sets of activity-time data at 230°C (**Figure 6.5**) for runs up to ~800 h.

	d = 0				d = 0.5				d = 1.0				d = 2.0			
$\boldsymbol{a}_\infty$	k_d[a] $\times 10^4$	α	β	r^2	k_d[a] $\times 10^4$	α	β	r^2	k_d[a] $\times 10^4$	α	β	r^2	k_d[a] $\times 10^4$	α	β	r^2
0	1.66	0.83	0.95	0.75	1.45	1.00	0.87	0.77	1.27	0.90	1.05	0.79	1.0	1.15	0.97	0.83
0.3	1.66	0.83	0.95	0.75	1.62	1.03	0.89	0.78	1.21	1.01	1.16	0.81	1.60	1.03	1.25	0.86
0.5	1.66	0.83	0.95	0.75	1.71	0.91	1. 1	0.80	1.82	0.99	1.18	0.84	2.16	1.12	1.40	0.89
0.7	1.66	0.83	0.95	0.75	1.53	1.0	1.22	0.84	1.66	1.12	1.43	0.89	2.16	1.36	1.83	0.90

[a] deactivation rate constant with units of $\text{bar}^{-(\alpha+\beta)}\text{day}^{-1}$.

Activity-time data at 230°C, different partial pressures with corresponding 1st and zero order GPLE fits with $\boldsymbol{a}_\infty$ values of 0 and 0.7 are plotted in Figure 6.6. The linear zero order GPLE does not fit the data well, since the slope of the data decreases with increasing time. On the other hand, for a $\boldsymbol{a}_\infty$ of 0.7, more curvature is evident which is closer to the nonlinear deactivation profiles. Apparently, the postulated model needs to be refined. Nevertheless, qualitative trends are captured well by the first order GPLE; it should also be emphasized that the deactivation data are plotted over a relatively narrow range of activity. By comparison, fits of the data to a SPLE are not even close to the data trends.

The approximate fit of the data to a 1st order GPLE with $\boldsymbol{a}_\infty$ of 0.7 is consistent with results of Argyle et al. [116] who found that a 1st order GPLE predicts deactivation rates due to carbon deposition better than other models. They also reported a large non zero value of $\boldsymbol{a}_\infty$ (0.56) from the first order GPLE fit of activity-time data for a 20 wt% Co/ 0.05 wt% Pt/Al_2O_3 reported by Moodley et al. [48]. That this value ($\boldsymbol{a}_\infty$ = 0.56) is somewhat lower than our value of 0.72 could be explained by obviously faster catalyst deactivation in Moodley's experiment and by an early (1-15 days) contribution due to sintering. Given the similar conditions for the two studies, a rough quantitative comparison of deactivation rates is possible.

6.3.2.2 Effects of temperature

Activity-time data for FTS were obtained in the FB reactor at four relatively high reaction temperatures (220, 230, 240, and 250°C) to study effects of reaction temperature on carbon deactivation rates of cobalt in FTS. All FTS tests were conducted over about 800 h at 20 bar with the same initial feed concentration (P_{H2} = 10 bar, P_{CO} = 5 bar, H_2/CO=2, remainder He); Runs 3, 6, 7, and 10, respectively; see Table 6.1.

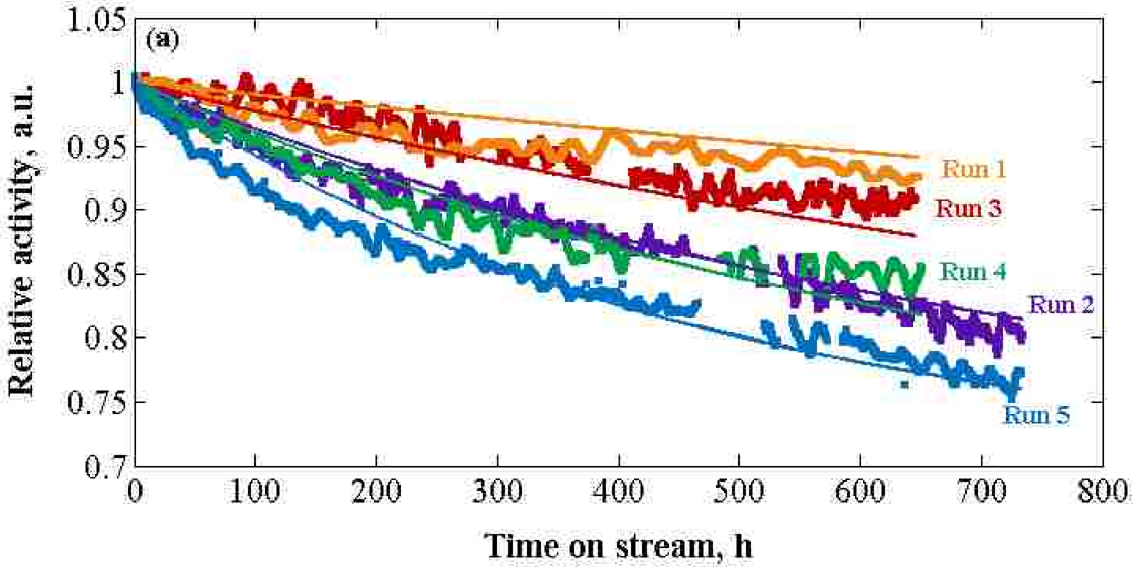

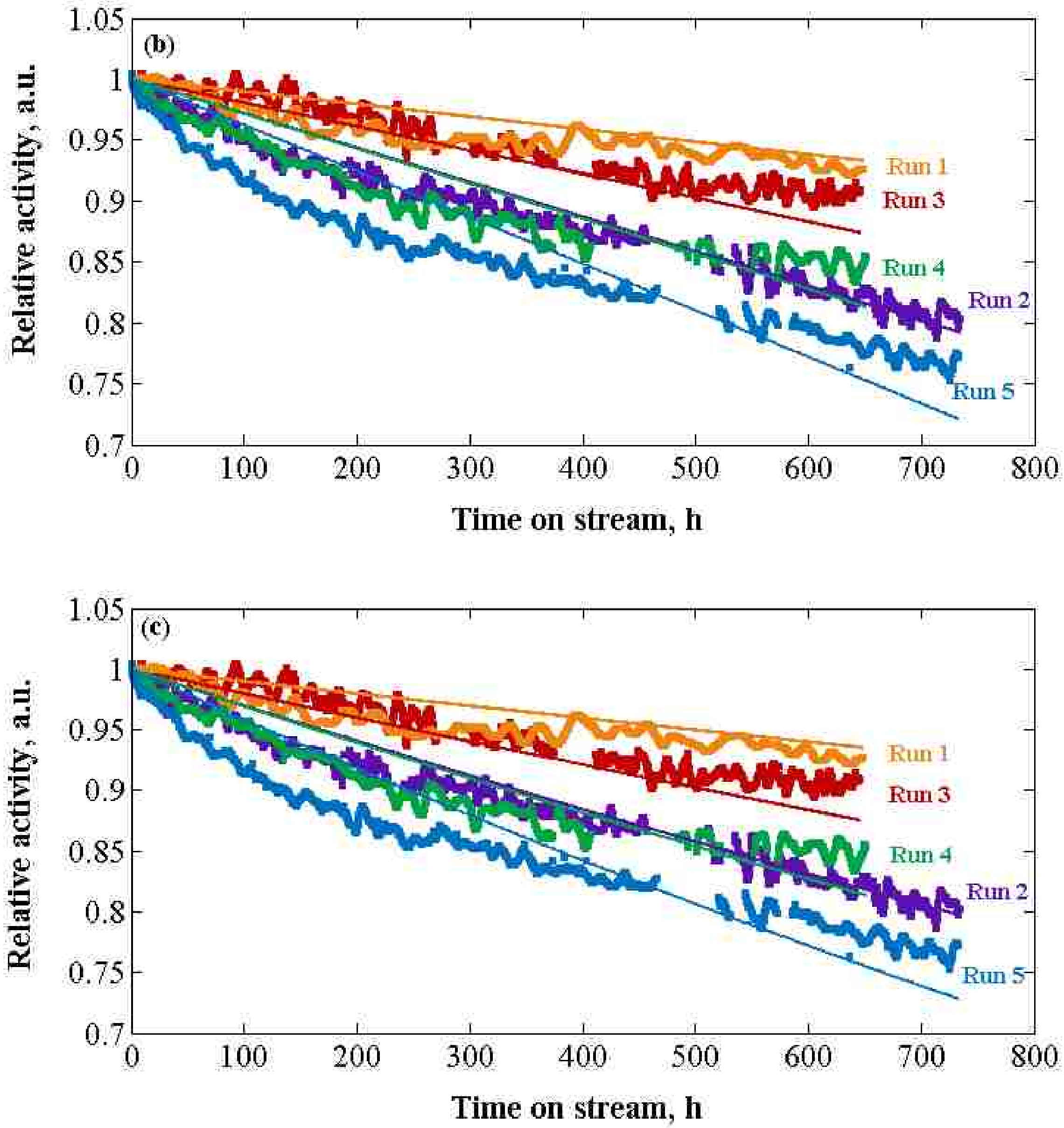

Figure 6.6. Deactivation data for CoPt/Al_2O_3 catalyst as a function of time at 230°C and 20 bar fit to GPLE (Equation 6.10) with (a) $\boldsymbol{a}_{\infty}$= 0.7 and d = 1, (b) $\boldsymbol{a}_{\infty}$= 0.7 and d = 0, (c) $\boldsymbol{a}_{\infty}$= 0 and d = 1.

As the initial feed concentration was the same for all four runs, activation energy for deactivation could be estimated from the Arrhenius dependence of the concentration-independent GPLE rate expression of the form

$$-\frac{\mathrm{da}}{\mathrm{dt}} = \mathrm{A}_d \exp\left(-\frac{\mathrm{E_d}}{\mathrm{RT}}\right)(\mathrm{a} - 0.7)^1 \qquad (6.11)$$

Activity-time data and their GPLE fit are presented in Figure 6.7. Data are predicted statistically well using equation 6.11 with an r^2 of 0.97. The pre-exponential factor (A_d) and activation energy for deactivation (E_d) were predicted to be 3.63E06 day^{-1} and 81 kJ/mol, respectively.

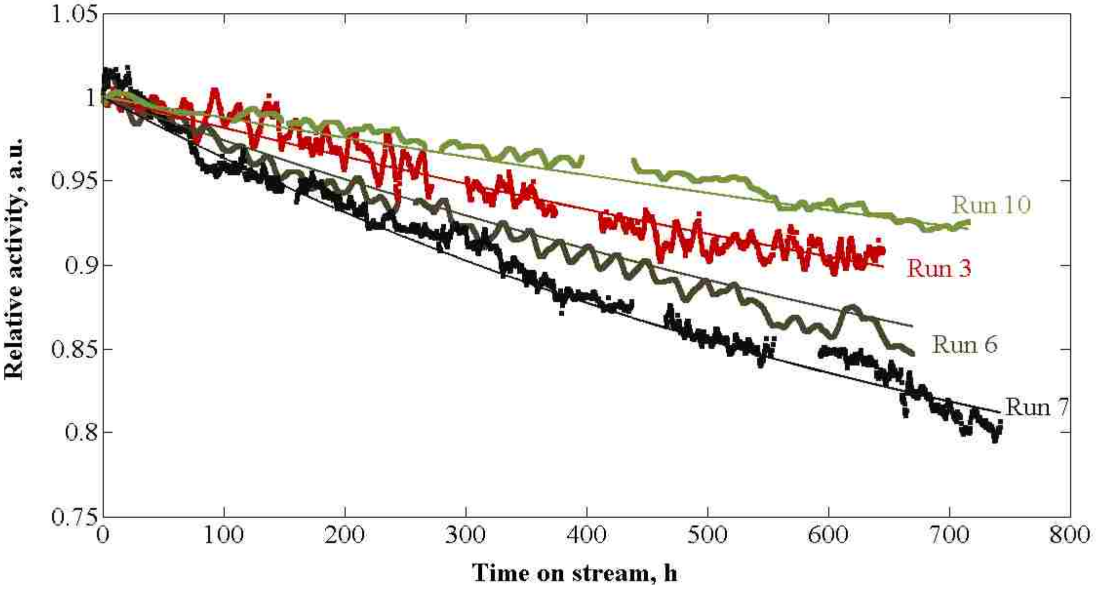

Figure 6.7. Deactivation data for CoPt/Al_2O_3 catalyst at different temperatures (Run 3: 230°C, Run 6: 240°C, Run 7: 250°C), P_{H2} = 10 bar, P_{CO} = 5 bar, P_{tot} = 20 bar fit to Equation 6.11.

Activity-time data obtained in all eight experiments, at the conditions shown in Table 6.1, were regressed to a deactivation model (based on Equation 6.10) using optimal values of reaction orders and a_∞ shown in Equation 6.12.

$$-\mathrm{d}\mathbf{a} / \mathrm{dt} = \mathrm{A} \times \exp\left(-\frac{\mathrm{E}}{\mathrm{RT}}\right) P_{H2}{}^{1.38}\, P_{CO}{}^{1.65} (\mathbf{a} - 0.7)^1 \qquad (6.12)$$

The pre-exponential factor and activation energy based on all 8 runs were found to be 71.5 bar$^{-3.03}$day^{-1} and 72 kJ/mol, respectively.

Figure 6.8 shows a parity plot of experimental and calculated values of activity for all eight deactivation data sets regressed to a GPLE form represented in Equation 6.12. Each data point in Figure 6.8 represents an average of activities over a period of 100 h.

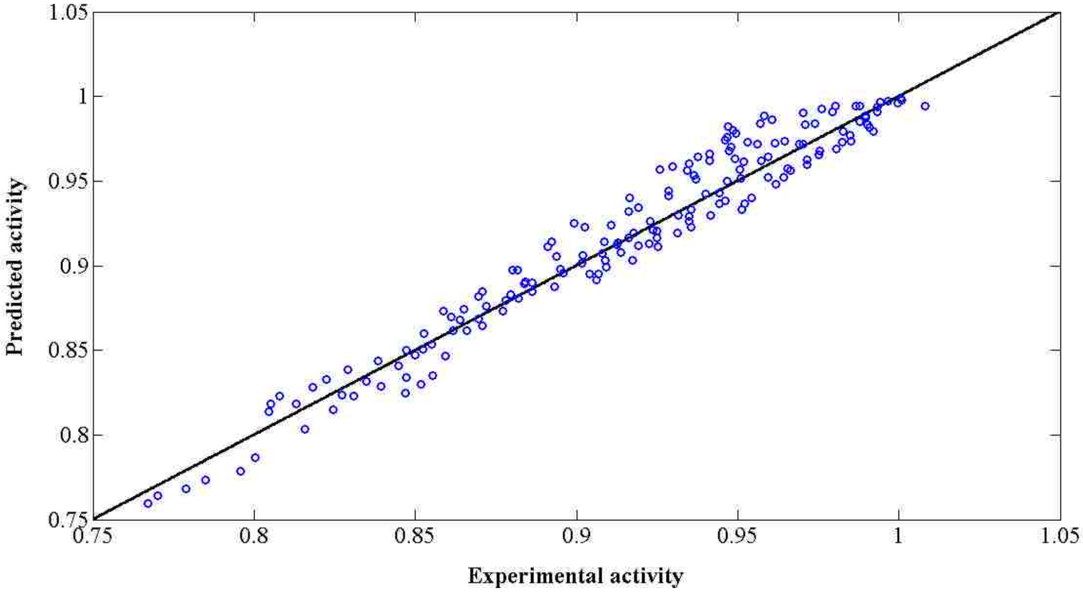

Figure 6.8. Parity plot of an overall deactivation model (Equation 6.12) for all the deactivation data (Runs 1-7 and 10). Each data point is an average of activities over a period of 100 h.

6.3.2.3 Comparison of deactivation kinetics with literature

Recently, Argyle et al. [116] studied the modeling of previously published experimental deactivation data for Co FT catalysts using GPLE expressions. They deconvoluted the sintering and/or cobalt aluminate formation from the overall deactivation rate enabling their independent calculation of deactivation kinetic parameters for carbon deposition. As shown in Table 6.7, at the same operating conditions (T = 230°C, H_2/CO = 2, and P = 20 bar), for similar cobalt catalysts and with carbon deposition as the principal deactivation mechanism, the reported 1st order deactivation rate constant is 3.7E-02 day^{-1} for a Sasol Co FT catalyst, which is two times higher than determined for the cobalt catalyst used in this study (1.7E-02 day^{-1}). Moreover, limiting activity for our catalyst is predicted to be 0.7 compared with 0.56 for Sasol Co catalyst. Activity is predicted to drop to 71% of the initial activity at 200 days for the cobalt catalyst in this study calculated from 1st order concentration-independent GPLE form. However, for the Sasol cobalt catalyst the activity at 200 days is estimated to reach the limiting activity of 56%. At a reaction temperature of 250°C the deactivation rate constant is shown to be 3.0E-02/d which is 20% lower than the value for Sasol's cobalt catalyst operated at 230°C.

Moodley et al. [4] also investigated effects of temperature on the deactivation of a cobalt FT catalyst in FTS at 20 bar, H_2/CO of 1.6 and TOS of 20 days at three different temperatures of 240, 260, 270°C. They reported an activation energy of 69 kJ/mol for the formation of polymeric carbon. The activation energy found in the present study (65 kJ/mol) is in very good agreement with their value.

Table 6.7. Comparison of the deactivation rate constants and $\mathbf{a}_\infty$ values of this study with Sasol for cobalt FT catalyst.

Catalyst and reference	TOS, days	T, °C	H_2/CO	P, bar	k_d[b], day^{-1}	E_d[c], kJ/mol	a_∞[d]
25 wt% Co/0.25 wt% Pt/Al_2O_3	27-30	230	2	20	1.7E-02	72	0.7
This study		250	2	20	3.0E-02		0.7
20 wt% Co/0.05 wt% Pt/Al_2O_3 Moodley et al. [4, 48] – Sasol [a]	18-55	230	2	20	3.7E-02	69	0.56

[a] The deactivation rate constants and a_∞ values were reported in the work by Argyle et al. [116] for deactivation only by carbon deposition

[b] k_d is the first order deactivation rate constant for carbon deposition with units of day^{-1}

[c] Activation energy for deactivation by carbon with unites of kJ/mol

[d] Normalized activity a is defined as the rate at time t divided by the initial rate; a_∞ is the asymptotic normalized activity.

6.4 Conclusions

1- The dependence of reaction rate on P_{H2} becomes more positive and on P_{CO} becomes more negative as temperature increases; in fact CO order changes from +0.31 to -0.64 as temperature increases from 210 to 240°C, respectively.

2- Activation energy does not change with P_{H2} at constant P_{CO} while it does increase from 107 to 169 kJ/mol as P_{CO} decreases from 6 to 2.7 bar.

3- A denominator term which includes P_{CO} should increase with temperature to account for negative dependence of CO with temperature; using θ_C as a MASI is consistent with this.

4- Addition of $K''P_{H2}$ as a 3rd denominator term allows change in P_{H2} dependency and thus improves the fit of all the data to give the best fit.

5- 1st order GPLE with $\boldsymbol{a}_\infty$ of 0.7 was found to reasonably predict the deactivation data.

6- At 230°C, deactivation rate by carbon deposition increases as both partial pressures of CO and H_2 increase with H_2 order of 1.38 and CO order of 1.65 using 1st order GPLE with $\boldsymbol{a}_\infty$ of 0.7.

7- At H_2/CO of 2, deactivation rate increases with increasing temperature from 220 to 250°C with activation energy of 72 kJ/mol.

Chapter 7 Accomplishments, Future Work and Recommendation

7.1 Accomplishments

Five most important overall contributions of this work to the technology of FT:

1- We developed a very active and stable supported Fe FT catalyst that is more active than any supported Fe FT catalyst previously reported and competitive with the best unsupported catalysts. More importantly, the catalyst is extremely stable, as evidenced by the fact that after 700 h on stream, its activity and productivity are still increasing. The key factor to this development was hydrothermally stable silica-doped alumina with large pore volume and pore diameter.

2- We developed a kinetic model for Co FT catalyst based on a realistic sequence of elementary steps which includes hydrogen-assisted dissociation of adsorbed CO and a parallel step which leads to carbon on the surface. It fits all 24 data points over a large range of temperature, P_{H2} and P_{CO} and the fit was excellent (r^2 value = 0.996).

3- We carried out an extensive study to investigate the effects of H_2 and CO partial pressures and temperature on the deactivation by carbon for Co FT catalyst by running twelve experiments over 800 h TOS, each at different T, P_{H2}, and P_{CO}. We provided, for the first time, new data defining quantitatively the long-term deactivation by carbon deposition in the absence of the other deactivation mechanisms.

4- We developed a deactivation model as a function of time, T, P_{H2}, and P_{CO} which fits eight deactivation runs including ~ 20,000 data points with r^2 value of 0.91. We also determined the activation energy for deactivation of 72 kJ/mol (at $H_2/CO = 2$).

5- We designed and developed a unique wax-extraction system which enabled us to characterize spent catalysts with ex-situ techniques after removing the wax. All the important steps including wax-extraction, vacuum drying, and passivation are done in the same system without the need of transferring the catalyst after wax-extraction in a glove-box to drying or passivation set-ups.

Ten specific discoveries/observations:

1- Large pore volume and pore diameters of the support accommodate higher metal loading without pore blocking. They may also aid uniform distribution of the active phase into the pores and greater accessibility of the active phase to the reactants; in fact, a correlation between intrinsic activity and pore diameter of the support was found in this study.

2- Large pore volume and pore diameters of the support also accommodate a greater amount of carbon and help in retarding the deactivation due to blockage of the pores by carbon deposits.

3- Silica is a more effective stabilizer than La for alumina supports. Silica as a dopant in alumina suppresses the phase transformation of γ-Al_2O_3 to α-Al_2O_3 at elevated temperatures and thus it enables effective dehydroxylation of the alumina surface at high temperatures.

4- Higher calcination temperature of the support results in greater removal of the hydroxyl groups and more effective reduction/carbiding (higher EOR), which consequently lead to higher activity.

5- Silica may anchor the active phase to the alumina surface and prevents active phase crystallites from deactivation by sintering.

6- The absolute values of H_2 and CO partial pressures effect deactivation by carbon for Co FT catalyst independently. In fact, deactivation rate increases with either increasing H_2 or CO partial pressures.

7- A higher quantity of polymeric carbon formed during FT reaction leads to higher deactivation rates.

8- A higher quantity of polymeric carbon also correlates with Co sites lost during reaction.

9- The effect of temperature on deactivation by carbon for Co FT catalyst depends on feed composition and/or H_2/CO ratio. At H_2/CO of 2, deactivation rate increases with increasing temperature; however, at H_2/CO of 1, the opposite trend was found; deactivation rate decreases with increasing temperature.

10- Regardless of temperature, methane selectivity increases as catalyst deactivates during FT reaction at high partial pressures of CO. However, methane selectivity was constant over 800 h at low CO partial pressure (P_{CO} = 5 bar).

7.2 Future work and recommendation

Based on the foregoing observations, the following future scientific investigations and activities are recommended.

7.2.1 Catalyst preparation and pretreatment

- As shown in Chapter 4, support material can significantly affect the activity, selectivity, and stability of the final catalyst. One of the important factors is the calcination temperature of the support. A paper that we're currently writing is considering four calcination temperatures of silica-doped alumina (AlSi) (700, 900, 1100, 1200°C) to study the effect of support calcination temperature on the properties of the final catalyst. The preliminary H_2-TPR, syngas-TPR and Mossbauer spectroscopy results show that supported Fe catalyst is more reducible with higher extent of reduction and carbiding when the AlSi is calcined at higher temperature. XRD results are also confirming mainly Fe_3O_4 phase for the catalyst with a support calcined at temperatures of 700 and 900°C, while both Fe_3O_4 and Fe^0 are present at higher calcination temperatures (1100 and 1200°C). FB tests for 40Fe/AlSi catalysts demonstrate over a factor of four increase in the activity when the AlSi was calcined at 1200°C compared with 700°C.
- 40Fe/AlSi prepared and tested in this study showed promising activity and stability; in fact, the activity is 3-6 times higher than other reported supported Fe catalysts [9, 17] and no deactivation was observed in 700 h TOS. The only drawback of this catalyst is its undesirably high methane selectivity. Therefore, studying the effect of preparation variables on the methane selectivity is of primary interest. One of the important variables that has a large effect on methane selectivity is potassium loading and its precursor. It has been shown that chelated metal complexes such as citrates would result in better

dispersion [135]. Furthermore, an unsupported Fe catalyst prepared in this lab with Fe, Cu and K citrate precursors showed very promising methane selectivity but low activity. Doubling the potassium loading did not affect the methane selectivity as shown in Chapter 3; however, it should be noted that it was tested on St. Gobein alumina support (rather than AlSi) and potassium bicarbonate was added at the end in a separate step (sequential impregnation). Recently, we've tested an Fe catalyst supported on AlSi with eight parts potassium using potassium citrate prepared by a co-impregnation method to have better Fe and K contact. Methane selectivity was only 3% compared with 9% for 40Fe/AlSi reported in Chapter 4 tested at 260°C, H_2/CO of 1, and 20 bar; however, the catalyst with higher potassium deactivated by 25% after 300 h TOS. More tests are needed to identify separate effects of potassium citrate and higher potassium loading. More specifically, two catalysts are being prepared; namely, 8KB-40Fe/AlSi and 4KC-40Fe/AlSi (KB = potassium bicarbonate and KC = potassium citrate).

- All of the catalysts were prepared at the same copper loading of 7.5 parts per 100 part Fe. Copper is known to be a hydrogenolysis catalyst which can favor the formation of light hydrocarbons. It would be interesting to study the effect of different loadings of copper on activity and selectivity. A catalyst with lower Cu loading (4Cu/100Fe) was prepared and will be tested. In addition, because of the synergistic effect of Cu and K, they should be optimized simultaneously for supported Fe catalyst. The optimal Cu and K loadings for unsupported Fe catalyst were found to be 1 and 2 nm^{-2}, respectively [10].
- Others have shown a nearly 100% increase in catalyst activity and significant effect on selectivity by using an optimized pretreatment for iron FT catalysts [8, 9, 12]. For example, very recently Chun et al. [136] reported a highly selective Fe FT catalyst

pretreated in CO_2-containing syngas. The reduction/carbiding of catalysts in this study were not optimized, but significant effect in activity and selectivity are expected from optimized catalyst pretreatment and reduction/carbiding procedures.

- Some variables that may affect cobalt catalyst properties especially methane selectivity but which were not investigated in this work include, but are not limited to, higher calcination temperature of the support (1200°C), modification of the support with basic elements such as Ba, K, Mg, or Mn, use of cobalt citrate as a precursor, and co-impregnation preparation (adding cobalt and noble metal in each step).

7.2.2 Main reaction kinetics and modeling

- There is very limited kinetic data for supported Fe catalyst since other researchers have failed to prepare an active supported Fe catalyst. A partial pressure study for the most active catalyst (40Fe/AlSi; Appendix C) of this study was done at a single temperature of 250°C; however, it would be very valuable to do a partial pressure study at different temperatures similar to what was done for the cobalt catalyst (Chapter 6) and compare the kinetics of the supported Fe catalyst with unsupported Fe catalysts or even with supported cobalt catalysts.
- More than a dozen kinetic rate expressions have been proposed for unsupported Fe catalyst and it is virtually impossible to distinguish between some models based on statistics when only macrokinetic data are available. Therefore, a combination of macrokinetic and microkinetic modeling are needed to better understand the mechanisms involving CO hydrogenation. This project is also in progress as we are still developing a microkinetic model for supported cobalt catalyst. Pre-exponential factors for the microkinetic model are found based on transition state theory and activation energies are

estimated by UBI-QEP [134] using heats of adsorption for C, H, and O. This work can also be done for supported Fe catalyst but kinetic data at different temperatures are needed.

7.2.3 Deactivation kinetics and modeling

- As shown in Chapter 4, all of the supported Fe catalysts showed some deactivation within 300-400 h TOS; except, Fe supported on AlSi which was extremely stable; in fact, the activity was increasing after a month of operation. The science of supported Fe FT catalyst will benefit from future studies on understanding why the Fe catalyst supported on AlSi does not deactivate while the other catalysts supported on different alumina supports do deactivate. We've recently started a project to study that by characterizing the freshly carbided samples and wax-extracted spent catalyst samples of 20Fe/AlSi, 20Fe/AlG, and 20Fe/AlA.
- There is still a lot to learn for the deactivation of cobalt catalysts. A few of the things, which were not investigated in this work include, but are not limited to: (1) the effect of deactivation on product distribution by analyzing liquid and wax products, (2) the effect of conversion on the deactivation of cobalt catalysts by carbon deposition in the absence of other deactivation mechanisms; this can be done using a catalyst with relatively large cobalt crystallite sizes, and (3) the effects of partial pressures of H_2 and CO at higher temperatures rather than just at 230°C, which was carried out in this study.
- Theoretical works, such as DFT calculations, are needed to understand the effect of reconstruction on catalyst deactivation or activation at different temperatures and carbon coverages. This work will help in understanding why faster deactivation was observed at

lower temperatures and high CO partial pressures, while deactivation rate increases with temperature at low CO partial pressures.

- Developing a deactivation model based on theory can impact FT science and technology. The deactivation mechanism by carbon deposition via C_2H_x species to form benzene rings, which can also include hydrocarbon chains, proposed by Niemanstverdriet's group [40, 43] can be used as a starting point to derive deactivation rate expressions based on elementary steps for deactivation by carbon deposition.

References

[1] R. Oukaci, A.H. Singleton, J.G. Goodwin Jr, Comparison of patented Co F–T catalysts using fixed-bed and slurry bubble column reactors, Applied Catalysis A: General, 186 (1999) 129-144.

[2] E.d. Smit, B.M. Weckhuysen, The renaissance of iron-based Fischer-Tropsch synthesis: on the multifaceted catalyst deactivation behaviour, Chemical Society Reviews, 37 (2008) 2758-2781.

[3] J. Sarkar, Platt's International Coal Report, in, 2007, pp. 17.

[4] D.J. Moodley, On the Deactivation of Cobalt-based Fischer-Tropsch Synthesis Catalysts, in, Eindhoven University of Technology, 2008.

[5] D.J. Moodley, J.v.d. Loosdrecht, A.M. Saib, J.W. Niemantsverdriet, Advances in Fischer-Trospch Synthesis, Catalysts, and Catalysis, in: B.H. davis, M.L. Occelli (Eds.) Advances in Fischer-Trospch Synthesis, Catalysts, and Catalysis, CRC Press Taylor & Francis group, 2010, pp. 49-81.

[6] J.R. Rostrup-Nielsen, J. Sehested, J.K. Nørskov, Hydrogen and synthesis gas by steam- and C02 reforming, in: Advances in Catalysis, Academic Press, 2002, pp. 65-139.

[7] D.B. Bukur, M. Koranne, X. Lang, K.R.P.M. Rao, G.P. Huffman, Pretreatment effect studies with a precipitated iron Fischer-Tropsch catalyst Applied Catalysis A: General, 126 (1995) 85-113.

[8] D.B. Bukur, X. Lang, Y. Ding, Pretreatment effect studies with a precipitated iron Fischer–Tropsch catalyst in a slurry reactor, Applied Catalysis A: General, 186 (1999) 255-275.

[9] J. Xu, C.H. Bartholomew, J. Sudweeks, D.L. Eggett, Design, synthesis, and catalytic properties of silica-supported, Pt-promoted iron Fischer–Tropsch catalysts, Topics in Catalysis, 26 (2003) 55.

[10] S. Li, S. Krishnamoorthy, A. Li, G.D. Meitzner, E. Iglesia, Promoted Iron-Based Catalysts for the Fischer–Tropsch Synthesis: Design, Synthesis, Site Densities, and Catalytic Properties, Journal of Catalysis, 206 (2002) 202-217.

[11] S. Li, G.D. Meitzner, E. Iglesia, Structure and Site Evolution of Iron Oxide Catalyst Precursors during the Fischer−Tropsch Synthesis, The Journal of Physical Chemistry B, 105 (2001) 5743-5750.

[12] D.B. Bukur, X. Lang, Highly Active and Stable Iron Fischer−Tropsch Catalyst for Synthesis Gas Conversion to Liquid Fuels, Industrial & Engineering Chemistry Research, 38 (1999) 3270–3275.

[13] D.B. Bukur, X. Lang, D. Mukesh, W.H. Zimmerman, M.P. Rosynek, C. Li, Binder/support effects on the activity and selectivity of iron catalysts in the Fischer-Tropsch synthesis, Industrial & Engineering Chemistry Research, 29 (1990) 1588–1599.

[14] Y. Yang, H.-W. Xiang, L. Tian, H. Wang, C.-H. Zhang, Z.-C. Tao, Y.-Y. Xu, B. Zhong, Y.-W. Li, Structure and Fischer–Tropsch performance of iron–manganese catalyst incorporated with SiO2, Applied Catalysis A: General, 284 (2005) 105-122.

[15] H.-J. Wan, B.-S. Wu, X. An, T.-Z. Li, Z.-C. Tao, H.-W. Xiang, Y.-W. Li, Effect of Al2O3 Binder on the Precipitated Iron-Based Catalysts for Fischer-Tropsch Synthesis, Journal of Natural Gas Chemistry, 16 (2007) 130-138.

[16] Y. Yang, H. Xiang, R. Zhang, B. Zhong, Y. Li, A highly active and stable Fe-Mn catalyst for slurry Fischer–Tropsch synthesis, Catalysis Today, 106 (2005) 170-175.

[17] R.J. O'Brien, L. Xu, S. Bao, A. Raje, B.H. Davis, Activity, selectivity and attrition characteristics of supported iron Fischer–Tropsch catalysts, Applied Catalysis A: General, 196 (2000) 173-178.

[18] D.B. Bukur, C. Sivaraj, Supported iron catalysts for slurry phase Fischer–Tropsch synthesis, Applied Catalysis A: General, 231 (2002) 201-214.

[19] R.J. O'Brien, L. Xu, R.L. Spicer, B.H. Davis, Activation study of precipitated iron Fischer-tropsch catalysts, Energy & Fuels, 10 (1996) 921-926.

[20] M. Rameswaran, C.H. Bartholomew, Effects of preparation, dispersion, and extent of reduction on activity/selectivity properties of iron/alumina CO hydrogenation catalysts, Journal of Catalysis, 117 (1989) 218.

[21] E. Iglesia, Design, synthesis, and use of cobalt-based Fischer-Tropsch synthesis catalysts, Applied Catalysis A: General, 161 (1997) 59-78.

[22] E. Iglesia, S.L. Soled, R.A. Fiato, Fischer-Tropsch Synthesis on Cobalt and Ruthenium. Metal Dispersion and Support Effects on Reaction Rate and Selectivity, Journal of Catalysis, 137 (1992) 212-224.

[23] B.G. Johnson, C.H. Bartholomew, D.W. Goodman, The role of surface structure and dispersion in CO hydrogenation on cobalt, Journal of Catalysis, 128 (1991) 231-247.

[24] N. Fischer, E. van Steen, M. Claeys, Structure sensitivity of the Fischer–Tropsch activity and selectivity on alumina supported cobalt catalysts, Journal of Catalysis, 299 (2013) 67-80.

[25] J.P. den Breejen, P.B. Radstake, G.L. Bezemer, J.H. Bitter, V. Frøseth, A. Holmen, K.P.d. Jong, On the Origin of the Cobalt Particle Size Effects in Fischer−Tropsch Catalysis, Journal of the American Chemical Society, 131 (2009) 7197-7203.

[26] N. Balakrishnan, B. Joseph, V.R. Bhethanabotla, Effect of Pt and Ru promoters on deactivation of Co catalysts by C deposition during Fischer–Tropsch synthesis: A DFT study, Applied Catalysis A: General, 462– 463 (2013) 107– 115.

[27] J. van de Loosdrecht, B. Balzhinimaev, J.A. Dalmon, J.W. Niemantsverdriet, S.V. Tsybulya, A.M. Saib, P.J. van Berge, J.L. Visagie, Cobalt Fischer-Tropsch synthesis: Deactivation by oxidation?, Catalysis Today, 123 (2007) 293-302.

[28] C.H. Bartholomew, R.J. Farrauto, Fundamentals of Industrial Catalytic Processes, Second ed., John Wiley & Sons, 2006.

[29] C.H. Bartholomew, P.K. Agrawal, J.R. Katzer, Sulfur Poisoning of Metals, in: H.P. D.D. Eley, B.W. Paul (Eds.) Advances in Catalysis, Academic Press, 1982, pp. 135-242.

[30] N.E. Tsakoumis, M. Rønning, Ø. Borg, E. Rytter, A. Holmen, Deactivation of cobalt based Fischer–Tropsch catalysts: A review, Catalysis Today, 154 (2010) 162-182.

[31] M. Sadeqzadeh, S. Chambrey, S. Piché, P. Fongarland, F. Luck, D. Curulla-Ferré, D. Schweich, J. Bousquet, A.Y. Khodakov, Deactivation of a Co/Al2O3 Fischer–Tropsch catalyst by water-induced sintering in slurry reactor: Modeling and experimental investigations, Catalysis Today, 215 (2013) 52-59.

[32] M. Sadeqzadeh, J. Hong, P. Fongarland, D. Curulla-Ferré, F. Luck, J.B.D. Schweich, A.Y. Khodakov, Mechanistic Modeling of Cobalt Based Catalyst Sintering in a Fixed Bed Reactor under Different Conditions of Fischer−Tropsch Synthesis, Industrial & Engineering Chemistry Research, 51 (2012) 11955−11964.

[33] M.J. Overett, B. Breedt, E.d. Plessis, W. Erasmus, J.v.d. Loosdrecht, Sintering as a deactivation mechanism for an alumina supported cobalt Fischer-Tropsch synthesis catalyst, in: Prepr. Pap.-Am. Chem. Soc., Div. Petr. Chem., 2008, pp. 126-128.

[34] A.M. Saib, A. Borgna, J. van de Loosdrecht, P.J. van Berge, J.W. Niemantsverdriet, XANES study of the susceptibility of nano-sized cobalt crystallites to oxidation during realistic Fischer–Tropsch synthesis, Applied Catalysis A: General, 312 (2006) 12-19.

[35] A.M. Saib, D.J. Moodley, I.M. Ciobîcă, M.M. Hauman, B.H. Sigwebela, C.J. Weststrate, J.W. Niemantsverdriet, J. van de Loosdrecht, Fundamental understanding of deactivation and regeneration of cobalt Fischer–Tropsch synthesis catalysts, Catalysis Today, 154 (2010) 271-282.

[36] P.H. Bolt, in, University of Utrecht, 1994.

[37] A.M. Hilmen, D. Schanke, K.F. Hanssen, A. Holmen, Study of the effect of water on alumina supported cobalt Fischer–Tropsch catalysts, Applied Catalysis A: General, 186 (1999) 169-188.

[38] G. Jacobs, T.K. Das, P.M. Patterson, J. Li, L. Sanchez, B.H. Davis, Fischer–Tropsch synthesis XAFS: XAFS studies of the effect of water on a Pt-promoted Co/Al2O3 catalyst, Applied Catalysis A: General, 247 (2003) 335-343.

[39] D.J. Moodley, A.M. Saib, J.v.d. Loosdrecht, C.A. Welker-Nieuwoudta, B.H. Sigwebela, J.W. Niemantsverdriet, The impact of cobalt aluminate formation on the deactivation of cobalt-based Fischer–Tropsch synthesis catalysts, Catalysis Today, 171 (2011) 192-200.

[40] C.J. Weststrate, A.C. Kizilkaya, E.T.R. Rossen, M.W.G.M. Verhoeven, I.M. Ciobica, A.M. Saib, J.W. Niemantsverdriet, Atomic and Polymeric Carbon on Co(0001): Surface Reconstruction, Graphene Formation, and Catalyst Poisoning, Journal of Physical Chemistry C, 116 (2012) 11575-11583.

[41] J.C.W. Swart, A Theoretical View on Deactivation of Cobalt-Based Fischer-Tropsch Catalysts, in: Department of Chemical Engineering, University OF Capetown, 2008.

[42] J.C.W. Swart, L.M. Ciobica, R.A. van Santen, E. van Steen, Intermediates in the formation of graphitic carbon on a flat FCC-Co(111) surface, Journal of Physical Chemistry C, 112 (2008) 12899-12904.

[43] C.J. Weststrate, I.M. Ciobica, A.M. Saib, D.J. Moodley, J.W. Niemantsverdriet, Fundamental issues on practical Fischer–Tropsch catalysts: Howsurface science can help, Catalysis Today, 228 (2014) 106-112.

[44] I.J.C. Geerlings, M.C. Zonnevylle, C.P.M. De Groot, The Fischer-Tropsch reaction on a cobalt (0001) single crystal, Catalysis Letters, 5 (1990) 309-314.

[45] T. Koerts, The reactivity of surface carbonaceous intermediates, in, Eindhoven University of Technology, 1992.

[46] D.-K. Lee, J.-H. Lee, S.-K. Ihm, Effect of Carbon Deposits on Carbon Monoxide Hydrogenation over Alumina-Supported Cobalt Catalyst, Applied Catalysis, 36 (1988) 199-207.

[47] C. Mirodatos, E. Brum Pereira, A. Gomez Cobo, J.A. Dalmon, G.A. Martin, CO hydrogenation over Ni- and Co-based catalysts: Influence of alkali addition on morphological and catalytic properties, Topics in Catalysis, 2 (1995) 183-192.

[48] D.J. Moodley, J. van de Loosdrecht, A.M. Saib, M.J. Overett, A.K. Datye, J.W. Niemantsverdriet, Carbon deposition as a deactivation mechanism of cobalt-based Fischer-Tropsch synthesis catalysts under realistic conditions, Applied Catalysis A: General, 354 (2009) 102-110.

[49] D. Peña, A. Griboval-Constant, V. Lecocq, F. Diehl, A.Y. Khodakov, Influence of operating conditions in a continuously stirred tank reactor on the formation of carbon species on alumina supported cobalt Fischer–Tropsch catalysts, Catalysis Today, 215 (2013) 43– 51.

[50] D.-K. Lee, J.-H. Lee, S.-K. Ihm, Effect of Carbon Deposits on Carbon Monoxide Hydrogenation over Alumina-Supported Cobalt Catalyst, Applied Catalysis, 36 (1988) 199-207.

[51] A. Barbier, A. Tuel, I. Arcon, A. Kodre, G.A. Martin, Characterization and catalytic behavior of Co/SiO2 catalysts: Influence of dispersion in the Fischer-Tropsch reaction, Journal of Catalysis, 200 (2001) 106-116.

[52] V. Gruver, X. Zhan, J. Engman, H.J. Robota, S.L. Suib, M. Polverejan, Deactivation of a Fischer-Tropsch catalyst through the formation of cobalt carbide under laboratory slurry reactor conditions, in: Prepr. Pap.-Am. Chem. Soc. Div. Pet. Chem., 2004, pp. 192-194.

[53] G. Jacobs, P.M. Patterson, Y. Zhang, T. Das, J. Li, B.H. Davis, Fischer–Tropsch synthesis: deactivation of noble metal-promoted Co/Al2O3 catalysts, Applied Catalysis A: General, 233 (2002) 215-226.

[54] A. Tavasoli, R.M.M. Abbaslou, A.K. Dalai, Deactivation behavior of ruthenium promoted Co/-gamma-Al2O3 catalysts in Fischer-Tropsch synthesis, Applied Catalysis A: General, 346 (2008) 58-64.

[55] O. Ducreux, J. Lynch, B. Rebours, M. Roy, P. Chaumette, In situ characterisation of cobalt based fischer-tropsch catalysts : A new approach to the active phase, in: A. Parmaliana, D. Sanfilippo, F. Frusteri, A. Vaccari, F. Arena (Eds.) Studies in Surface Science and Catalysis, Elsevier, 1998, pp. 125-130.

[56] F. Tihay, G. Pourroy, M. Richard-Plouet, A.C. Roger, A. Kiennemann, Effect of Fischer–Tropsch synthesis on the microstructure of Fe–Co-based metal/spinel composite materials, Applied Catalysis A: General, 206 (2001) 29-42.

[57] G.L. Bezemer, J.H. Bitter, H.P.C.E. Kuipers, H. Oosterbeek, J.E. Holewijn, X. Xu, F. Kapteijn, A.J. van Dillen, K.P. de Jong, Cobalt Particle Size Effects in the Fischer−Tropsch Reaction Studied with Carbon Nanofiber Supported Catalysts, Journal of the American Chemical Society, 128 (2006) 3956-3964.

[58] I.M. Ciobica, R.A.v. Santen, P.J.v. Berge, J.v.d. Loosdrecht, Adsorbate induced reconstruction of cobalt surfaces, Surface Science, 602 (2008) 17–27.

[59] J. Wilson, C. de Groot, Atomic-Scale Restructuring in High-Pressure Catalysis, The Journal of Physical Chemistry, 99 (1995) 7860-7866.

[60] I.M. Ciobica, R.A. van Santen, Carbon Monoxide Dissociation on Planar and Stepped Ru(0001) Surfaces, The Journal of Physical Chemistry B, 107 (2003) 3808-3812.

[61] C.H. Bartholomew, B.F. Woodfield, B. Huang, R.E. Olsen, L. Astle, Method for making highly porous, stable metal oxide with a controlled pore structure, in: Brigham Young University, USA, 2011.

[62] M.K. Mardkhe, Facile Synthesis and Characterization of a Thermally Stable Silica-Doped Alumina with Tunable Surface Area, Porosity, and Acidity, in: Department of Chemistry and Biochemistry, Brigham Young University, Provo, 2014.

[63] M.K. Mardkhe, B.F. Woodfield, C.H. Bartholomew, A method of producing thermally stable and high surface area Al2O3 catalyst supports, in: Brigham Young University, USA, 2013.

[64] S. Liu, Q. Liu, J. Boerio-Goates, B.F. Woodfield, Preparation of a wide array of ultra-high purity metals, metal oxides, and mixed metal oxides with uniform particle sizes, Journal of Advanced Materials, 39 (2007) 18-23.

[65] B. Huang, C.H. Bartholomew, B.F. Woodfield, Improved calculations of pore size distribution for relatively large, irregular slit-shaped mesopore structure, Microporous and Mesoporous Materials, 184 (2014) 112-121.

[66] C. Chu, M. Hamidy, K. Nobe, Pore-size distributions of coper oxide-alumina catalysts, Journal of Chemical & Engineering Data, 16 (1971) 327–331.

[67] B.L. Critchfield, Statistical Methods For Kintetic Modeling Of Fischer-Tropsch Synthesis On A Supported Iron Catalyst, in, Brigham Young University, Provo, 2006.

[68] D. Massiot, F. Fayon, M. Capron, I. King, S. Le Calvé, B. Alonso, J.-O. Durand, B. Bujoli, Z. Gan, G. Hoatson, Modelling one- and two-dimensional solid-state NMR spectra, Magnetic Resonance in Chemistry, 40 (2002) 70-76.

[69] T. Ressler, WinXAS: a Program for X-ray Absorption Spectroscopy Data Analysis under MS-Windows, Journal of Synchrotron Radiation, 5 (1998) 118-122.

[70] B. Ravel, ATOMS: crystallography for the X-ray absorption spectroscopist, Journal of Synchrotron Radiation, 8 (2001) 314-316.

[71] J.J. Rehr, R.C. Albers, Theoretical approaches to x-ray absorption fine structure, Reviews of Modern Physics, 76 621.

[72] M. Newville, B. Ravel, D. Haskel, J.J. Rehr, E.A. Stern, Y. Yacoby, Analysis of multiple-scattering XAFS data using theoretical standards, Physica B: Condensed Matter, 208–209 (1995) 154-156.

[73] M.E. Dry, in part A, The Fischer-Tropsch Synthesis, in: J.R. Anderson, M. Boudart (Eds.), Springer-Verlag, 1981, pp. 159-255.

[74] R.B. Anderson, The Fischer-Tropsch Synthesis, Academic Press, New York, 1984.

[75] H.M.T. Galvis, J.H. Bitter, C.B. Khare, M. Ruitenbeek, A.I. Dugulan, K.P.d. Jong, Supported Iron Nanoparticles as Catalysts for Sustainable Production of Lower Olefins, Science, 335 (2012) 835-838.

[76] M.E. Dry, in part A, in: J.R. Anderson, M. Boudart (Eds.) The Fischer-Tropsch Synthesis, Springer-Verlag, 1981, pp. 159-255.

[77] B.H. Davis, Technology development for iron Fischer-Tropsch catalysis, in, University of Kentucky, 1999.

[78] W. Ma, G. Jacobs, U.M. Graham, B.H. Davis, Fischer-tropsch synthesis: effects of K loading on the water-gas shift reaction and liquid hydrocarbon formation rate over precipitated iron catalysts, Topics in Catalysis, 57 (2014) 561-571.

[79] K. Keyvanloo, J.B. Horton, W.C. Hecker, M.D. Argylea, Effects of Preparation Variables on an Alumina-Supported FeCuK Fischer-Tropsch Catalyst, Catalysis Science & Technology, (2014).

[80] K.M. Brunner, Novel iron catalyst and Fixed-Bed reactor model for the Fischer-Tropsch synthesis, in: Chemical Engineering Department, Brigham Young University, Provo, 2012.

[81] M.E. Dry, G.J. Oosthuizen, The correlation between catalyst surface basicity and hydrocarbon selectivity in the Fischer-Tropsch synthesis, Journal of Catalysis, 11 (1968) 18-24.

[82] C.-H. Zhang, Y. Yang, B.-T. Teng, T.-Z. Li, H.-Y. Zheng, H.-W. Xiang, Y.-W. Li, Study of an iron-manganese Fischer–Tropsch synthesis catalyst promoted with copper, Journal of Catalysis, 237 (2006) 405–415.

[83] K. Keyvanloo, W.C. Hecker, B.F. Woodfield, C.H. Bartholomew, Highly Active and Stable Supported-Iron Fischer-Tropsch Catalysts: Effects of Support Properties and SiO2 Stabilizer on Catalyst Performance, Journal of Catalysis, 319 (2014) 220-231.

[84] W. Ma, Y. Ding, V.H.C. Vazquez, D. Bukur, Study on catalytic performance and attrition stregnth of the Ruhrchemie catalyst for the Fischer-Tropsch synthesis in a stirred tank slurry reactor, Applied Catalysis A: General, 268 (2004) 99-106.

[85] K. Keyvanloo, M.K. Mardkhe, T.M. Alam, C.H. Bartholomew, B.F. Woodfield, W.C. Hecker, Supported Iron Fischer−Tropsch Catalyst: Superior Activity and Stability Using a Thermally Stable Silica-Doped Alumina Support, ACS Catalysis, 4 (2014) 1071.

[86] P.J.v. Berge, J.v.d. Loosdrecht, E.A. Caricato, S. Barradas, Process for producing hydrocarbons from a synthesis gas, and catalysts therefor, in: Sasol Technology, 1999.

[87] P. Gibson, The Development and Commercialization of a Supported Cobalt Fischer-Tropsch Synthesis Catalyst for the Sasol Gas-to-Liquids Process, in: Syngas Convention, Cape Town, South Africa, 2012.

[88] H.M.T. Galvis, J.H. Bitter, T. Davidian, M. Ruitenbeek, A.I. Dugulan, K.P.d. Jong, Iron Particle Size Effects for Direct Production of Lower Olefins from Synthesis Gas, Journal of the American Chemical Society, 134 (2012) 16207−16215.

[89] H.M.T. Galvis, J.H. Bitter, C.B. Khare, K.P.d. Jong, Production of lower olefins from synthesis gas, in: N.O.f.S. Research (Ed.), 2012.

[90] B.d. Tymowski, Y. Liu, C. Meny, C. Lefèvre, D. Begin, P. Nguyen, C. Pham, D. Edouard, F. Luck, C. Pham-Huu, Co–Ru/SiC impregnated with ethanol as an effective catalyst for the Fischer–Tropsch synthesis, Applied Catalysis A: General, 419-420 (2012) 31-40.

[91] M.C. Ribeiro, G. Jacobs, B.H. Davis, D.C. Cronauer, A.J. Kropf, C.L. Marshall, Fischer-Tropsch Synthesis: An In-Situ TPR-EXAFS/XANES Investigation of the Influence of Group I Alkali Promoters on the Local Atomic and Electronic Structure of Carburized Iron/Silica Catalysts, The Journal of Physical Chemistry C, 114 (2010) 7895-7903.

[92] B.L. Bhatt, E.S. Schaub, E.C. Hendorn, D.M. Herron, D.W. Studer, D.M. Brown, in: G.J. Stiegel, R.D. Srivastava (Eds.) Proceedings of the Liquefaction Contractors Review Conference, US Department of Energy, Pittsburgh, PA, 1992, pp. 403.

[93] P. Gibson, Syngas to Hydrocarbons: The Sasol Journey, in: Syngas Convention, Cape Town, South Africa, 2012.

[94] M.V. Cagnoli, S.G. Marchetti, N.G. Gallegos, A.M. Alvarez, R.C. Mercader, A.A. Yeramian, Influence of the support on the activity and selectivity of high dispersion Fe catalysts in the Fischer-Tropsch reaction, Journal of Catalysis, 123 (1990) 21-30.

[95] J. Barrault, C. Forquy, J.C. Menezo, R. Maurel, Selective hydrocondensation of CO to light olefins with alumina-supported iron catalysts, Reaction Kinetics and Catalysis Letters, 15 (1980) 153-158.

[96] T. Horiuchi, L. Chen, T. Osaki, T. Sugiyama, K. Suzuki, T. Mori, A novel alumina catalyst support with high thermal stability derived from silica-modified alumina aerogel, Catalysis Letters, 58 (1999) 89-92.

[97] S. Ek, A. Root, M. Peussa, L. Niinistö, Determination of the hydroxyl group content in silica by thermogravimetry and a comparison with 1H MAS NMR results, Thermochimica Acta, 379 (2001) 201-212.

[98] C. Picard, A. Larbot, J. Sarrazin, P. Janknecht, P. Wilderer, Ceramic membranes for ozonation in wastewater treatment, Ann. chem. Sci. Master, 26 (2001) 13-22.

[99] H. Fang, J.F. Gao, H.T. Wang, C.S. Chen, Hydrophobic porous alumina hollow fiber for water desalination via membrane distillation process, Journal of Membrane Science, 403-404 (2012) 41-46.

[100] W.H. Lee, C.H. Bartholomew, Multiple reaction states in CO hydrogenation on alumina-supported cobalt catalysts, Journal of Catalysis, 120 (1989) 56-271.

[101] Ø. Borg, S. Eri, E.A. Blekkan, S. Storsæter, H. Wigum, E. Rytter, A. Holmen, Fischer–Tropsch synthesis over γ -alumina-supported cobalt catalysts: Effect of support variables, Journal of Catalysis, 248 (2007) 89–100.

[102] W.H. Zimmerman, D.B. Bukur, Reaction kinetics over iron catalysts used for Fischer-Tropsch Synthesis, The Canadian Journal of Chemical Engineering, 68 (1990) 292.

[103] W. Ma, G. Jacobs, U. Graham, B. Davis, Fischer–Tropsch Synthesis: Effect of K Loading on the Water–Gas Shift Reaction and Liquid Hydrocarbon Formation Rate over Precipitated Iron Catalysts, Topics in Catalysis, 57 (2014) 561-571.

[104] J.C.W. Kuo, Two stage process for conversion of synthesis gas to high quality transportation fuels, in, Mobil Research and Developement Corp., Paulsboro, N.J., 1985.

[105] A.M. Saib, M. Claeys, E.v. Steen, Silica supported cobalt Fischer–Tropsch catalysts: effect of pore diameter of support, Catalysis Today, 71 (2002) 395–402.

[106] A.Y. Khodakov, Fischer-Tropsch synthesis: Relations between structure of cobalt catalysts and their catalytic performance, Catalysis Today, 144 (2009) 251–257.

[107] A. Brenner, J. R. L. Burwell, The surface chemistry of molybdenum in states of lower oxidation on alumina, Journal of Catalysis, 52 (1978) 353-363.

[108] C.H. Bartholomew, M.W. Stoker, L. Mansker, A. Datye, Effects of pretreatment, recation, and promoter on microphase structure and Fischer-Tropsch activity of precipitated iron catalysts, Studies in Surface Science and Catalysis, 126 (1999) 265-272.

[109] T. Horiuchi, T. Osaki, T. Sugiyama, K. Suzuki, T. Mori, Maintenance of large surface area of alumina heated at elevated temperatures above 1300 C by preparing silica-containing pseudoboehmite aerogel, Journal of Non-Crystalline Solids, 291 (2001) 187-198.

[110] W.E.E. Stone, G.M.S.E. Shafei, J. Sanz, S.A. Selim, Association of soluble aluminum ionic species with a silica-gel surface: a solid-state NMR study, The Journal of Physical Chemistry, 97 (1993) 10127-10132.

[111] F.R. Chen, J.G. Davis, J.J. Fripiat, Aluminum coordination and Lewis acidity in transition aluminas, Journal of Catalysis, 133 (1992) 263-278.

[112] M. Heemeier, M. Frank, J. Libuda, K. Wolter, H. Kuhlenbeck, M. B¨aumer, H.-J. Freund, The influence of OH groups on the growth of rhodium on alumina: a model study, Catalysis Letters, 68 (2000) 19–24.

[113] A.K. Chakraborty, Range of solid solutions of silica in spinel type phase, Advances in Applied Ceramics, 105 (2006) 297-303.

[114] R.P. Mogorosi, N. Fischer, M. Claeys, E.v. Steen, Strong-metal–support interaction by molecular design: Fe–silicate interactions in Fischer–Tropsch catalysts, Journal of Catalysis, 289 (2012) 140-150.

[115] G.A. Fuentes, Catalyst deactivation and steady-state activity: A generalized power-law equation model, Applied Catalysis, 15 (1985) 33-40.

[116] M.D. Argyle, T.S. Frost, C.H. Bartholomew, Cobalt Fischer–Tropsch Catalyst Deactivation Modeled Using Generalized Power Law Expressions, Topics in Catalysis, 57 (2014) 415–429.

[117] J. van de Loosdrecht, F.G. Botes, I.M. Ciobica, A. Ferreira, P. Gibson, D.J. Moodley, A.M. Saib, J.L. Visagie, C.J. Weststrate, J.W. Niemantsverdriet, 7.20 - Fischer–Tropsch Synthesis: Catalysts and Chemistry, in: J. Reedijk, K. Poeppelmeier (Eds.) Comprehensive Inorganic Chemistry II (Second Edition), Elsevier, Amsterdam, 2013, pp. 525-557.

[118] G.E.P. Box, Fitting empirical data, Annals of the New York Academy of Sciences, 86 (1960) 792–816.

[119] P.G. Menon, Coke on catalysts - harmful, harmless, invisible and beneficial types Journal of Molecular Catalysis, 59 (1990) 207-220.

[120] G. Jacobs, P.M. Patterson, Y. Zhang, T. Das, J. Li, B.H. Davis, Fischer–Tropsch synthesis: deactivation of noble metal-promoted Co/Al2O3 catalysts, Applied Catalysis A: General, 233 (2002) 215–226.

[121] M.E. Dry, Sasol's Fischer-Tropsch experience, Hydrocarbon Processing, 61 (1982) 121-124.

[122] M.K. Niemela, A.O.I. Krause, The long-term performance of Co / SiO2 catalysts in CO hydrogenation, Catalysis Letters, 42 (1996) 161-166.

[123] H.W. Pennline, S.S. Pollack, Deactivation and regeneration of a promoted transition-metal-zeolite catalyst, Industrial & Engineering Chemistry Product Research and Development, 25 (1986) 11-14.

[124] M. Bremaud, P. Fongarland, J. Anfray, S. Jallais, D. Schweich, A.Y. Khodakov, Influence of syngas composition on the transient behavior of a Fischer–Tropsch continuous slurry reactor, Catalysis Today, 106 (2005) 137-142.

[125] D. Peña, A. Griboval-Constant, C. Lancelot, M. Quijada, N. Visez, O. Stéphan, V. Lecocq, F. Diehl, A.Y. Khodakov, Molecular structure and localization of carbon species in aluminasupported cobalt Fischer–Tropsch catalysts in a slurry reactor, Catalysis Today, 228 (2014) 65-76.

[126] W. Zhou, J.-G. Chen, K.-G. Fang, Y.-H. Sun, The deactivation of Co/SiO2 catalyst for Fischer–Tropsch synthesis at different ratios of H2 to CO, Fuel Processing Technology, 87 (2006) 609-616.

[127] M. Sadeqzadeh, S. Chambrey, J. Hong, P. Fongarland, F. Luck, D. Curulla-Ferré, D. Schweich, J. Bousquet, A.Y. Khodakov, Effect of Different Reaction Conditions on the Deactivation of Alumina-Supported Cobalt Fischer–Tropsch Catalysts in a Milli-Fixed-Bed

Reactor: Experiments and Modeling, Industrial & Engineering Chemistry Research, 53 (2014) 6913-6922.

[128] W. Ma, G. Jacobs, B. Todic, D.B. Bukur, B.H. Davis, Fischer-Tropsch synthesis: Influence of process conditions on deactivation of Ru and Re promoted 25%Co/Al2O3 catalysts, in: 23rd North American Catalysis Society Meeting, Louisville, Kentucky, US, 2013.

[129] P.H. Bolt, F.H.P.M. Habraken, J.W. Geus, Formation of Nickel, Cobalt, Copper, and Iron Aluminates fromα- andγ-Alumina-Supported Oxides: A Comparative Study, Journal of Solid State Chemistry, 135 (1998) 59-69.

[130] G. Jacobs, Y. Ji, B.H. Davis, D. Cronauer, A.J. Kropf, C.L. Marshall, Fischer–Tropsch synthesis: Temperature programmed EXAFS/XANES investigation of the influence of support type, cobalt loading, and noble metal promoter addition to the reduction behavior of cobalt oxide particles, Applied Catalysis A: General, 333 (2007) 177-191.

[131] G. Jacobs, W. Ma, B.H. Davis, Influence of Reduction Promoters on Stability of Cobalt/γ-Alumina Fischer-Tropsch Synthesis Catalysts, Catalysts, 4 (2014) 49-76.

[132] www.r-project.org.

[133] Q. Qin, D. Ramkrishna, Modeling of Surface Structure of Supported Catalysts. Application to Deactivation of FT Reactors Industrial & Engineering Chemistry Research, 43 (2004) 2912-2921.

[134] S. Storsæter, D. Chen, A. Holmen, Microkinetic modelling of the formation of C1 and C2 products in the Fischer–Tropsch synthesis over cobalt catalysts, Surface Science, 600 (2006) 2051–2063.

[135] A.J. van Dillen, R.J.A.M. Terörde, D.J. Lensveld, J.W. Geus, K.P. de Jong, Synthesis of supported catalysts by impregnation and drying using aqueous chelated metal complexes, Journal of Catalysis, 216 (2003) 257-264.

[136] D.H. Chun, J.C. Park, S.Y. Hong, J.T. Lim, C.S. Kim, H.-T. Lee, J.-I. Yang, S. Hong, H. Jung, Highly selective iron-based Fischer-Tropsch catalysts activated by CO2-containing syngas, Journal of Catalysis, 317 (2014) 135-143.

Appendix A. Calculations of expansion factor, rate of CO+H_2, P_{H2} and P_{CO}

Calculations of the expansion factor:

Two main reactions for Fe FTS:

$$CO + 2H_2 \rightarrow CH_2 + H_2O \qquad (1)$$

$$CO + H_2O \rightarrow CO_2 + H_2 \qquad (2)$$

Calculation is done for 40Fe/AlSi reported in Table 4.9.

$S_{CO2} = 46\%$ $S_{CH4} = 9.6\%$ $S_{C2H6} = 2.8\%$

We are assuming: $S_{C2H4} = 2.8\%$ $S_{C3} = 4\%$ $S_{C4} = 3\%$

$P_{H20} = 6$ atm $P_{CO0} = 9$ atm $P_{He} = 5$ atm

$y_{gas} = S_{CH4} + S_{C2H6} + S_{C2H4} + S_{C3} + S_{C4} = 22.2\%$

Overall reaction considering S_{CO2} of 46%:

$$CO + 0.62H_2 \rightarrow 0.54CH_2 + 0.46CO_2 + 0.08H_2O$$

Assumptions:
Water remains in gas phase
C_{5+} as liquid phase

1.62 + 5/9 (He) → 0.46 + 0.54 × y_{gas} + 5/9 (He)

2.17 moles → 1.13 moles

$$\varepsilon = \frac{N_T - N_{T0}}{N_{T0}}$$

$$\varepsilon = \frac{1.13-2.17}{1.13} = -0.479$$

Expansion factor for the given feed composition

Calculation of $r_{CO} + r_{H2}$ from r_{CO} and S_{CO2}:

$-r_{CO} = r_1 + r_2$ $-r_{H2} = 2r_1 - r_2$

$-r_{CO} - r_{H2} = 3r_1$

$- r_1 = -r_{CO} (1 - S_{CO2})$

$-(r_{CO} + r_{H2}) = -3 \times r_{CO} (1 - S_{CO2})$

Calculation of Pr_{H2} and P_{CO} in terms of X_{CO}:

$$P_{H2}(X_{CO}) = \frac{P_{H20} - 2P_{CO0} \times X_{CO}(1 - S_{CO2}) + P_{CO0} \times X_{CO} \times S_{CO2}}{(1 - \varepsilon_{CO} \times X_{CO})}$$

$P_{H2}(X_{CO}) = \frac{P_{H20} - P_{CO0} \times X_{CO}(3S_{CO2} - 2)}{(1 - \varepsilon_{CO} \times X_{CO})}$ Outlet P_{H2} in terms of X_{CO}

$P_{CO}(X_{CO}) = \frac{P_{CO0}(1 - X_{CO}(1 - S_{CO2}))}{(1 - \varepsilon_{CO} \times X_{CO})}$ Outlet P_{CO} in terms of X_{CO}

Appendix B. Comparison of integral and differential reactor performance

Rate and rate constant calculations with integral and differential methods:

Calculations are done for 40Fe/AlSi reported in Table 4.9 at X_{CO} = 72%.

P_{H20} = 0.6 MPa

P_{CO0} = 0.93 MPa

P_{tot} = 2.2 MPa

W = 0.2 g

V_{CO0} = 8.2 ml/min

X_{COf} = 0.72

S_{CO2} = 0.458

P_{STP} = 101325 Pa

T_{STP} = 273.15 K

R = 8.314 Pa.m^3/mol.K

$$F_{CO0} = \frac{P_{STP}.V_{CO}}{R.T_{STP}} = 21.952\ mmol/h$$

Integral method:

$$\frac{W}{F_{CO0}} = \int_0^{X_{COf}} \frac{1}{-r_{CO}} dX_{CO}$$

$$r_{CO} = k_{CO}.P_{CO}{}^{-0.221}.P_{H2}{}^{0.877}$$

$P_{CO} = f(X_{CO})$ See appendix A

$P_{H2} = f(X_{CO})$ See appendix A

$$k_{CO} = \frac{F_{CO0}}{W} \int_0^{X_{COf}} \frac{1}{k_{CO}.P_{CO}(X_{CO})^{-0.221}.P_{H2}(X_{CO})^{0.877}} dX_{CO}$$

$k_{CO} = 151.115\ \frac{mmol}{g.h.MPa^{0.656}}$ Integral value of CO rate constant

$$k_{COH2} = 3k_{CO}.(1 - \mathrm{S}_{\mathrm{CO2}})$$

$k_{COH2} = 245.713 \frac{mmol}{g.h.MPa^{0.656}}$ Integral value of CO+H_2 rate constant

$$X_{COave} = \frac{X_{COf}}{2} = 0.36$$

$r_{COave} = r_{CO}(X_{COave}) = 82.802 \ \frac{mmol}{g.h}$ Average rate from inlet to outlet of the reactor

Differential method:

$$r_{CO} = \frac{X_{COf}.F_{CO0}}{W} = 79.027 \ \frac{mmol}{g.h}$$

$$P_{H2ave} = \frac{P_{H20} + P_{H2}(X_{COf})}{2} = 0.458 \ MPa$$

$$P_{COave} = \frac{P_{CO0} + P_{CO}(X_{COf})}{2} = 0.891 \ MPa$$

$$k_{diff} = \frac{r_{CO}}{P_{COave}{}^{-0.221}.P_{H2ave}{}^{0.877}}$$

$k_{diff} = 152.677 \ \frac{mmol}{g.h.MPa^{0.656}}$ Differential value of CO rate constant using average values of P_{H2} and P_{CO}

$k_{error} = \frac{k_{diff} - k_{CO}}{k_{diff}} = 1.023\%$ The error between the integral and differential rate constant

Appendix C. Steady-state FB data for supported Fe catalyst (40Fe/AlSi)

Table C 1. Steady-state kinetic data for 40Fe/AlSi catalyst for T = 230-260°C, P_{H2} = 2-9 atm, P_{CO} = 3-9 atm and P = 20 atm.

T, °C	TOS, h	Inlet P_{H2}[a]	Inlet P_{CO}[a]	H_2/CO	CO rate[b]	H_2+CO rate[c]	X_{H2}	X_{CO}	HC Prod.[d]	S_{CH4}, %	S_{CO2}, %	S_{C2H6}, %	S_{C3+}, %
250	96	6.3	6.3	1.0	57.6	125.1	0.19	0.16	0.39	8.9	34.7	2.2	51.3
230	121	6.3	6.3	1.0	17.5	42.6	0.12	0.08	0.14	8.9	26.4	1.9	59.8
261	149	6.3	6.3	1.0	109.6	224.2	0.22	0.21	0.70	9.1	37.7	2.4	48.1
240	177	6.3	6.3	1.0	31.9	71.8	0.19	0.15	0.22	8.5	34.2	2.2	52.3
220	201	6.3	6.3	1.0	8.8	20.1	0.15	0.12	0.06	7.9	30.5	2.1	56.8
250	217	6.3	6.3	1.0	60.5	135.0	0.21	0.17	0.40	9.0	35.5	2.3	50.5
261	223	6.3	6.3	1.0	112.6	228.3	0.22	0.21	0.71	9.2	38.4	2.4	47.3
250	245	3.9	6.0	0.7	42.7	82.6	0.28	0.20	0.26	6.8	43.0	1.8	46.0
251	266	8.8	5.9	1.5	79.9	183.0	0.15	0.18	0.55	11.5	31.3	3.0	51.2
251	282	6.0	4.0	1.5	41.0	93.6	0.15	0.18	0.27	11.4	33.8	2.9	49.6
250	292	6.3	6.3	1.0	61.9	133.1	0.20	0.17	0.41	9.1	35.8	2.3	49.9
261	318	6.3	6.3	1.0	114.8	236.5	0.23	0.22	0.71	9.4	38.9	2.5	46.4
250	341	5.7	8.7	0.7	55.7	108.1	0.29	0.20	0.35	6.9	40.5	1.8	47.9
250	358	1.9	3.0	0.7	30.3	54.9	0.26	0.21	0.17	7.2	45.1	1.8	44.0
250	382	3.0	3.0	1.0	40.1	78.8	0.19	0.20	0.24	9.1	41.8	2.2	44.0
250	400	8.5	8.6	1.0	75.4	160.0	0.21	0.19	0.50	9.1	35.2	2.4	50.2
250	417	6.3	6.3	1.0	62.5	131.0	0.19	0.17	0.40	9.3	37.5	2.4	47.7
260	441	6.3	6.3	1.0	114.9	234.0	0.23	0.22	0.70	9.6	40.0	2.6	44.9
260	463	3.9	5.9	0.7	83.6	153.0	0.30	0.23	0.49	7.4	44.2	1.9	43.8
261	540	6.3	6.3	1.0	112.7	230.8	0.23	0.21	0.66	9.9	41.3	2.7	43.1
250	545	6.3	6.3	1.0	61.5	132.0	0.20	0.17	0.38	9.6	39.1	2.5	45.1
250	573	6.3	6.3	1.0	61.5	130.8	0.19	0.17	0.39	9.5	38.1	2.4	46.6
250	598	6.3	6.3	1.0	62.6	134.8	0.20	0.17	0.39	9.5	38.3	2.5	46.3
250	628	6.3	6.3	1.0	62.6	133.0	0.20	0.17	0.39	9.5	38.2	2.4	46.3
261	653	6.3	6.3	1.0	118.4	240.8	0.24	0.23	0.72	9.5	39.7	2.6	45.2
261	680	5.7	8.7	0.7	106.2	200.2	0.32	0.24	0.63	7.5	43.4	2.0	43.9
250	702	6.3	6.3	1.0	65.1	136.8	0.20	0.18	0.41	9.2	37.8	2.3	47.3
261	713	6.3	6.3	1.0	117.9	237.9	0.23	0.23	0.71	9.6	40.2	2.6	45.2

[a] atm

[b] mmol(CO)/g_{cat}/h

[c] mmol(CO+H_2)/g_{cat}/h

[d] g_{HC}/g_{cat}/h

Appendix D. Steady-state FB data in absence of deactivation for cobalt catalyst

The steady state activity and selectivity data in absence of deactivation for 25 wt% Co/0.25 wt% Pt/AlSi is presented in Table D.1.

Table D 1. Steady-state kinetic data for 25 wt% Co/0.25 wt% Pt/AlSi catalyst for T = 210-240°C, P_{H2} = 6-12 bar, P_{CO} = 2.6-6 bar and P = 20 bar.

T, °C	Inlet P_{H2}[a]	Inlet P_{CO}[a]	Feed H_2/CO	rate, mmol/g/h	X_{CO}	X_{H2}	HC Productivity, g_{HC}/g_{cat}/h	S_{CH4}, %	S_{CO2}, %	S_{C2H6}, %	S_{C3+}, %
210	11.96	3.99	3.00	17.4	0.13	0.10	0.15	26.60	0.31	1.36	71.73
210	7.96	5.98	1.33	15.7	0.16	0.25	0.16	12.26	0.87	1.14	85.73
210	7.95	4.01	1.98	14.4	0.22	0.22	0.14	21.08	0.56	2.73	75.63
210	7.98	2.67	2.99	12.2	0.28	0.19	0.10	32.12	0.48	1.90	65.51
210	5.97	4.00	1.49	11.1	0.17	0.25	0.11	16.12	0.92	1.46	81.50
220	11.96	3.99	3.00	36.9	0.14	0.08	0.33	25.63	0.38	1.65	72.34
219	7.97	3.99	2.00	26.6	0.10	0.12	0.25	20.76	0.61	1.63	77.00
219	7.97	5.98	1.33	27.8	0.07	0.11	0.28	14.28	0.98	1.26	83.48
220	5.98	3.99	1.50	22.7	0.08	0.14	0.22	17.67	1.00	1.65	79.68
219	7.99	2.65	3.01	25.8	0.15	0.11	0.22	27.86	0.55	2.00	69.60
220	11.96	3.99	3.00	34.8	0.13	0.08	0.32	25.45	0.34	1.59	72.62
231	7.97	4.00	1.99	69.9	0.15	0.17	0.67	19.95	0.82	3.11	76.12
235	7.98	2.66	3.00	103.3	0.30	0.24	1.05	28.03	0.92	3.12	67.93
232	7.96	5.98	1.33	56.4	0.07	0.12	0.57	14.62	1.33	1.41	82.64
231	5.99	3.99	1.50	50.2	0.09	0.13	0.44	17.13	1.13	1.76	79.98
232	11.96	3.99	3.00	91.2	0.15	0.12	0.68	26.55	0.50	1.92	71.02
231	7.97	4.00	1.99	67.5	0.14	0.16	0.66	19.80	0.83	3.01	76.36
239	7.96	3.99	1.99	100.0	0.19	0.21	0.95	19.80	1.06	2.25	76.89
242	11.96	3.99	3.00	146.8	0.24	0.19	1.09	37.03	1.23	3.87	57.87
238	5.98	3.99	1.50	70.0	0.14	0.21	0.69	16.92	1.46	1.94	79.68
238	7.97	5.98	1.33	65.2	0.09	0.15	0.65	15.43	1.53	1.55	81.49
241	7.98	2.65	3.01	134.5	0.33	0.24	1.15	28.62	0.89	3.95	66.54
239	7.96	3.99	1.99	95.1	0.17	0.20	0.93	19.90	0.98	2.20	76.92

[a] bar

Appendix E. Rate expression derivation for Model 8, Chapter 6

$$CO(g) + S \leftrightarrow CO - S \tag{1}$$

$$H_2(g) + 2S \leftrightarrow 2H - S \tag{2}$$

$$CO - S + H - S \rightarrow C - S + OH - S \tag{3}$$

$$CO - S + H - S \leftrightarrow HCO - S + S \tag{4}$$

$$HCO - S + H - S \leftrightarrow CH - S + OH - S \tag{5}$$

$$C - S + H - S \rightarrow CH - S + S \tag{6}$$

$$CH - S + H - S \rightarrow CH_2 - S + S \tag{7}$$

$$OH - S + H - S \rightarrow H_2O(g) + 2S \tag{8}$$

$$K_1 = \frac{\theta_{CO}}{P_{CO}\theta_V} \quad \Rightarrow \quad \theta_{CO} = K_1 P_{CO} \theta_V$$

$$K_2 = \frac{{\theta_H}^2}{P_{H2}\theta_V} \quad \Rightarrow \quad \theta_H = {K_2}^{1/2} {P_{H2}}^{1/2} \theta_V$$

$$K_4 = \frac{\theta_{HCO}\theta_V}{\theta_{CO}\theta_H} \quad \Rightarrow \quad \theta_{HCO} = \frac{K_4 \theta_{CO} \theta_H}{\theta_V} = K_1 {K_2}^{1/2} K_4 P_{CO} {P_{H2}}^{1/2} \theta_V$$

$$\frac{d\theta_C}{dt} = 0 \;\; \Rightarrow \; r_3 = r_6 \; \Rightarrow \;\; k_3 \theta_{CO} \theta_H = k_6 \theta_C \theta_H \;\; \Rightarrow \;\; \theta_C = \frac{k_3}{k_6} K_1 P_{CO} \theta_V$$

$$\frac{d\theta_{CH}}{dt} = 0 \; \Rightarrow \; r_7 = r_5 + r_6$$

$$\frac{d\theta_{OH}}{dt} = 0 \; \Rightarrow \; r_8 = r_5 + r_3$$

r_5 is quasi-equilibrium; therefore, the net is zero.

$\Rightarrow r_7 = r_6$ and $r_8 = r_3$ but since $r_3 = r_6$, then $r_8 = r_7$.

$$r_8 = r_7 \;\; \Rightarrow \; k_7 \theta_{CH} \theta_H = k_8 \theta_{OH} \theta_H \;\; \Rightarrow \;\; \theta_{OH} = \frac{k_7}{k_8} \theta_{CH}$$

$K_5 = \frac{\theta_{OH}\theta_{CH}}{\theta_{HCO}\theta_H} \;\Rightarrow\; {\theta_{CH}}^2 = \frac{K_5 k_8}{k_7}\theta_{HCO}\theta_H \;\Rightarrow\; \theta_{CH} = \left(\frac{K_1K_2K_4K_5k_8}{k_7}\right)^{1/2} {P_{CO}}^{1/2}{P_{H2}}^{1/2}\theta_V$

Site balance:

$$1 = \theta_V + \theta_{CO} + \theta_H + \theta_C + \theta_{HCO} + \theta_{CH} + \theta_{OH}$$

$$1 = \theta_V + K_1P_{CO}\theta_V + {K_2}^{1/2}{P_{H2}}^{1/2}\theta_V + \frac{k_3}{k_6}K_1P_{CO}\theta_V + K_1{K_2}^{1/2}K_4P_{CO}{P_{H2}}^{1/2}\theta_V +$$

$$\left(\frac{K_1K_2K_4K_5k_8}{k_7}\right)^{1/2}\;(1+\frac{k_7}{k_8}){P_{CO}}^{1/2}{P_{H2}}^{1/2}\,\theta_V$$

If we assume r_7 is hydrogenation step:

$r_{HC\,formation} = r_{CH2} = r_7 = k_7\theta_{CH}\theta_H$

$$r = \frac{(K_1K_4K_5k_7k_8)^{1/2}K_2{P_{CO}}^{1/2}P_{H2}}{\left(1 + K_1P_{CO} + {K_2}^{1/2}{P_{H2}}^{1/2} + \frac{k_3}{k_6}K_1P_{CO} + K_1{K_2}^{1/2}K_4P_{CO}{P_{H2}}^{1/2} + \left(\frac{K_1K_2K_4K_5k_8}{k_7}\right)^{1/2}(1+\frac{k_7}{k_8}){P_{CO}}^{1/2}{P_{H2}}^{1/2}\right)^2}$$

If we assume θ_{CO}, θ_H, θ_C as MASI, then:

$$r = \frac{(K_1K_4K_5k_7k_8)^{1/2}K_2{P_{CO}}^{1/2}P_{H2}}{\left(1 + K_1P_{CO} + {K_2}^{1/2}{P_{H2}}^{1/2} + \frac{k_3}{k_6}K_1P_{CO}\right)^2} = \frac{(K_1K_4K_5k_7k_8)^{1/2}K_2{P_{CO}}^{1/2}P_{H2}}{\left(1 + (1+\frac{k_3}{k_6})K_1P_{CO} + {K_2}^{1/2}{P_{H2}}^{1/2}\right)^2}$$